INEEL/EXT-04-02561

In-Vessel Retention Strategy for High Power Reactors

Final Report

Idaho National Engineering and Environmental Laboratory:
J. L. Rempe, Lead U. S. Principal Investigator

Seoul National University:
K. Y. Suh, Lead Korean Principal Investigator

Pennsylvania State University:
F. B. Cheung, U. S. Collaborating Principal Investigator

Korea Atomic Energy Research Institute:
S. B. Kim, Korean Collaborating Principal Investigator

January 2005

Idaho National Engineering and Environmental Laboratory
Bechtel BWXT Idaho, LLC

INEEL/EXT-04-02561

In-Vessel Retention Strategy for High Power Reactors

Final Report

Idaho National Engineering and Environmental Laboratory:
J. L. Rempe, Principal Investigator

Seoul National University:
K. Y. Suh, Principal Investigator

Pennsylvania State University:
F. B. Cheung, Principal Investigator

Korea Atomic Energy Research Institute:
S. B. Kim, Principal Investigator

January 2005

Idaho National Engineering and Environmental Laboratory
Idaho Falls, Idaho 83415

Prepared for the
U.S. Department of Energy
Assistant Secretary for
Environmental Management
Under DOE Idaho Operations Office
Contract DE-AC07-99ID13727

INTERNATIONAL NUCLEAR ENERGY RESEARCH INITIATIVE

Project Title: In-vessel Retention Strategy for High Power Reactors

Principal Investigator (U.S.):
Joy Rempe
Idaho National Engineering and Environmental Laboratory, INEEL

Principal Investigator (International):
K. Y. Suh, Seoul National University (SNU)

Collaborators:
F. B. Cheung, Pennsylvania State University (PSU)
S. B. Kim, Korea Atomic Energy Research Institute, (KAERI)

Project Number: 2002-022-K (Task II)

Project Start Date: January 1, 2002

Project End Date: December 31, 2004

EXECUTIVE SUMMARY

In-vessel retention (IVR) of core melt is a key severe accident management strategy adopted by some operating nuclear power plants and proposed for some advanced light water reactors (ALWRs). If there were inadequate cooling during a reactor accident, a significant amount of core material could become molten and relocate to the lower head of the reactor vessel, as happened in the Three Mile Island Unit 2 (TMI-2) accident. If it is possible to ensure that the vessel head remains intact so that relocated core materials are retained within the vessel, the enhanced safety associated with these plants can reduce concerns about containment failure and associated risk. For example, the enhanced safety of the Westinghouse Advanced 600 MWe PWR (AP600), which relied upon External Reactor Vessel Cooling (ERVC) for IVR, resulted in the U.S. Nuclear Regulatory Commission (US NRC) approving the design without requiring certain conventional features common to existing LWRs. However, it is not clear that currently proposed external reactor vessel cooling (ERVC) without additional enhancements could provide sufficient heat removal for higher-power reactors (up to 1500 MWe). Hence, a collaborative, three-year, U.S. - Korean International Nuclear Energy Research Initiative (INERI) project was completed in which the Idaho National Engineering and Environmental Laboratory (INEEL), Seoul National University (SNU), Pennsylvania State University (PSU), and the Korea Atomic Energy Research Institute (KAERI) investigated the performance of ERVC and an in-vessel core catcher (IVCC) to determine if IVR is feasible for reactors up to 1500 MWe.

Research Objective

As an ultimate objective, this project developed specific recommendations to improve the margin for IVR in high-power reactors. The systematic approach applied to develop these recommendations combined state-of-the-art analytical tools and key U.S. and Korean experimental facilities. Recommendations focussed on modifications to enhance ERVC (improved data, vessel coatings to enhance heat removal, and an enhanced vessel/insulation configuration to facilitate steam venting) and modifications to enhance in-vessel debris coolability (enhanced IVCC configuration, thickness, and material). Improved analytical tools and experimental data were used to evaluate options that could increase the margin associated with these modifications. This increased margin has the potential to improve plant economics (owing to reduced regulatory requirements) and increase public acceptance (owing to reduced plant risk). This program focussed on the Korean Advanced Power Reactor -1400 MWe (APR1400) design. However, margins offered by each modification were evaluated such that results can easily be applied to a wide range of existing and advanced reactor designs.

Report Content and Organization

This final report highlights key accomplishments from this project. Section 1 provides introductory information about the project organization and the APR1400 plant design on which this project focussed. Detailed information about the objectives and accomplishments from each task completed in this project may be found in Sections 2 through 5. Section 6 highlights results and conclusions that can be drawn from results obtained from each task. Section 7 provides programmatic information, such as the status of each task with respect to planned schedule and budget. This executive summary is provided to highlight accomplishments from this research project.

Project Approach and Organization

As indicated in Figure ES-1, this three-year project included four tasks. In Task 1, which was completed during the first year of this research program, calculations were conducted to define representative bounding late phase melt conditions. Characteristic parameters from those bounding conditions (thermal loads, pressure, relocated mass, etc.) were used to design an optimized in-vessel core catcher (IVCC) in Task 2 and ERVC enhancements in Task 3. Task 2 and 3 activities, which were initiated in the first year of this project, were completed during the third year of this project. In Task 4, collaborators assessed the improved margin obtained with Task 2 and 3 design modifications. As shown in Figure ES-2, key U.S. and Korean experimental facilities and state-of-the-art analytical tools were applied to investigate options that could enhance ERVC and IVCC performance.

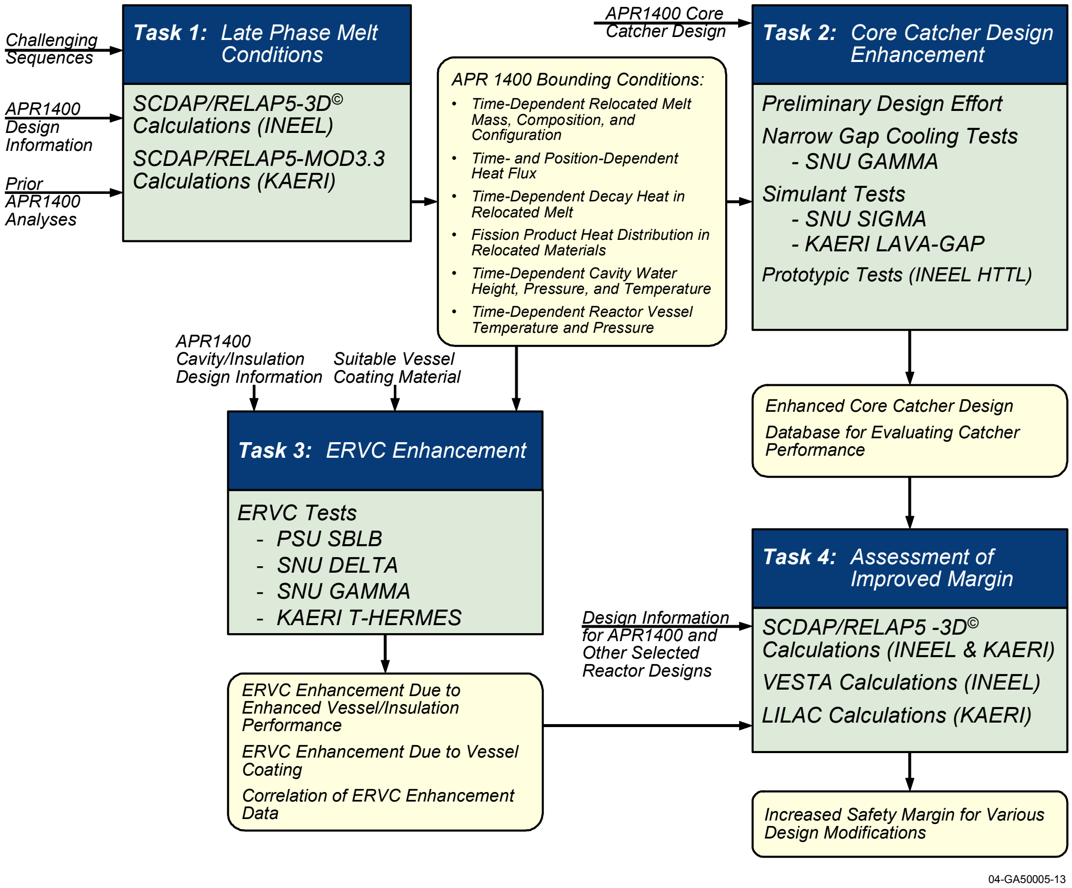

Figure ES-1. Project approach

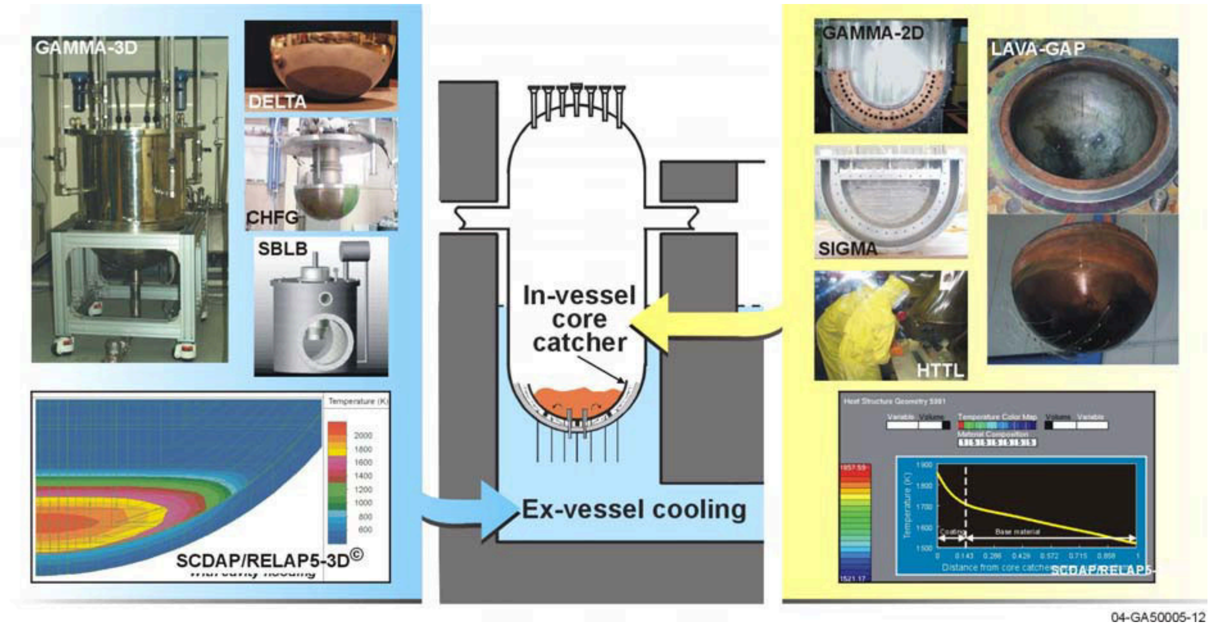

Figure ES-2. Key U.S. and Korean experimental facilities and state-of-the-art analytical tools applied to investigate options that could enhance ERVC and IVCC performance.

Key Program Accomplishments

Key accomplishments from this three year program are highlighted in this section. Note that these accomplishments include items required to meet task objectives outlined in the original proposal for this project and items that meet overall NERI objectives. As indicated below, this project not only advanced the state-of-the art in research pertaining to IVR, but also helped prepare graduate students to join the nuclear engineering workforce.

➔ ***Task 1 SCDAP/RELAP5-3D© and SCDAP/RELAP5MOD3.3 calculations completed to provide late-phase melt conditions.***

The objective of the Task 1 effort was to obtain quantify representative late-phase melt conditions that could affect the potential for IVR of core melt following a severe accident in the APR1400. The late-phase melt conditions of specific interest include the melt mass and its composition, temperature, and power (due to decay heat generation). Several severe accident transients were selected for analysis that would lead to bounding estimates of the potential melt conditions. Results generated through completion of this task were used as inputs in the design of a core catcher (in Task 2) and the enhancement of ERVC (in Task 3). The results were also used in Task 4 as base values to estimate improvements in IVR margins that could be achieved through incorporation of concepts developed through the Task 2 and 3 design efforts. To accomplish the task objective, INEEL applied the SCDAP/RELAP5-3D© code and KAERI applied the SCDAP/RELAP5/MOD3.3 and SCDAP/RELAP5-3D© codes to the APR1400 plant. As indicated in Figure ES-3, fairly detailed plant models were developed using information from Korea Hydro and Nuclear Power Company, Ltd.[ES-2] KAERI and INEEL models and input were similar, except for modifications that allowed the SCDAP/RELAP5/MOD3.3 input to be used as input for SCDAP/RELAP5-3D©. Some of the key conclusions and insights from this task are highlighted below.

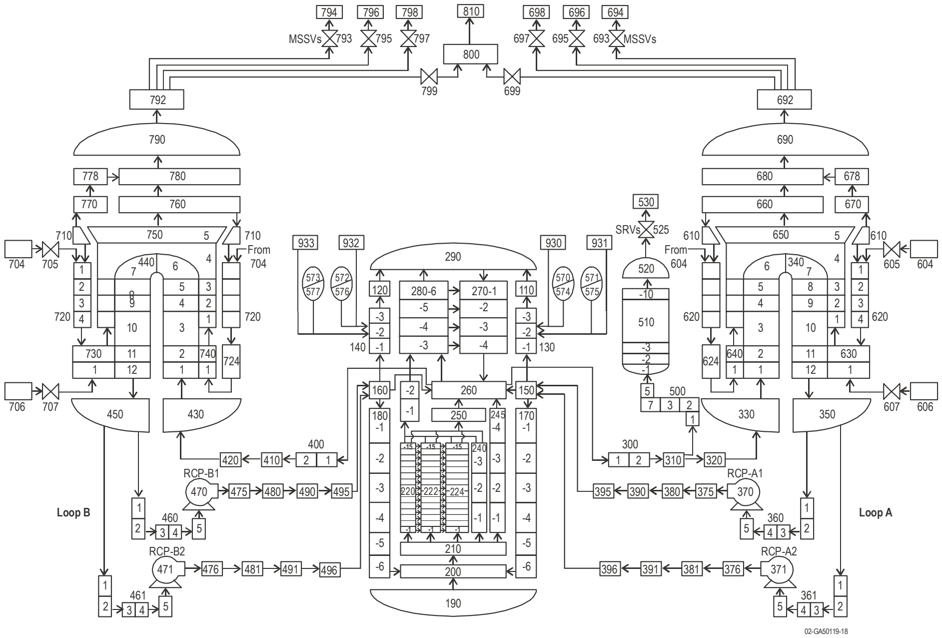

Figure ES-3. INEEL SCDAP/RELAP5-3D© model nodalization of APR1400.

SBO and LOCA transients were selected for analysis.

Although an extensive series of severe accident calculations is required to identify bounding transients, Loss of Coolant Accidents (LOCAs), Station BlackOuts (SBOs), and Loss of FeedWater (LOFW) scenarios were assumed to be major IVR scenarios. Accordingly, a cold leg break (representing the LOCA response) and an SBO with LOFW (to combine remaining dominant IVR scenarios) were selected for analysis.

SCDAP/RELAP5/MOD3.3 results are similar to SCDAP/RELAP5-3D© results.

Predicted values for vessel failure time, hydrogen generation, melt relocation masses, melt relocation volumes, decay heat in the relocated corium, and power densities in the relocated corium were compared. As indicated in Table ES-1, differences are not considered significant.

Table ES-1. Comparison of the SCDAP/RELAP5/Mod3.3 results with SCDAP/RELAP5-3D© results.

	SBO		**Large Break LOCA (9.6 inch Break)**	
	MOD3.3	**MOD-3D©**	**MOD3.3**	**MOD-3D©**
Reactor Vessel Failure Time (sec)	13242	11100	4910	4990
Total H_2 Generation Mass (kg)	836	912	139	169
Total Power (MW)	44.8	47.4	57.9	51.2
Total Corium Mass in the LP (ton)	142.9	145.0	114.1	119.0
Corium Volume in the LP (m^3)	18.5	19.0	13.8	14.7
Power Density (MW/m^3)	2.23	2.49	3.97	3.48

Calculation results indicate a LOCA yields the most severe lower head thermal loads.

A 0.0465 m^2 break in one of the cold legs in the primary coolant loop containing the pressurizer resulted in core melt and relocation into the lower head by 4,990 s (see Table ES-2). The timing of this relocation was earlier than all other transients analyzed (by as much as 6,110 s). Consequently, power retained in the melt was relatively high (because the decay period after reactor trip was relatively short). The high decay power associated with this relocation yielded the highest thermal load for the APR1400 lower head.

Table ES-2. Late-phase melt conditions predicted by SCDAP/RELAP5-3D© for APR1400 transients.

		Relocated Mass (kg)				**Corium Characteristics at Time of Relocation**				
Transient	**Time of Relocation (s)**	**UO_2**	**ZrO_2**	**Zr**	**Total**	**Depth (m)**	**Temperature (K)**	**Power (MW)**	**Power Density (MW/m^3)**	**Average Vessel Heat Flux (MW/m^2)[a]**
SBO	10,600	111,000	21,200	8,300	144,000[b]	1.86	3,390	52.0	2.72	0.161 to 1.45
LOCA	4,990	108,000	5,180	3,520	119,000[c]	1.60	3,460	51.2	3.48	0.182 to 1.64

a. Assuming a hemispherical configuration, without sensible heat effects, for quasi-steady conditions, with estimated limits of heat loss from the upper corium surface (at 10 and 90% of the total decay heat level).

b. Includes 250 kg Zr, 2,350 kg of control rod absorber material, and 180 kg of stainless steel from earlier relocations.

c. Includes 276 kg Zr, 2,350 kg of control rod absorber material, and 95 kg of stainless steel from earlier relocations. Note VESTA calculations considered additional melting of structural material for cases where vessel failure is delayed (e.g., the base case mass of SS was assumed as 100,000 kg.

Late-phase melt conditions include large masses that relocate at high temperatures.

Regardless of the transient considered, results for all calculations include relocation of large melt masses (~100,000 kg total, or more) at high temperatures (~3,000 K, or higher). These results appear to be consistent with the nature of the transients considered. Specifically, all cases involved complete core dryout and subsequent core heatup in a steam environment. Protracted periods (~1 h, or more) of complete core uncovery were sustained in each calculation, leading to development of large core melt masses at temperatures well above the fuel liquidus.

In the absence of any ERVC enhancements, estimated heat fluxes that must be removed from the lower head to ensure IVR of core melt in APR1400 exceed predicted heat fluxes and corresponding CHF values predicted for the Westinghouse AP600 reactor.

Estimated lower head average heat fluxes for the APR1400 transients considered ranged from 0.147 to 1.64 MW/m^3, which exceed peak lower head heat fluxes predicted for the Westinghouse AP600 reactor by factors as high as ~2.3. Furthermore, the estimated APR1400 average heat fluxes exceed the current estimates of the maximum CHF by as much as a factor of ~1.2. These results indicate IVR may not be feasible without additional measures such as the use of a core catcher and/or modifications to enhance ERVC.

➔ ***Task 2 activities to develop and evaluate an enhanced In-Vessel Core Catcher completed.***

The objective of Task 2 was to develop an enhanced in-vessel core catcher (IVCC) design for the APR1400 and provide sufficient data to evaluate if this design will enhance in-vessel debris coolability in the reactor. The approach adopted for developing an APR1400 IVCC design is illustrated in Figure ES-4.

As shown in this figure, initial efforts focused on developing a preliminary in-vessel design. This was done at INEEL using a combination of scoping materials, flow, thermal, and structural analyses and scoping materials interaction tests. In addition, more detailed experimental data were obtained in two areas to support analysis of this IVCC. First, data were needed to estimate the heat that can be removed from the narrow "engineered" gap between the IVCC and the inner surface of the reactor vessel. As indicated in Figure ES-4, data were obtained from the GAMMA facilities at SNU and the CHFG facility at KAERI to formulate a complete "narrow gap" boiling curve. Second, data were needed to understand the heat loads to the core catcher and demonstrate the viability of materials proposed for the IVCC. As illustrated Figure ES-4, these needs were addressed by conducting tests in several facilities: the SIGMA facilities at SNU were used to develop natural convection heat transfer correlations, the LAVA-GAP facility at KAERI was used to assess the impact of the IVCC on thermal heat loads to the vessel, and INEEL's High Temperature Test Laboratory (HTTL) was used to assess the potential for materials interactions.

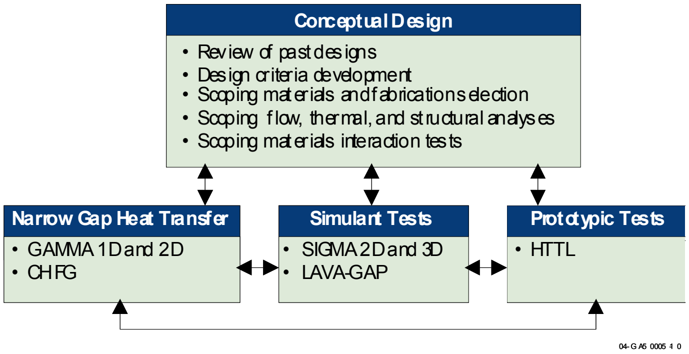

Figure ES-4. Task 2 approach to developing an enhanced core catcher design.

Evaluations completed in this INERI suggest that the proposed IVCC concept is viable and will reduce heat loads to the vessel for a range of severe accident conditions. However, it should be noted that only preliminary IVCC design and evaluations were completed in this INERI. More detailed analyses and testing are needed before an IVCC could be implemented into a reactor. In particular, tests are needed to confirm the long-term endurance of proposed materials to hydrodynamic loads during operating and accident conditions. In addition, confirmatory tests of irradiation and coolant chemistry effects on coating performance may be warranted. Key conclusions and insights from this effort are summarized below.

Conceptual IVCC design for the APR1400 completed.

Several in-vessel and ex-vessel core catcher concepts proposed in the literature were reviewed by INEEL as an initial step for developing an IVCC design. After reviewing these various approaches, a list of design goals and criteria was formulated for developing an APR1400 IVCC design. These goals and criteria provided guidance in selecting the configuration, dimensions, and materials for the APR1400 IVCC. As shown in Figure ES-5, the core catcher design proposed by INEEL in this INERI consists of several interlocking sections that are machined to fit together when inserted into the lower head. The use of interconnected sections of the core catcher reduces manufacturing costs and simplifies installation. Each section of the IVCC consists of two material layers with an option to add a third layer (if deemed necessary): a base material, which has the capability to support and contain the mass of core materials that may relocate during a severe accident; an oxide coating material on top of the base material, which resists interactions with high-temperature core materials; and an optional coating on the bottom side of the base material to prevent any potential oxidation of the base material during the lifetime of the reactor.

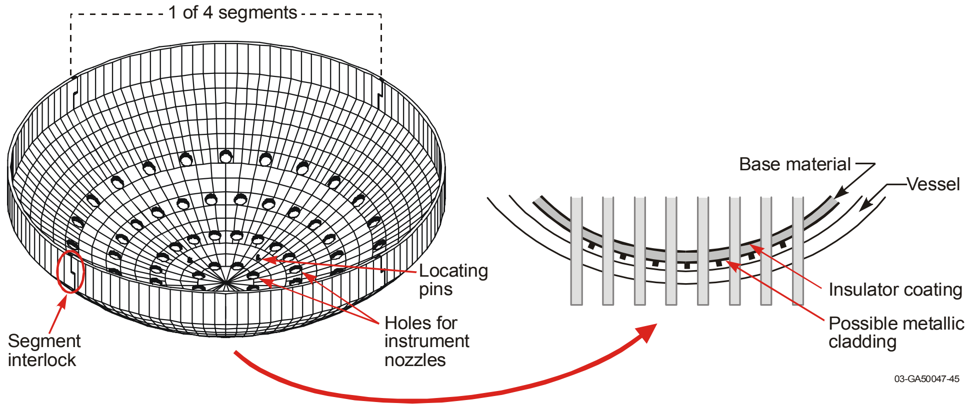

Figure ES-5. Conceptual design of proposed APR1400 IVCC design.

Scoping analyses and materials testing used to select IVCC materials

INEEL used a combination of scoping materials, flow, thermal, and structural analyses and scoping materials interaction tests (see Figure ES-6) to identify IVCC materials. Results suggest that the core catcher base material should be either carbon steel or a stainless steel, such as SS 304. However, the use of stainless steel is recommended because it would preclude the need for a corrosion-resistant undercoating on the IVCC. Evaluation efforts suggest that the insulator coating should be applied using thermal plasma spray techniques. Although several coatings appear viable, results suggest that the insulator coating should consist of a 500 µm thick ZrO_2 coating over a 100-200 µm thick bond coating of Inconel 718.

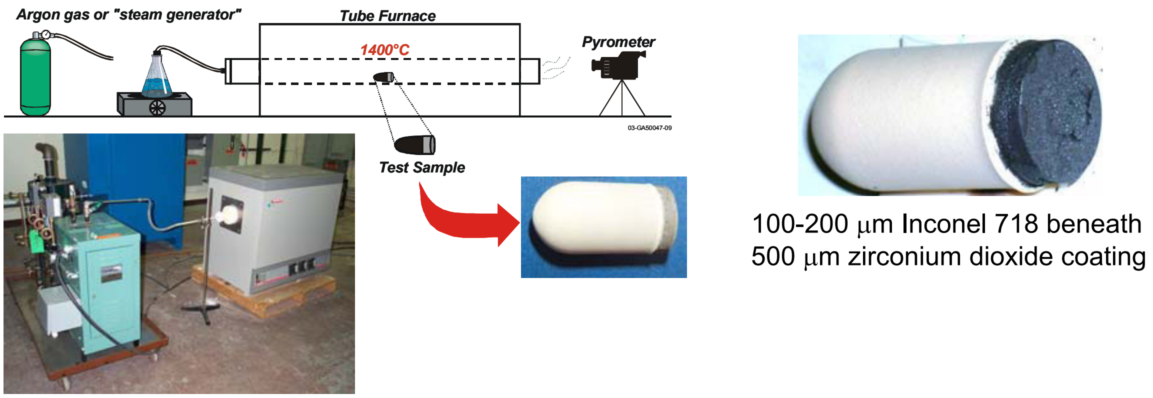

Figure ES-6. Setup for high temperature materials testing in steam with sample before and after testing.

Key insights and a new correlation to quantify heat transfer in the narrow gap between the IVCC and the reactor vessel lower head developed using GAMMA facilities.

SNU completed a series of fundamental studies to develop engineering correlations and to visualize the complex flow patterns in narrow gaps using the GAMMA 1D (Gap Apparatus Mitigating Melt Attack One Dimensional) apparatus. In addition, the GAMMA 2D (Gap Apparatus Mitigating Melt Attack Two Dimensional) experiments were performed to investigate the effects of gap size and pressure on CHF. Key insights from these studies are summarized below.

- The gap size and surface orientation effects play an important role in interpreting the general two-phase flow behavior as well as the CHF data. There exists a critical gap size commensurate to the average vapor layer thickness that enhances the heat transfer rate with increasing mass flux at certain surface orientations.
- The CHF generally increases as the gap size increases, but the increasing rate decreases as the gap increases. In particular, the CHF in the 10 mm gap is smaller than the value at any other gap sizes at the fully downward-facing location, 180°. At the vertical location, 90°, as is generally believed, the CHF increases as the gap size increases. The CHF in gap boiling is affected by the gap size as well as by the induced flow within the channel.
- There is a transition angle for each gap size. The transition angle increases as the gap size increases in this study. The transition angles for the 2, 5 and 10 mm gaps in this study were found to be 165°, 170° and 175°, respectively. However, the transition angle was not discernible for the gap size of 1 mm and the pool boiling in the unconfined space.
- A semi-empirical CHF correlation was developed for the near-vertical gap boiling using dimensional analysis of the CHF during natural convective boiling in confined channels because the existing correlation could not reasonably predict the data obtained in this study. This correlation agrees with the experimental data within ± 20%.

Using results from this INERI, SNU recommends that the correlations summarized in Table ES-3 be applied for predicting heat transfer in the narrow gap between the IVCC and the reactor vessel.

Table ES-3. Recommended correlations.

Film boiling	**Layer thickness (10), critical vapor film Re (25.1)**	
Nucleate and transition boiling $\frac{q''}{\Delta T_{sat}}\frac{L}{k_l} = C\left[\frac{k_l \Delta T_{sat}}{\rho_g \Delta h_{lv} v_l}\right]^{n1}\left[\frac{pL}{\sigma}\right]^{n2}$ $L = \left[\frac{\sigma}{g(\rho_l - \rho_v)}\right]^{0.5}$	Transition boiling	C=1.2×10^{14}; n1=-5.5, n2=0.32
	Nucleate boiling (higher wall superheat)	C=2.2; n1=-0.1, n2=0.32
	Nucleate boiling (lower wall superheat)	C=1.1; n1=0.3, n2=0.32
CHF $\frac{q''_{CHF}}{\rho_v h_{lv}}\sqrt[4]{\frac{\rho_v^2}{g\sigma(\rho_l - \rho_v)}} = C$	Flow instability	CCFL
	$C = 0.151\sin^{0.25}\theta$	$C = \frac{0.1042\left(\sin\theta / 1-\cos\theta\right)^{e}}{1 + 0.1375\left(\rho_v / \rho_l\right)^{0.21} D / s}$ $e = -0.3944\ln\frac{s}{1.0} + 2.02 \quad (0.5 \le s \le 5)$

New data and insights about the heat load from relocated corium to the IVCC obtained using SIGMA tests.

The SIGMA (Simulant Internal Gravitated Material Apparatus) tests considered high modified Rayleigh number, Ra′, turbulent natural convection in a molten pool. The internal heating method is employed in the test by using cable-type heaters. The main results include the heat split fraction, angular heat flux distribution, and temperature distribution inside the molten pool. Tests were conducted in SIGMA 2D, which is a two-dimensional semicircular pool with diameter, height, and width of 500 mm, 250 mm, and 100 mm and in SIGMA 3D, which is a hemispherical pool employing the same internal heating method used in SIGMA 2D (see Figure ES-7). Some key insights gained from these tests are discussed below.

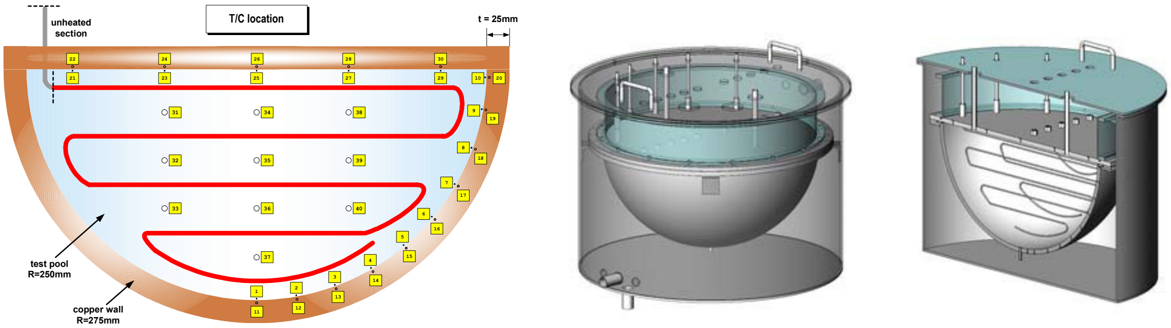

(a) SIGMA 2D

(b) SIGMA 3D

Figure ES-7. Schematics of SIGMA test sections

- The average Nu_{up} numbers obtained from SIGMA tests concur with most of the literature data. The average Nu_{dn} numbers obtained from SIGMA tests fall between data obtained from the literature.
- The ratio of the local to average Nu on the upper wall was unity at all locations. The heat flux profile along the lower wall and average upward heat transfer within this Ra′ range were in good agreement with the data obtained from previous numerical and experimental studies. The heat input increase results in an increase in Nu_{up} and Nu_{dn}, but with no change in the heat split ratio (Nu_{up}/Nu_{dn}) which was about 1.7, except for the case where $Ra' = 2.94\times10^{12}$ and Nu_{up}/Nu_{dn} = 2.1. The lowest heat transfer occurred at the bottom of the pool, which was a stagnation point, while the highest value was observed in the upper corner of the pool.
- When the top surface of the pool was insulated, the local heat flux was greater than in the uninsulated case by about 6%. In case of the adiabatic upper boundary condition, the internal heat transported by the strong buoyancy-induced flows was transferred sideward rather than upward in the upper region.

Simulant melt experiments in the LAVA-GAP facility completed to investigate the thermal and metallurgical performance of the IVCC.

The main objectives of the KAERI LAVA-GAP experiments were to examine the feasibility and sustainability of the IVCC under the various test conditions using hemispherical test sections and simulant melt. The uniqueness of the LAVA-GAP experiments is its ability to provide thermal and metallurgical data on the performance of an internally coated hemispherical IVCC in direct contact with high temperature simulant melt in a unique one-tenth scale facility (see Figure ES-8). As part of this INERI, a total of six tests (see Table ES-4) were completed that evaluated the impact of vary several condition parameters, such as the material of IVCC base material, the gap size between the IVCC and the lower head vessel, and the insulator coating and bond coat material. The major technical conclusions from the these simulant tests and associated LILAC calculations are discussed below.

Table ES-4. LAVA-GAP experimental test conditions.

Test	Simulant Melt	Gap Size	Base Steel	Insulator Coating	Bond Coat
LAVA-GAP-2	Al_2O_3, 60kg	10 mm	Carbon steel	Not applied	Not applied
LAVA-GAP-3	Al_2O_3, 60kg	10 mm	Carbon steel	92% ZrO_2 + 8% Y_2O_3, 0.5 mm	95% Ni + 5% Al
LAVA-GAP-4	Al_2O_3, 60kg	5 mm	Stainless steel	92% ZrO_2 + 8% Y_2O_3, 0.5mm	95% Ni + 5% Al
LAVA-GAP-5	Al_2O_3, 60kg	5 mm	Stainless steel	92% ZrO_2 + 8% Y_2O_3, 0.6mm	Not applied
LAVA-GAP-6	Al_2O_3, 60kg	10 mm	Stainless steel	92% ZrO_2 + 8% Y_2O_3, 0.5mm	Inconel 718
LAVA-GAP-7	Al_2O_3, 60kg	5 mm	Stainless steel	92% ZrO_2 + 8% Y_2O_3, 0.5mm	Inconel 718

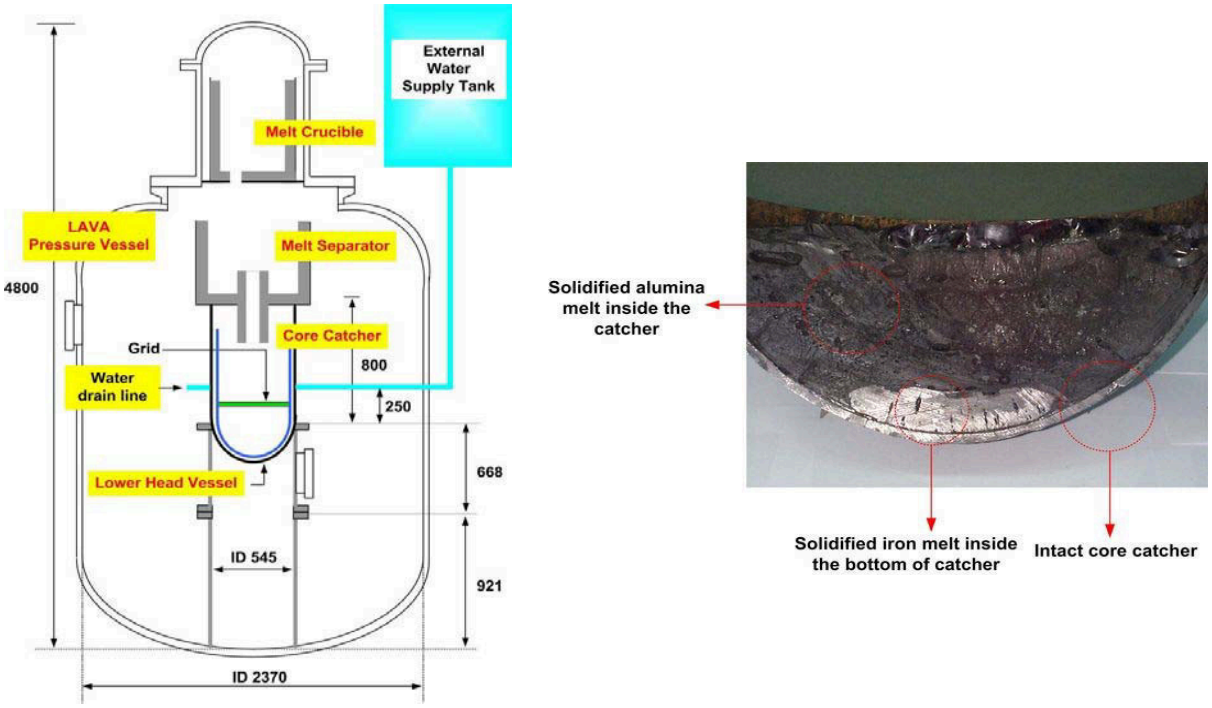

Figure ES-8. Schematic diagram of the LAVA-GAP facility (dimensions in mm) with LAVA-GAP-3 test section.

- In several tests (LAVA-GAP-2 and LAVA-GAP-3), the internally coated IVCC has better thermal performance compared with the uncoated IVCC.
- LILAC calculation results suggest that the coating layer lessened the thermal attack transferred to the core catcher and improved the integrity of the core catcher for LAVA-GAP-3 test conditions.
- Metallurgical inspections for the LAVA-GAP-3 test specimen indicate that the base carbon steel showed stable and pure chemical compositions without any oxidation and interaction with the internal coating layer. Hence, these metallurgical inspection results suggest that the ZrO_2 coating protected the carbon steel base material.

- In other tests, internally coated core catchers experienced failures. These failures were attributed to differences in experimental conditions, such as gap size and material of the base steel. For example, the 5 mm thick gap in the LAVA-GAP-4 and LAVA-GAP-5 tests imply that this gap size is too narrow to allow sufficient water ingression and steam venting. It should also be noted that the LAVA-GAP test conditions were conservative in that there was no water present inside the IVCC (as expected to be present during a severe accident in an LWR).
- LAVA-GAP tests suggest that the IVCC heat removal capability be enhanced by increasing the gap size between the IVCC and the vessel lower head (the gap size should be larger than 5 mm) and that the outer surface of the IVCC be coated with a microporous coating to enhance heat transfer from the IVCC.

HTTL prototypic materials tests investigate IVCC thermal and metallurgical performance.

Prototypic tests were completed to evaluate if candidate core catcher materials interact with high-temperature materials expected to relocate during a severe accident. Figure ES-9 shows the test assembly used for prototypic testing at the INEEL High Temperature Test Laboratory (HTTL). As shown in Figure ES-9, the crucible stands within a stainless steel enclosure ideally suited for high temperature testing with radioactive materials. Within the carbon steel crucible are placed high temperature, insulating materials. The simulated core catcher or “trough” was fabricated by machining out a curved region in a rectangular stainless steel (SS 304) block on which thermal plasma spraying techniques were used to apply a 100-200 µm bond coat of Inconel 718 beneath a 500 µm thick coating of zirconium dioxide. Results from prototypic tests indicate that proposed core catcher materials and coatings would provide additional protection to the reactor vessel from materials that relocate from the reactor core during a severe accident. Tests conducted in inert and steam conditions indicate that the proposed coating materials protect the core catcher substrate without any interactions with prototypic corium materials.

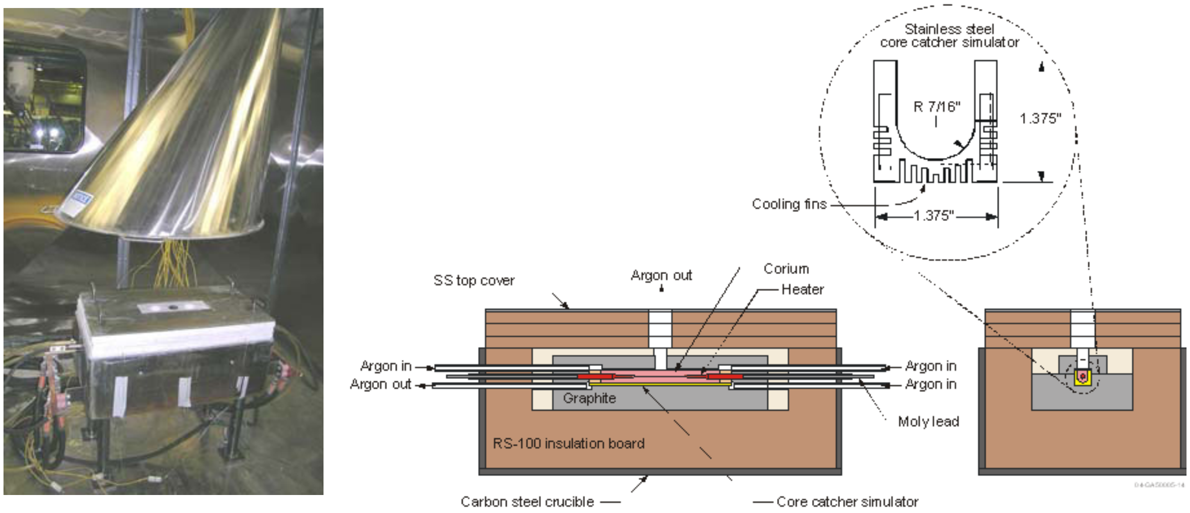

Figure ES-9. HTTL test assembly used for prototypic testing.

➔ ***Task 3 activities for developing and evaluating options to enhance ERVC completed.***

In Task 3, CHF on the outer surface of a simulated APR1400 reactor vessel was studied experimentally. The goal was to select an enhanced vessel/insulation design and a suitable vessel coating for CHF enhancement so as to substantially increase the thermal margin for IVR. Toward this end, ERVC tests were conducted using prototypic water (i.e., non-ionized tap water as expected for a flooded cavity) to evaluate the performance of various coating materials and to select a suitable bottleneck configuration at the minimum gap location for the enhanced vessel/insulation design. The vessel coating should promote downward facing boiling on the vessel outer surface and a suitable bottleneck configuration should facilitate steam venting through the annular channel between the vessel and the insulation structure, both of which should lead to considerable CHF enhancement.

In Task 3, various types of experiments were performed at SNU, PSU, and KAERI to obtain essential information. Key ERVC issues that were considered in Task 3 included delayed flooding of the reactor vessel owing to the large volume between the cavity floor and the lower head, local CHF limits for downward facing boiling on the vessel outer surface, thermal margin for maintaining the integrity of the reactor vessel, methods for ERVC enhancement, two-phase natural circulation through the gap between the reactor vessel and the insulation structure, and choking limit for steam venting during ERVC. To provide insights for addressing these key issues, boiling and two-phase flow tests were conducted in the DELTA and GAMMA facilities at SNU, the SBLB facility at PSU, and the HERMES-HALF facility at KAERI. Key insights gained from these tests are summarized below.

ERVC investigated with SNU DELTA-1D, DELTA-3D, and GAMMA-3D facilities.

At SNU, tests were completed for Task 3 using three facilities: DELTA 1D, DELTA 3D and GAMMA 3D.

- DELTA 1D is designed to estimate the effect of inclination angle on interfacial wavy motion. The experimental apparatus (Figure ES-10) includes a test section, a viewing chamber, a boiler and a flow line to initiate and maintain the film boiling process. The test section is mounted on one side of the viewing chamber, and two glass windows are placed for the front and side views. In the DELTA 1D tests, one could observe the interfacial wavy motion of vapor film from the inclined flat plates. The measured wall temperatures took on similar values except at 5 mm from the leading edge because of the thinnest vapor film observed there. The interfacial wavelength of vapor film flow could unfortunately not be visualized due to thin vapor film thicknesses.

Figure ES-10. DELTA 1D test apparatus.

- DELTA 3D quenching tests were performed to observe the angular and curved effects on film boiling heat transfer. Figure ES-11 illustrates the DELTA 3D experimental apparatus, which includes a heated hemispherical test section that is submerged in a tank containing demineralized water. Comparisons between DELTA-3D data and previous studies indicate that the heat transfer coefficients obtained from the DELTA tests are greater than those from numerical analysis for laminar film boiling. Thus, the film boiling regime in the DELTA-3D tests is not simply laminar, but involves more complexities like the Helmholtz instability. For the DELTA-3D tests, the film boiling heat transfer coefficients considering interfacial wavy motion agree better with the experimental results within ± 4.5% than those for laminar film boiling analysis without interfacial wave consideration. But the difference between laminar film boiling heat transfer coefficients and measured film boiling heat transfer coefficients is relatively smaller than those in the 294 mm diameter tests, so the simple laminar film boiling regime is considered to span a greater portion of the 120 mm test section area than of the 294 mm test section.

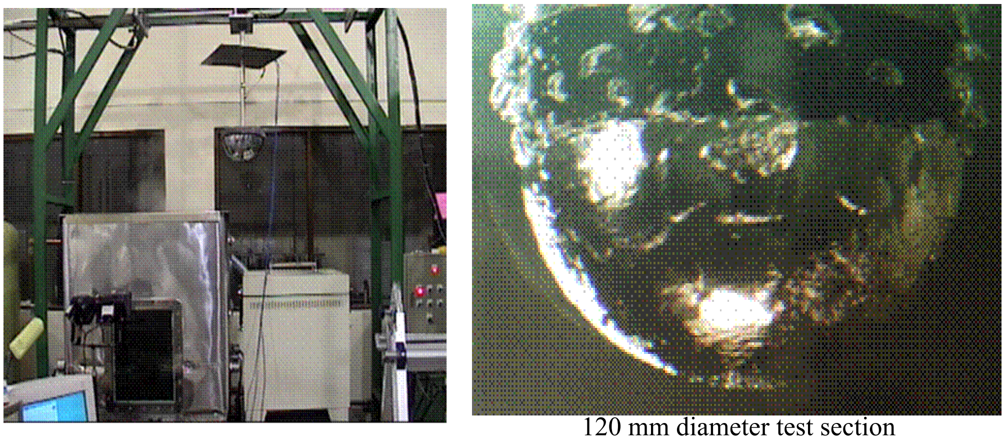
120 mm diameter test section

Figure ES-11. DELTA 3D test apparatus with representative visualization results.

- GAMMA 3D (Figure ES-12) is designed to measure the heat transfer coefficient and CHF for ERVC conditions. The experimental factors include gap size, mass flow rate, pressure, the forced convection or natural circulation condition, and the initial subcooling. GAMMA 3D results indicated that CHF values decrease as the inclination angle increases for large inlet subcooling. In other words, the angular qualities are augmented by the increase in enthalpy as the angle increases. The film boiling heat transfer coefficients on the downward-facing hemisphere were measured and analyzed.

Figure ES-12. GAMMA 3D test apparatus.

Insights and correlations for ERVC enhancements gained from tests in PSU SBLB facility.

Steady state boiling experiments using test vessels with and without coatings were conducted in the PSU Subscale Boundary Layer Boiling (SBLB) facility for the cases with and without an enhanced thermal insulation to investigate the separate effect as well as the integral effect of the enhanced insulation design and vessel coatings. The SBLB test facility consists of a water tank with a condenser assembly, a heated hemispherical test vessel with or without an insulation simulator, a data acquisition system, a photographic system, and a power control system. Figure ES-13 shows the SBLB water tank with an enhanced vessel/insulation design. Key insights from these investigations are summarized below.

Figure ES-13. Overall view of SBLB water tank with APR1400 vessel/insulation simulator.

- For plain vessels without coatings or thermal insulation, the local boiling curve tended to shift upward and to the right as the angular position was increased from the bottom center toward the test vessel's equator. For a given wall superheat, higher nucleate boiling rates were obtained in the locations downstream of the bottom center. The local CHF exhibited a minimum at the bottom center location and increased monotonically with angular position toward the vessel's equator.
- Unlike the trend observed for plain vessels, the local boiling curve for coated vessels without thermal insulation did not shift monotonically upward and to the right as the angular position was increased from the bottom center toward the equator of the test vessel. The local CHF limit at the bottom center was actually higher than the values for adjacent downstream locations up to $\theta = 28^{\circ}$. The local CHF exhibited a minimum at the $\theta = 14^{\circ}$ location rather than at the bottom center. This non-monotonic behavior of the local CHF variation was largely due to the capillary effect of the micro-porous coatings, where there was a continuous liquid supply from all radial directions toward the bottom center.
- For the case with thermal insulation, the nucleate boiling rates do not exhibit monotonic trend either, i.e., the local boiling curve does not shift upward and to the right monotonically with increasing angular position. Rather, the local CHF limit tended to increase from the bottom center at first, then decrease toward the minimum gap location, and finally increase toward the equator. This non-monotonic behavior is evidently due to the local variation of the two-phase motions in the annular channel between the test vessel and the insulation structure.

- The optical and SEM records showed that the micro-porous layer coatings had the form of a porous matrix composed of interconnected channels and different pores on the surface. Improvement in nucleate boiling heat transfer and CHF could be attributed to the structure of the porous layer itself and the capillary action it induced. The matrix of cavities and voids within the coating effectively trapped vapor, which served as active nucleation sites. These sites in turn were fed with liquid flowing through the interconnected channels. The pores on the surface of the porous coating served as flow inlets for liquid supply to the heating surface, leading to appreciable enhancements in the local CHF limits.
- Micro-porous aluminum coating appeared to be very durable. Even after many cycles of steady state boiling, the vessel coating remained rather intact, with no apparent changes in color or structure. Moreover, the heat transfer performance of the coating was found to be highly desirable with an appreciable CHF enhancement but very little effect of aging. Although similar heat transfer performance was observed for micro-porous copper coating, the latter was found to be much less durable and tended to degrade after several cycles of boiling. It appeared that the most suitable coating material for ERVC is micro-porous aluminum coating.
- For a coated hemispherical vessel with thermal insulation, the bubbles were generated at a higher frequency compared to that for a plain vessel without thermal insulation. This clearly indicates that a vessel with micro-porous surface coating would give rise to a shorter boiling cycle. This enhanced boiling cycle explains the increased nucleate boiling rate for a coated vessel because more latent heat of vaporization could be transferred per unit time from the reactor surface.
- For a coated vessel with thermal insulation, the vapor bubbles generated in the bottom center region did not tend to agglomerate. This behavior could be due to the availability of vapor escape paths provided by the coating's porous cavities. Although vapor bubbles tended to disperse on the coated vessel, a higher boiling site density led to higher heat removal, i.e., a higher boiling rate.
- Depending on the angular position, a local CHF enhancement of 200% to 330% over a plain vessel could be achieved using an enhanced insulation structure with vessel coatings (see Figure ES-14). It appears that ERVC with the use of vessel coatings and an enhanced insulation structure could provide sufficient cooling for high-power reactors such as APR1400.

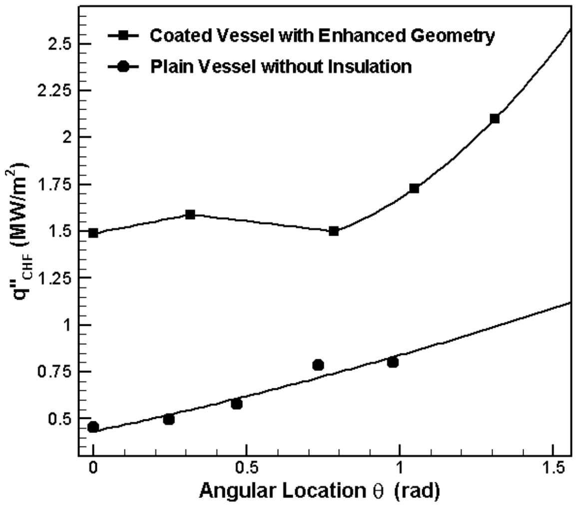

Figure ES-14. Variations of the local CHF limit on the vessel outer surface for cases with and without vessel coating and enhanced insulation

Key insights about enhanced vessel /insulation configuration heat transfer gained from tests conducted in HERMES-HALF facility.

To observe and evaluate the two-phase natural circulation phenomena through the gap between the reactor vessel and the insulation in the APR1400 under external reactor vessel cooling, a HERMES-HALF experiment was performed in KAERI. The HERMES-HALF is a non-heating (air/water) experimental study on the two-phase natural circulation through the annular gap between the reactor vessel and the insulation. The objectives of this HERMES-HALF study are to observe and evaluate the two-phase natural circulation phenomena through the gap between the reactor vessel and the insulation in the APR1400. That is, the circulation flow rate, three dimensional effect, and flow instability in the gap between the APR1400 reactor vessel and insulation were simulated by the HERMES-HALF experiments. For these purposes, a half-scaled experimental facility was prepared utilizing results of a scaling analysis to simulate the APR1400 reactor and insulation system.

- Flow observations indicate that choking flows occurred in the region near the shear keys (see Figure ES-15). In cases with larger air injection rates and smaller outlet areas, higher recirculation flows were observed in the region near the shear keys. Because of choking phenomena, periodic air back flow occurred near the minimum gap region under conditions with higher air injection rates. Therefore, design modifications in the minimum gap region are required to ensure sufficient flow through the gap.

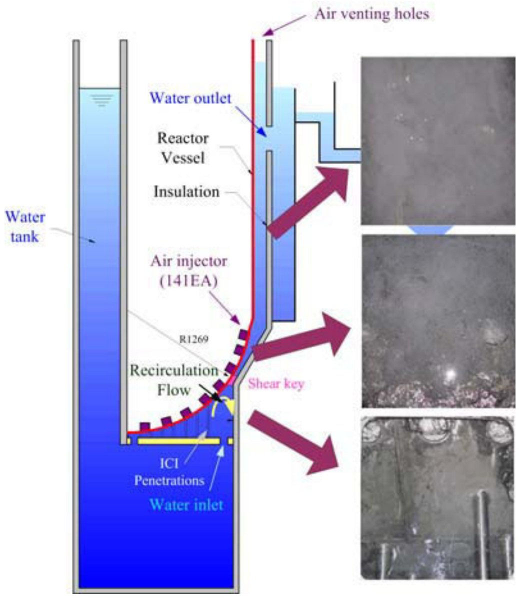

Figure ES-15. Visualization results of the HERMES-HALF experiment with a 10% (838 m^3/hr) air injection rate of the maximum air flow rate suggested by the IVR evaluations.

- Relationships between the re-circulation flow rate and the parameters in the insulation design were examined. As the water inlet areas increased, the natural circulation mass flow rates asymptotically increased and converged to a certain value. The outlet area also influenced the re-circulation flow rate. Experimental correlations on the natural circulation mass flow rates along the variation of the inlet / outlet area and wall heat flux were suggested.

- For inlet and outlet areas of 0.15 m^2, the natural circulation flow rate could be increased up to 200 kg/s at high heat flux conditions. Based on KAIST and SULTAN results, this natural circulation flow rate values leads to about 1.3 – 1.45 MW/m^2 CHF values at the top of the lower head vessel (90 degrees) which indicate more efficient cooling than occurs in pool boiling.
- To maximize the heat removal capability by enhancing the re-circulation flow rate through the reactor vessel/insulation gap, extensive experimental results are required to evaluate a wider range of design parameters, such as the inlet position and outlet location. Also, a detailed 3-dimensional flow analysis is necessary to evaluate the local effect, such as choking phenomena near the shear key. To apply the experimental data to the real situation, the similarity of the non-heating experiment to the heating experiment should be verified.

➔ *Task 4 activities completed to evaluate enhanced IVR margin associated with options proposed in this INERI.*

The objective of Task 4 is to assess the impact of Task 2 and 3 IVR design recommendations. Scenarios evaluated in Task 1 were re-evaluated using Task 2 and 3 design recommendations to enhance core catcher and ERVC performance. Assessments were conducted using several analytical tools. In these evaluations, INEEL applied the SCDAP/RELAP5-3D© and VESTA codes. KAERI applied the LILAC and RELAP codes and a lumped parameter model.

Calculation results show that proposed enhancements are needed to provide additional margin for IVR when the vessel is subjected to Task 1 bounding heat loads. In many of the cases evaluated, the enhanced cooling associated with a coated reactor vessel or an enhanced vessel/insulation configuration was sufficient to reduce heat fluxes below CHF. Even greater margins for IVR were predicted for cases with both a coated vessel and an enhanced vessel/insulation configuration. Analyses also suggest that significant additional cooling is possible with an IVCC. Highlights from these calculations are summarized below.

SCDAP/RELAP5-3D© predictions suggest proposed IVR enhancements reduce vessel heat fluxes below CHF.

SCDAP/RELAP5-3D©[ES-1] is an advanced, state-of-the-art, best-estimate computer code designed for simulating severe reactor accidents. The code predicts the thermal-hydraulic response of the reactor coolant system (RCS) and the progression of damage associated with reactor core and reactor vessel heatup. Links with other detailed, mechanistic codes can and have been used to integrate fission product transport and containment response into accident simulations. For Task 4, SCDAP/RELAP5-3D© was modified to allow simulation of ERVC from reactor vessels with microporous coatings, optimized insulation, and the combination of coatings and insulation based on PSU experimental results. Modifications were also added to simulate ERVC from plain vessels as a reference for gauging any potential IVR improvements that may be derived from implementing any of the ERVC enhancements. Calculations were completed using relocation conditions associated with a large loss-of-coolant accident (LOCA) in the APR1400 (see Table ES-2).

Initial evaluations indicated that the coefficient assumed by SCDAP/RELAP5-3D© for modeling heat transfer when molten materials are in direct contact with the reactor vessel (in the absence of a solidified corium crust) was invalid for molten pools with high decay heat like the LOCA-1 case. Although data are not available for quantifying this heat transfer coefficient, a series of iterative calculations were completed to determine a value (600 W/m^2-K) that appeared to yield physically reasonable results.

Results suggest that plain vessels without any of the proposed enhancements will fail by melt through. However, calculations indicate wall thinning is limited if proposed ERVC enhancements are included. SCDAP/RELAP5-3D© predictions for the ratio of vessel surface heat flux to the CHF for vessels with microporous coatings at 6,000 and 9000 s (~0.7 and 1.1 hr after molten fuel relocation) are shown in Figure ES-16. These results indicate that the selected molten corium-to-vessel heat transfer coefficient of 600 W/m^2-K can lead to large vessel surface heat fluxes, with some closely approaching, but not exceeding, the CHF at specific angular positions. Hence, comparisons of plain and coated vessel SCDAP/RELAP5-3D© predictions indicate the use of microporous coatings has significant IVR benefits.

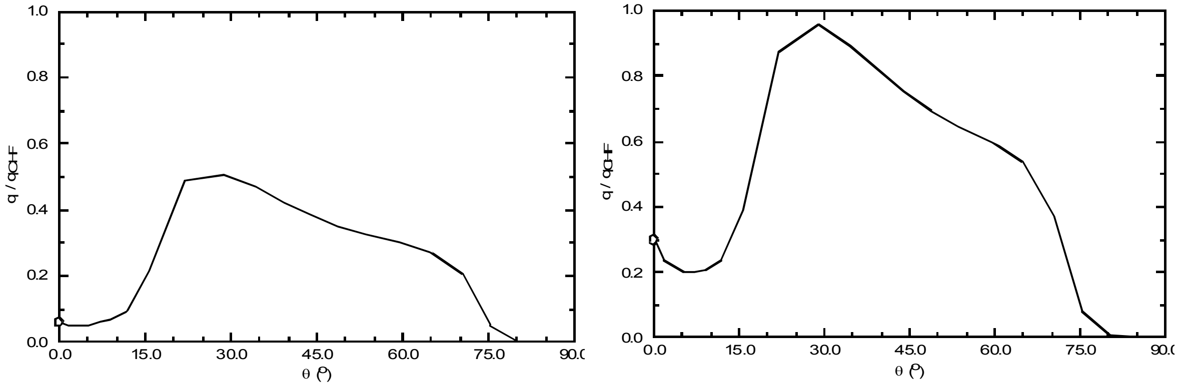

(a) 6,000 seconds (b) 9,000 seconds

Figure ES-16. The ratio of vessel surface heat flux to the CHF for a coated vessel at selected times.

VESTA results suggest that either of the proposed IVR enhancements can preclude vessel heat fluxes from exceeding the CHF.

The VEssel Statistical Thermal Analysis (VESTA) code was developed to independently verify AP600 IVR evaluation results submitted to the US NRC by Westinghouse and assess the impact of additional uncertainties and other debris configurations. In VESTA, statistical distributions for the heat flux to the vessel wall from various assumed debris configurations are compared with statistical distributions calculated for the CHF from the submerged vessel surface. VESTA uncertainty distributions are Bayesian distributions, which are ultimately combined by a Monte Carlo sampling to yield a distribution on the probability of vessel heat fluxes exceeding the CHF (or if the vessel isn't submerged, the heat transfer rate from the vessel to the reactor cavity). VESTA can consider several types of debris configurations, decay heat power production associated with actinide and fission product heating, heat sources in the metallic material, and uncertainty distributions for a wide range of parameters. A key benefit of the VESTA code is that it allows users to consider the impact of input parameter uncertainties. Hence, VESTA can be applied to obtain point estimates and probability density functions (pdfs) for desired outputs. Heat transfer processes and phenomena modeled by VESTA are described in Reference ES-4.

Two debris endstate configurations were considered in the VESTA calculations: Configuration A, a stratified configuration with an upper metallic layer; and Configuration C, a stratified configuration with a lower metallic layer. (see Figure ES-17). Several types of cases were evaluated for each debris endstate.

- A base case without an IVCC or enhanced ERVC.
- Bases case sensitivities to assumed steel relocation mass.
- Sensitivities that simulate the use of an IVCC.
- Sensitivities to various types of enhanced ERVC.

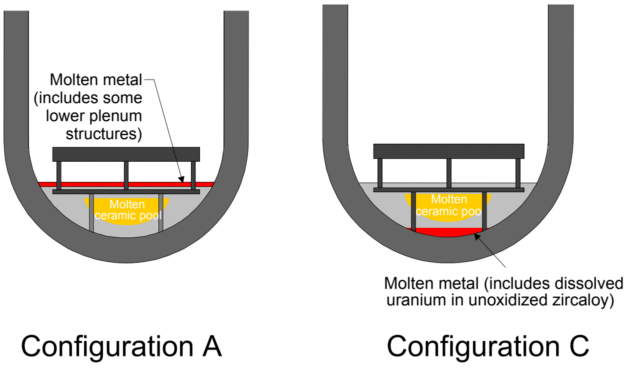

Figure ES-17. Debris configurations evaluated for the APR1400.

VESTA results for base case conditions in a Configuration A endstate indicate:

- Peak heat fluxes and associated CHF ratios occur near the top of the ceramic pool beneath the metallic layer.
- A small, but non-zero, probability exists for the CHF ratio to exceed 1.0.
- An IVCC must prevent melt relocation for at least 4 hours in order to maintain vessel heat fluxes below the CHF.
- Either of the explored ERVC enhancements are sufficient to reduce vessel heat fluxes below the CHF. If one considers uncertainties, the additional reduction offered by an enhanced insulation design is required to maintain heat fluxes below the CHF.
- An IVCC must decrease heat fluxes by at least a factor of 2 for this configuration.
- ERVC enhancements may decrease heat fluxes by factors of 2 to 5.

Point estimate results in Figure ES-18(a) illustrate the increased margin offered by proposed ERVC enhancements. As shown in Figure ES-18(b), the pdfs predicted for Configuration A for a case with an enhanced vessel/insulation configuration indicate that the vessel heat flux remains below the CHF.

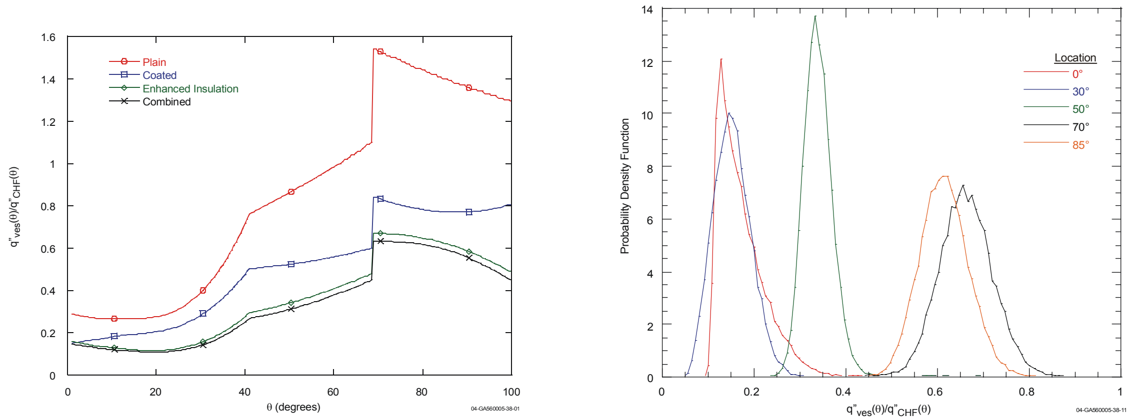

(a) Point estimate values for ERVC enhancements

(b) Uncertainty analysis for enhanced insulation/vessel configuration

Figure ES-18. Configuration A results for cases with proposed ERVC enhancements.

VESTA results for base case conditions in a Configuration C endstate suggest:

- Higher heat fluxes occur at vessel locations adjacent to the ceramic layer.
- CHF ratios peak at two locations for this configuration: near the bottom center of the vessel and near the top of the ceramic pool.
- Ether an IVCC, which can prevent relocation onto the vessel for at least 4 hours) or a vessel with the combined ERVC enhancements considered in this study are sufficient to maintain vessel heat fluxes below the CHF.

In summary, VESTA results suggest that any of the proposed IVR enhancements maintain vessel heat fluxes below the CHF. Depending upon the selected IVR enhancement and debris endstate configuration, IVR margins may increase by factors ranging from two to four.

LILAC results similar to values predicted by lumped parameter model.

LILAC is a multi-dimensional thermal-hydraulic analysis code that solves the Reynolds-averaged Navier-Stokes and energy equations as governing equations. Turbulent flows are modeled by two-equation turbulence models (κ-ε - and κ-ω models) or large eddy simulation, and a molten pool crust is modeled using an enthalpy-porosity method. The main purpose of the LILAC code is the analysis of thermal-hydraulic phenomena of core melt that relocates to a reactor vessel lower head. Currently, LILAC can simulate multi-layered conjugate heat transfer with melt solidification.

The thermal characteristics of a molten pool in the lower head vessel for the 3 inch LOCA cases were analyzed using the LILAC code, and the calculated thermal load on the reactor vessel wall was compared to that obtained using a lumped parameter model. In this study, the stratified two-layer molten pool is solved separately based on the postulation that the oxidic layer is entirely surrounded by its crust. The calculated heat flux distribution along with pool angle is very similar to that of the lumped parameter analysis. The thermal load from the metallic layer is linearly distributed in results from the LILAC code simulation (see Figure ES-19). However, the averaged heat flux is approximately same as the result of the lumped parameter calculation (see below). From this comparative study between the CFD and lumped parameter analyses, it was concluded that the lumped parameter analysis is simple but useful for predicting the thermal loads on the reactor vessel during a severe accident.

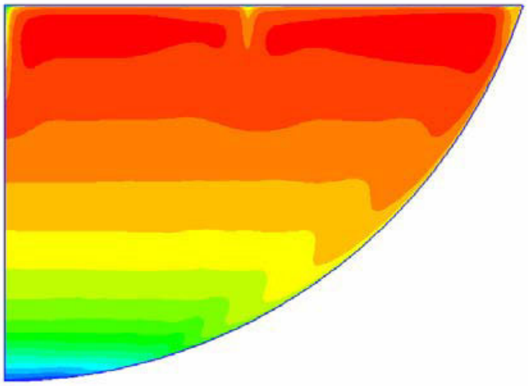

Figure ES-19. LILAC predicted temperature distribution in the oxidic pool.

Lumped Parameter method applied.

Using a lumped-parameter (LP) model, the thermal load to the reactor vessel from the molten pool was analyzed for the APR1400. For eight cases of hypothetical severe accidents simulated using the SCDAP/RELAP code, the relocated molten material masses was imported into the lumped parameter code. The heat flux distribution in the vessel wall for the chosen severe accidents were calculated using the LP code and compared to the CHF values that are applied on the vessel outer wall during ERVC. The plain CHF, which is normally found in literature, is too low to remove the thermal loads applied during the severe accidents. When the CHF is enhanced by surface coating and vessel insulation structure, it is seen that the thermal loads from the half of the selected severe accidents especially small break LOCA and total loss of feedwater (TLFW) with safety depressurization system (SDS) can be effectively removed by ex-vessel cooling. The subcooling of the cooling water slightly increases the magnitude of the CHF. The enhanced CHF with the effect from the 5 degree subcooling is greater than the thermal loads from all the cases except the 9.6 inch LOCA (see Figure ES-20). This suggests that enhanced CHF with subcooling can effectively remove the thermal loads from the stratified molten pools in most cases.

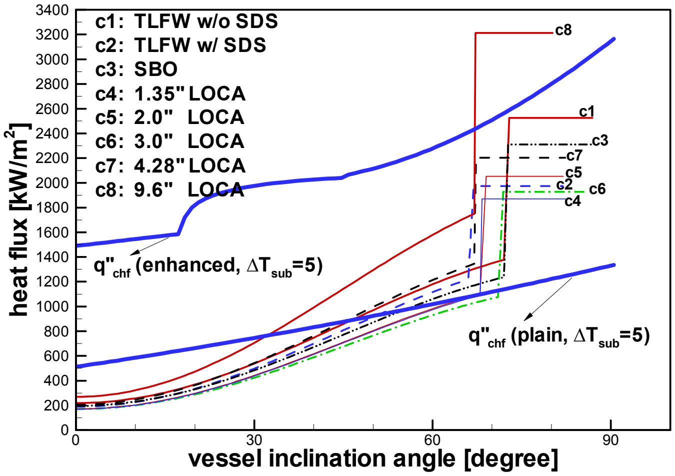

Figure ES-20. Comparisons of thermal load distributions for accidents scenarios with CHF correlations with 5 degree subcooling.

➔ ***Supported six students that successfully completed graduate degrees.***

University participation in this INERI allowed the following seven students to obtain graduate degrees.

- S. J. Kim, M.S. in Nuclear Engineering, Seoul National University, February 2003.
- Y. H. Kim, PhD in Nuclear Engineering, Seoul National University, February 2004.
- H. M. Son, M.S. in Nuclear Engineering, Seoul National University, February 2006 (Expected).
- C. S. Kim, PhD in Nuclear Engineering, Seoul National University, February 2006 (Expected).
- S. W. Noh, PhD in Nuclear Engineering, Seoul National University, February 2007(Expected).
- S. D. Lee, PhD in Nuclear Engineering, Seoul National University, February 2007(Expected).
- M. B. Dizon, M.S. in Mechanical Engineering, Pennsylvania State University, December 2002.
- J. Yang, M.S. in Mechanical Engineering, Pennsylvania State University, December 2002.
- J. Yang, PhD in Mechanical and Nuclear Engineering, Pennsylvania State University, August 2005 (Expected).

➔ ***Completed programmatic requirements on or ahead of schedule.***

Figure ES-21 contains a project milestone schedule Gant chart, and Table ES-5 lists project milestones. As indicated in this figure and table, all programmatic requirements were completed on schedule.

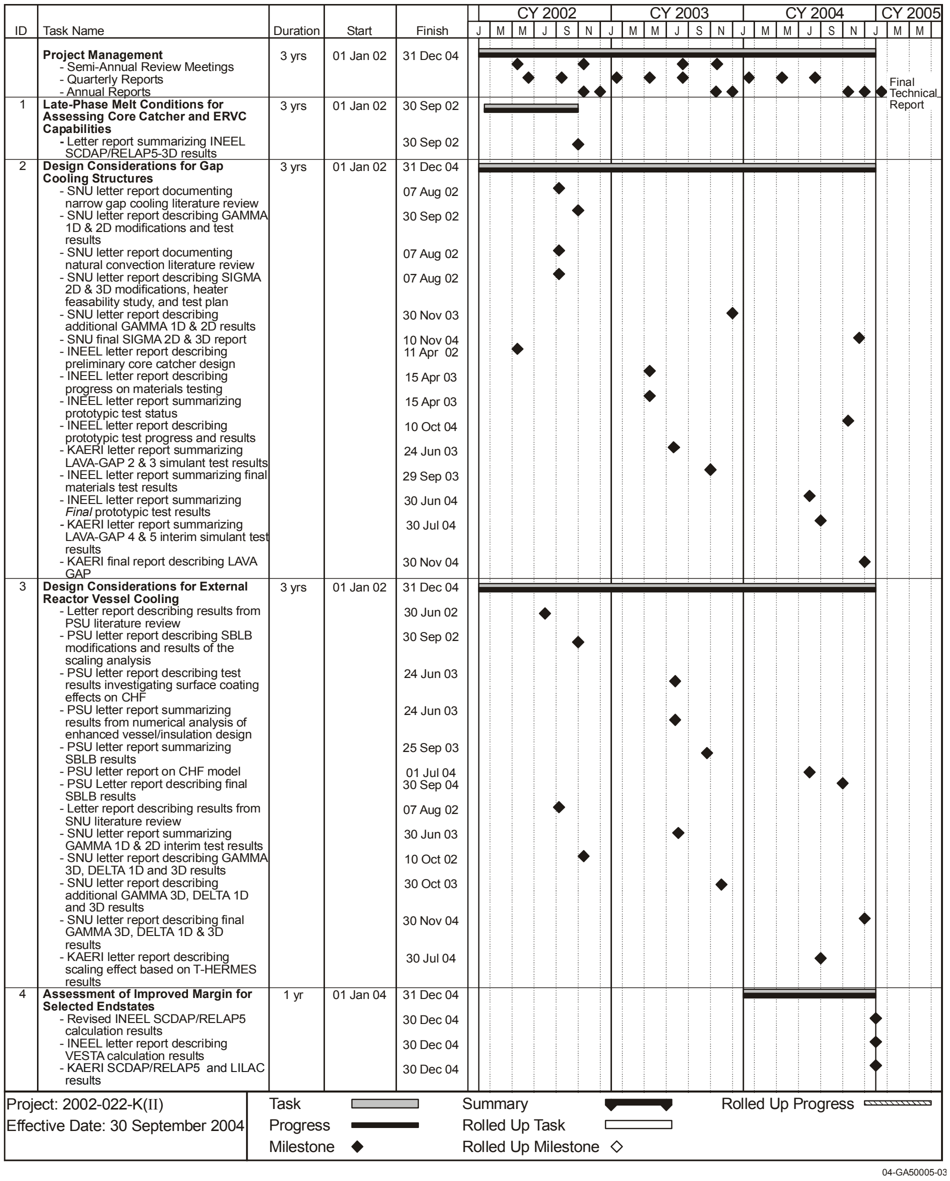

ID	Task Name	Duration	Start	Finish
	Project Management	3 yrs	01 Jan 02	31 Dec 04
	- Semi-Annual Review Meetings			
	- Quarterly Reports			
	- Annual Reports			
1	**Late-Phase Melt Conditions for Assessing Core Catcher and ERVC Capabilities**	3 yrs	01 Jan 02	30 Sep 02
	- Letter report summarizing INEEL SCDAP/RELAP5-3D results			30 Sep 02
2	**Design Considerations for Gap Cooling Structures**	3 yrs	01 Jan 02	31 Dec 04
	- SNU letter report documenting narrow gap cooling literature review			07 Aug 02
	- SNU letter report describing GAMMA 1D & 2D modifications and test results			30 Sep 02
	- SNU letter report documenting natural convection literature review			07 Aug 02
	- SNU letter report describing SIGMA 2D & 3D modifications, heater feasability study, and test plan			07 Aug 02
	- SNU letter report describing additional GAMMA 1D & 2D results			30 Nov 03
	- SNU final SIGMA 2D & 3D report			10 Nov 04
	- INEEL letter report describing preliminary core catcher design			11 Apr 02
	- INEEL letter report describing progress on materials testing			15 Apr 03
	- INEEL letter report summarizing prototypic test status			15 Apr 03
	- INEEL letter report describing prototypic test progress and results			10 Oct 04
	- KAERI letter report summarizing LAVA-GAP 2 & 3 simulant test results			24 Jun 03
	- INEEL letter report summarizing final materials test results			29 Sep 03
	- INEEL letter report summarizing *Final* prototypic test results			30 Jun 04
	- KAERI letter report summarizing LAVA-GAP 4 & 5 interim simulant test results			30 Jul 04
	- KAERI final report describing LAVA GAP			30 Nov 04
3	**Design Considerations for External Reactor Vessel Cooling**	3 yrs	01 Jan 02	31 Dec 04
	- Letter report describing results from PSU literature review			30 Jun 02
	- PSU letter report describing SBLB modifications and results of the scaling analysis			30 Sep 02
	- PSU letter report describing test results investigating surface coating effects on CHF			24 Jun 03
	- PSU letter report summarizing results from numerical analysis of enhanced vessel/insulation design			24 Jun 03
	- PSU letter report summarizing SBLB results			25 Sep 03
	- PSU letter report on CHF model			01 Jul 04
	- PSU Letter report describing final SBLB results			30 Sep 04
	- Letter report describing results from SNU literature review			07 Aug 02
	- SNU letter report summarizing GAMMA 1D & 2D interim test results			30 Jun 03
	- SNU letter report describing GAMMA 3D, DELTA 1D and 3D results			10 Oct 02
	- SNU letter report describing additional GAMMA 3D, DELTA 1D and 3D results			30 Oct 03
	- SNU letter report describing final GAMMA 3D, DELTA 1D & 3D results			30 Nov 04
	- KAERI letter report describing scaling effect based on T-HERMES results			30 Jul 04
4	**Assessment of Improved Margin for Selected Endstates**	1 yr	01 Jan 04	31 Dec 04
	- Revised INEEL SCDAP/RELAP5 calculation results			30 Dec 04
	- INEEL letter report describing VESTA calculation results			30 Dec 04
	- KAERI SCDAP/RELAP5 and LILAC results			30 Dec 04

Project: 2002-022-K(II)
Effective Date: 30 September 2004

Figure ES-21. INERI project schedule Gant chart

.

Table ES-5. INERI Milestones and Completion Dates

Milestone / Task Description	Planned Completion Date	Actual Completion Date
Project Management and Integration		
Semi-Annual Review Meetings	April 15, 2002	April 15, 2002
	October 7, 2002	October 7-8, 2002
	July 8, 2003	July 8, 2003
	October 5, 2003	October 5, 2003
	June 2004	June 17-19, 2004
Quarterly Reports	May 14, 2002	May 14, 2002
	August 14, 2002	August 2, 2002
	January 15, 2003	January 15, 2003
	April 15, 2003	April 15, 2003
	July 15, 2003	July 14, 2003
	January 15, 2004	January 14, 2004
	April 15, 2004	April 12, 2004
	July 15, 2004	July 12, 2004
	October 15, 2004	October 15, 2004
Annual Reports	October 31, 2002	October 14, 2002
	October 15, 2003	October 14, 2003
Task 1: Late Phase Melt Conditions for Assessing Core Catcher and ERVC Capabilities		
Letter report summarizing INEEL SCDAP/RELAP5-3D results	November 15, 2002	September 30, 2002
Letter report summarizing KAERI SCDAP/RELAP5 results	December 15, 2004	December 15, 2004
Task 2: Core Catcher Design Enhancement		
INEEL Letter report describing preliminary core catcher design	October 10, 2002	April 11, 2002
INEEL letter report describing progress on materials testing	April 30, 2003	April 15, 2003
INEEL letter report summarizing prototypic test status	April 30, 2003	April 15, 2003
INEEL letter report summarizing interim prototypic test results	September 30, 2003	September 29, 2003
INEEL letter report summarizing final materials test results	March 18, 2004	March 18, 2004
INEEL letter report summarizing prototypic test results	June 30, 2004	June 30, 2004
SNU letter report documenting narrow gap cooling literature review	August 7, 2002	August 7, 2002
SNU letter report describing GAMMA 1D & 2D facility and test results	October 10, 2002	September 30, 2002
SNU letter report documenting natural convection literature review	August 7, 2002	August 7, 2002
SNU letter report describing SIGMA 2D & 3D, heater feasibility study, & test plan	August 7, 2002	August 7, 2002
SNU letter report summarizing GAMMA 1D and 2D interim results.	June 30, 2003	June 30, 2003
SNU letter report describing additional GAMMA 1D & 2D results	November 30, 2003	November 28, 2003
SNU letter report with SIGMA 2D & 3D results	November 30, 2004	November 30, 2004
KAERI letter report describing LAVA facility & test plans, and results	October 19, 2002	October 19, 2002
KAERI letter report summarizing LAVA-GAP 2 &3 simulant test results	June 30, 2003	June 24, 2003
KAERI letter report summarizing LAVA-GAP 4 & 5 interim simulant test results	July 30, 2004	July 30, 2004
KAERI letter report summarizing LAVA-GAP simulant test results	November 30, 2004	November 28, 2004
Task 3: External Reactor Vessel Cooling Design Enhancement		
Letter report describing results from SNU literature review	August 7, 2002	August 7, 2002
Letter report describing results from PSU literature review	June 30, 2002	June 25, 2002
PSU letter report describing SBLB modifications and results of scaling analysis	September 30, 2002	September 30, 2002
PSU letter report describing test results investigating surface coating effects on CHF	June 30, 2003	June 24, 2003
PSU letter report summarizing numerical analysis of improved vessel/insulation	June 30, 2003	June 24, 2003
PSU letter report summarizing tests investigating surface coating and improved vessel/insulation arrangement.	September 30, 2003	September 25, 2003
PSU letter report describing the development of a hydrodynamic CHF model	July 1, 2004	July 1, 2004
PSU letter report describing final SBLB results	September 30, 2004	September 30, 2004
SNU letter report describing GAMMA 3D, DELTA 1D & 3D modifications and results	October 10, 2002	October 10, 2002
SNU letter report describing additional GAMMA 3D, DELTA 1D & 3D test results	November 30, 2003	November 27, 2003
SNU final letter report describing GAMMA 3D, DELTA 1D & 3D results	November 30, 2004	November 27, 2004
KAERI letter report describing scaling and 3-D effects based on T-HERMES results	July 30, 2004	July 30, 2004
Task 4: Assessment of Improved Margin		
INEEL VESTA and SCDAP/RELAP5 results	December 30, 2004	December 29, 2004
KAERI SCDAP/RELAP5, LILAC, and Lumped Parameter results	December 30, 2004	December 29, 2004

➔ ***Completed fifty-one peer-reviewed papers for publication (ten in archival journals and forty-one in conference proceedings). and twenty-six letter reports.***

As listed in Table ES-6, this INERI has yielded (and continues to yield) several peer-reviewed conference and journal publications. Note that most of these papers were collaborative efforts. All of these documents received appropriate export control reviews prior to their release. Electronic copies of final papers are available on the CD transmitted with this report

Table ES-6. INERI Publications

Publications	Status
Archival Journals	
Y. H. Kim, S. J. Kim, K. Y. Suh, J. L. Rempe, F. B. Cheung, S. B. Kim, "Internal Vessel Cooling Feasibility Attributed by Critical Heat Flux in Inclined Rectangular Gap, *submitted to Nuclear Technology,* January 2005.	Draft paper submitted
Y. H. Kim, S. J. Kim, S. W. Noh, K. Y. Suh, J. L. Rempe, F. B. Cheung, S. B. Kim, "Visualization of Boiling Phenomena in Inclined Rectangular Gap," *submitted to the International Journal of Multiphase Flow,* January 2005.	Final paper submitted
C. S. Kim, K. Y. Suh, J. L. Rempe, F. B. Cheung, S. B. Kim, "Effect of Interfacial Wavy Motion on Film Boiling Heat Transfer from Isothermal Downward-facing Hemispheres," *submitted to Nuclear Engineering and Design*, January 2005.	Draft paper accepted
K.H. Kang, R.J. Park, S.B. Kim, F. B. Cheung, K. Y. Suh, and J. L. Rempe, "Simulant Melt Experiments on Thermal and Metallurgical Performance of the In-vessel Core Catcher," *submitted to Nuclear Technology,* June 2004.	Draft paper submitted
J. Rempe, D. Knudson, K. Condie, K. Y. Suh, F. B. Cheung, and S. B. Kim, "An Enhanced In-Vessel Core Catcher for Improving In-Vessel Retention Margins," *Invited paper, submitted to Nuclear Technology for NURETH10 Special Edition*, May 24, 2004.	Final paper submitted
M. B. Dizon, J. Yang, F. B. Cheung, J. L. Rempe, K. Y. Suh, and S. B. Kim, "Effects of Surface Coating on the Critical Heat Flux for Pool Boiling from a Downward Facing Surface, *Journal of Enhanced Heat Transfer*, Vol. 11, pp. 133-150, 2004.	Final paper published
F. B. Cheung, J. Yang, M. B. Dizon, J. L. Rempe, K. Y. Suh, and S. B. Kim, "Scaling of Downward Facing Boiling and Steam Venting in a Heated Hemispherical Annular Channel," *International Journal of Transport Phenomena,* Vol. 6, pp. 81-96, 2004	Final paper published
J. Rempe, D. Knudson, K. Condie, K. Y. Suh, F. B. Cheung, and S. B. Kim, "Conceptual Design of an In-vessel Core Catcher," *Nuclear Engineering and Design*, *Invited paper for ICONE11 Special Edition*, **230** (2004) 311-325.	Final paper published
J. Rempe, D. Knudson, K. Condie, K. Y. Suh, F. B. Cheung, and S. B. Kim, "Corium Retention for High Power Reactors by an In-vessel Core Catcher in Combination with External Reactor Vessel Cooling," *Nuclear Engineering and Design*, *Invited paper for ICONE11 Special Edition*, **230** (2004) 293-309.	Final paper published
D. Knudson, J. Rempe, K. Condie, K. Y. Suh, F. B. Cheung, and S. B. Kim, "Late-phase Melt Conditions affecting the Potential for In-Vessel Retention in High Power Reactors," *Nuclear Engineering and Design, Invited paper for ICONE11 Special Edition*, **230** (2004) 133-150.	Final paper published
Conference Proceedings and Presentations	
C. S. Kim, M. J. Yu, K. Y. Suh, J. Rempe, F. B. Cheung, and S.-B. Kim, "Film Boiling on Downward Facing Flat Plates with Varying Inclination Angles," 2005 ASME Heat Transfer Conference, San Francisco, CA, July 17-22, 2005.	Abstract submitted
S. D. Lee, H. M. Son, K. Y. Suh, J. Rempe, F. B. Cheung, and S.-B. Kim, "Prandtl Number Dependent Natural Convection in a Rectangular Pool with Internal Heat Sources," 2005 ASME Heat Transfer Conference, San Francisco, CA, July 17-22, 2005.	Abstract accepted
J. Yang, F. B. Cheung, J. L. Rempe, K. Y. Suh, and S. B. Kim, Correlations of Nucleate Boiling Heat Transfer and Critical Heat Flux for External Reactor Vessel Cooling, 2005 ASME Heat Transfer Conference, San Francisco, CA, July 17-22, 2005.	Draft paper submitted
J. Rempe, K. Y. Suh, F.-B. Cheung, and S.-B. Kim, "Insights from Investigations of In-Vessel Retention for High Power Reactors," *submitted to the 11th International Topical Meeting on Nuclear Reactor Thermal-Hydraulics (NURETH-11),* Popes Palace Conference Center, Avignon, France, October 2-6, 2005.	Abstract accepted
S. W. Noh, Y. H. Yu, J. K. Lee, K. Y. Suh, J. L. Rempe, F. B. Cheung, S. B. Kim, "Critical Heat Flux in Inclined Rectangular Narrow Long Channel," 2005 International Congress on Advances in Nuclear Power Plants (ICAPP'05), Seoul, Korea, May 15-19, 2005.	Abstract accepted
J. Yang, F. B. Cheung, J. Rempe, K. Suh, and S.-B. Kim, "Critical Heat Flux for Downward-facing Boiling on a Coated Hemispherical Vessel Surrounded by an Insulation Structure," *2005 International Congress on Advances in Nuclear Power Plants (ICAPP'05),* Seoul, Korea, May 15-19, 2005.	Draft paper submitted
J. L. Rempe, D. L. Knudson, K. G. Condie, F. B. Cheung, K. Y. Suh, and S. B. Kim, "Increased Margin Associated with Options to Enhance In-Vessel Retention," *2005 International Congress on Advances in Nuclear Power Plants (ICAPP'05),* Seoul, Korea, May 15-19, 2005.	Draft paper submitted

Table ES-6. INERI Publications

Publications	Status
C. S. Kim, K. Y. Suh, J. L. Rempe, F. B. Cheung, S. B. Kim, "Film Boiling Heat Transfer Modeling for Relatively Large-Diameter Downward-Facing Hemisphere," *4th Japan-Korea Symposium on Nuclear Thermal Hydraulics and Safety*, Sapporo, Japan, November 28 – December 1, 2004.	Presented and published
J. J. Kim, Y. H. Kim, S. J. Kim, S. W. Noh, K. Y. Suh, "Boiling Visualization and Critical Heat Flux Phenomena in Narrow Rectangular Gap," *4th Japan-Korea Symposium on Nuclear Thermal Hydraulics and Safety*, Sapporo, Japan, November 28 – December 1, 2004.	Presented and published
K. H. Lee, S. D. Lee, K. Y. Suh, "Natural Convection Heat Transfer with Low Prandtl Number Fluid," *ANS Winter Meeting*, Washington D. C., USA, November 14-18, 2004.	Presented and published
J. J. Kim, Y. H. Kim, K. Y. Suh, "Critical Heat Flux Propagation in Asymmetric Narrow Circular Channel," *ANS Winter Meeting*, Washington D. C., USA, November 14-18, 2004.	Presented and published
Y. H. Kim, S. J. Kim, J. J. Kim, S. W. Noh, K. Y. Suh, J. L. Rempe, and F. B. Cheung, S. B. Kim, "Critical Heat Flux Phenomena in One-Dimensional Narrow Gap," *3rd International Symposium on Two-Phase Flow Modeling and Experimentation*, Pisa, Italy, 22-24 September 2004	Presented and published
J. Yang, F. B. Cheung, J. L. Rempe, K. Y. Suh, and S. B. Kim, "Downward Facing Boiling and Steam Venting under Simulated ERVC Conditions," *Sixth International Topical Meeting on Nuclear Reactor Thermal Hydraulics, Operations and Safety (NUTHOS6),* Nara, JAPAN, October 4-8, 2004.	Presented and published
J. Yang and F. B. Cheung, "A Hydrodynamic CHF Model for Downward Facing Boiling on a Coated Vessel, *Sixth International Topical Meeting on Nuclear Reactor Thermal Hydraulics, Operations and Safety (NUTHOS6),* Nara, JAPAN, October 4-8, 2004.	Presented and published
K. H. Kang, R. J. Park, S. B. Kim, K. Y. Suh, F. B. Cheung, and J. L. Rempe, "Thermal and Metallurgical Performance of the Multi-layered In-vessel Core Catcher During Severe Accident," *Sixth International Topical Meeting on Nuclear Reactor Thermal Hydraulics, Operations and Safety (NUTHOS6),* Nara, JAPAN, October 4-8, 2004.	Presented and published
J. Rempe, K. Y. Suh, F.-B. Cheung, and S.-B. Kim., "In-Vessel Retention - Recent Efforts and Future Needs," *Sixth International Topical Meeting on Nuclear Reactor Thermal Hydraulics, Operations and Safety (NUTHOS6),* Nara, JAPAN, October 4-8, 2004.	Presented and published
J. Yang, M. B. Dizon, F-B. Cheung, J. L. Rempe, K. Y. Suh, and S-B. Kim, "Critical Heat Flux for Downward Facing Boiling on a Coated Hemispherical Surface," 2004 *Heat Transfer/Fluids Engineering Summer Conference*, Charlotte, NC, July 2004.	Final paper submitted
J. Yang, M. B. Dizon, F-B. Cheung, J. L. Rempe, K.Y. Suh, and S-B. Kim, "CHF Enhancement by Vessel Coating for External Reactor Vessel Cooling," *2004 International Congress on Advances in Nuclear Power Plants (ICAPP '04),* Pittsburgh, PA, USA, June 13-17, 2004.	Presented and published
K. H. Kang, R. J. Park, W. S. Ryu, S-B. Kim, K.Y. Suh, F-B. Cheung, and J. L. Rempe, "Thermal and Metallurgical Response of the In-vessel Core Catcher According to the Gap Size with the Lower Head Vessel," *International Congress on Advances in Nuclear Power Plants (ICAPP '04),* Pittsburgh, PA, USA, June 13-17, 2004.	Presented and published
K. Condie, J. Rempe, D. Knudson, K. Y. Suh, F-B. Cheung, and S-B. Kim, "Design and Evaluation of an Enhanced In-Vessel Core Catcher," *2004 International Congress on Advances in Nuclear Power Plants (ICAPP '04),* Pittsburgh, PA, USA, June 13-17, 2004.	Presented and published
J. J. Kim, Y. H. Kim, S J Kim, S. W. Noh, K.Y. Suh, J.L. Rempe, F-B. Cheung, and S-B. Kim, "Critical Heat Flux in Inclined Rectangular Narrow Gaps," *2004 International Congress on Advances in Nuclear Power Plants (ICAPP'04)*, Pittsburgh, PA, USA, June 13-17, 2004.	Final paper presented
K. H. Lee, S.D.Lee, K.Y. Suh, J.L. Rempe, F-B. Cheung, and S-B. Kim, "Prandtl Number Dependent Natural Convection with Internal Heat Sources," *2004 International Congress on Advances in Nuclear Power Plants (ICAPP'04)*, Pittsburgh, PA, USA, June 13-17, 2004.	Final paper presented
C. S. Kim, K. Y. Suh, J. L. Rempe, F.-B. Cheung, and S.-B. Kim, "Film Boiling on Downward Quenching Hemisphere of Varying Sizes," *Twelfth International Conference on Nuclear Engineering (ICONE12),* Washington, DC, April 2004	Presented and published
K. H. Kang, R. J. Park, S. B. Kim, K. Y. Suh, F. B. Cheung, and J. L. Rempe, Experiments on Performance of the Multi-Layered In-Vessel Core Catcher, *Twelfth International Conference on Nuclear Engineering (ICONE12),* Washington, DC, April 2004.	Presented and published
J. Rempe, D. Knudson, K. Condie, W. D. Swank, K. Y. Suh, F.-B. Cheung, and S.-B. Kim, "Materials Interaction Tests to Identify Base and Coating Materials for an Enhanced In-Vessel Core Catcher Design," *Twelfth International Conference on Nuclear Engineering (ICONE12)*, Washington, DC, April 2004.	Presented and published
S. W. Noh, Y. H. Kim, S. J. Kim, K. Y. Suh, J. L. Rempe, F. B. Cheung, and S. B. Kim, "An Experimental Study of Critical Heat Flux in Large Inclined One-Dimensional Channels," *Tenth International Topical Meeting on Nuclear Reactor Thermal Hydraulics (NURETH-10),* Seoul, Korea, October 2003	Presented and published
F. B. Cheung, J. Yang, M. B. Dizon, J. L. Rempe, K. Y. Suh, F.-B. Cheung, and S.-B. Kim, "On the Enhancement of External Reactor Vessel Cooling of High-Power Reactors." *Tenth International Topical Meeting on Nuclear Reactor Thermal Hydraulics (NURETH-10),* Seoul, Korea, October 2003.	Presented and published

Table ES-6. INERI Publications

Publications	Status
F. B. Cheung, et al., "Limiting Factors for External Reactor Vessel Cooling, *Tenth International Topical Meeting on Nuclear Reactor Thermal Hydraulics (NURETH-10),* Seoul, Korea, October 2003.	Presented and published
J. L. Rempe, D. L. Knudson, K. G. Condie, K. Y. Suh, F.-B. Cheung, and S.-B. Kim, "Development of an Enhanced In-Vessel Core Catcher for Improving IVR Margins," *Tenth International Topical Meeting on Nuclear Reactor Thermal Hydraulics (NURETH-10),* Seoul, Korea, October 2003.	Presented and published
K. H. Kang, R. J. Park, S. B. Kim, K. Y. Suh, F. B. Cheung, and J. L. Rempe, "Experiments on Enhancement of In-vessel Corium Retention through In-Vessel Core Catcher," *Tenth International Topical Meeting on Nuclear Reactor Thermal Hydraulics (NURETH-10),* Seoul, Korea, October 2003.	Presented and published
S. J. Kim, Y.H. Kim, S. W. Noh, K. Y. Suh, J. L. Rempe, F. B. Cheung, and S. B. Kim "Experimental Study of Critical Heat Flux in Inclined Rectangular Gap," *GENES4/ANP2003*, Kyoto*,* Japan; September 2003.	Presented and published
Y. H. Kim, S.J. Kim, S. W. Noh, and K. Y. Suh, "Critical Heat Flux in Narrow Gap in Two-Dimensional Slices under Uniform Heating Condition," *the 17th International Conference on Structural Mechanics in Reactor Technology (SMiRT-17)*, Prague, Czech, August 2003	Presented and published
M. B. Dizon, J. Yang, F. B. Cheung, J. L. Rempe, K. Y. Suh, and S. B. Kim, "Effects of Surface Coating on Nucleate Boiling Heat Transfer from a Downward Facing Surface, *2003 ASME Summer Heat Transfer Conference*, Las Vegas, Nevada, July 2003.	Presented and published
F. B. Cheung, J. Yang, M. B. Dizon, J. L. Rempe, K. Y. Suh, and S. B. Kim, "Scaling of Downward Facing Boiling and Steam Venting in a Reactor Vessel/Insulation System," *2003 ASME Summer Heat Transfer Conference*, Las Vegas, Nevada, July 2003.	Presented and published
S. D. Lee and K. Y. Suh, "Natural Convection Heat Transfer in a Small Hemispherical Vessel, *Second International Conference on Heat Transfer, Fluid Mechanics and Thermodynamics*, Victoria Falls, Zambia, June 2003	Presented and published
Y.H. Kim, S. J. Kim, S. W. Noh, and K. Y. Suh, "Critical Heat Flux in One-Dimensional Downward-Heated Channel," *American Nuclear Society (ANS) Annual Meeting*, San Diego, California, June 2003	Presented and published
Y. H. Kim and K. Y. Suh, "Maximum Boiling Heat Transfer in Two-Dimensional Slice Narrow Gap with Downward-Facing heating," *Second International Conference on Heat Transfer, Fluid Mechanics and Thermodynamics*, Zambia, June 2003	Presented and published
K. Y. Suh, Y. H. Kim, S. D. Lee, C. S. Kim, J. L. Rempe, F. B. Cheung, and S. B. Kim, "Engineered Safety Features for In-Vessel Retention of Large Power Reactors*," Second International Congress on Advanced Power Plants*, Cordoba, Spain, May 2003.	Presented and published
S.J. Kim, Y.H. Kim, K. Y. Suh, J. L. Rempe, F. B. Cheung, and S. B. Kim, "One-Dimensional Downward-facing Critical Heat Flux Concerning Surface Orientation and Gap Size Effects," *Second International Congress on Advanced Power Plants,* Cordoba, Spain, May 2003.	Presented and published
J. L. Rempe, D. L. Knudson, K. G. Condie, K. Y. Suh, F.-B. Cheung, and S.-B. Kim, "A Strategy to Develop Enhanced In-Vessel Retention for Higher Power Reactors," *Eleventh International Conference on Nuclear Engineering (ICONE11),* Tokyo, Japan, April 2003.	Presented and published
J. L. Rempe, D. L. Knudson, K. G. Condie, K. Y. Suh, F.-B. Cheung, and S.-B. Kim, "Preliminary Investigations to Develop an Enhanced In-vessel Core Catcher Design," *Eleventh International Conference on Nuclear Engineering (ICONE11),* Tokyo, Japan, April 2003.	Presented and published
D. L. Knudson, J. L. Rempe, K. G. Condie, K. Y. Suh, F.-B. Cheung, and S.-B. Kim, "Late-Phase Melt Conditions Affecting the Potential for In-Vessel Retention in High Power Reactors," *Eleventh International Conference on Nuclear Engineering (ICONE11),* Tokyo, Japan, April 2003.	Presented and published
Project Reports (In additional to input received for Quarterly and Annual Reports, the following reports were exchanged).	
J. Rempe and D. Knudson, *Margin for In-Vessel Retention in the APR1400 - VESTA and SCDAP/RELAP5-3D Analyses,* INEEL/EXT-04-02549, December 2004.	Final Report Issued
J. T. Kim, R. J. Park, and S. B. Kim, A*ssessment of IVR (In-Vessel Retention) Enhancement using SCDAP/RELAP5 and LILAC Codes,* KAERI/GP-230/2005, December 2004.	Final Report Issued
F. B. Cheung, J. Yang, and M. B. Dizon, *SBLB Results for Task 3 on External Reactor Vessel Cooling (ERVC) Boiling Data and CHF Enhancement Correlations*, PSU/MNE-2004-INEEL-3, December 2004.	Final Report Issued
K. Y. Suh, C. S. Kim, and S. W. Noh, *Report on DELTA 1D & 3D Experiments and GAMMA 3D Results,* SNU/NE-2004-INEEL-2, November 30, 2004.	Final Report Issued
K. Y. Suh, S. D. Lee, and K. H. Lee, *Report on SIGMA 3D Experiments and Results,* SNU/NE-2004-INEEL-1, November 30, 2004.	Final Report Issued
K. H. Kang, R. J. Park, S. B. Kim, Experiments on Enhancement of In-vessel Corium Retention through In-vessel Core Catcher; Experimental Results of the LAVA-GAP-6 & 7 Tests, KAERI/GP-228/2004, November 2004.	Final Report Issued
F. B. Cheung, J. Yang, and M. B. Dizon, *SBLB Results for Task 3 on External Reactor Vessel Cooling (ERVC) Boiling Data and CHF Enhancement Correlations,* PSU/MNE-2004-INEEL-2, September 30, 2004.	Final Report Issued

Table ES-6. INERI Publications

Publications	**Status**
F. B. Cheung, J. Yang, and M. B. Dizon, A Hydrodynamic CHF Model for Downward Facing Boiling on a Coated Vessel, PSU/MNE-2004-INEEL-1, July 1, 2004.	Final Report Issued
K. S. Ha and S. B. Kim, Scaling Effect and 3-D Effect Based on T-HERMES Results, KAERI/GP-223/2004, July 30, 2004.	Final Report Issued
K. H. Kang, R. J. Park, S. B. Kim, *Experiments on Enhancement of In-vessel Corium Retention through In-vessel Core Catcher: Experimental Results of the LAVA-GAP-4 & 5 Tests,* KAERI/GP-220/2004, July 2004.	Final Report Issued
K. H. Kang, R. J. Park, S. B. Kim, *Experiments on Enhancement of In-vessel Corium Retention through In-vessel Core Catcher: Experimental Results of the LAVA-GAP-2 & 3 Tests*, KAERI/GP-221/2004, June 2004.	Final Report Issued
J. L. Rempe and K. G. Condie, *Prototypic Testing of Core Catcher Materials,* INEEL/EXT-03-00378, June 2004.	Final Report Issued
J. L. Rempe, K. G. Condie, and W. D. Swank, *Core Catcher Materials Selection and Fabrication*, INEEL/EXT-03-00377, March 2004.	Final Report Issued
F. B. Cheung, J. Yang, and M. B. Dizon, *A Hydrodynamic CHF Model for Downward Facing Boiling on a Coated Vessel,* Report #PSU/MNE-2004-INEEL-1, July 1, 2004.	Final Report Issued
F. B. Cheung, J. Yang, and M. B. Dizon, *SBLB Results for Task 3 on External Reactor Vessel Cooling (ERVC) Design Enhancements,* Report #PSU/MNE-2003-INEEL-3, September 25, 2003.	Final Report Issued
J. Yang, M. B. Dizon, and F. B. Cheung, *Numerical Analysis of Steam Venting in the Annular Channel of an Enhanced Vessel/Insulation Design,* PSU/MNE-2003-INEEL-2, June 24, 2003.	Final Report Issued
M. B. Dizon, J. Yang, and F. B. Cheung, *Effects of Surface Coating on the Enhancement of the Critical Heat Flux on the Outer Surface of a Hemispherical Test Vessel,* PSU/MNE-2003-INEEL-1, June 24, 2003.	Final Report Issued
F. B. Cheung and M. B. Dizon, *Literature Survey on the Enhancement of Nucleate Boiling Heat Transfer and Critical Heat Flux Using Surface Coatings and/or Other Relevant Techniques,* Report #PSU/MNE-2002-INEEL-1, June 30, 2002.	Final Report Issued
K. Y. Suh, Y. H. Kim, C. S. Kim, S. J. Kim, and S. W. Noh, *SNU Letter Report Describing Additional GAMMA 3D, DELTA 1D and 3D Results*, SNU/NE-2003-INEEL-2, November 28, 2003.	Final Report Issued
K. Y. Suh, Y. H. Kim, J. J. Kim, S. J. Kim, S. W. Noh, *SNU Letter Report Summarizing GAMMA 1D and 2D Interim Results*, SNU/NE-2003-INEEL-1, November 28, 2003.	Final Report Issued
K. Y. Suh, Y. H. Kim C. S. Kim, S. J. Kim, and S. W. Noh, *Literature Survey on Experiments on Heat Transfer Coefficients for the External Reactor Vessel Cooling,* SNU/NE-2002-INEEL-4, August 7, 2002.	Final Report Issued
K. Y. Suh and S. D. Lee, Report on SIGMA 2D & 3D Modifications, Feasibility Study, and Test Plan, SNU/NE-2002-INEEL-3, August 7, 2002	Final Report Issued
K. Y. Suh, Y. H. Kim and S. J. Kim, *Literature Survey on the Effect of Surface Orientation and Gap Size on the Critical Heat Flux in the Narrow Gap Cooling Experiments*, SNU/NE-2002-INEEL-2, August 7, 2002.	Final Report Issued
K. Y. Suh, Y. H. Kim and S. J. Kim, *Critical Heat Flux in the Narrow Gap Cooling Experiments GAMMA 1D and 2D Experiments,* SNU/NE-2002-INEEL-1, September 30, 2002.	Final Report Issued
K. H. Kang and S. B. Kim, Improvement of In-vessel Corium Retention through Internal and External Cooling using In-vessel Core Catcher, KAERI/GP-227/2004, October 2002.	Final Report Issued

References

ES-1. The SCDAP/RELAP5-3D© Development Team, *SCDAP/RELAP5-3D© Code Manuals*, INEEL/EXT-02/00589, Idaho National Engineering and Environmental Laboratory, May 2002.

ES-2. S. J. Oh, “Realistic Approach to IVR for APR1400”, Korea Hydro and Nuclear Power Company, Ltd., presentation during meetings at the Idaho National Engineering and Environmental Laboratory, July 2002.

ES-3. L. J. Siefken et al., SCDAP/RELAP5/MOD3.3 Code Manual, NUREG/CR-6150, INEL-96/0422, January 2001.

ES-4. Rempe, J. L., et al., *Potential for AP600 In-Vessel Retention through Ex-Vessel Flooding, Technical Evaluation Report,* INEEL/EXT-97-00779, Idaho National Engineering and Environmental Laboratory, December 1997.

CONTENTS

1. INTRODUCTION

Idaho National Engineering and Environmental Laboratory

In-vessel retention (IVR) of core melt is a key severe accident management strategy adopted by some operating nuclear power plants and proposed for some advanced light water reactors (ALWRs) and next-generation (GEN IV) reactors. If there were inadequate cooling during a reactor accident, a significant amount of core material could become molten and relocate to the lower head of the reactor vessel, as happened in the Three Mile Island Unit 2 (TMI-2) accident. If it is possible to ensure that the vessel head remains intact so that relocated core materials are retained within the vessel, the enhanced safety associated with these plants can reduce concerns about containment failure and associated risk. For example, the enhanced safety of the Westinghouse Advanced 600 MWe PWR (AP600) resulted in the United States Nuclear Regulatory Commission (US NRC) approving the design without requiring certain conventional features common to existing LWRs.

However, it is not clear that currently proposed external reactor vessel cooling (ERVC) without additional enhancements could provide sufficient heat removal for higher-power reactors (up to 1500 MWe). Hence, the US Department of Energy (US DOE) and the Korean Ministry of Science and Trade (MOST) sponsored a US-Korean International Nuclear Energy Research Initiative (INERI) project[1-1] to the Idaho National Engineering and Environmental Laboratory (INEEL), Seoul National University (SNU), Pennsylvania State University (PSU), and the Korea Atomic Energy Research Institute (KAERI) to investigate the performance of ERVC and core catchers to determine if IVR is feasible for reactors up to 1500 MWe.

1.1. Objective

The ultimate objective of this project was to develop specific recommendations to improve the margin for IVR in high-power reactors. The systematic approach applied to develop these recommendations combined state-of-the-art analytical tools and key US and Korean experimental facilities. Recommendations focus on modifications to enhance ERVC (through improved data, vessel coatings to enhance heat removal, and an enhanced vessel/insulation configuration to facilitate steam venting) and modifications to enhance in-vessel debris coolability (through an enhanced in-vessel core catcher configuration with optimum thickness and materials specifications). This project applied improved analytical tools and obtained new experimental data to evaluate options that could increase the margin associated with these modifications. This increased margin has the potential to improve plant economics (owing to reduced regulatory requirements) and increase public acceptance (owing to reduced plant risk). Because the design information available for GEN IV reactors is insufficient, this project focussed upon the Korean Advanced Power Reactor 1400 MWe (APR1400) design. However, margins offered by each modification were evaluated such that results can easily be applied to a wide range of existing reactors, advanced reactor designs, and GEN IV reactor designs.

1.2. Project Organization

This three-year project included four tasks. In Task 1, which was completed during the first year of this research program, SCDAP/RELAP5-3D© calculations were conducted to define representative bounding late phase melt conditions. Characteristic parameters from those bounding conditions (thermal loads, pressure, relocated mass, etc.) were used to design an optimized core catcher (in Task 2) and ERVC enhancements (in Task 3). Task 2 and 3 activities, which were initiated in the first year of this project, were completed during the third year of this project. In Task 4, collaborators assessed the improved margin obtained with Task 2 and 3 design modifications. Margins are presented such that the impact of these modifications can easily be applied to other reactor designs. As indicated in Figure 1-1, key facilities and capabilities of each collaborator were used to complete these tasks.

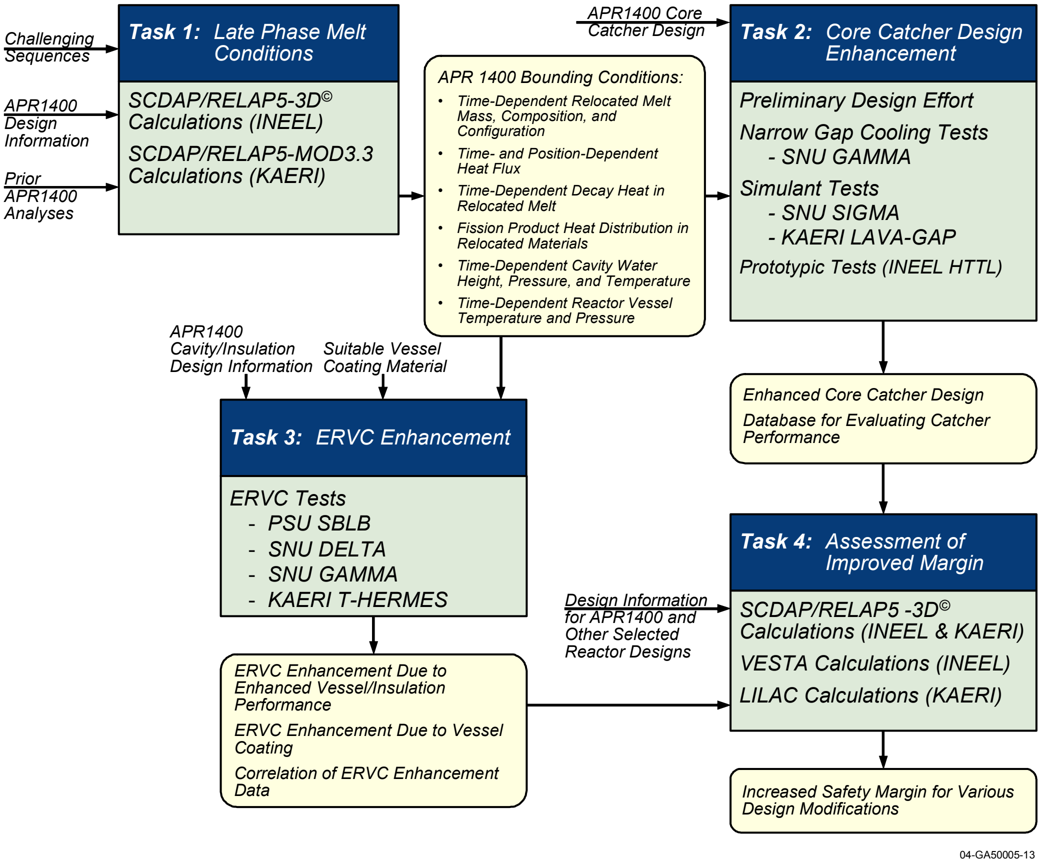

Figure 1-1. Project approach

1.3. Background

As discussed in Section 1.1, this project used improve analytical methods and new experimental data to evaluate two enhanced methods proposed to ensure IVR (see Figure 1-2): an in-vessel core catcher to promote internal cooling of relocated corium materials in the lower head and a flooded reactor cavity to enhance external cooling of the reactor vessel. One or more of these mechanisms are used by a host of advanced and proposed GEN IV reactor designs, including the Westinghouse AP600, the Westinghouse

AP1000, the KAERI Simple and Intelligent PWR with Bloc Type/Double Vessel, and the Framatome SWR1000. To demonstrate the operation of these mechanisms, this project focussed on the design of the Korean Advanced Power Reactor 1400 MWe (APR1400), the plant design studied in this project.

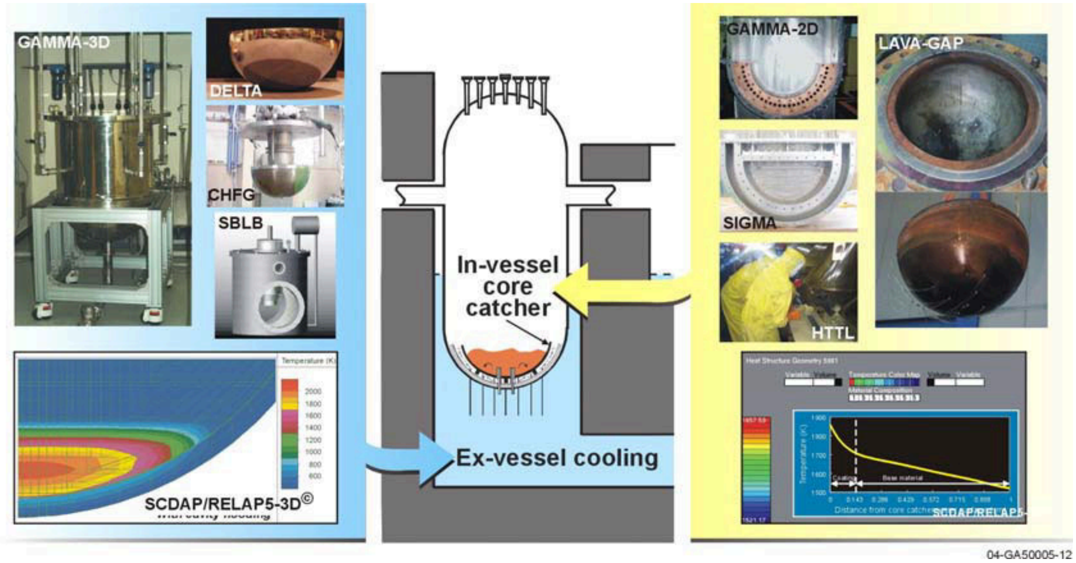

Figure 1-2. Key U.S. and Korean experimental facilities and state-of-the-art analytical tools are applied to investigate options that could enhance external reactor vessel cooling and internal core catcher performance.

The APR1400, whose rated electric power is 1400 MWe, is an evolutionary advanced light water reactor. APR1400 reactor vessel internal structures are similar to those used in the CE System 80+ reactor.[1-2] As shown in Figure 1-3, most of the coolant flow entering the four cold legs is directed downward along the downcomer into a flow baffle and then up through flow plates toward the lower core support plate. Sixty-one in-core instrumentation nozzles penetrate the APR1400 lower head.

1.4. Report Contents

This document summarizes activities and accomplishments completed in this joint US-Korean INERI project. Sections 2 through 5 summarize results from each task completed. Section 6 highlights results and conclusions that can be drawn from results obtained from each task. Section 7 provides programmatic information, such as the status of each task with respect to planned schedule and budget.

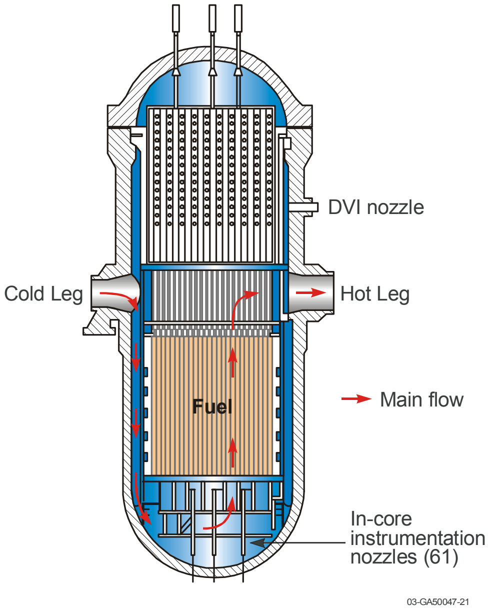

Figure 1-3. APR1400 reactor vessel internals.

1.5. References

1-1. Rempe, J. L., et al., *In-Vessel Retention Strategy for High-Power Reactors,* proposal submitted in response to Program Announcement LAB NE-INERI-2001001, August 30, 2001.

1-2. Combustion Engineering, Inc., *CE Standard Safety Analysis Report (CESSAR) Design Certification, System 80+ Standard Design,* up through Amendment W, June 17, 1994.

2. TASK 1: LATE-PHASE MELT CONDITIONS

2.1. Objective and Overview of Task 1

The objective of Task 1 is to use the SCDAP/RELAP5-3D©[2-1] and SCDAP/RELAP5/MOD3.3 codes to quantify late-phase melt conditions that could affect the potential for in-vessel retention (IVR) of core melt following a severe accident in the Korean Advanced Power Reactor 1400 MWe (APR1400). The late-phase melt conditions of specific interest include the melt mass and its composition, temperature, and power (due to decay heat generation). Several severe accident transients were selected for analysis that would lead to bounding estimates of the potential melt conditions. As discussed in Section 1, results generated through completion of this task were used as inputs in the design of a core catcher (in Task 2) and the enhancement of external reactor vessel cooling (ERVC) (in Task 3). The results were also used in Task 4 as base values to estimate improvements in IVR margins that could be achieved through incorporation of concepts developed through the Task 2 and 3 design efforts.

To accomplish the task objective, INEEL applied the SCDAP/RELAP5-3D© code and KAERI applied the SCDAP/RELAP5/MOD3.3 and SCDAP/RELAP5-3D© codes to the APR1400 plant. This section highlights selected portions of these activities. INEEL calculational efforts are summarized in Section 2.2, and KAERI efforts are summarized in Sections 2.3 and 2.4. Conclusions and key insights are given in Section 2.5. A more detailed description of these activities can be found in References 2-2 through 2-4.

2.2. INEEL SCDAP/RELAP5-3D© Calculations

Idaho National Engineering and Environmental Laboratory

In order for INEEL to apply the SCDAP/RELAP5-3D© to the APR1400, a plant model was needed, steady state calculations with the model were performed to serve as a starting point for subsequent SCDAP/RELAP5-3D© transient analyses, severe accident transients were selected, and finally, the actual transient calculations were completed. This section summarizes selected portions of these activities. Specifically, following a brief description of the SCDAP/RELAP5-3D© code in Section 2.2.1, the model is described in Section 2.2.2, and selected results are presented in Section 2.2.3. A more detailed description of these activities can be found in Reference 2-2.

2.2.1. Description of SCDAP/RELAP5-3D©

SCDAP/RELAP5-3D© is an advanced, state-of-the-art, best-estimate computer code designed for simulating severe reactor accidents. The code predicts the thermal-hydraulic response of the reactor coolant system (RCS) and the progression of damage associated with reactor core and reactor vessel heatup. Links with other detailed, mechanistic codes can and have been used to integrate fission product transport and containment response into accident simulations.

SCDAP/RELAP5-3D© is composed of RELAP5, SCDAP, COUPLE, and MATPRO modules. RELAP5 is based on a two-fluid, non-equilibrium model for calculating RCS thermal-hydraulics, including flow through porous media with fully integrated, multi-dimensional thermal-hydraulic and kinetic modeling capabilities. SCDAP contains models for predicting core damage progression, including fuel rod ballooning with corresponding changes in hydraulic flow paths, heatup and oxidation of fuel rods and related core components, fuel melting and in-core molten pool formation, and relocation of molten corium to the lower head accounting for interaction with the lower core support plate and other lower head structures. COUPLE provides a two-dimensional finite element framework for detailed simulation of any reactor area of interest. It is typically applied in predicting lower head response following corium relocation. MATPRO contains an extensive library of data and subroutines used to establish material properties and reaction rates in conjunction with reactor simulation.

SCDAP/RELAP5-3D© has complete flexibility that allows modeling individual components, separate subsystems, or an entire reactor complex with fully-integrated control system logic. This code flexibility arises from a combination of user-definable boundary conditions and a comprehensive set of user-selectable components (i.e., pipes, pumps, turbines, valves, accumulators, separators, fuel rods, control rods, control blades, core shrouds). The code is fully capable of simulating the effects of virtually any postulated reactor accident including (but not limited to) scenarios covering the complete range of potential break sizes (or loss of coolant accidents), station blackout events, anticipated transients without scram, reactivity insertion accidents, and secondary system faults (turbine trips, loss of feedwater, valve failures, etc.). The IVR modeling capabilities of SCDAP/RELAP5-3D© are of particular interest in this analysis. Major processes associated with heat transfer from a stratified corium bed or a homogeneously-mixed corium bed can be simulated using SCDAP/RELAP5-3D©.

2.2.2. APR1400 Model Description

The SCDAP/RELAP5-3D© model of the APR1400 was derived from information provided by Korea Hydro and Nuclear Power Company, Ltd.[2-5] The resulting model nodalization is shown in Figure 2-1. As indicated in the figure, the model includes the reactor vessel; two hot legs feeding two steam generators (SGs); four cold legs, each with a primary reactor coolant pump (RCP); and a pressurizer with a power operated relief valve (PORV) attached to one of the hot legs. (In this model, an “A” is used as a designator for components on the side of the reactor with the pressurizer and a “B” is used as a designator for components on the opposite side of the reactor.) Four safety injection tanks (SITs), four connections to an in-containment refueling water storage tank (IRWST), and a limited part of the secondary piping are also included. The model has a total of 250 RELAP5 volumes, 316 RELAP5 junctions, and 284 RELAP5 heat structures (not shown in the figure). The active core consists of three parallel flow channels (numbered 220, 222, and 224), each divided into 15 volumes in the axial direction with radial cross flow connections. A SCDAP fuel rod component and a SCDAP control rod component were used to represent the fuel loading in each core flow channel. (Empty guide tubes were represented by a separate RELAP5 heat structure.) A COUPLE two-dimensional finite element mesh with 234 nodes and 204 elements was used to represent the reactor vessel lower head and the internal region of the lower head that could potentially fill with relocated corium (see Figure 2-2).

2.2.3. Selected SCDAP/RELAP5-3D© Results

SCDAP/RELAP5-3D© transient analyses were required to quantify late-phase melt conditions that could affect the potential for IVR of core melt following severe accidents in APR1400. These transient analyses were conducted after applying the model described in Section 2.2.2 in a steady state analysis to obtain initial conditions that represent the stable full power operating conditions in the APR1400.

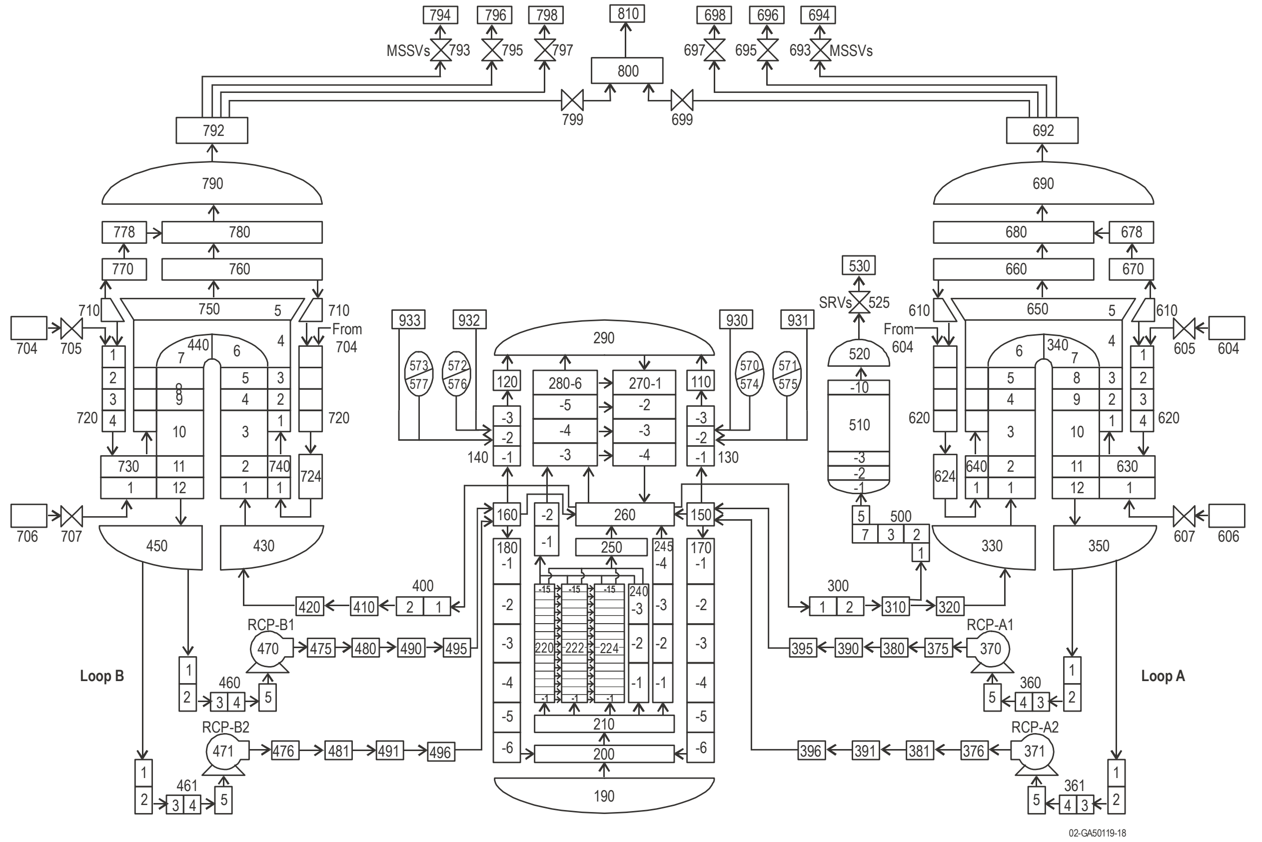

Figure 2-1. INEEL SCDAP/RELAP5-3D$^{©}$ model nodalization of APR1400.

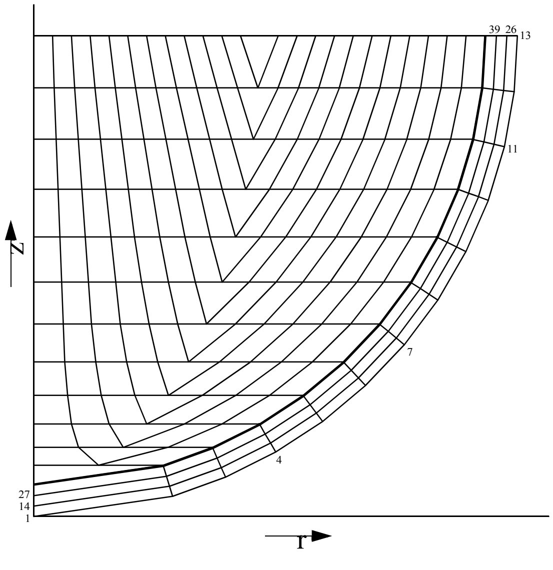

Figure 2-2. COUPLE two-dimensional finite element mesh representing the lower head of the APR1400 reactor vessel (with selected node numbers after correcting the position of nodes 14, 26, 27, and 39).

2.2.3.1. Transient Selection

The goal associated with selecting severe accidents for consideration here was to try to identify transients that will bound potential late-phase melt conditions in the APR1400. If that goal is achieved, core catcher designs and ERVC enhancements can presumably be developed to ensure IVR of core melt for all possible APR1400 scenarios.

Unfortunately, identifying transients that will bound potential late-phase melt conditions is complicated. For example, large loss of coolant accidents (LOCAs) may be more severe than small LOCAs, primarily because makeup systems normally offset small coolant losses. It is conceivable, however, that small LOCAs (with some loss or degradation of makeup) could be more severe than otherwise comparable large LOCAs relative to late-phase melt conditions. This could occur because, among other possibilities, more water/steam may be available for exothermic oxidation following a small break. Higher oxidation rates could lead to higher core melt fractions and larger melt relocations into the lower head. A series of detailed severe accident analyses could be completed to deterministically sort through numerous scenarios (and variations thereof) to identify the bounding transients relative to late-phase melt conditions. Instead of embarking on such a series of severe accident calculations, LOCAs, station blackout (SBO) accidents, and loss of feedwater (LOFW) sequences were assumed to be among the major IVR-related scenarios based on reactor analysis experience. Accordingly, two basic transients, see Table 2-1, were selected including a cold leg break to represent the APR1400 LOCA response and a SBO with LOFW to combine the remaining IVR scenarios.

In addition to attempting to select bounding transients, conservative accident definitions relative to late-phase melt conditions were also adopted as indicated in Table 2-1. Perhaps one of the most conservative definitions was the assumed failure of all safety injection systems (other than passive injection via the SITs). That assumption, along with others listed in the table, yields sequences that are expected to have very low probabilities of occurring. However, this conservative approach is consistent with the goal of establishing bounding late-phase melt conditions. Furthermore, the resulting late-phase melt conditions, regardless of their probability of developing, will allow the desired quantification of improvements in IVR margins that are achievable through use of ERVC enhancements and the core catcher designed in this program. Higher probability sequences, with expected reductions in the severity of the late-phase melt conditions, should be adequately bounded as a result.

Table 2-1. Severe accident transients selected for SCDAP/RELAP5-3D© analysis.

Transient	Description
SBO	• Loss of all AC power (with failure of backup generators, without recovery) • Reactor and RCP trip on loss of power without automatic RCS depressurization • Loss of all SG feedwater with SGA[a] depressurization via stuck open main steam safety valve • All safety injection systems fail • Without IRWST flow • Normal SIT operation
LOCA	• Break in cold leg A[a] (area = 0.0465 m^2) • Reactor and RCP trip on break • All safety injection systems fail • Without IRWST flow • Normal SIT operation

a. Where ‘A’ designates the reactor coolant loop containing the pressurizer.

2.2.3.2. Transient Results

Two SCDAP/RELAP5-3D© transient calculations were completed to quantify potential late-phase melt conditions for the APR1400. Table 2-2 lists the timing of key events predicted in the calculations.

Table 2-2. Sequence of transient events.

Event	Time (in seconds) for	
	SBO	LOCA
Transient initiation due to - loss of AC power (with failure of backup generators) - 0.0465 m^2 break in cold leg A[a]	 0 	 0
Reactor and RCP trip	0	0
SG main steam isolation valves (MSIVs) close	2	0
Loss of SG feedwater (with failure of auxiliary feedwater)	5	0
SGA steam safety valve fails open on first challenge	8	nc[b]
Pressurizer empties (97% void in bottom of pressurizer)	223[c]	67[d]
First pressurizer PORV challenge and onset of PORV cycling	890	np[e]
SGs dryout (99% void in bottom of SGA / SGB secondaries)[a]	1,090 / 2,380	np / np
Pressurizer refills due to RCS heating and expansion (1% void in top)	2,920	np
Vapor collects in SG U-tubes ending liquid full loop natural circulation	~3,530	np
Collapsed liquid level falls below top of fuel rods	4,320	119
Vapor in the core exit begins to superheat	4,500	212
Onset of SIT injection	np	212
Top of fuel rods reflooded by SIT injection	np	254
SITs empty	np	876
Collapsed liquid level falls below top of fuel rods for second time	np	970
Onset of core oxidation (> 0.01 kg of H_2 produced)	4,960[f]	2,190[g]
Collapsed liquid level falls below bottom of fuel rods	5,440	2,090
Onset of fuel melting	5,810	3,660
Pressurizer drains a second time and remains empty (99% void in bottom)	6,500	np
Pressurizer surge line fails by creep rupture	7,650	np
First relocation into the lower head	8,800	3,280
First relocation of molten fuel into the lower head	10,600	4,990[h]
Creep rupture failure of lower head and end of calculation	10,900	np

a. Where ‘A’ designates the reactor coolant loop containing the pressurizer.
b. Not considered in this calculation.
c. Due to initial RCS cooldown and shrinkage.
d. Due to LOCA.
e. Not predicted before the end of the calculation.
f. In total, 869 kg of H_2 was generated.
g. In total, 169 kg of H_2 was generated.
h. Calculation terminated at the time of relocation.

SBO Calculations

The SBO transient began with a complete loss of AC power while the APR1400 was operating at steady state conditions. Consequently, control rod drives lost power, the reactor tripped, and the main feedwater pumps and primary RCPs started to coastdown. A closing time of 2 s was assumed for the SG main steam isolation valves (MSIVs) following reactor trip. The flow of feedwater was reduced to zero before feedwater pump coastdown was complete because the main feedwater valves were assumed to close in 5 s. At that point, SG secondaries were effectively isolated. Recovery of power and/or feedwater was not considered.

After isolation, SG pressures increased as a result of secondary inventory boiling due to natural circulation flow of primary coolant and the corresponding heat transfer of core decay power. SG pressures increased until secondary relief valve opening set points were reached. SGA relief valves were assumed to fail open when first challenged, resulting in SGA depressurization. SGB pressures were maintained between the opening and closing pressures of the relief valves.

The RCS pressure initially decreased because the RCS was cooled by natural circulation heat transfer to SG secondaries. SGA provided most of the early RCS cooling because the secondary saturation temperature was significantly reduced through depressurization of that generator due to the assumed failure of its safety valve. However, without a source of feedwater, heat transfer from the RCS diminished as SG inventories boiled away. Consequently, the RCS pressure began to increase after SG dryout; ultimately challenging the pressurizer PORVs. The RCS pressure remained between opening and closing set points of the PORVs thereafter (see Figure 2-3).

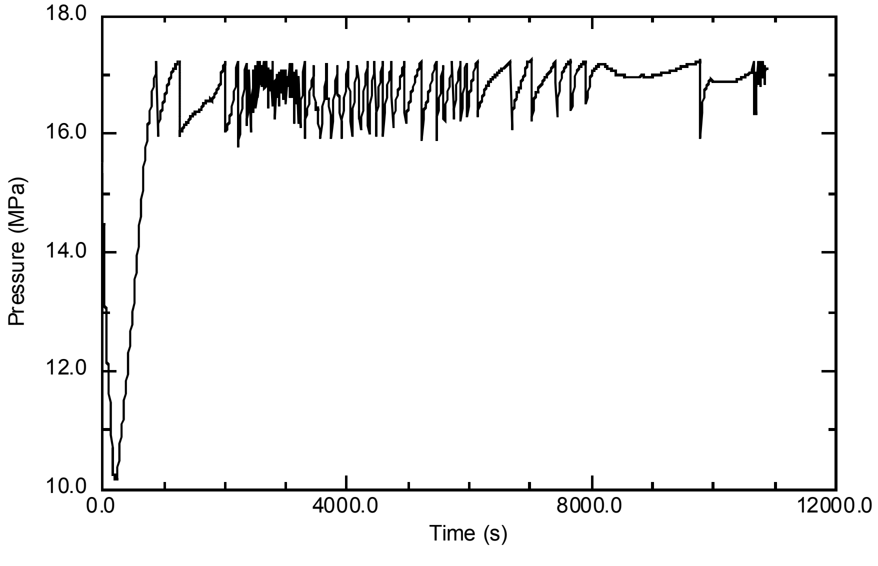

Figure 2-3. RCS pressure in the SBO transient.

RCS inventory was lost through the cycling pressurizer PORVs, which emptied the pressurizer (a final time) and led to core uncovery and heatup. Core uncovery and heatup are represented by Figures 2-4 and 2-5, respectively. Figure 2-4 is the collapsed liquid level in the reactor vessel. Figure 2-5 is the maximum cladding surface temperature prior to the onset of fuel melting. Thereafter, the figure represents the maximum temperature in the core region (which will be the temperature of the molten debris). Fuel rod oxidation was an important part of the heatup. Decay heat and the energy associated with the exothermic oxidation process was distributed into the hot leg and surge line during each pressurizer PORV cycle. As a result, a surge line creep rupture failure was predicted before core relocation and lower head failure. Although surge line failure was predicted, simulating the break and the corresponding RCS depressurization was not included because doing so would be inconsistent with the objective of quantifying bounding late-phase melt conditions.

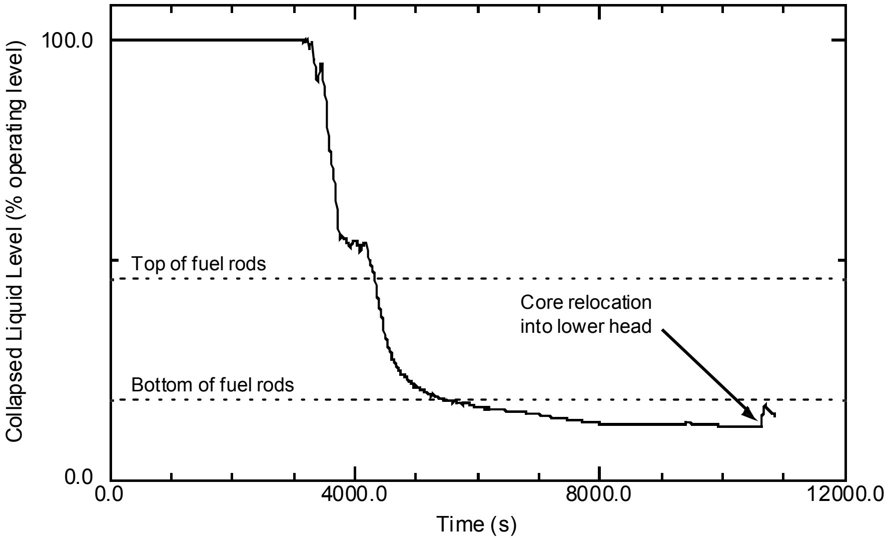

Figure 2-4. Reactor vessel collapsed liquid level in the SBO transient.

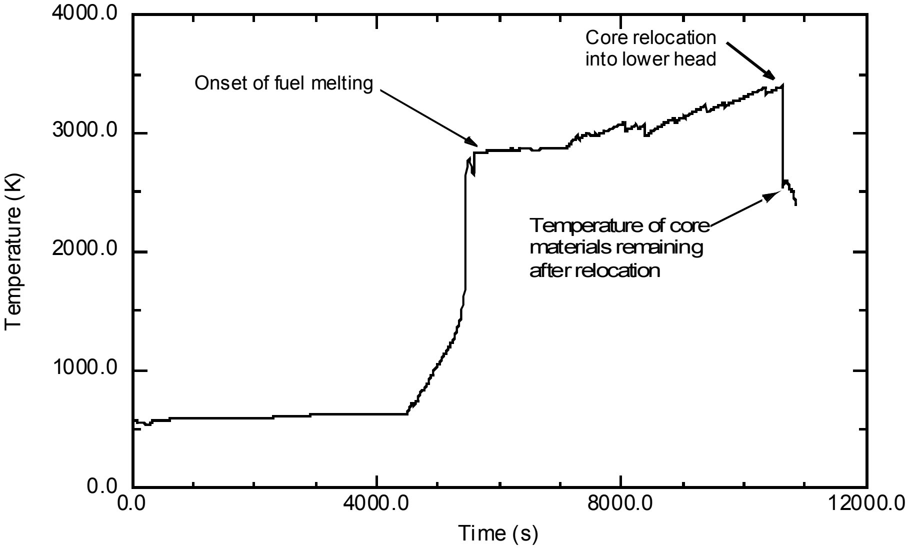

Figure 2-5. Maximum core temperature in the SBO transient.

SCDAP/RELAP5-3D© results indicating the surge line will fail before core relocation and lower head failure during an APR1400 SBO transient affect IVR margins. If the RCS depressurizes through a surge line break, core heatup and relocation will be delayed due to injection from the SITs. Furthermore, the

RCS will be at low pressure when relocation does occur, which means the time between core relocation and lower head failure will increase (because lower head failure is affected by both temperature and pressure). Therefore, surge line failure could delay lower head failure because core relocation will be delayed and the time between core relocation and lower head failure will be extended.

LOCA Calculations

The LOCA-1 transient was initiated, with the APR1400 at steady state conditions, by a 0.0465 m^2 break in one of the cold legs in the primary coolant loop containing the pressurizer. The break flow, led to rapid RCS depressurization (shown in Figure 2-6) and early draining of the pressurizer.

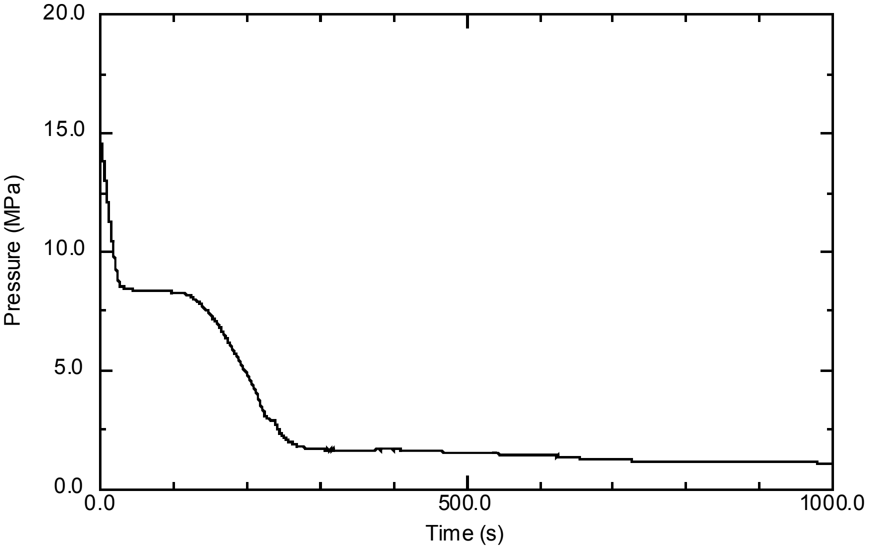

Figure 2-6. RCS pressure in the LOCA transient.

RCS depressurization led to SIT injections starting at 212 s. The collapsed liquid level had fallen below the top of the fuel rods by that time as indicated in Figure 2-7. However, injection flow from the SITs was sufficient to reflood the active core and keep the fuel rods completely covered until 970 s.

Core heatup began after the SITs emptied and the core began to uncover. Consequently, the onset of oxidation was predicted at 2,190 s as core temperatures approached 1000 K as indicated in Figure 2-8. Heat added as a result of oxidation, in combination with the continual depletion of RCS inventory through the break, led to fuel melting beginning at 3,660 s. Without recovery of core cooling, the in-core molten pool grew until a large relocation of molten core materials into the lower head was predicted at 4,990 s.

2.2.3.3. Late-Phase Melt Conditions

Late-phase melt conditions for the APR1400 transients analyzed are summarized in Table 2-3. In all calculations, large corium masses and high corium temperatures were predicted.

Decay power results were used to estimate the average heat flux that must be removed from the APR1400 reactor vessel lower head to ensure IVR of the corium. This estimate was made assuming a hemispherical configuration, without sensible heat effects, for quasi-steady conditions, with reasonable

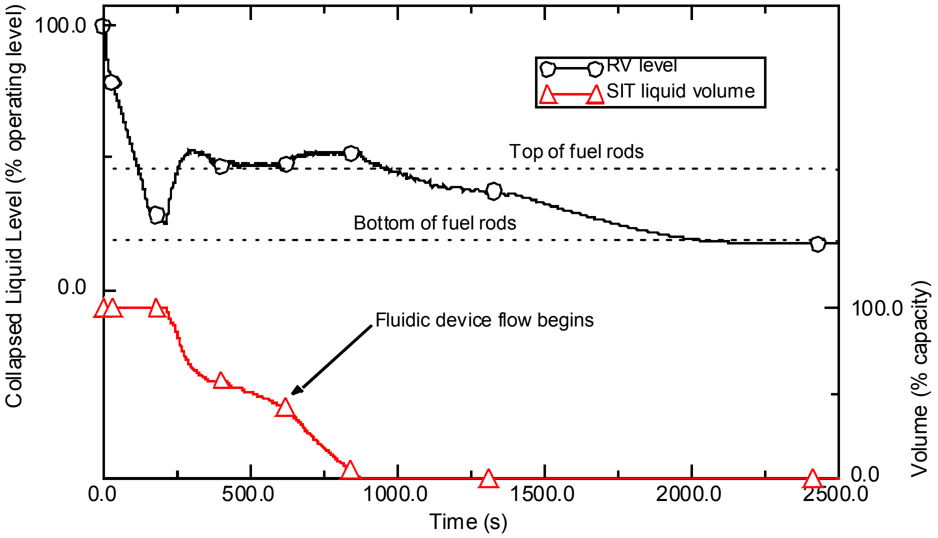

Figure 2-7. Reactor vessel collapsed liquid level relative to SIT liquid volume in the LOCA transient.

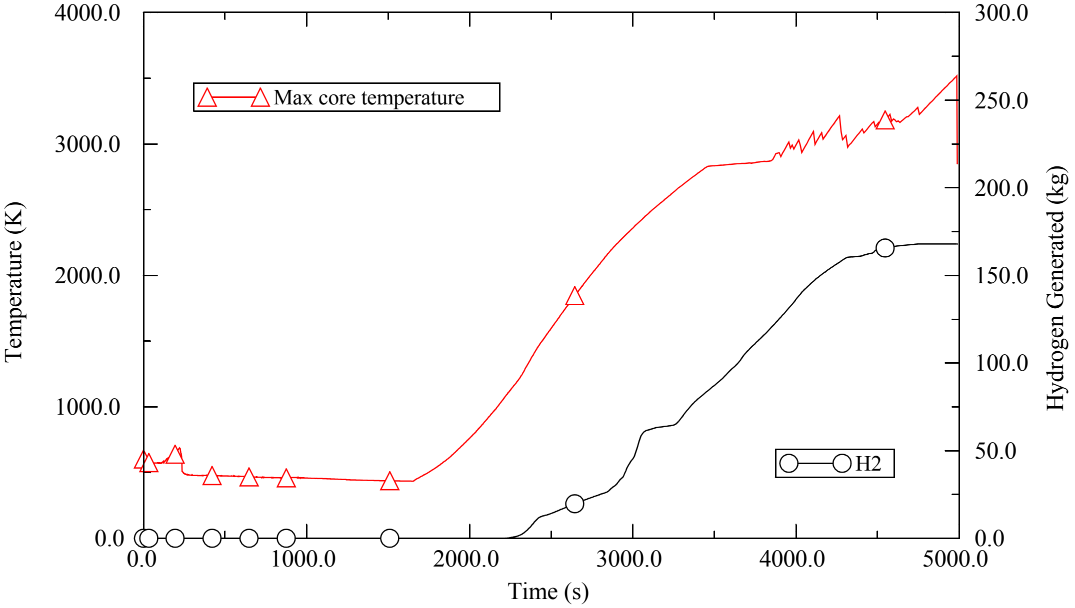

Figure 2-8. Maximum core temperature relative to hydrogen generation in LOCA-1.

limits for upward heat loss. The limits for the upward loss were set at 10 and 90% of the total decay heat level, which was reinforced by SCDAP/RELAP5-3D© results that indicated an upward loss of ~20% of the total power at the time of relocation in all transients. In selecting these limits, it was also acknowledged that heat that is not rejected upward must be removed from the exterior of the lower head in quasi-steady

Table 2-3. Late-phase melt conditions for APR1400 transients.

Transient	Time of Relocation (s)	Relocated Mass (kg)				Corium Characteristics at Time of Relocation				
		UO_2	ZrO_2	Zr	Total	Depth (m)	Temperature (K)	Power (MW)	Power Density (MW/m^3)	Estimated Average Vessel Heat Flux (MW/m^2)[a]
SBO	10,600	111,000	21,200	8,300	144,000[b]	1.86	3,390	52.0	2.72	0.161 to 1.45
LOCA	4,990	108,000	5,180	3,520	119,000[c]	1.60	3,460	51.2	3.48	0.182 to 1.64

a. Assuming a hemispherical configuration, without sensible heat effects, for quasi-steady conditions, with estimated limits of heat loss from the upper corium surface (at 10 and 90% of the total decay heat level).

b. Includes 250 kg Zr, 2,350 kg of control rod absorber material, and 180 kg of stainless steel from earlier relocations.

c. Includes 276 kg Zr, 2,350 kg of control rod absorber material, and 95 kg of stainless steel from earlier relocations.

state conditions. Resulting values of the estimated average heat flux for APR1400 ranged from 0.161 to 1.64 MW/m^3 as listed in Table 2-3.

Average heat flux values estimated for APR1400 are higher than values predicted for other advanced reactor designs. Specifically, peak heat fluxes for the Westinghouse AP600 reactor were calculated to be ~0.7 MW/m^2 (Reference 2-6). Estimates for the APR1400 average heat flux are as much as a factor of ~2.3 larger. The estimated values also exceed current predictions of the maximum critical heat flux (CHF) for submerged (externally flooded) hemispheres. Specifically, the peak CHF for the Westinghouse Advanced Passive Light Water Reactor - 600 MWe (AP600) hemispherical geometry has been calculated to be ~1.4 MW/m^2 (Reference 2-6). Estimates for the APR1400 average debris heat flux to the vessel are as much as a factor of ~1.2 larger than these CHF estimates. However, as discussed in Reference 2-2, the above calculations did not consider the following phenomena that may reduce the challenge for IVR:

- ***RCS depressurization.*** There is a high probability for RCS depressurization through creep rupture failure of the RCS piping in APR1400 SBO accidents. This depressurization could be expected without relying on plant equipment/systems for automatic RCS depressurization. Specifically, surge line failure, due only to flows induced by cycling pressurizer PORVs, was predicted before core relocation and lower head failure in all SBO calculations completed. Although surge line failures were not modeled, it is clear that the calculated results would have differed significantly if credit had been taken for RCS depressurization corresponding with such failures. If the RCS was allowed to blowdown through a predicted surge line break, core heatup and relocation would have been delayed due to injection from the SITs. Any delay in relocation will reduce the corium decay power level, and thereby reduce the heat flux that would have to be removed from the lower head to ensure IVR of the melt. Furthermore, the RCS would have been at low pressure when relocation finally occurred. Because lower head failure is affected by both temperature and pressure, the time between core relocation and lower head failure would have increased due to depressurization.
- ***Corium dilution.*** Average heat fluxes, as estimated for APR1400 transients and listed in Table 2-3, are functions of corium power and volume. Steel structures within the vessel represent a potentially significant component in the volume of relocated corium. Those structures, which primarily include steel in upper and lower plenum regions and steel in the lower core support plate, were not subject to relocation in this analysis because plant design details needed for simulation of their relocation were not available. However, if steel accounting was added to the APR1400 model, heat

fluxes could be reduced. In a stratified configuration (in which the oxidic material lies below a metallic layer), steel addition can proportionately increase the depth of the overlying metallic layer and thereby reduce the corresponding heat flux through that layer to the lower head wall. In a homogeneous configuration, steel addition can simply increase the corium volume without altering the decay power. Consequently, the average heat flux to the lower head wall is reduced through dilution of the corium.

- ***Lower head heat transfer.*** The lower head was assumed to be perfectly insulated because the objective of this analysis was limited to predicting bounding late-phase melt conditions (without specific interests in detailed calculations of the lower head response). Without heat transfer from the vessel, the time between corium relocation and lower head failure was predicted to be very short. In such cases, however, the time needed for development of steady state natural convection in the molten corium pool is not available (As indicated in Reference 2-7, a protracted period is required before pool transient heat transfer will approach steady state heat transfer).

2.3. KAERI SCDAP/RELAP5/MOD3.3 Calculations

Korea Atomic Energy Research Institute

The main objective of the present study is to identify the state of the in-vessel materials in the reactor vessel lower plenum at vessel failure in the high and low pressure sequences in APR 1400. To achieve this objective, high-pressure transients of a total loss of feed water (TLFW) to the steam generators and a station blackout (SBO) and low-pressure transients due to 1.35, 2, 3, 4.28, and 9.6 inch break Loss Of Coolant Accidents (LOCAs) without safety injection were evaluated by KAERI using the SCDAP/RELAP5/MOD3.3 computer code[2-8] from transient initiation to reactor vessel failure. In the TLFW sequence, three transients with/without depressurization of the reactor coolant system (RCS) using the pressurizer power operated safety relief valve (POSRV), and with pressurizer surge line failure by hot steam from the core have been simulated. In the SBO sequence, two transients with/without pressurizer surge line failure have been simulated. Best estimate calculations from initiating events of 1.35 inch, 2 inch, 3 inch, 4.28 inch, and 9.6 inch break SBLOCAs without the safety injection to reactor vessel failure have been carried out using the SCDAP/RELAP5/MOD 3.3 computer code in conditions with the actuation of the safety injection tanks (SIT). The present results on the SBO and the 9.6 inch break LOCA without safety injection are compared with the SCDAP/RELAP5-3D© results completed by INEEL (see Section 2.2).

2.3.1. Input Model

Figure 2-9 shows the SCDAP/RELAP5 nodalization for APR1400. The main input was prepared by KHNP,[2-5] based on the design specification outlined in the standard safety analysis report of the APR 1400. The input model for SCDAP/RELAP5/MOD3.3 calculation was a combination of the RELAP5,[2-9] SCDAP,[2-10] and COUPLE[2-11] input models. Heat structures for the fuel rods and the lower part of the reactor vessel in the RELAP5 input model were replaced by SCDAP and COUPLE input models, respectively. In the RELAP5 models, the reactor core was simulated as 3 channels to evaluate thermal-hydraulic behavior in detail and each channel was composed of 10 axial volumes. Each primary coolant loop consisted of a hot leg, a steam generator (SG) that had a U-tube modeled using 12 volumes, suction legs, reactor coolant pumps (RCPs), and cold legs. A surge line and a pressurizer were attached to one of the hot leg in the primary coolant loop.

The steam generator secondary side consists of a cylindrical shell, a downcomer through which main feedwater is supplied, a separator, and a steam dome. The main and auxiliary feedwater are modeled as time dependent volumes. Main steam safety valves (MSSV), and main steam isolation valve (MSIV) are also modeled for steady state simulation of APR 1400. The turbine is modeled as a time dependent volume. Heat transfer in the components such as steam generator U-tubes where heat transfer occurs is modeled by attaching RELAP5 heat structure model to the volumes of those components.

In the SCDAP input model, component numbers for the fuel and the control rods were 3 and 3, respectively, in this study. The axial node number of the fuel and control rods was 10 in each component in order to simulate ballooning and relocation after rupture of the fuel cladding accurately, and the radial nodes numbers for the fuel and the control rods were 6 and 2, respectively. In the COUPLE input, the lower part of the reactor vessel divided into 234 nodes and 204 elements. A gap conductance model was used to sim-

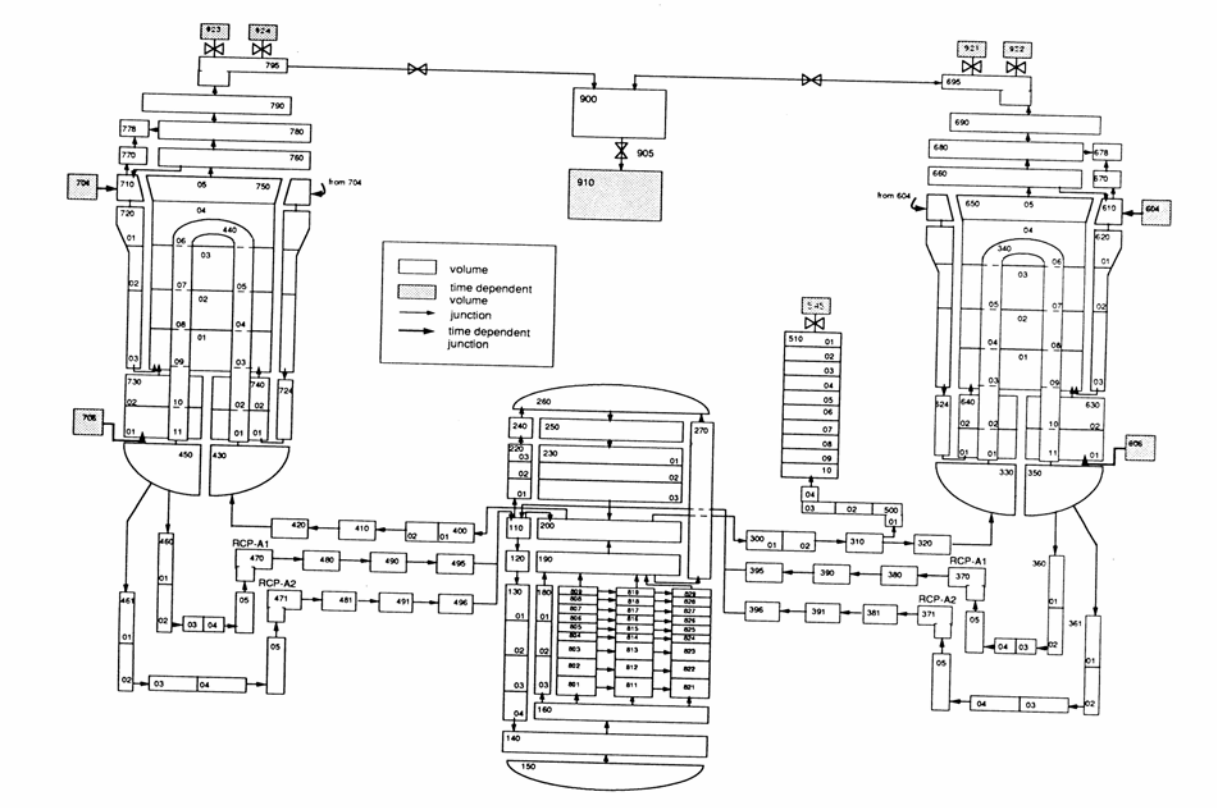

Figure 2-9. KAERI SCDAP/RELAP5 nodalization for APR1400.

ulate contact resistance and gap cooling between the relocated corium and the reactor vessel in this calculation. More detailed input models are described in References 2-3 and 2-4.

2.3.2. Results and Discussion

The steady state conditions obtained from the SCDAP/RELAP5/MOD3.3 simulation are used as initial conditions for the transient calculation. The occurrence times of major events predicted in the SCDAP/RELAP5/MOD3.3 computer code calculation in the high pressure sequences are summarized in Table 2-4. The TLFW transient, which is initiated when the main and auxiliary feedwater are lost, is assumed to occur at 0 sec. Because the main and auxiliary feedwater are not supplied to both steam generators following the transient at 0 sec, the steam generator secondary side water level decreases due to the steam generation by boiling and finally the steam generators can not act as effective heat sinks any more when the steam generator secondary sides dry up. The reactor and the RCP are tripped due to the low steam generator level and coolant sub-cooling margin, respectively. Because the core decay heat is not completely eliminated by the steam generators due to the decreased steam generator secondary side's water level, the pressure and temperature of the RCS increase. The SRVs (Safety Relief Valves) of the steam generator regulated the pressure of the secondary side. The RCS pressure increases up to 17.3 MPa, which is the opening pressure of the pressurizer POSRV. Following this time the RCS pressure fluctuates between the opening (17.3 MPa) and closing pressure (16.6 MPa) of the pressurizer POSRV.

Table 2-4. Significant events of high pressure sequences in APR 1400.

Events	TLFW		SBO
	Without SDS	With SDS	
Transient Initiated	0	0	0
Actuation of SDS	-	1,109	-
Core Uncovery	2,568	1,672	5,574
Actuation of SITs	(4,730)[a]	1,924	(8,304)
Core Melting	3,856	7,942	7,073
Surge Line Failure	(4,605)	-	(8,180)
First Corium Relocation to the Lower Plenum	7,685 (10,387)	8,958	11,899 (14,267)
Reactor Vessel Failure	9,109 (-)	10,305	13,242 (15,500)
Total Oxidation Fraction (%)	54.8 (55.5)	38.5	56.0 (56.1)

a. Note: ( ): Surge Line Failure Case

The zircaloy cladding is ruptured and zirconium dioxide relocated to the lower part of the core when the fuel rod cladding temperature reaches 2500 K at 3856 sec. At this time the dissolved fuel rod also relocated to the lower core and formed a cohesive debris bed. The debris forms at the bottom of the fuel rods, where the liquefied mixture resolidified. The melting temperature of zirconium dioxide is 2,960 K, and that of uranium dioxide is 3,120 K in this calculation. The flow blockage in the lower part of the core region occurred because of fuel melting and cohesive debris formation. Molten pool that is supported by the crust containing the molten pool is formed initially in the lower part of the core. The pressurizer surge line was ruptured by creep at 4605 sec prior to the reactor lower head vessel failure. If the pressurizer surge line didn't ruptured, the crust containing the molten pool fails at 7685 sec due to the temperature increase caused by decay heat from the dissolved fuel rod in the molten pool that decreases the crust thickness. The molten pool slumps to the lower plenum of the reactor vessel when the crust fails. Finally, the reactor lower head vessel failure occurs at 9109 sec in the TLFW transient.

There are many uncertainties on pressurizer surge line failure, such as natural circulation of hot steam, failure mechanism, and failure size, during a severe accident. For this reason, the high-pressure sequences with and without surge line failure have been simulated in the present study. In the pressurizer surge line failure case, it is assumed that the full size of pipe diameter was ruptured by the hot steam. When the pressurizer surge line was ruptured due to the hot steam from the core at 4605 sec, the RCS pressurizer rapidly decreased and the SITs actuated, which resulted in approximately a 40 minutes delay of reactor vessel failure time. In the case of TLFW with SDS (safety depressurization system), where the operator opened the pressurizer POSRV at 10 minutes after the initial opening of POSRV. The pressurizer pressure rapidly decreased and the SITs actuated, which results in approximately a 20-minute delay in reactor vessel failure time.

The SBO transient initiated when all AC powers supplied to the plant are lost. The transient is assumed to occur at 0 sec when the reactor is tripped due to the loss of AC power. At the same time the turbine, the RCP, and main feedwater pumps are also tripped. Also, the turbine driven auxiliary feed water pump is assumed to have failed. Since the core decay heat is not completely eliminated by the steam generators due to the decreased steam generator secondary side water level, the pressure and temperature of the RCS increase. The SRVs of the steam generator regulated the pressure of the secondary side. The RCS pressure increases up to 17.3 MPa that is the opening pressure of the pressurizer POSRV. Following this time the RCS pressure fluctuates between the opening (17.3 MPa) and closing pressure (16.6 MPa) of the pressurizer POSRV. The pressurizer surge line was ruptured by creep at 8180 sec prior to the reactor lower head vessel failure. If the pressurizer surge line was not ruptured, the crust containing the molten pool fails at 11899 sec since temperature increase caused by the decay heat from the dissolved fuel rod in the molten pool decreases the thickness of the crust. Finally, the reactor vessel was failed at 13242 sec. When the pressurizer surge line failure was simulated, the reactor vessel failure time was delayed approximately 35 minutes in the SBO transient.

The occurrence times of major events predicted by SCDAP/RELAP5/MOD3.3 computer code calculation in the low pressure sequences are summarized in Table 2-5. The LOCA was assumed to occur at 0 sec by a cold leg break. As the fuel rod temperature increases, the internal pressure of the fuel rod increases since fission products in the fuel rod are released to the gap between the fuel and the cladding. The increase of pressure difference between inside and outside of the fuel rod cladding leads to ballooning of the cladding that is aided by the fact that ductility of the cladding has been increased due to the temperature increase. Ballooning of the fuel rod cladding continues, and finally the cladding fails by overstrain. Fuel rod cladding temperature increases since heat transfer from the fuel rod to the surrounding coolant decreases following the initiation of core uncovery. The fuel rod cladding temperature reaches 1000 K, and cladding oxidation occurs.

Table 2-5. Significant events of low pressure sequences in APR 1400.

Events	1.35 inch	2 inch	3 inch	4.28 inch	9.6 inch
Transient Initiated	0	0	0	0	0
Core Uncovery	4,622	3,270	1,458	748	1,808
Actuation of SITs	8,580	4,534	2,110	996	190
End of SIT Actuation	-	17,890	17,300	5,850	988
Core Melting	5,817	4,385	7,639	7,120	2,675
First Relocation of Corium to the Lower Plenum	17,875	16,951	20,201	8,170	3,306
Reactor Vessel Failure	24,400	17,890	21,835	9,550	4,910
Total Oxidation Fraction (%)	49.1	44.5	42.8	32.9	9.3

When the pressurizer pressure decreases to 625 psia, the SITs are actuated. Fuel rod is ruptured and relocated to the lower part of the core when the fuel rod cladding temperature reaches 2500 K. The SITs actuations lead to delay core-melting times, but the delay time is different due to differences in the assumed break size. The dissolved fuel rod is relocated to the lower part of the core and forms a cohesive debris bed. A molten pool that is supported by the crust is formed in the lower part of the core. The crust containing the molten pool fails due to temperature increase caused by decay heat from dissolved fuel rod in the molten pool that decreases the crust thickness. The molten pool slumps to the lower plenum of the reactor vessel when the crust fails. Finally the reactor vessel in the 1.35-inch, 2-inch, 3-inch, 4.28-inch, and

9.6 inch break SBLOCA with actuation of the SITs is failed by creep at 24,400, 17890, 21835, 9550, and 4,910 sec, respectively. The coolant injection into the vessel by actuation of the SITs postpones the reactor vessel failure time.

Figure 2-10 shows the pressurizer pressure during the TLFW transients. When the TLFW transient occurs at 0 sec, the main feedwater is not supplied to the steam generator and the MSIV is closed. Hence the steam generator secondary side pressure increases up to the setting pressure (8.75 MPa) of the safety relief valve. The RCS pressure increases slightly due to the reduced heat transfer through the steam generator U-tubes, and then decreases due to the reduced core decay power. The RCS pressure increases up to the setting pressure of the pressurizer POSRV (17.3 MPa), and then the RCS inventory is lost through the opened POSRV. When the RCS pressure decreases to the closing setting pressure of the POSRV (16.6 MPa), the POSRV closes and the pressure builds up again. The RCS pressure fluctuates between the opening and closing set point pressure of the pressurizer POSRV. The pressurizer pressure rapidly decreases to the SITs set point in the RCS depressurization case and the surge line failure case. When the injected water entered the core from the SITs, it boiled, raising the pressurizer pressure. The increased pressure terminated the coolant injection by SITs actuation, and the pressure decreased again. When the pressure decreased low enough again, more coolant was injected. This cycling of the SITs actuation slowed the depressurization. When the molten core material relocated to the lower plenum, the pressurizer pressure increased because of coolant boiling in the lower plenum of the reactor vessel. At the reactor vessel failure, the pressurizer maintains a high value in the base case TLFW sequence, but it maintains low value in the TLFW with RCS depressurization case. The pressurizer pressure of the SBO sequence is very similar to that of the TLFW sequence.

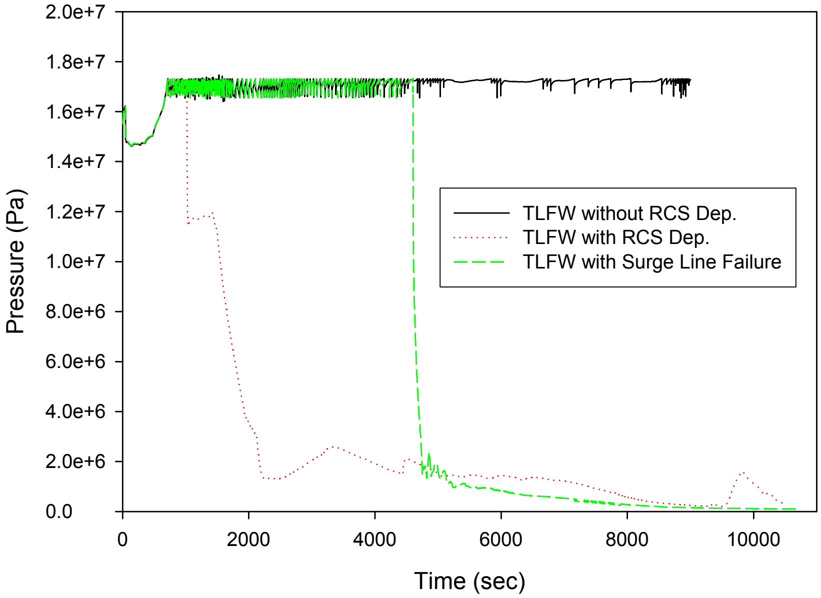

Figure 2-10. SCDAP/RELAP5/MOD3.3 results for the pressurizer pressure in the high pressure sequences.

Figure 2-11 shows the pressurizer pressure in the SBLOCA without safety injection. After the LOCAs occur at 0 sec, the pressurizer pressure rapidly decreases to the saturation pressure corresponding to the hot leg temperature at the beginning of the transient. As the coolant began to boil, the expansion of the coolant caused by boiling was able to equal to compensate the break flow, and the pressurizer maintained saturation pressure. In the small break LOCAs without safety injection, the pressurizer pressure increases due to the coolant boiling. The volumetric flow out through the break greater than the coolant expansion caused by boiling, and the pressure began to decrease again. The steady decrease in the pressurizer pressure stopped after the SITs began coolant injection to the RCS (Reactor Coolant System). When the injected liquid entered the core, it boiled, raising the pressurizer pressure. The increased pressure terminated the coolant injection by SITs actuation, and the pressure decreased again. When the pressure decreased low enough again, more coolant was injected. This cycling of the SITs actuation slowed the depressurization. A decrease in break size leads to a decrease in the SITs cycling frequency, because of the break flow rate. When the molten core material relocated to the lower plenum, the pressurizer pressure increased because of coolant boiling in the lower plenum. Most of LOCA sequences except for 1.35 inch break, the pressurizer maintains a low pressure at reactor vessel failure.

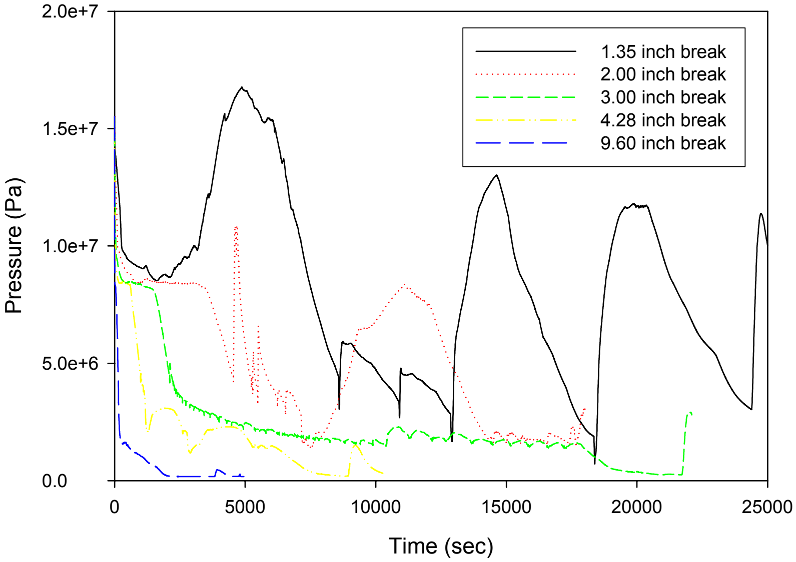

Figure 2-11. SCDAP/RELAP5/MOD3.3 results for the pressurizer pressure in the low pressure sequences.

2.3.3. Initial Conditions of Corium in the Lower Plenum

Table 2-6 shows the final melt compositions in the lower plenum of the APR 1400 reactor vessel in the high pressure sequences. In all sequences, approximately 80 - 90% of the core material of 154.2 tons was melted and relocated to the lower plenum of the reactor vessel at the time of reactor vessel failure in the APR 1400, which resulted in reactor vessel failure by creep. In this table, ZrO_2 and Zr masses are dependent on the oxidation fraction in Table 2-4. The volumetric heat source in the corium pool was estimated as 2.23-2.37 MW/m^3. Corium temperature was approximately 2,800 - 3,300 K at reactor vessel failure. Table 2-7 shows the final melt composition in the lower plenum of the APR 1400 reactor vessel in the low pressure sequences. In all sequences, approximately 80 - 90% of the core material of 154.2 tons was melted and relocated to the lower plenum of the reactor vessel at the time of reactor vessel failure in the APR 1400, which resulted in reactor vessel failure by creep. Volumetric heat source in the corium pool was estimated as 1.9-3.7 MW/m^3. The corium temperature was predicted to be approximately 2,900 - 3,400 K at the time of reactor vessel failure. The highest volumetric heat source sequence is the 9.6 inch break LOCA without safety injection in APR 1400, because this sequence leads to early reactor vessel failure.

Table 2-6. Final melt compositions in the lower plenum at reactor vessel failure in high pressure sequences of APR 1400.

Events	TLFW		SBO
	Without SDS	With SDS	
Reactor Vessel Failure Time (sec)	9,109	10,305	13,242
Total Decay Heat (MW)	47.8	46.0	44.8
Corium Depth (m)	1.86	1.64	1.83
Corium Mass (ton); Total = 154.2	145.7	120.2	142.9
Fuel Mass (ton); Total =120.0	113.2	94.7	110.8
ZrO_2 Mass (ton)	18.2	9.8	19.0
Zr Mass (ton); Total =33.6	11.7	13.6	10.8
Corium Temperature (K)	>2,900	2,852	3,311
Heat Generation Rate (MW/m^3)	2.37	2.36	2.23

Table 2-7. Final melt compositions in the lower plenum at reactor vessel failure in low pressure sequences of APR 1400.

Events	1.35 inch	2 inch	3 inch	4.28 inch	9.6 inch
Reactor Vessel Failure Time (sec)	24,400	17,890	21,835	9,550	4,910
Total Decay Heat (MW)	37.8	41.3	39.6	48.5	57.9
Corium Depth (m)	1.82	1.65	1.67	1.54	1.54
Corium Mass (ton); Total = 154.2	143.1	121.9	124.3	121.5	114.1
Fuel Mass (ton); Total = 120.0	112.9	99.6	100.8	99.2	107.3
ZrO_2 Mass (ton)	15.2	13.4	10.7	8.6	2.8
Zr Mass (ton); Total = 33.6	12.7	6.7	10.5	11.0	4.7
Corium Temperature (K)	3,378	3,083	3,380	2,910	3,150
Heat Generation Rate (MW/m^3)	1.9	2.2	2.1	2.6	3.7

The inputs for the SCDAP/RELAP5 calculations at KAERI and INEEL are almost the same, except some modifications made by INEEL that allowed the SCDAP/RELAP5/MOD3.3 input to be used as input for SCDAP/RELAP5-3D© (see Reference 2-12). The prominent differences that distinguish

SCDAP/RELAP5-3D© from SCDAP/RELAP/MOD3.3 input are associated with its linkage to the thermal/hydraulic analysis capabilities of RELAP5-3D©, and some specific model differences are explained in Reference 2-13.

Table 2-8 compares the SCDAP/RELAP5/MOD3.3 results on melt state with INEEL SCDAP/RELAP5-3D© results for the APR1400 SBO and 9.6 inch break LOCA (see Section 2.2). As indicated in Table 2-8, the hydrogen generation mass predicted by SCDAP /RELAP3/MOD3.3 is a little lower than that the value predicted by SCDAP/RELAP5-3D©. The mass of corium predicted to relocate to the lower plenum of the APR1400 reactor vessel at the time of vessel failure was also slightly lower in the SCDAP/RELAP3/MOD3.3 than in the SCDAP/RELAP5-3D© calculations. The power density predicted by SCDAP/RELAP3/MOD3.3 in the SBO sequence is a little lower than that predicted by SCDAP/RELAP5-3D©; but in the 9.6 inch break LOCA sequence, the SCDAP/RELAP5/MOD3.3 power density is a little higher. In general, the SCDAP/RELAP5/MOD3.3 results are very similar to the SCDAP/RELAP5-3D© results.

Table 2-8. Comparison of the SCDAP/RELAP5/Mod3.3 results with SCDAP/RELAP5-3D© results.

	SBO		Large Break LOCA (9.6 inch Break)	
	MOD3.3	**MOD-3D© (SBO-1)**	**MOD3.3**	**MOD-3D©**
Reactor Vessel Failure Time (sec)	13242	11100	4910	4990
Total H_2 Generation Mass (kg)	836	912	139	169
Total Power (MW)	44.8	47.4	57.9	51.2
Total Corium Mass in the LP (ton)	142.9	145.0	114.1	119.0
Corium Volume in the LP (m^3)	18.5	19.0	13.8	14.7
Power Density (MW/m^3)	2.23	2.49	3.97	3.48

2.4. KAERI SCDAP/RELAP5-3D© Calculations

Korea Atomic Energy Research Institute

KAERI received the SCDAP/RELAP5-3D©[2-1] from INEEL and installed it on a DEC workstation. Best estimate calculation from initiating events to reactor vessel failure in a 9.6 inch Large Break Loss of Coolant Accident (LBLOCA), a total loss of feed water, and a station blackout (SBO) of the APR (Advanced Power Reactor) 1400 using this computer code have been performed to compare with the SCDAP/RELAP5/MOD3.3 results on the melt relocation status in the lower plenum of the reactor vessel at reactor vessel failure. During the SCDAP/RELAP5-3D simulation, the program was stopped for the above three initiating events of the APR1400 with the same error messages of “Transient terminated by thermodynamic property failure in the bottom of the core (Vapor phase property call had error)”. As the first step to solve the calculation error of the SCDAP/RELAP5-3D, the maximum time step was reduced from 0.1 to 0.0001and re-calculated, but the same error messages had happened. As the second step, Activate Option 61 on Card 1 in the SCDAP/RELAP5-3D input was used, but there was also the same error message. The sequence analysis using SCDAP/RELAP5-3D is halted, because of difficulties to solve problems without the source program of the SCDAP/RELAP5-3D computer code.

2.5. Conclusions

The objective of Task 1 was to obtain quantify representative late-phase melt conditions that could affect the potential for IVR of core melt following a severe accident in APR1400. Resulting late-phase melt conditions were used in the design of a core catcher and enhancements in ERVC. To accomplish the task objective, INEEL applied the SCDAP/RELAP5-3D© code and KAERI applied the SCDAP/RELAP5/MOD3.3 and SCDAP/RELAP5-3D© codes to the APR1400 plant.

The inputs for the SCDAP/RELAP5 calculations at KAERI and INEEL were almost the same, except some modifications made by INEEL that allowed the SCDAP/RELAP5/MOD3.3 input to be used as input for SCDAP/RELAP5-3D©. The prominent differences that distinguish SCDAP/RELAP5-3D© from SCDAP/RELAP/MOD3.3 input are associated with its linkage to the thermal/hydraulic analysis capabilities of RELAP5-3D©, and some specific model differences.

Key conclusions and insights resulting from this effort are discussed below.

SBO and LOCA transients were selected for analysis.

Attempts were made to select severe accidents that would lead to bounding estimates of potential late-phase melt conditions for the APR1400. However, identifying bounding transients is complicated. Although an extensive series of severe accident calculations could be performed to identify bounding transients, LOCAs, SBOs, and LOFW scenarios were assumed to be major IVR scenarios. Accordingly, a cold leg break (representing the LOCA response) and an SBO with LOFW (to combine remaining dominant IVR scenarios) were selected for analysis.

SBO results indicate that the surge line will fail by creep rupture before corium relocation and lower head failure.

Surge line failure by creep rupture was predicted before core relocation and lower head failure during an SBO transient in the APR1400. Although simulation of a break at the time of surge line failure was not considered, prediction of surge line failure is significant because it favorably affects late-phase conditions. Specifically, if the RCS depressurizes through a surge line failure, SITs will empty, cool the core, and delay relocation. Corium decay power (and the severity of the lower head thermal attack) will be reduced as a result. In addition, the lower head attack will proceed at low (containment) pressure, which will extend survival of the lower head. Further heating of the RCS piping and additional failures could be expected with APR1400 model refinement to account for potential development of natural circulation flows, particularly hot leg countercurrent flow.

In general, the SCDAP/RELAP5/MOD3.3 results are very similar to the SCDAP/RELAP5-3D© results.

Predicted values for vessel failure time, hydrogen generation, melt relocation masses, melt relocation volumes, decay heat in the relocated corium, and power densities in the relocated corium were compared and differences not considered significant.

Calculation results indicate a LOCA yields the most severe lower head thermal loads.

A 0.0465 m^2 break in one of the cold legs in the primary coolant loop containing the pressurizer resulted in core melt and relocation into the lower head by 4,990 s. The timing of this relocation was earlier than all other transients analyzed (by as much as 6,110 s). Consequently, power retained in the melt was relatively high (because the decay period after reactor trip was relatively short). High decay power associated with this relocation yielded the highest thermal load for the APR1400 lower head. Without modification to enhance ERVC or without the use of a core catcher, IVR may not be feasible in this case.

Late-phase melt conditions include large masses that relocate at high temperatures.

Regardless of the transient considered, results for all calculations include relocation of large melt masses (~100,000 kg total, or more) at high temperatures (~3,000 K, or higher). These results appear to be consistent with the nature of the transients considered. Specifically, all cases involved complete core dryout and subsequent core heatup in a steam environment. Protracted periods (~1 h, or more) of complete core uncovery were sustained in each calculation, leading to development of large core melt masses at temperatures well above the fuel liquidus.

In the absence of any ERVC enhancements, estimated heat fluxes that must be removed from the lower head to ensure IVR of core melt in APR1400 exceed predicted heat fluxes for the Westinghouse AP600 reactor and corresponding estimates of the maximum CHF for this plant.

Estimated lower head average heat fluxes for the APR1400 transients considered ranged from 0.147 to 1.64 MW/m^3, which exceed peak lower head heat fluxes predicted for the Westinghouse AP600 reactor by factors as high as ~2.3. Furthermore, the estimated APR1400 average heat fluxes exceed the current estimates of the maximum CHF by as much as a factor of ~1.2. These results indicate IVR may not be feasible without additional measures such as the use of a core catcher and/or modifications to enhance ERVC.

There was no way to ensure that transients considered actually produced bounding estimates of the late-phase melt conditions.

Attempts were made to select severe accident transients that would lead to bounding estimates of the potential late-phase melt conditions. Although a logical transient selection process was applied, there was no clear way to ensure that the selected transients would indeed lead to the desired bounding conditions. Having acknowledged that limitation, however, it appears reasonable to conclude that late-phase melt conditions established through this study are approaching upper bounds. That conclusion is based on physical limits of the APR1400 core. Specifically, predicted melt masses have approached core totals and the predicted melt temperatures are well above the fuel liquidus. Consequently, the resulting late-phase melt conditions appear to be very well suited for subsequent use in the design of an APR1400 core catcher and the evaluation of ERVC enhancements. This conclusion holds even though the predicted late-phase melt conditions are expected to have a very low probability of developing.

The potential effects of RCS depressurization, corium dilution, lower head heat transfer, and the corium configuration endstates must be considered, in conjunction with ERVC and core catcher effects, in detailed lower head analyses to determine the viability of IVR of corium in APR1400.

As discussed in Section 1, these additional analyses were completed in Task 4 of this project (and results are presented in Section 5).

2.6. References

2-1. The SCDAP/RELAP5-3D© Development Team, *SCDAP/RELAP5-3D© Code Manuals*, INEEL/EXT-02/00589, Idaho National Engineering and Environmental Laboratory, May 2002.

2-2. D. Knudson, J. Rempe, K. Condie, K. Y. Suh, F. B. Cheung, and S. B. Kim, "Late-phase Melt Conditions affecting the Potential for In-Vessel Retention in High Power Reactors," *Nuclear Engineering and Design, Invited paper for ICONE11 Special Edition*, **230** (2004) 133-150.

2-3. R. J. Park et al., *Analysis of High Pressure Severe Accident Sequences using SCDAP/RELAP5/MOD3.3*, ICONE 11, Tokyo, Japan, April 2003.

2-4. R. J. Park et al., *Effect of Safety Injection Tanks on Late Phase Melt Progression in a Small Break LOCA without Safety Injection*, NTHAS3, Kyungju, Korea, October 2002.

2-5. S. J. Oh, "Realistic Approach to IVR for APR1400", Korea Hydro and Nuclear Power Company, Ltd., presentation during meetings at the Idaho National Engineering and Environmental Laboratory, July 2002.

2-6. J. L. Rempe, et al., *Potential for AP600 In-Vessel Retention through Ex-Vessel Flooding, Technical Evaluation Report,* INEEL/EXT-97-00779, Idaho National Engineering and Environmental Laboratory, December 1997.

2-7. J. L. Rempe and C. M. Allison, "Improved Models for Predicting Heat Transfer from a Molten Pool," *Transactions from the 1995 ANS Winter Meeting, Thermal Hydraulics Division Proceedings*, San Francisco, CA., October 1995.

2-8. L. J. Siefken et al., SCDAP/RELAP5/MOD3.3 Code Manual, NUREG/CR-6150, INEL-96/0422, January 2001.

2-9. The RELAP5 Development Team, *RELAP5/MOD3 Code Manual,* NUREG/CR-5535, INEL-95/0174, 1995.

2-10. Allison, C. M. et al., *SCDAP/MOD1/V0: A Computer Code for the Analysis of LWR Vessel Behavior During Severe Accident Transients,* IS-SAAM-83-002, 1984.

2-11. E. C. Lemmon, "COUPLE/FLUID: A Two Dimensional Finite Element Thermal Conduction and Advection Code," EGG-ISD-SCD-80-1, 1980.

2-12. K-INERI, "2002 Annual Report, 3. TASK 1: Late Phase Melt Conditions", December 2002

2-13. SCDAP/RELAP5-3D, "An Advanced Computer Code for Reactor Accident Analysis, Table 1," SCDAP/RELAP5-3D home page http://www.inel.gov/relap5/scdap/scdap.htm, June 2002

3. TASK 2: CORE CATCHER DESIGN ENHANCEMENT

3.1. Objective and Overview of Task 2

The objective of Task 2 was to develop a core catcher design for the APR1400 and provide sufficient data to evaluate if this core catcher design will enhance in-vessel debris coolability in the reactor. The approach adopted for developing an APR1400 core catcher design is illustrated in Figure 3-1. As shown in this figure, initial efforts focused on developing a preliminary in-vessel design. This was done at INEEL using a combination of scoping materials, flow, thermal, and structural analyses and scoping materials interaction tests. In addition, more detailed experimental data were obtained in two areas. First, data were needed to estimate the heat that can be removed from the narrow "engineered" gap between the in-vessel core catcher (IVCC) and the inner surface of the reactor vessel lower head. As indicated in Figure 3-1, data were obtained from the GAMMA facilities at SNU and the CHFG facility at KAERI to formulate a complete "narrow gap" boiling curve. Second, data were needed to understand the heat loads to the core catcher and demonstrate the viability of materials proposed for the IVCC. As illustrated Figure 3-1, these needs were addressed by conducting tests in several facilities: the SIGMA facilities at SNU were used to develop natural convection heat transfer correlations, the LAVA-GAP facility at KAERI was used to assess the impact of a core catcher on thermal heat loads to a reactor vessel, and INEEL's High Temperature Test Laboratory (HTTL) was used to assess the potential for materials interactions.

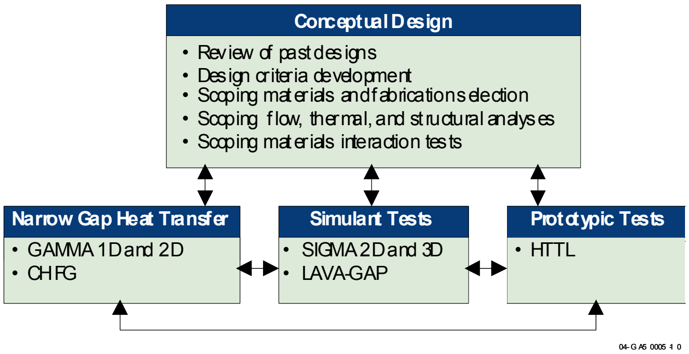

Figure 3-1. Task 2 approach to developing an enhanced core catcher design.

Results from Task 2 activities are summarized in this section. More detailed information about various tasks described in this section may be found in References 3-1 through 3-12. Section 3.2 summarizes preliminary core catcher design efforts completed by INEEL. Section 3.3 summarizes efforts by SNU to obtain narrow gap cooling data. Sections 3.4 and 3.5 summarize simulant core catcher design and evaluation tests completed by SNU and KAERI, respectively. Section 3.6 summarizes prototypic testing efforts completed by INEEL. Section 3.7 summarizes insights and conclusions gained from Task 2 core catcher development tasks.

3.2. Preliminary Core Catcher Design Development

Idaho National Engineering and Environmental Laboratory

3.2.1. Previous Design Efforts

As documented in Reference 3-1, several in-vessel and ex-vessel core catcher concepts proposed in the literature were reviewed as an initial step for developing a core catcher design. Some of the key approaches associated with these concepts include:

- *A geometry to contain relocated corium that enhances cooling and freezing by lower plenum water.* Many designs “catch” relocated corium in a structure that can contain and cool the corium (through fins and narrow gap cooling).
- *High-temperature materials to reduce corium decay power density.* Some designs use materials that form a lower temperature eutectic with uranium dioxide in the corium and dilutes the decay heat power density (kW/m^3) in relocated materials.
- *Materials to chemically absorb fission products and associated decay heat.* Some designs use a glass material, that catches and absorbs heat from relocating corium until it becomes a molten mass containing dissolved uranium and fission products.
- *Multiple structures to reduce corium decay heat and retain corium materials.* Some multiple structure designs incorporate a sacrificial layer above a container that can structurally support the cooled corium. As the corium forms a eutectic with the sacrificial layer, the power density of the corium material is lowered (reducing the heat load to the underlying container).

After reviewing these various approaches, a list of design goals and criteria was formulated for developing a APR1400 core catcher design. These goals and criteria, which are listed in Table 3-1, provided guidance in selecting the configuration, dimensions, and materials for the APR1400 core catcher.

Table 3-1. IVCC design goals.

Design Goals
• The core catcher shall prevent recriticality of relocated material.
• The core catcher shall fit within the reactor vessel.
• The core catcher shall reduce the decay heat power density of relocating corium.
• The core catcher shall contain relocated material (size, structurally, thermal shock resistance).
• The core catcher shall be as inexpensive as possible.
• The core catcher shall facilitate long-term coolability using passive means.
• Interactions between core catcher materials and relocated debris shall not result in exothermic reactions or generation of combustible gases.
• The core catcher shall not present a seismic hazard.
• The core catcher shall be stable for the lifetime of the reactor.[a]
• The core catcher shall be easily installed and maintained.
• The core catcher shall not adversely affect reactor performance or coolant circulation.

[a] The APR1400 is designed for a 60 year lifetime.

3.2.2. Core Catcher Geometry and Fabrication

The core catcher design proposed for this project builds upon an IVCC concept proposed by Hwang and Suh.[3-13] However, the new core catcher design consists of several interlocking sections (see Figure 3-2). The use of multiple sections reduces cost and simplifies manufacture and installation. The sections are machined such that they fit together when inserted into the lower head. Each section is attached to locating pins or clasps in the reactor vessel. For reactor designs with penetrations, such as the APR1400, the core catcher is manufactured with holes to accommodate lower head penetrations. This IVCC is designed to contain relocated materials, providing an "engineered gap" between the relocated core materials and the water-filled reactor vessel. As water in this gap begins to boil, steam will escape through the gap between the vessel and the core catcher and through gaps between instrumentation tubes and perforations in the core catcher. Each section of the core catcher (see Figure 3-2) consists of two material layers with an option to add a third layer (if deemed necessary): a base material, which has the capability to support and contain the mass of core materials that may relocate during a severe accident; an insulator coating material on top of the base material, which resists interactions with high-temperature core materials; and an optional coating on the bottom side of the base material to prevent any potential oxidation of the base material during the proposed 60-year lifetime of the reactor.

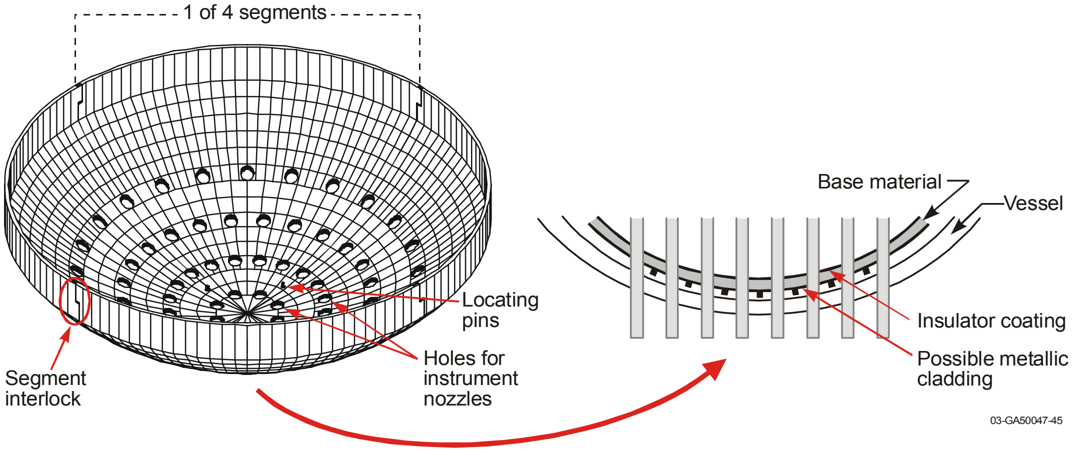

Figure 3-2. Conceptual design of proposed APR1400 IVCC design.

Various types of application methods, such as chemical vapor deposition, thermal plasma spraying, and painting, were reviewed; and preliminary evaluation suggests that the insulator coating should be applied via a plasma spray process. The plasma spray process, which is relatively inexpensive, can provide a chemically stable, rugged, dense, and bonded coating of materials for any desired thickness. To optimize the performance of the plasma spray coating, several options are available, such as substrate surface preparation, plasma spray coating parameter optimization, and the inclusion of a "bond" coating between the base material and the insulating overlayer. INEEL investigated all three of these options in this project.

3.2.3. Material Property Considerations

During the first year of this project, scoping materials evaluations identified candidate substrate and coating materials for the core catcher. These evaluations considered thermal, structural, and nuclear material properties.

Stainless steel 304 and carbon steel SA533 were identified as candidate base materials. Thermal and structural properties for these materials are similar.[3-14] Although carbon steel is less expensive than stainless steel, the use of stainless steel avoids the need to add a corrosion-resistant undercoating on the core catcher.

From a wide spectrum of oxide materials, cerium dioxide, magnesium oxide, and zirconium dioxide were identified as promising candidates for the core catcher upper surface coating. All three materials have relatively high melting points and low thermal conductivities.[3-15,3-16] The coating materials were also evaluated for their ability to resist cracking (and protect the base material) using a parameter suggested by Winkelmann and Schott.[3-17]

In addition, the potential for interactions between the core catcher and relocated corium materials was evaluated using phase diagram information.[3-18] Although initial evaluations suggested that MgO material properties were superior, the cost for ZrO_2 powder is considerably less. In addition, there is considerably more experience with applying yttria-stabilized ZrO_2 using plasma spray techniques. Hence, it was decided to evaluate both coatings (As discussed in Section 3.2.4, scoping analyses suggest that CeO_2 performance was less desirable as a coating). However, difficulties in spraying high purity MgO limited evaluations to considering the performance of coatings that contained MgO. Specifically, MgO-containing coatings could only be evaluated that were prepared from mixed MgO/Al_2O_3 powders and compounds of magnesium aluminate and magnesium zirconate.

As discussed in Reference 3-19, the use of bond coatings has been found to improve the performance of thermal spray coatings. INEEL investigated three bond coating materials: 100% nickel, a 95% nickel / 5% aluminum alloy, and Inconel 718. References 3-20 through 3-22 indicate that these materials have similar melting temperatures (1610-1730 K), but much higher thermal conductivities than proposed base materials. However, information in Reference 3-22 suggests that the inclusion of aluminum in the bond coating could lead to reactions with iron and coating materials at relatively low temperatures.

The coefficient of thermal expansion is an important consideration in evaluating if the coatings and base are compatible. Figure 3-3 compares thermal expansion coefficients of candidate insulator coating, base, and bond coating materials.[3-14, 3-23] Results in the figure indicate that magnesium oxide may be a good choice for an insulator coating material because its expansion and contraction are most closely aligned with the expansion and contraction of proposed base materials. Curves in Figure 3-3 also suggest that the nickel bond coating material may reduce differences between expansion of proposed oxide coating and base materials.

3.2.4. Scoping Analyses

Scoping analyses and materials interaction tests were performed to gain additional insights about core catcher design and viability. Results from these analyses are summarized below. More detailed information about these calculations can be found in Rempe, et al.[3-4]

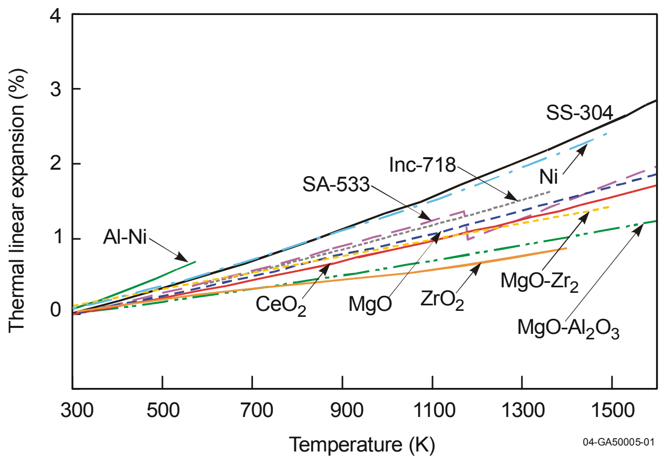

Figure 3-3. Insulator, bond, and base material thermal expansion coefficients.

Simple thermal analyses were performed using the SCDAP/RELAP5-3D© code to gain insights about the thickness and materials that should be selected for the core catcher base and coating materials. A range of conditions were investigated that reflect the anticipated conditions to which the core catcher might be subjected. Upper and lower values for parameters were selected based on the estimated space available within the lower plenum for the core catcher, and methods available for fabricating a core catcher as well as the estimated heat transfer from relocated debris and narrow gap cooling. Figure 3-4 shows the simple RELAP hydrodynamic model used for simulating the thermal response of the core catcher. As shown in the figure, a single RELAP volume was used to represent the hydrodynamic conditions of fluid entering the vessel (Volume 500) and a single volume was used to represent the fluid in the reactor vessel (Volume 598). These two volumes are connected by a junction. Note that fluid and vapor may travel to and from the reactor vessel volume, depending on conditions in the vessel.

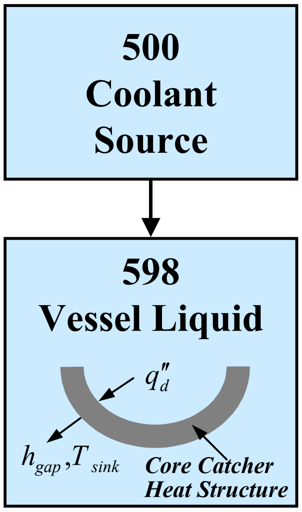

Figure 3-4. RELAP hydrodynamic model.

Results from scoping SCDAP/RELAP5-3D© calculations indicate that the thermal performance of insulator coatings are primarily affected by their thermal conductivity and melting temperature. Hence, cerium dioxide is less desirable because its melting temperature is approximately 400 ºC lower than other oxide materials evaluated. Results also indicate that the core catcher thermal performance is not significantly impacted by the type of steel (SS304 or SA533B1) selected for the base material, the thickness of the base or coating material, or the porosity of the coating material.

A structural assessment was completed to determine an appropriate core catcher thickness to support the mass of materials that may relocate during a severe accident. Although a linked structural / thermal analysis would provide a more detailed basis for selecting the core catcher thickness, an initial estimate for the required core catcher thickness was obtained from a simple structural analysis that assumed relocated masses were bounded by SCDAP/RELAP5-3D© APR1400 results reported in Knudson, et al.[3-24] As shown in Figure 3-5, the assumed relocated materials approximately fill a core catcher with a thickness, $t_{catcher}$. The maximum load to the core catcher was calculated by estimating the load to a central portion of the core catcher with radius, r_{cyl}, assuming that the core materials were molten and level within the core catcher. Results suggest that the core catcher's base material should be at least 2 cm thick to support the loads associated with relocated materials during a severe accident (and smaller thicknesses may be possible, depending upon heat removal capabilities associated with narrow gap cooling).

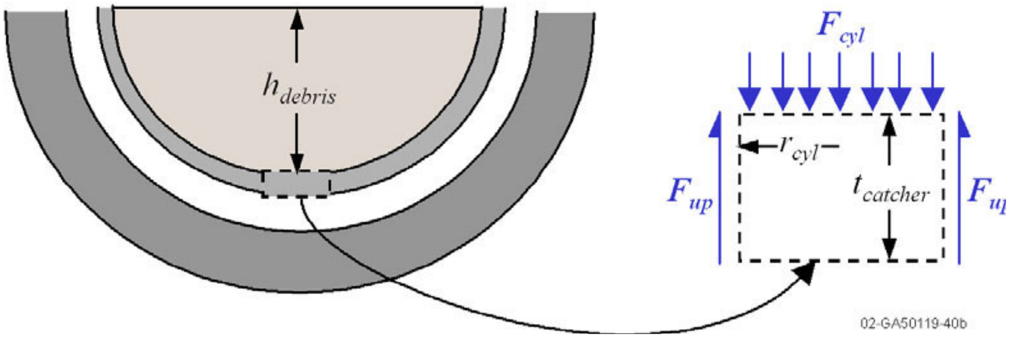

Figure 3-5. Geometry assumed to estimate forces on a central cylinder of the core catcher.

It is envisioned that the core catcher would be placed just above the inner surface of the reactor vessel (creating a vessel-to-core catcher gap of approximately 0.5 cm). To alleviate concerns about the impact of a core catcher on coolant flow in the reactor, a simple analysis was performed to demonstrate that the mass flow diverted by the core catcher is minimal. Using the geometry shown in Figure 3-6, a relationship was developed for estimating the ratio of the mass flowrate under the core catcher to the mass flowrate through the downcomer, $\dot{m}_{CC}/\dot{m}_{DC}$. Results indicate that only 2% of the RCS flow from the downcomer may be diverted beneath the core catcher if it is placed approximately 0.5 cm above the reactor vessel inner surface. Hence, initial investigations suggest that the impact of the core catcher on RCS flow is negligible. However, confirmatory testing is needed to verify the long-term endurance of the core catcher design to hydrodynamic loads during operating and accident conditions.

In summary, results from scoping thermal and structural analyses suggest that an IVCC is feasible. In addition to gaining insights about the thickness and materials for each layer of the core catcher, analyses showed that the impact of the core catcher on coolant flow in the reactor vessel is minimal. As discussed below, additional insights about the core catcher design were also obtained from materials interaction tests.

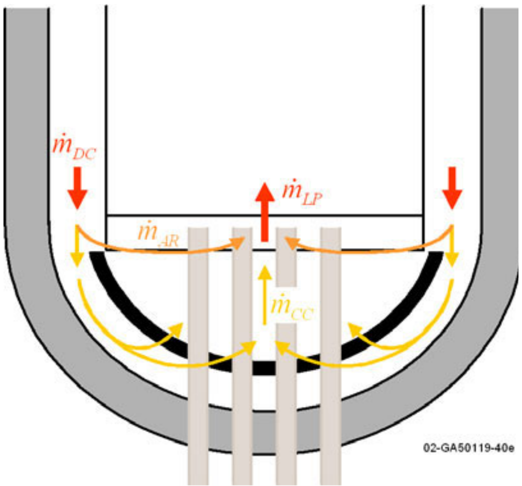

Figure 3-6. Geometry assumed for flow analysis.

3.2.5. Materials Interaction Tests

As part of the investigation to select an appropriate core catcher coating, high temperature tests were conducted to determine if materials interactions occur at temperatures lower than the melting temperature of core catcher base and coating materials. In addition, sensitivity studies were performed to optimize thermal spray parameters for coating materials.

Figure 3-7 contains a photo of an uncoated and a coated samples. Samples were machined from 1inch stainless steel (SS 304) rod. Each sample was approximately 2 inches long.

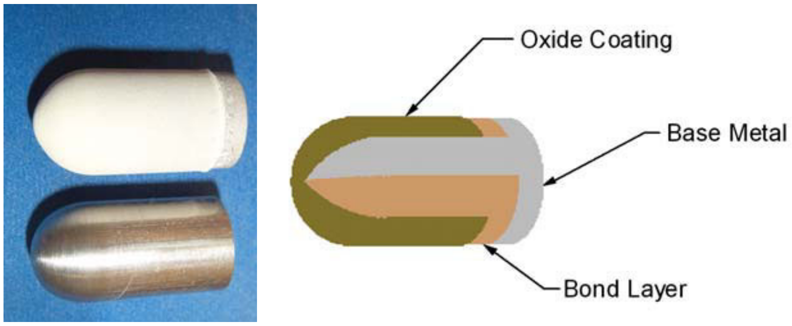

Figure 3-7. Samples with and without spray coating and diagram illustrating spray coating layers.

Figure 3-8 illustrates the configuration used to heat samples in a tube furnace. Although this horizontal tube furnace is rated at 1700 ºC, the furnace temperature was set to 1400 ºC during these tests (because this temperature is just below the stainless steel melting point). This temperature was checked (and found to be accurate) with a two-color optical pyrometer. As shown in Figure 3-8, a steam or argon environment was obtained by flowing the vapor or gas through one end of the tube furnace for a period of 30 minutes prior to testing. At the end of the planned test period (a 5 minute warm-up at the furnace entrance followed by 10 minutes at full temperature), the flow is stopped, and the specimen is slowly removed from the furnace. Samples were individually tested to avoid unwanted interactions between oxides.

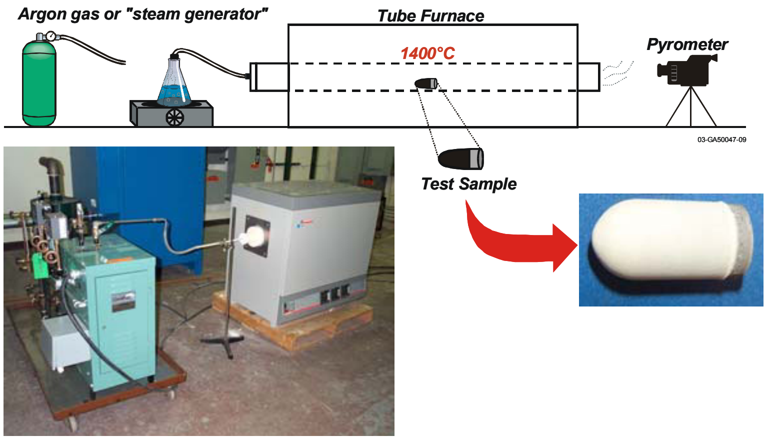

Figure 3-8. Diagram and photo illustrating setup for materials tested in steam.

Samples were prepared for conducting the tests listed in Table 3-2. As discussed above, several types of ceramic coatings were considered. Because ZrO_2 coatings are less expensive and widely used, initial investigations considered this ceramic material. Then, samples with coatings containing MgO were prepared with the bond coating/coating thickness combinations deemed to yield the optimum performance. Detailed information about results from other tests may be found in Rempe, et al.[3-5] Results from selected tests are presented in this section.

Table 3-2. Coating parameter sensitivities

Parameter	Range
Coating Thickness	200, 500, and 1000 μm
Bond Coating	100-200 μm thick Ni, Ni-Al, or Inconel-718 bond coating or no bond coating.
Oxide Material	zirconium dioxide magnesium oxide[a] magnesium zirconate spinel magnesium aluminate
Thermal Spray Parameters[b]	Nominal case Fewer cracks / lower density More cracks / higher density

a. As noted above, Al_2O_3 powder was "mixed" with the magnesium oxide in order to obtain a thermal spray coating.

b. Varied range of thermal spray parameters, such as carrier gas composition, carrier gas flowrate, torch current, standoff distance, and traverse speed, to obtain desired coating properties.

Figure 3-9 compares endstates from samples tested in steam to investigate the impact of coating thickness. As evidenced by the gray oxide material on the outer surface of all three samples in this figure, materials interactions and substrate oxidation occurred irrespective of coating thickness. However, coating thickness significantly affects the amount and type of degradation. Comparisons of the endstates shown in Figure 3-9 suggest that coatings thinner than 500 μm allowed oxygen to penetrate to the underlying steel and degrade the sample's outer surface. There was a tendency for coatings to remain intact as thickness was increased. However, some cracking and flaking occurred during cooldown of samples with thicker coatings. In steam tests, the 200 μm coated sample became perforated with large holes. As shown in Figure

3-9, gray material is present on the outer surface of samples with thicker coatings that were tested in steam. However, this material appears to have "flowed" from uncoated regions of the samples along the intact outer surface of the coatings (see flow patterns in Figure 3-9). Hence, results suggest that coatings should be at least 500 μm thick.

220 μm in steam

500 μm in steam

1000 μm in steam

Figure 3-9. Impact of coating thickness

Endstates from samples with coatings that performed the best are shown in Figure 3-10. As shown in this figure, the sample coated with a 500 μm coating of zirconium dioxide over a 100-200 μm Inconel 718 bond coating experienced no materials interactions or cracking. Although the sample coated with magnesium zirconate also performed well and experienced no materials interactions, cracking was evident during cooldown. Therefore, the zirconium dioxide coating with the Inconel 718 bond coating was deemed to perform better, and prototypic tests conducted to support the core catcher design effort (see Section 3.6) used this coating.

100-200 μm Inconel 718 beneath 500 μm zirconium dioxide

500 μm magnesium zirconate

Figure 3-10. Bond coating / oxide material combinations with superior performance

3.3. Narrow Gap Cooling

Seoul National University

3.3.1. Introduction

Tests were conducted to investigate the critical heat flux (CHF) associated with bubble behavior that may affect the entire state of the heat transfer mode in the narrow gap boiling. In this sense, the CHF test sections need to address key features of the engineering device to simulate the in-vessel retention (IVR) environment applicable to the APR1400 (Advanced Power Reactor 1400 MWe). In particular, the major issues are centered about such geometric parameters affecting the CHF as the surface orientation and the gap size. Hence, research on the CHF during pool boiling in confined channels is important as a fundamental study well as for its industrial application. Owing to the complex flow mode, however, quite a few investigators have suffered from difficulties in interpreting the heat transfer phenomena in highly confined channels. Additionally, the CHF triggering mechanism still defies full understanding due mostly to the effect of surface orientation.

Thus, a series of fundamental studies were performed to develop engineering correlations as well as to visualize the complex flow patterns taking account of heated surface orientation, heated channel length, and gap size using the GAMMA 1D (Gap Apparatus Mitigating Melt Attack One Dimensional) apparatus at the Seoul National University. In addition, the GAMMA 2D (Gap Apparatus Mitigating Melt Attack Two Dimensional) experiments were performed to investigate the effects of gap size and pressure on the thermal hydraulic phenomena dominating the gap CHF mechanism.

3.3.2. GAMMA 1D Test Apparatus

This study adopted a heater assembly that was fabricated utilizing a copper block test heater attached by a thin film resistor. Its first consideration was to ease the use of the sophisticated devices for visualization of the vapor behavior. The second was to avoid the use of the larger direct current capacity requiring a large contact area between the electric cable nodes and copper block. By affixing a thin film resistor having a resistance of 20Ω, the copper block belonging to the heater assembly had the wetted surface area of 15×35 mm^2 in width by length. Three chromel-alumel (K-type) thermocouples were inserted to the hole off the wetted surface by 0.6 mm and the depths of 5, 17.5 and 30 mm in the direction of the flow channel, respectively. Essentially, the test heater was slightly coated with nickel to protect against oxidation.

The stainless steel housing holding the heater assembly was designed to ascertain the most effective insulation on the heated section. Primarily, the inner surface of the housing had to be polished smoothly so that the interior of the housing could be evacuated efficiently. The insulation efficiency was surprisingly high for vacuums of 10^{-4} torr, and such state-of-the-art vacuum technique sizably reduces the heat loss from the bottom of the copper block heater. Pyrex glass was embedded into the edge of the housing and designed to precisely maintain the gap sizes of 1, 2, 5 and 10 mm, and to visualize the test apparatus having a narrow rectangular channel. To help understand the current experimental apparatus, Figure 3-11 presents the structural heater block, Pyrex glass, and housing.

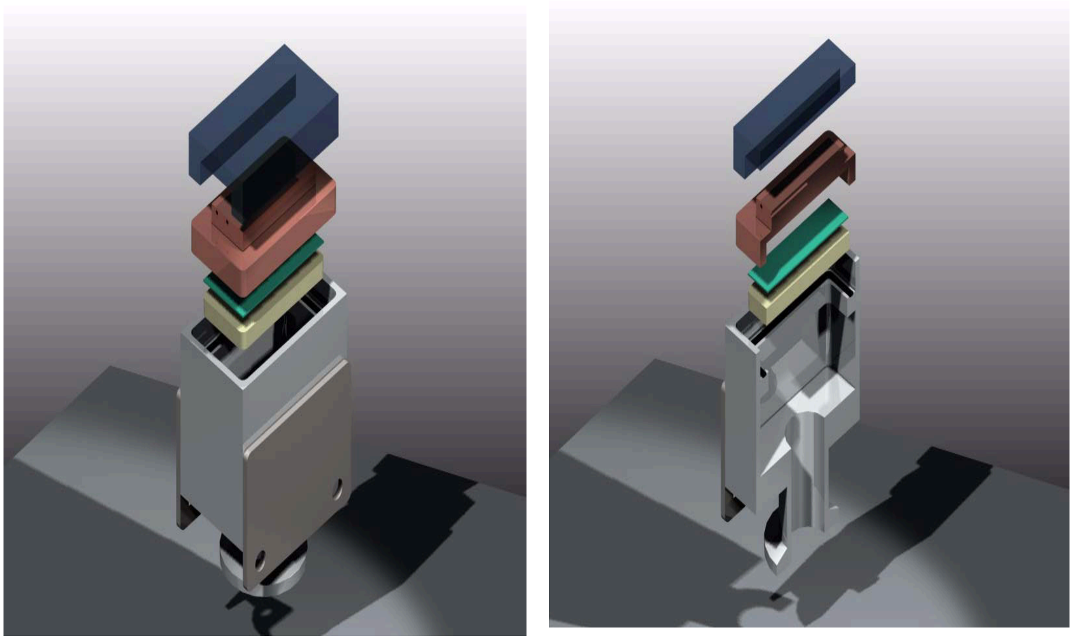

Figure 3-11. Solid view of the GAMMA 1D heater assembly.

The water pool was evacuated for the purpose of insulation similar to the stainless steel housing. Two stainless steel tanks constitute the water pool and the space between those could be evacuated by vacuum pumping. Hence, this could function to keep a steady thermodynamic state of water at the atmospheric pressure, in which eight immersion type heaters having the electric capacity of 2 kW were homogeneously inserted to the test pool to pre-heat the demineralized water in the test pool up to the saturated state. A reflux condenser was equipped in the test pool itself to maintain the pressure in the water pool.

This study is focused on the acquisition of quantitative heat transfer information as well as on the visual inspection of the bubble behavior from the initiation of the boiling to the vicinity of the CHF. The test apparatus was arranged as shown in Figure 3-12. Prior to each test, the heater surface was cleaned with acetone. The water pool was deaerated by running the immersion-type heaters at the atmospheric saturated boiling condition for at least an hour prior to reading the data.

Maintaining the thermodynamic saturated condition at atmospheric pressure, the heat flux was gradually increased at a rate of 3% of CHF utilizing a direct power supply. At each stage, vapor behavior in the confined channels and open periphery was photographed through the view port using a high speed digital camera at 4000 fps, in which several high capacity light sources provided illumination for the high speed photography. Together with visualization, the heated surface temperature was monitored using HP VEE5.0 and stored in the data file format. While monitoring the temperature, the CHF was judged to occur when the surface temperature rose in a rapid slope. The CHF was determined as the highest average heat flux that gave a stable temperature reading plus one half of the last average power increment (~3% of the CHF). In order to protect the thin film resistor from burnout, the electrical power was turned off immediately after the surface temperature had reached 190^{o}C.

After appropriate analysis of the heat flux and temperature data, the CHF values were determined for all the surface orientation angles within ±5%. In calculating the uncertainties associated with the experimental data readings, propagation of error was utilized. The K-type thermocouples were calibrated

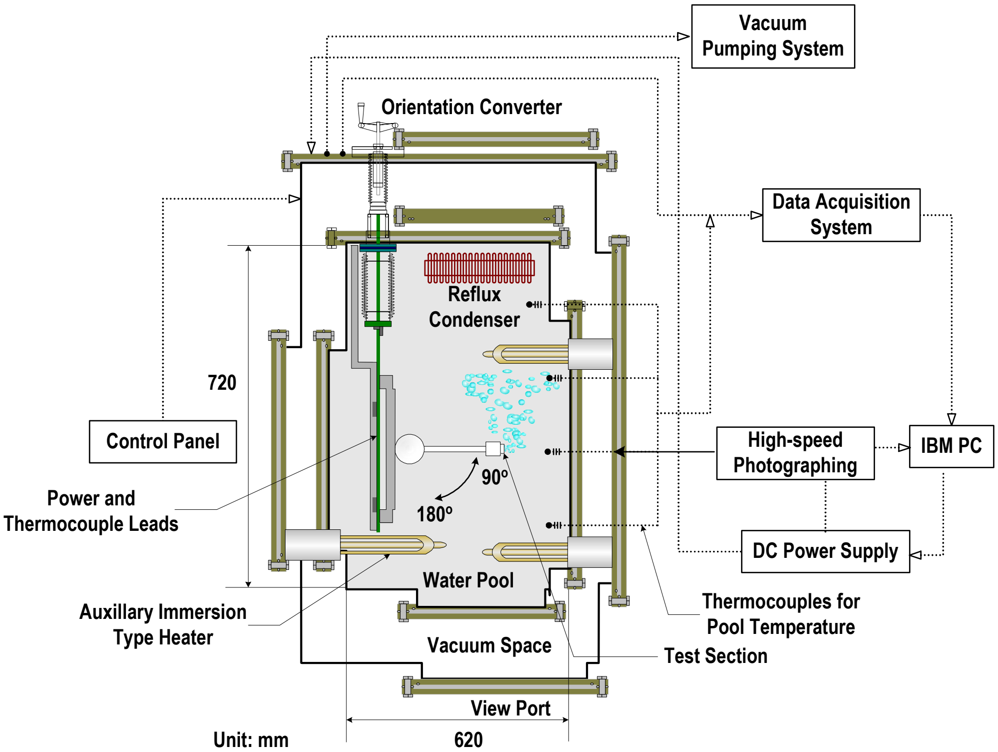

Figure 3-12. Schematic diagram of the GAMMA 1D test apparatus.

for a maximum uncertainty of ±0.1°C. The uncertainty in the heat flux due to instrumentation limitations was estimated to be 1%. As mentioned earlier, this study adopted the vacuum pumping method to minimize the heat loss from the sides other than the side adjacent to the working fluid. Hence, the heat loss was considered to be negligible enough to ascertain full energy transfer from the heated surface to the working fluid.

3.3.3. GAMMA 1D Test Results

The boiling curves were plotted on the basis of the temperature history data for each gap size and heat flux data within ±5%. The gap boiling curve is different than the general boiling curve with the conventional log-log representation of heat flux versus wall superheat as shown in Figure 3-13 for each gap size with varying angles. As the gap size increases, the boiling curves tend to merge except for the downward-facing region as plotted in Figure 3-13. This signifies that the CHF mechanism in the downward-facing region may be completely different from that at other angles. Strictly speaking, the sharp temperature rise at the downward-facing orientation may rather be attributed to the concept of dryout heat flux (DHF) than the classical definition of CHF.

In order to understand the fundamental CHF and related thermal hydraulic phenomena, one-dimensional test heater assembly was utilized in the experiment to obtain results and to explain the combined effect of gap size and the gravity force in the rectangular channel. Figure 3-14 presents the CHF data plotted against the gap size and surface inclination angle. Figure 3-15 shows the CHF data for pool boiling with open periphery as well as gap boiling. Visual inspection of the fluid motion in the rectangular

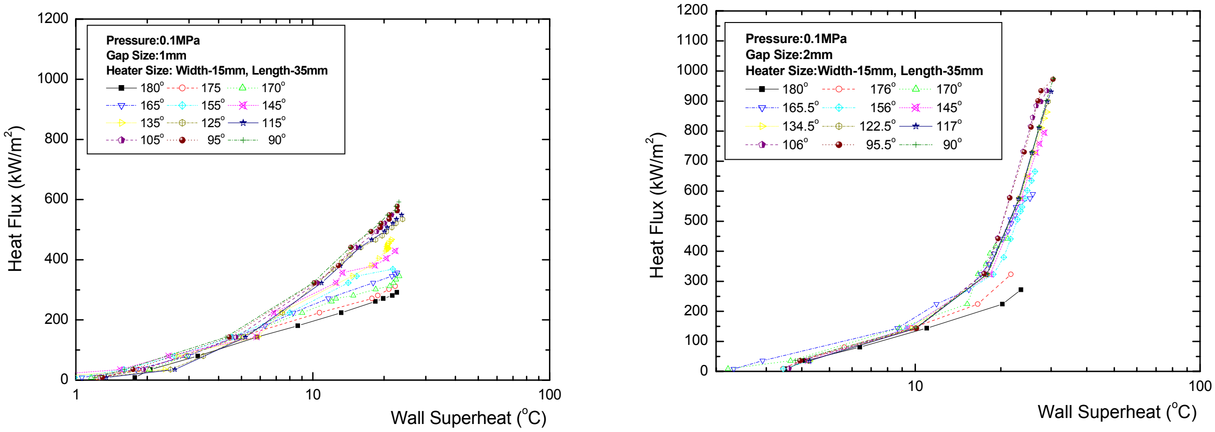

(a) 1 mm gap

(b) 2 mm gap

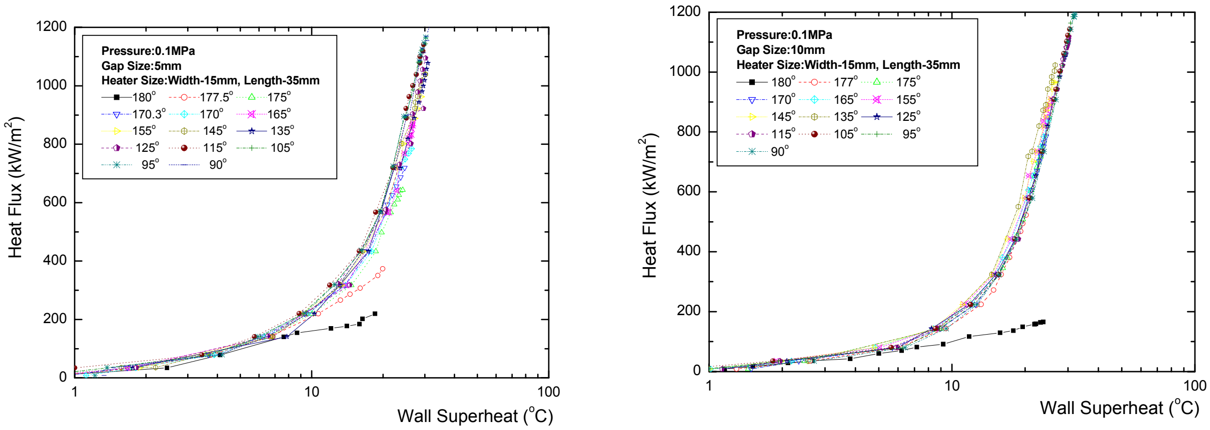

(c) 5 mm gap

(d) 10 mm gap

Figure 3-13. Angular boiling curves for varying gaps.

channel revealed that the Helmholtz instability was not detected in the gaps of 1 and 2 mm. However, such instability manifested itself in the gap of 5 mm at certain inclination angles. In particular, a wavelength of about 21 mm was observed at the vertical position (90°) in the gap of 10 mm.

Generally, the vapor behavior in the narrow gap plays an important role in triggering the CHF. It has generally been claimed that the CHF decreases as the gap size decreases. Contrary to this general belief, however, the present study has found opposing results at certain surface inclination angles. At the vertical location (90°), in consistency with the general belief, the CHF decreases as the gap size decreases. However, the CHF for the gap size of 10 mm is smaller than that for any other gap sizes at the fully downward-facing location (180°) as shown in Figures 3-14 and 3-15.

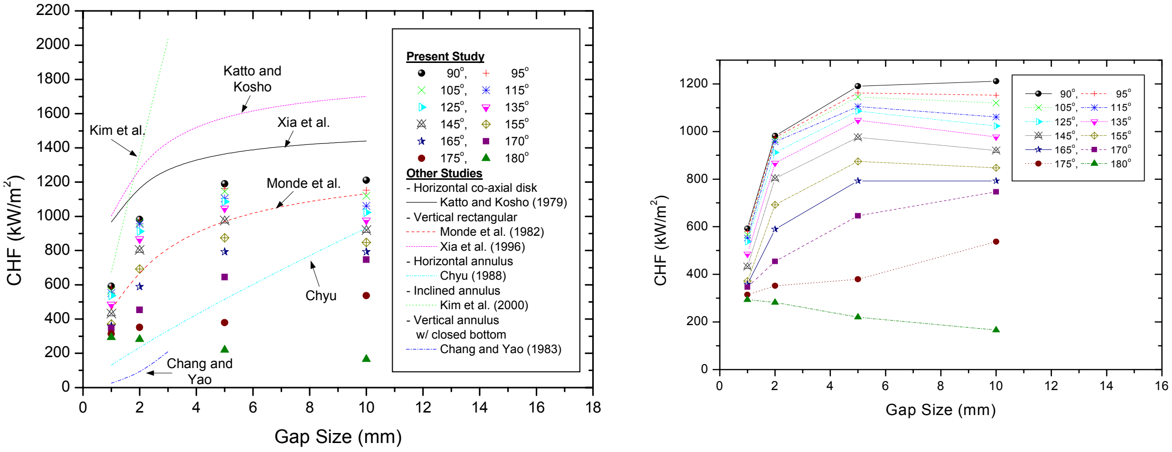

(a) comparison with other studies

(b) current results for differing angles

Figure 3-14. Effect of gap size on the CHF.

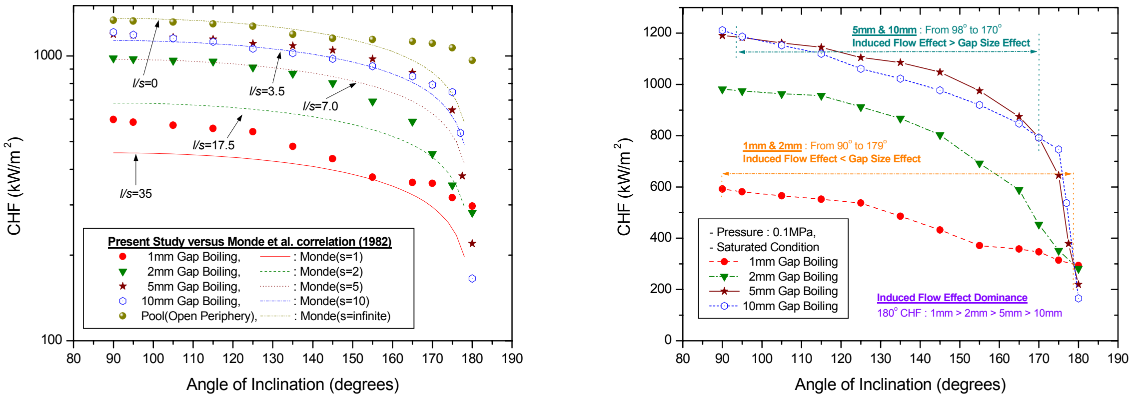

(a) effect of surface orientation angle on the CHF

(b) effect of induced flow and gap size on the CHF in gap boiling

Figure 3-15. Effect of surface orientation angle on the CHF.

The CHF generally increases as the gap size increases, but the increasing rate decreases with an exception at the fully downward-facing angle as shown in Figure 3-14(a) where the current experimental data are compared with other results reported in the literature. In the vertical rectangular geometry of Monde et al.[3-25] and Xia et al.,[3-26] the increasing trend of the CHF with the gap size is compared against the present experimental data. It is found that the CHF changing trend differs with the geometry. Albeit the overall behavior of the CHF in the horizontal co-axial disk is comparable, the CHF is grossly overpredicted. Monde et al.'s correlation[3-25] is observed to reasonably represent the current experimental data.

Accounting for the gravity effect, the Monde et al. correlation is compared against the CHF in the gap and pool boiling as shown in Figure 3-15(a). The Monde et al. correlation underestimates the CHF for the 1, 2 and 5 mm gaps. On the other hand, the correlation satisfactorily predicts the CHF for the 10 mm gap and pool boiling for most of the angles below, say, 150°. Figures 3-15(a) and 3-15(b) demonstrate that the

CHF for the 1 and 2 mm gaps decreases as the inclination angle increases and as the gap size decreases except at the fully downward-facing location (180^{o}). At the downward-facing angle, the bubble formed in the gap less than its own thickness is affected by the induced flow effect due to the gap structure. To paraphrase, the bubbles in the narrow gap can more easily escape from the restricted channel than those in the gap whose size exceeds the bubble thickness. Whereas the bubbles in the 1, 2 and 5 mm gaps tend to be ejected due to the induced flow effect, the bubble in the 10 mm gap is stagnated. That is, the induced flow effect increases as the gap size decreases at the fully downward-facing location.

When the bubble thickness is less than the gap size, particularly in the 10 mm gap, the bubble tends to be stagnated. Contrary to the case for the 10 mm gap, the bubbles in the 1, 2 and 5 mm gaps tend to be ejected dynamically. If the bubble is compressed in the smaller gaps by the confined channel geometry, pressure is built up within the bubble relative to the surrounding fluid. The pressure drop results, as the bubble is expelled from the channel to the open pool. The pressure drop in the two-phase flow carries three terms: friction, phase change, and gravity. For example, in the homogeneous equilibrium model the pressure drop may be spelled out as

$$pressure \quad drop = \frac{friction + phase\,change + gravity}{1 + compressibility}$$

The above equation may be more precisely worded out as

$$pressure\,drop = \frac{friction + phase\,change\,due\,to\,boiling\,or\,condensation + gravity}{1 + \left[vapor\,compressibility + liquid\,compressibilty + flashing\right]}$$

If the vapor and liquid layers are in mechanical equilibrium, pressure is uniform throughout both phases at a given cross-section. Then, the pressure drop due to friction and that due to boiling are nearly equal at all streamwise locations, providing closure to the separated flow model. However, in case of the boiling experiment, the pressure drop due to friction generally is 30~40% of phase change due to boiling. It may be that the major source of the pressure drop in the current boiling experiment is friction and phase change due to boiling.

The bubbles escape from the inclined gap by mainly the buoyancy force. However, at the near horizontal locations, the buoyancy force cannot effectuate bubble release until the bubbles coalesce to grow large enough. Hence, the main driving force for the bubble ejection is pressure drop due to bubble squeezing. The smaller the gap size, the greater the pressure buildup.

Hence, at the fully downward-facing location, the CHF decreases as the gap size increases contrary to the trend at other locations. However, the CHF in pool boiling with open periphery is greater than the CHF in the gap cooling because the bubble in the pool boiling with open periphery is free to escape in the azimuthal directions. Though the CHF values for the 5 and 10 mm gaps both decrease as the inclination angle increases, the CHF for the 10 mm gap is less than that for the 5 mm gap over a wide range of angles due to absence of the induced flow effect in the 10 mm gap as shown in Figure 3-15(b).

The flow rate depends on the balance between the driving force and the pressure drop. The driving force for the 5 mm gap is greater than that for the 10 mm gap due to high void fraction within the confined channel space. Given the flow rate, the pressure drop for the 5 mm gap is greater than that for the 10 mm gap. Then, the mass flux for the 5 mm gap can exceed that for the 10 mm gap due to the smaller flow area over a span of the inclination angles.

Consequently, there can be a range of inclination angles over which the CHF increases as the gap size decreases. Interestingly enough, this newly theorized thermal hydraulic phenomenon appears to unmistakably take place at the fully downward-facing angle for all the gap sizes examined in this work, and occasionally over some range of angles for the 5 and 10 mm gaps. Therefore, the CHF in the gap boiling is affected by the gap size as well as by the induced flow within the gap.

In recent years, some investigators have mentioned the existence of a transition angle at which the CHF changes with a rapid slope.

Howard and Mudawar[3-27] suggested that based on the vapor behavior observed just prior to the CHF, the surface orientations can be divided into three regions: upward-facing ($0^o \sim 60^o$), near-vertical ($60^o \sim 165^o$) and downward-facing ($>165^o$). Yang et al.[3-28] noticed that a transition angle exists in the boiling behavior from vertical-like to downward-facing between 150^o and 174^o. The boundary between the near-vertical and downward-facing regions is generally defined as the transition angle.

In the present study, certain transition angles were also identified for different gap sizes. For the gap size of 1 mm and pool boiling with open periphery, the existence of a transition angle was not discernible as shown in Figures 3-16(a) and 3-16(b). However, in the experiments for the gaps of 2, 5 and 10 mm, rather distinct transition angles were observed as shown in Figure 3-16(a). For the gaps of 2, 5 and 10 mm, the transition angles were found to be 165^o, 170^o and 175^o, respectively.

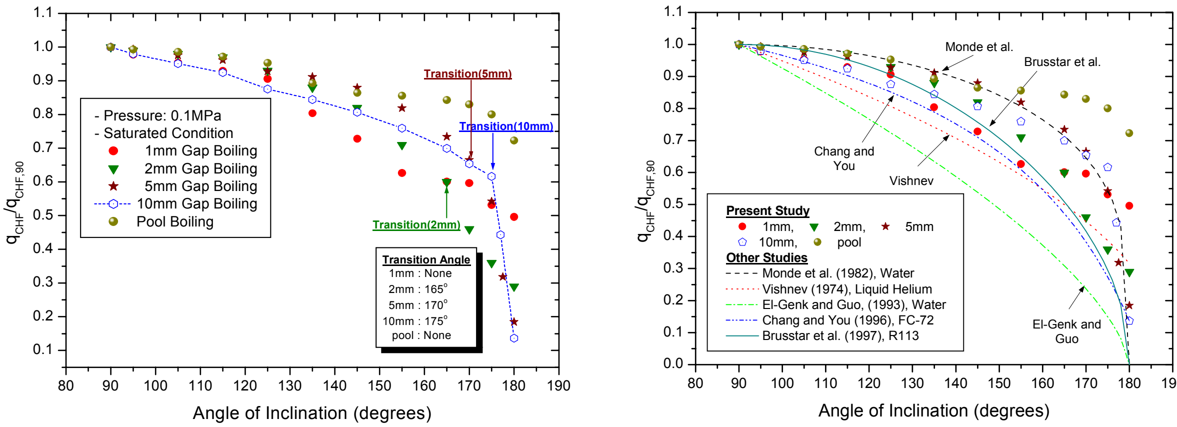

(a) transition angles for different gaps

(b) comparison of present study with other studies for the angle effect

Figure 3-16. Effect of surface orientation angle on the CHF.

At heat fluxes approaching the CHF, the boiling process can be divided into two regions with categorically different slopes in terms of the nondimensionalized CHF. In this study, the near-vertical region is defined as the angular range from vertical (90^o) to transition and the downward-facing region is defined as angular span from transition to completely downward-facing (180^o).

Howard and Mudawar[3-27] and Yang et al.[3-28] had claimed a transition angle for the pool boiling CHF with open periphery, while the current investigation could not necessarily confirm their claims. The reason may well be that the aspect ratio of the heater width to length in this study is considerably smaller than that in their experiments. Specifically, the heater aspect ratio is 2.3 in this work versus 10.9 and 10 in Howard and Mudawar,[3-27] and Yang et al.,[3-28] respectively. Note also that the values of $q_{CHF}/q_{CHF,90}$ for differing gap sizes are broadened as the surface inclination angle increases as shown in Figures 3-16(a) and 3-16(b).

The nondimensionalized form of the correlations in the cited literature is seen to shift for differing fluids, which appears to support El-Genk and Guo's assertion[3-29] that different correlations be used for different fluids in describing the effect of orientation on the CHF. Howard and Mudawar[3-27] confirmed different transition angles for different fluids, viz. 150° for liquid helium, and 160° to 165° for water and FC-72.

Figure 3-16(b) suggests that one nondimensionalized equation cannot possibly correlate the experimental data at various inclination angles, because the dimensionless CHF values tend to spread with increasing angles beyond the acceptable error range. That is, the nondimensionalized correlation will be affected not only by different fluid properties but also by the surface orientation effect. It is also noted that the Monde et al.[3-25] and Chang and You[3-30] correlations provide respectively with the upper and lower bounds for the data taken from the present study.

In Figure 3-17, several two-phase flow photographs in the vicinity of the CHF are presented in terms of the surface orientation angle in the 5 and 10 mm gaps. They lend themselves to physical insight to explain the combined effect of gap size and gravity force in the rectangular channel. With the aid of Figure 3-17, visual inspection of the fluid motion in the rectangular channel revealed that the Helmholtz instability was not detected in the gaps of 1 and 2 mm due to the smaller gap size than bubble layer thickness. In most surface inclinations of the 5 mm gap boiling, similar dispersed and coalesced vapor motion by the gap structure was detected excepting at certain inclination angles that may be interpreted as the Helmholtz instability motion.

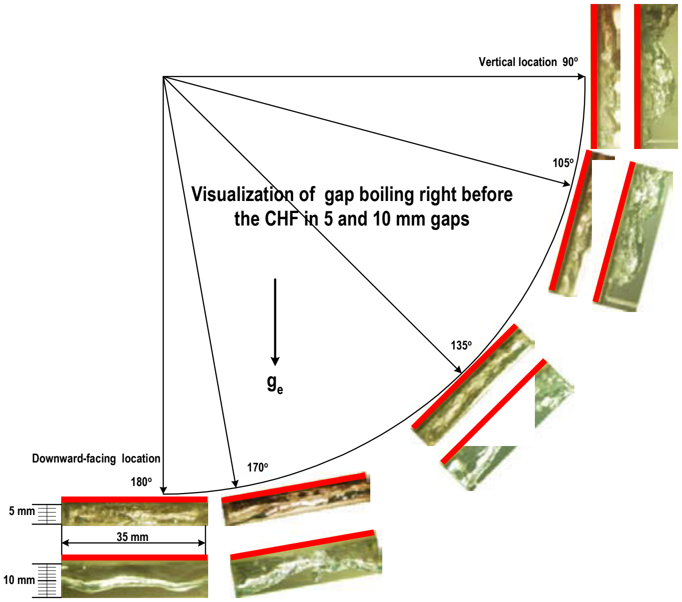

Figure 3-17. Flow visualization at CHF- concerning surface orientation (5 and 10 mm).

In case of the 10 mm gap boiling, however, the Helmholtz instability exists over the broad surface inclination angle. In particular, a wavelength of about 21 mm was observed at the vertical position in the 10 mm gap. Departing the angle of 180°, most of the vapor motions in the 10 mm gap have the characteristic of the Helmholtz instability approaching the CHF, which is epitomized as the surface inclination nears the vertical location.

3.3.4. GAMMA 2D Test Apparatus

If the CHF phenomena are experimentally studied with azimuthal angle dependency, the complicated enough heat removal mechanism in the narrow gap can physically be understood. A series of experimental investigations of the cooling mechanism in the narrow gaps, focusing on the CHF, were carried out. Figure 3-18 illustrates the GAMMA 2D test loop, which consists of a rod heater, a heat exchanger and a coolant control system.

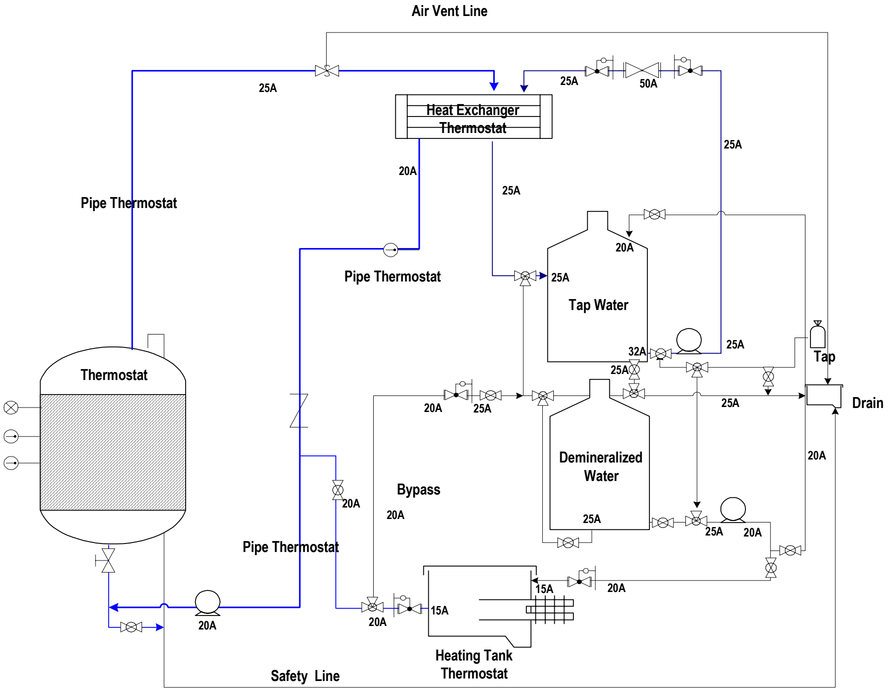

Figure 3-18. Schematic diagram of the GAMMA 2D test loop.

The boiling experiment was designed in the closed loop at atmospheric and elevated pressures. The stainless steel pressure vessel was manufactured to provide the gap sizes of 1, 2 and 5 mm between the copper block and the pressure vessel itself. The experiment was performed using de-mineralized water. The generated steam in the pressure vessel is sent to the heat exchanger through the stainless pipe. The steam on the primary side is condensed by the fluid on the secondary side of the heat exchanger installed at 2 m high. The heat exchanger controls the pressure of the test vessel so that its heat capacitance is designed twice the total power of the heater rods. The coolant flow rate on the secondary side is controlled by the automatic controller, which generates the output signal of valve open by a digital pressure input signal. To finely control the system pressure, the air-pressure valves are used. As the experimental facility consists of a closed loop, the first step necessary to run the experiments is to purge the air accumulated in the experimental loop. The air trapped in the closed loop will tend to deteriorate the heat transfer in the heat exchanger so that the water circulation may be slowed down. Initially, the heater power is maintained at a low level and then the pressure is set at a predetermined value. All the temperature readings are processed by a data acquisition system and carefully observed. If the temperature readings are believed to reach a quasi-steady state, the heater power is increased in a stepwise manner. When all the temperature readings increase monotonically, the heater power is turned off. The heat flux measurements were taken at different power levels with the rod heater power increased in steps, allowing for steady state to be achieved before the data were taken. The power was increased until temperature escalated. The CHF was calculated from the input power of rod heaters just before the boiling crisis. The CHF was defined as the largest steady-state flux attained during testing. At the CHF, vapor covered the surface essentially insulating it from cooling. Consequently, heat supplied by the cartridge heaters could not be removed by the liquid and remained in the copper to cause a temperature rise and gradient decrease. Therefore, the CHF was detected during testing by an unsteady increase in the wall temperature accompanied by a sudden decrease in the wall heat flux.

The temperature of the heating surface as well as the heat flux across the heating surface is determined by means of two K-type thermocouples of 1 mm in diameter located along the radial axis of circular copper block. When the heat flux is compared with the electric input, it is found that the heat loss from the circular copper block is less than the 10% of the total input. Figure 3-19 demonstrates the installed thermocouples in circular copper block. In order to determine the local wall flux and the wall temperature, thirty-eight K-type thermocouples were inserted at nineteen angles along the heating surface as illustrated in Figure 3-19. The K-type thermocouples were calibrated for a maximum uncertainty of $\pm 1^{\circ}$C. At each location, the thermocouple beads were epoxied into small holes which were precisely drilled with respect to each other and the heated wall. The temperature data from thermocouples were obtained from the computer based data acquisition system mainframe of HP VXI-E8406A functioned with the module of HP-E1413C. Temperature data readings were 10 times in a second, which were saved to PC by the HP-VEE5.0 data acquisition software. The CHF was signified during testing by a sharp slope in the wall temperature.

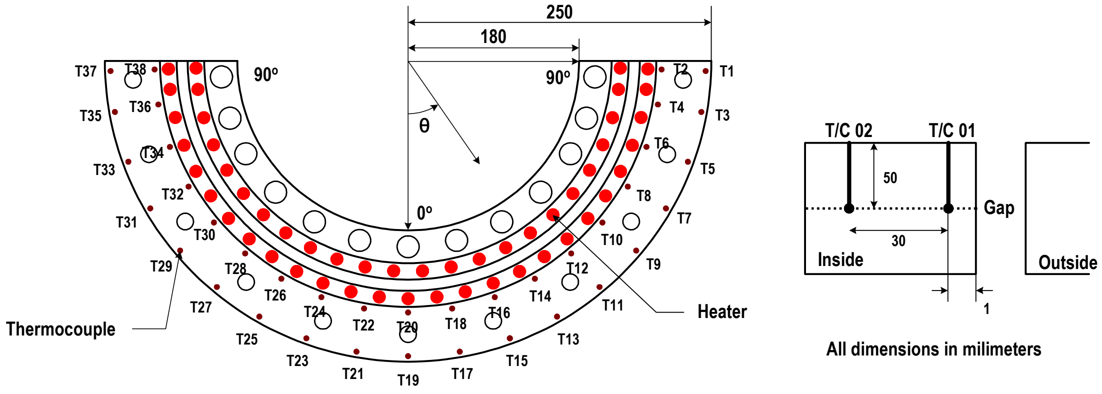

Figure 3-19. GAMMA 2D Heaters and thermocouples in circular copper block.

Additionally, the heating surface was cleaned with acetone prior to each test. The water in the thermostat was deaerated by running the immersion type heaters for at least an hour prior to reading the data. Although this study is focused on the quantitative investigation of CHF, data in the nucleate boiling regime prior to reaching CHF were also obtained. Maintaining the saturation condition by using the pressure control device, heat flux of the surface was gradually increased through cartridge heaters controlled by the silicon controlled rectifier (SCR). While monitoring the temperature, the CHF was determined to occur when the surface temperature is not sustained in a steady state or rises with a gradual slope. The CHF value was determined as the highest average heat flux that gave a stable temperature reading. Input to the heaters in circular heater copper bock in increments that are less than 3% of each preceding heat flux is increased, and finally the point is reached at which the surface temperature runs away.

3.3.5. GAMMA 2D Test Results

The temperature curve was obtained for each experimental run to obtain the value of the CHF. Figure 3-20 depicts the temperature curve for the 1 mm gap and system pressure of 0.4 MPa. Observe that the temperature at the bottom is lower than at the upper region in the steady-state condition prior to CHF. At CHF, the temperature at the bottom is rapidly increased. After the temperature at the bottom is increased, the temperature in the upper region is successively increased. In this study, the temperatures are observed to increase successively from the bottom to the top region in the 1 and 2 mm gaps. Hence, the mechanism of the CHF in the 1 and 2 mm gaps for the circular narrow gap is propagation of dryout, not top flooding.

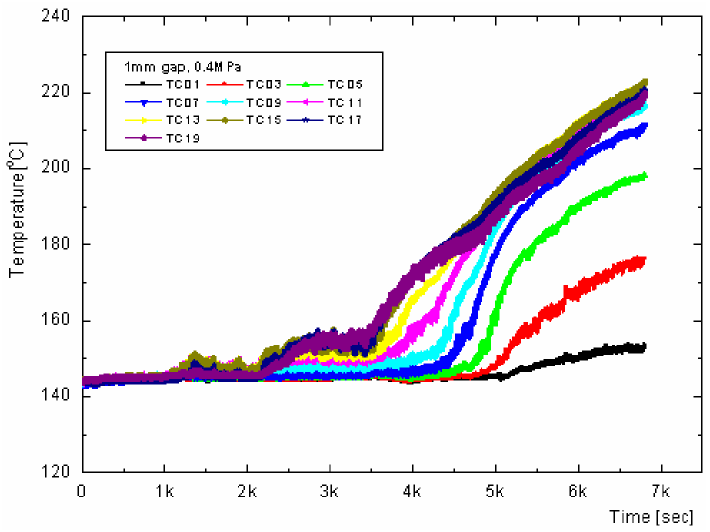

Figure 3-20. Temperature behavior in 1 mm gap, 0.4 MPa.

Figure 3-21 presents the temperature history for the 5 mm gap at 0.1 MPa. Contrary to the cases of the 1 and 2 mm gaps, the CHF occurred at the bottom at the latest. The CHF took place near the top, which triggered the top flooding propagating the CHF to the bottom.

Although the local dryout did take place in GAMMA 2D, the dryout did not result from the CCFL (Counter-Current Flow Limit), but rather from downward-facing heating. However, in the CHFG test with three- dimensional geometry, a CCFL brought about the local dryout and finally the global dryout in the hemispherical narrow gaps. Note that the bubbles can migrate more freely at the bottom of the hemispherical channel than of the circular channel. Increase in the gap size leads to increase in the critical power. Figure 3-22 displays results for the 1, 2 and 5mm gap tests with varying pressures.

3.3.6. CHF Correlation in the Near-Vertical Region

It has been shown that surface orientations can be divided into two regions, i.e. near-vertical and downward-facing, each of which is associated with a unique CHF triggering mechanism. Howard and Mudawar[3-27] insisted that the vast differences observed between the vapor behavior within the two distinct regions indicate that a single overall pool boiling CHF model cannot possibly account for all the observed orientation effect, but instead different models should be developed for the regions.

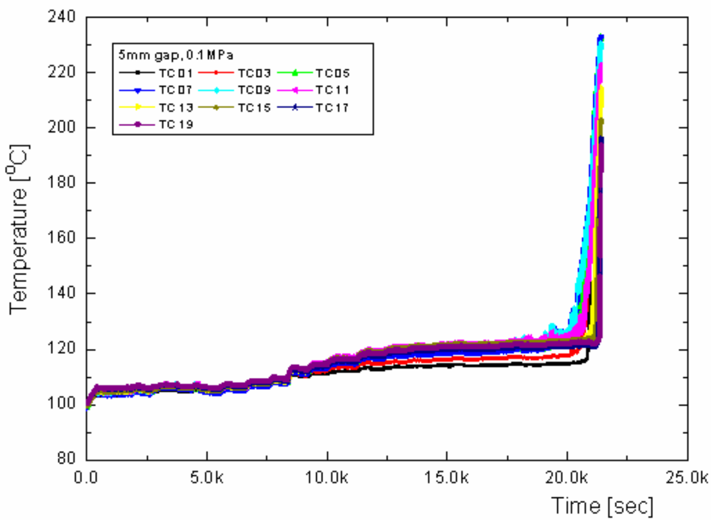

Figure 3-21. Temperature behavior in 5 mm gap, 0.1 MPa.

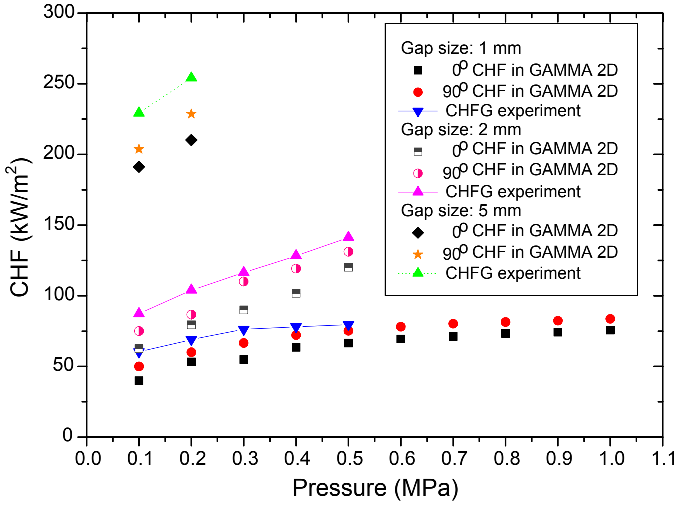

Figure 3-22. CHF and critical power to pressure for differing gap sizes.

In this study, correlation of the CHF in the near-vertical region is suggested. Monde et al.[3-25] suggested a generalized correlation of the CHF data in the vertical narrow rectangular channel with the aid of dimensional analysis developed by Katto.[3-31] In Monde et al.'s model,[3-25] the inclination angle and the heater width were not considered. In this study, their model is modified so as to account implicitly for the effect of the inclination angle and the heater width.

With the aid of dimensional analysis developed by Katto,[3-31] the following correlating equation can be obtained for the CHF during natural convective boiling in confined channels in the near-vertical region

$$\frac{q_{CHF}/\rho_g h_{fg}}{\sqrt[4]{\sigma g \sin(\theta)\left(\rho_f-\rho_g\right)/\rho_g^2}} = \frac{C_1}{1+C_2\left(\rho_f/\rho_g\right)^{C_3}\left(g\sin(\theta)(\rho_f-\rho_g)s^2/\sigma\right)^{C_4}\left(D_h/s\right)} \qquad (3\text{-}1)$$

where $D_h = \dfrac{2wl}{w+l}$ is the equivalent heated surface diameter.

When D_h/s approaches zero, the right side of Eq. (3-1) is reduced to C_1. This C_1 value corresponds to the constant predicted not only by Kutateladze[3-32] but also by Lienhard et al.[3-33] for the pool boiling CHF in many different geometries. Taking an average for the left side of Eq. (3-1) for the CHF at all the angles in pool boiling except at 180^o in this study, the C_1 value is obtained as 0.17 with the RMS error of 2.4%.

To determine the remaining constants C_2, C_3 and C_4 in Eq. (3-1), the following form of Eq. (3-1) may be assumed for the CHF data.

$$\frac{s}{D_h}\left(\frac{0.17\cdot\sqrt[4]{\sigma g\sin(\theta)(\rho_f-\rho_g)/\rho_g^2}}{q_{CHF}/\rho_g h_{fg}}-1\right)=C_2\left(\frac{\rho_f}{\rho_g}\right)^{C_3}\left(\frac{g\sin(\theta)(\rho_f-\rho_g)s^2}{\sigma}\right)^{C_4} \tag{3-2}$$

The CHF data are rearranged as shown in Figure 3-23 to evaluate the exponent C_4 in Eq. (3-2). Figure 3-23 shows that the left side of Eq. (3-2) is independent of $g\sin(\theta)(\rho_f - \rho_g)s^2/\sigma$. Then, the value of C_4 is taken as zero. When the least squares method is used for the average value of the CHF for each gap size as well as for the pool boiling, the constants C_2 and C_3 can be obtained. This procedure yields the values of C_2 and C_3 as 6.8×10^{-4} and 0.62, respectively.

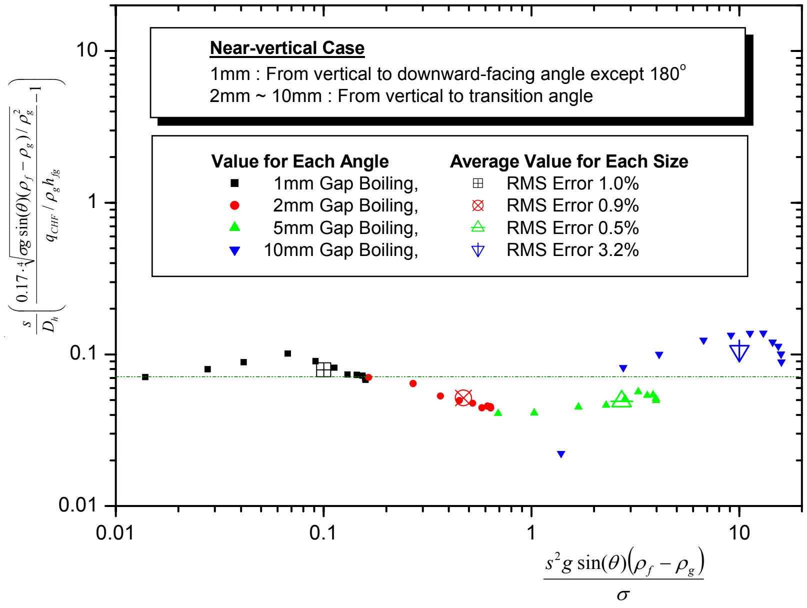

Figure 3-23. Effect of Bond number on the CHF.

When the equivalent heated surface diameter is introduced to account for the width effect, a generalized correlation equation in the near-vertical region based on the CHF data in the present study can be obtained as follows

$$\frac{q_{CHF}/\rho_g h_{fg}}{\sqrt[4]{\sigma g\sin(\theta)\left(\rho_f-\rho_g\right)/\rho_g^2}}=\frac{0.17}{1+6.8\times10^{-4}\cdot\left(\rho_f/\rho_g\right)^{0.62}\left(D_h/s\right)} \tag{3-3}$$

Equation (3-3) turns out to be similar to the Monde et al. correlation,[3-25] which used the aspect ratio of the heated length to the gap size, in lieu of the equivalent heated surface diameter to the gap size. Figure 3-15(a) shows that the Monde et al. correlation underestimates the CHF data for gap boiling in the present study.

Figure 3-24 shows that Eq. (3-3) predicts the experimental data within an accuracy of ±20%. The CHF data predicted by Eq. (3-3) are compared against the measured data taken from literature in Figure 3-25. It is seen that the developed correlation is in fair agreement with the experimental data of Fujita et al.[3-34] Albeit the CHF correlation appears to be in poor agreement with the experimental data of Monde et al.[3-25] for gaps smaller than 1 mm, the developed correlation is in good agreement with the experimental data for gap sizes exceeding 1 mm.

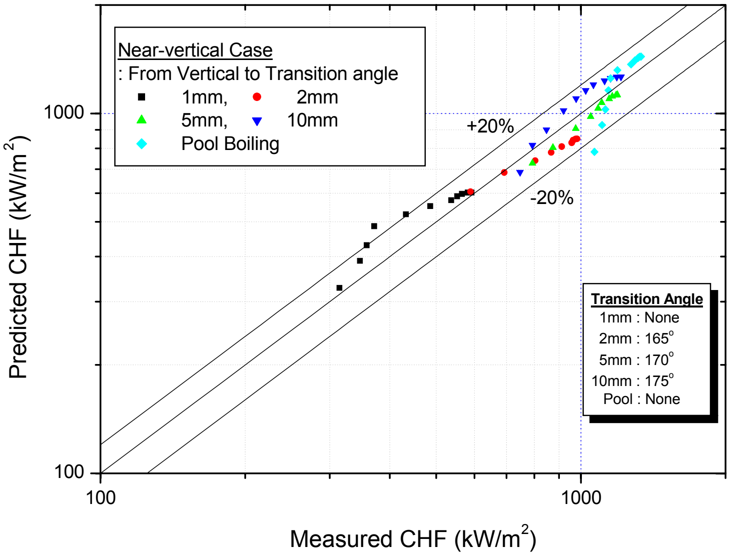

Figure 3-24. Comparison between measured and predicted CHF.

The smaller the width of flow channel is, the less complicated the flow path is. The developed correlation may not satisfactorily be applied to small gap sizes with small widths, because the CHF in gaps smaller than 1 mm with widths less than 10 mm may be influenced by the heated length rather than by the equivalent surface heated diameter.

However, if the widths are greater than 10 mm, the developed correlation may as well be applicable to small gap sizes. Also, Figure 3-25 compares the developed correlation with the experimental data for the annular tube taken from Kim et al.[3-35] Though the developed correlation concurs with the experimental data for the annular tube within a band of ±40%, the constants in Eq. (3-1) ought to be altered. In the annular tube, the left side of Eq. (3-2) usually depends on the Bond number ($g\sin(\theta)(\rho_f - \rho_g)s^2/\sigma$). The value of C_4 in Eq. (3-2) is not zero. If dimensional analysis is performed for the experimental data in the annular tube, more accurate prediction may be obtained.

As far as application to nuclear safety analysis is concerned, it must be noted that this correlation is based on the experimental data taken from the test sections scaled down from the reactor. The correlation developed from the 1D reduced test section is applied to prediction of test results from the GAMMA 2D

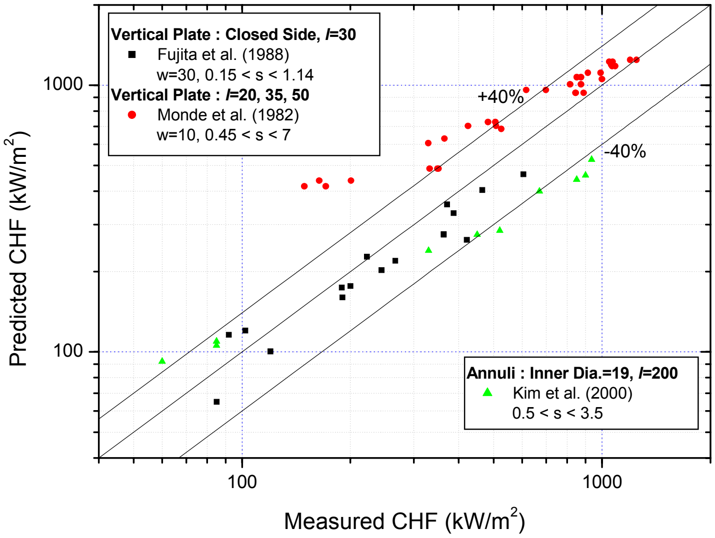

Figure 3-25. Comparison of the developed correlation with other experimental data.

apparatus as shown in Figure 3-26. In the 1 and 2 mm gaps, there is a difference between the CHF values at atmospheric pressure. Nevertheless, the CHF values for the 5 and 10 mm gaps in the GAMMA 2D test accord with those of this study at atmospheric pressure. A common point in the heat transfer mechanism for this study and the GAMMA 2D test is that thermal hydraulic phenomena are similar to pool boiling in the 5 and 10 mm gaps. Heat removal in the 1 and 2 mm gaps is not quite satisfactory in either GAMMA 1D or GAMMA 2D. Yet, the CHF values in the 5 and 10 mm gaps are relatively high approaching those for pool boiling in this study. Hence, the developed correlation can only be applied to the GAMMA 2D test with larger gaps exceeding 5 mm. The reactor application is recommended only as a first approximation on account of geometric variables associated with the developed correlation.

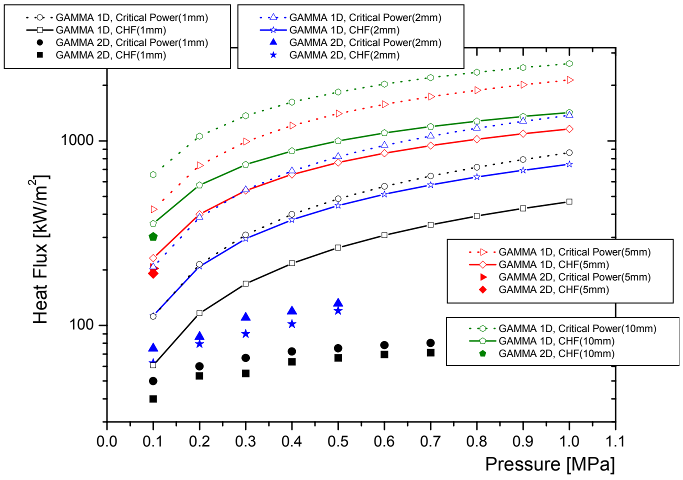

Figure 3-26. Comparison of the developed correlation with experimental data from GAMMA 2D (Dh= 177.4 mm).

3.3.7. Narrow Gap Cooling Model

We investigated the model for narrow gap cooling. In the film boiling regime, the heat transfer coefficient was calculated with laminar vapor flow and interfacial wavy motion. The DELTA 3D test results for the spherical surface revealed that the angular vapor film thickness is maintained below 1 mm. If there is a negligible effect of counter-current flow limit (CCFL), the film boiling heat transfer coefficient in the narrow gap will be similar to that in pool boiling due to minute steam flow rates. SNU recommended that the film boiling heat transfer coefficients be calculated from the DELTA 3D test results.

In the transition and nucleate boiling regimes, SNU recommended the Kutateladze formula for pool nucleate pool boiling used by Zhang et al.,[3-36] Okano et al.,[3-37] and Murase et al.[3-38] The GAMMA 1D test results indicated that the CHF values for the near-vertical surfaces for gaps exceeding 5 mm were similar to those in the open periphery. In addition, the bubble layer thickness is less than the gap size. Thus, the boiling curves for the gap cooling will be similar to those for pool boiling.

The CHF for gap cooling was generally lower than that for pool boiling due to the CCFL effect. As the inclination angle increases from downward-facing (0^{o}) to vertical (90^{o}) direction, the critical power increases. Hence, the CHF by the inclination angle is considered to be less than that by CCFL. SNU utilized the CHF dependent on the inclination angle referenced from Howard and Mudawar's correlation[3-27] and that dependent on CCFL effect from Park et al.'s correlation.[3-39] Figure 3-27 shows the angular CHF values dependent on inclination angle and CCFL. Except for the downward-facing location, the CHF by CCFL is less than that by the inclination angle. Table 3-3 presents correlations proposed in this study.

Table 3-3. Recommended correlations.

Film boiling	**Layer thickness (10), critical vapor film Re (25.1)**	
Nucleate and transition boiling $\frac{q''}{\Delta T_{sat}}\frac{L}{k_l} = C\left[\frac{k_l \Delta T_{sat}}{\rho_g \Delta h_{lv} v_l}\right]^{n1}\left[\frac{pL}{\sigma}\right]^{n2}$ $L = \left[\frac{\sigma}{g(\rho_l - \rho_v)}\right]^{0.5}$	Transition boiling	C=1.2×10^{14}; n1=-5.5, n2=0.32
	Nucleate boiling (higher wall superheat)	C=2.2; n1=-0.1, n2=0.32
	Nucleate boiling (lower wall superheat)	C=1.1; n1=0.3, n2=0.32
CHF	Flow instability	CCFL
$\frac{q''_{CHF}}{\rho_v h_{lv}}\sqrt[4]{\frac{\rho_v^2}{g\sigma(\rho_l - \rho_v)}} = C$	$C = 0.151\sin^{0.25}\theta$	$C = \frac{0.1042\left(\sin\theta / 1-\cos\theta\right)^{e}}{1+0.1375\left(\rho_v / \rho_l\right)^{0.21} D/s}$ $e = -0.3944\ln\frac{s}{1.0} + 2.02 \quad (0.5 \le s \le 5)$

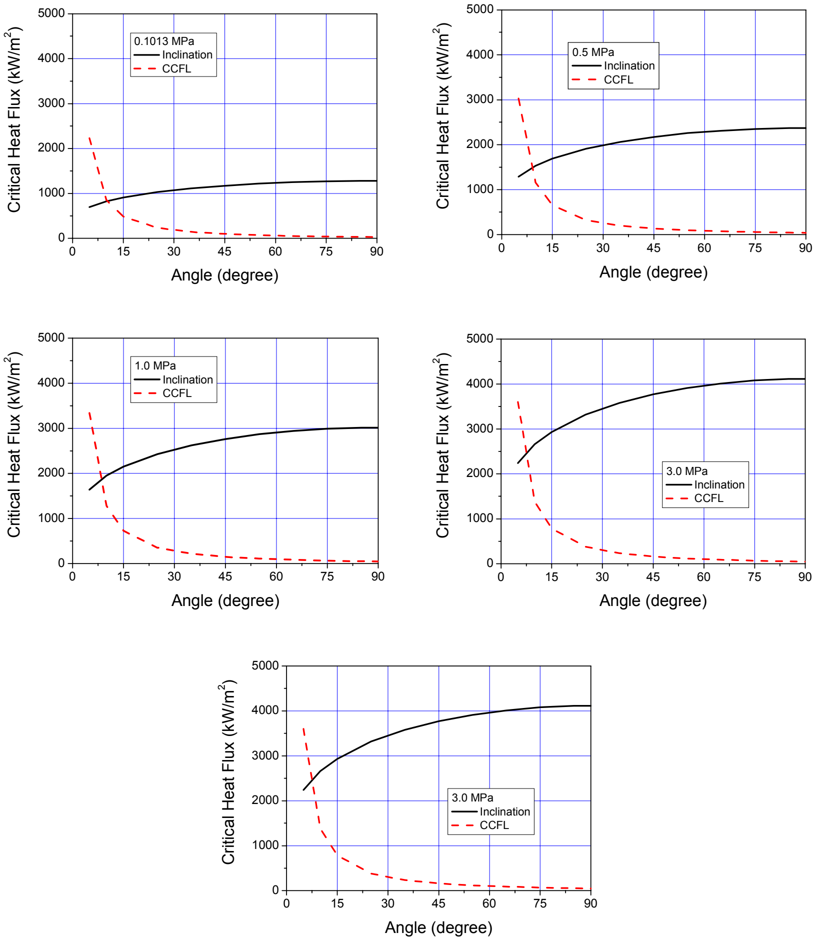

Figure 3-27. Comparison between two CHF values by CCFL and flow instability.

3.3.8. Summary and Conclusions

In this study, the CHF experiments were carried out for narrow gaps of 1, 2, 5 and 10 mm, in which the surface orientation effect was taken into account by facing the rectangular heater assembly having a heater length of 35 mm from vertical location (90^o) to downward-facing location (180^o) utilizing the distilled water at atmospheric pressure. In addition, boiling heat transfer experiments were conducted in the circular narrow gap as a first step to investigating the inherent cooling mechanism in the hemispherical narrow gaps. Finally, the narrow gap cooling model was developed by the comparison with CCFL CHF mechanism and flow instability CHF mechanism. Key conclusions from the study may be summarized as follows.

Visualization study of both the gap and pool boiling phenomena was conducted by using the high-speed camera devices. Differential behavior between pool and gap boiling in the inclined downward- and upward-facing regions, 45^{o}and 135^o, respectively, was addressed in terms of the gravitational and buoyant forces. The pool and gap boiling phenomena in the vertical region, 90^o, were photographed approaching the CHF, in which the buoyant force dominates over all the other physical forces. The gap boiling characteristics were studied to reveal the situation in which the difficulty of vapor escape from the channel gives rise to the lower CHF as the gap size increases.

The gap size and surface orientation effects play an important role in interpreting the general two-phase flow behavior as well as the CHF data. There exists a critical gap size commensurate to the average vapor layer thickness enhancing the heat transfer rate with increasing mass flux at certain surface orientation, thus the combined effect of gap size and surface orientation on the CHF may give crucial hints at analyzing the phenomenological outcome. Associated with photographs, the quantitative CHF data were obtained, where the CHF generally increases as the gap size increases, but the increasing rate decreases as the gap increases. In particular, the CHF in the 10 mm gap is smaller than the value at any other gap sizes at the fully downward-facing location (180^o). At the vertical location (90^o), as is generally believed, the CHF increases as the gap size increases. The CHF in gap boiling is affected by the gap size as well as by the induced flow within the channel.

Competence of pressure force exerted on the liquid-vapor interface and the momentum of vapor generation tend to maintain the sinusoidal wave. In the present study, the interfacial instability of vapor layer was detected in the 10 mm gap boiling for which the critical wavelength was measured to be λ_c= 10~10.5 mm.

There is a transition angle for each gap size. The transition angle increases as the gap size increases in this study. The transition angles for the 2, 5 and 10 mm gaps in this study were distinctly found to be 165^o, 170^o and 175^o, respectively. However, the transition angle was not discernible for the gap size of 1 mm and the pool boiling in the unconfined space. The ratio of $q_{CHF}/q_{CHF,90}$ for each size at the same angle gets spread as the surface inclination angle increases.

A semi-empirical CHF correlation was developed for the near-vertical gap boiling using dimensional analysis of the CHF during natural convective boiling in confined channels because the existing correlation could not reasonably predict the data obtained in this study. This correlation agrees with the experimental data within ± 20%.

In the CHFG experiments for the hemispherical narrow gaps and visualization experiments performed at KAERI, the CCFL occurred at the top end of the gap and prevented water from penetrating the gap. That is, the CCFL brought about local dryout and finally the CHF in the hemispherical narrow gaps. However, the starting point of CHF in the GAMMA 2D experiment differed from the results of the CHFG experiment. The CHF took place at the bottom earlier than at the top for the 1 and 2 mm gaps. Hence, the CHF mechanism in the circular channel with the narrow gaps is not CCFL, but rather dryout for the 1 and 2 mm gaps.

For the 5 mm gap the rapid temperature rise occurred first near the top and then propagated toward the bottom. That is, the CHF mechanism for the 5 mm gap is top flooding. The main mechanisms of CHF occurrence can differ with gap sizes contingent upon the propagation of dryout or top flooding. The flow limitation occurred due to transition from bubbly flow to slug and plug flow. The increasing temperature in the bottom region is due to dryout. The reason is that the coalescence and departure between isolated bubbles and slugs by downward-facing heating are not sufficiently supported.

Comparison between the CHF by CCFL and flow instability shows that the CCFL CHF correlations must be applied for the narrow gap cooling boiling regime during the most severe accident conditions except the case of small core melt fraction.

3.4. Small Scale Simulant Testing

Seoul National University

3.4.1. Introduction

During a severe accident, the molten core can relocate to the lower plenum of the reactor vessel and form a hemispherical pool. Should there be no effective cooling mechanisms, the core debris may heat up on account of decay power. The molten core material will threaten the structural and thermal integrity of the reactor vessel. The extent and urgency of this threat depend primarily on the intensity of the internal heat sources and the consequent distribution of heat fluxes on the vessel wall in contact with the molten core material. The SIGMA (Simulant Internal Gravitated Material Apparatus) tests are concerned with a high modified Rayleigh number, Ra′, turbulent natural convection in a molten pool. The internal heating method is employed in the test by using cable-type heaters. The main results include the heat split fraction, angular heat flux distribution, and temperature distribution inside the molten pool.

3.4.2. SIGMA 2D Test Apparatus

The apparatus consists of a two-dimensional (2D) semicircular pool with diameter, height, and width of 500 mm, 250 mm, and 100 mm, respectively, as shown in Figure 3-28. Dinh et al.[3-40] recommended that a slice width-to-height ratio greater than 0.25 be adopted for the slice experiment so as to eliminate the effect of the walls. The pool's curved wall, with a 25 mm thick copper plate, is cooled by a regulated water loop. A water-cooling system is used to maintain the temperature of water surrounding the test section constant with time. The thermal insulator insulates the semicircular front and rear plates. Two thin cable-type heaters, with a diameter of 4.2 mm and a length of 2000 mm, are used to simulate internal heating in the pool following Kolb et al.,[3-41] and Lee and Suh.[3-42] They are uniformly distributed in the semicircular pool supplying a maximum of 3 kW power tantamount to $Ra' = 3\times10^{13}$.

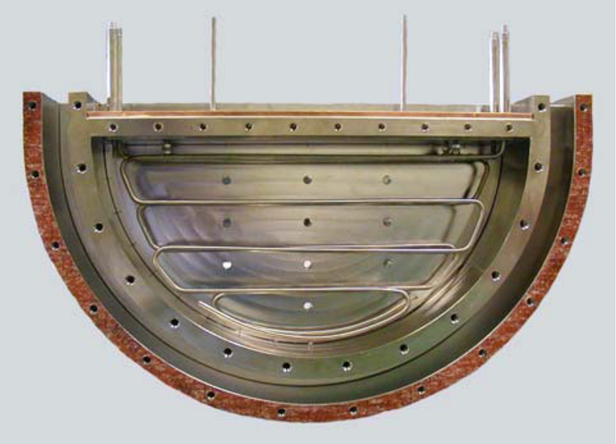

Figure 3-28. Picture of the SIGMA 2D test section.

Figure 3-29 illustrates the twenty T-type thermocouples mounted in the copper wall and through the test section from the bottom (= 0°) to just below the equator (= 88°) with the interval of 10° in order to obtain local lower heat fluxes. Ten thermocouples are installed at the upper plate. Another ten thermocouples are immersed in the water pool. All the thermocouples were calibrated prior to tests.

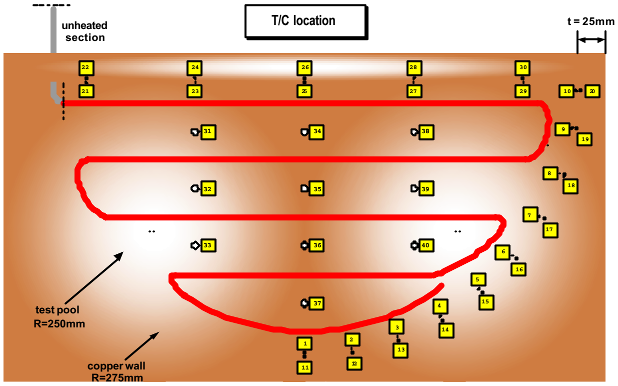

Figure 3-29. Schematic diagram of the SIGMA 2D heater and thermocouple locations.

Figure 3-30 presents the fluid temperature at five different locations in the pool. The average rate of temperature rise is 0.044 /sec with a standard deviation of ± 0.0007 /sec.

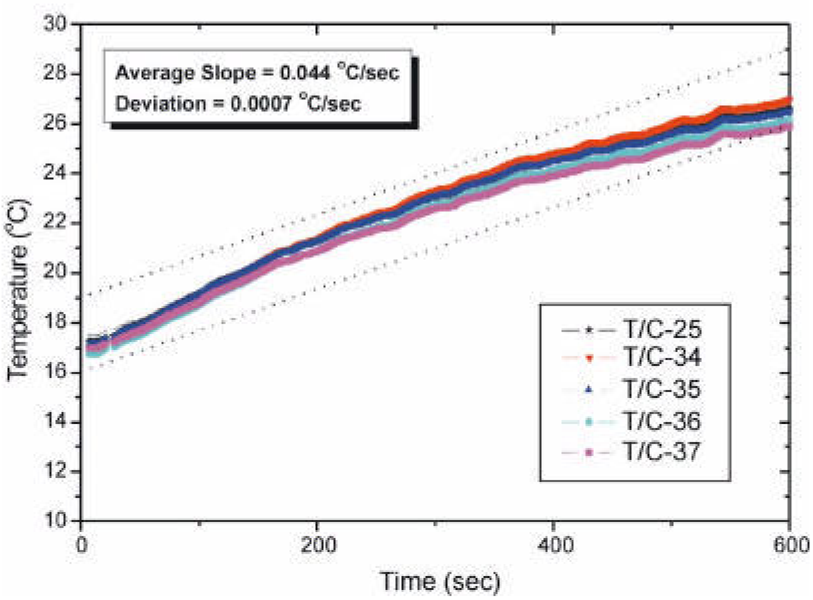

Figure 3-30. Temperature rise at different locations.

3.4.3. SIGMA 2D Test Results

Figure 3-31 presents the average upward Nusselt number, Nu_{up}. SNU conducted five tests with Ra′ = 1.87×10^{11}, 1.06×10^{12}, 2.94×10^{12}, 6.61×10^{12}, and 1.67×10^{13}, respectively. The present data concur with most of the literature data except Mayinger et al.'s (1976) numerical analysis.

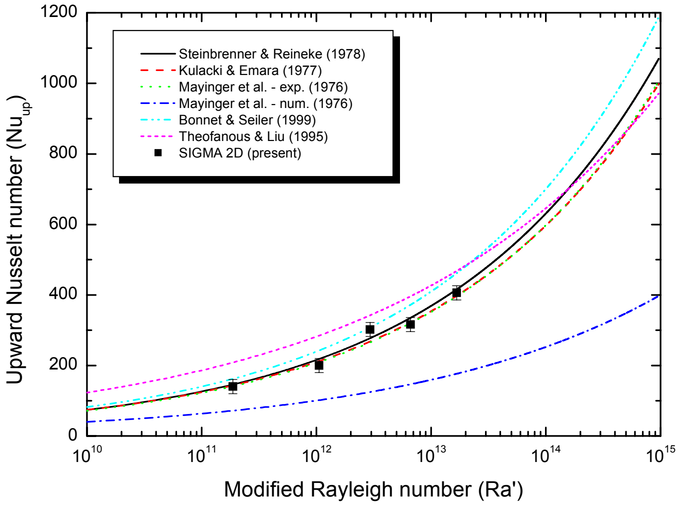

Figure 3-31. Average upward Nusselt number.

Figure 3-32 shows the average downward Nusselt number, Nu_{dn}. The current data fall between Mayinger et al.[3-43] and Kelkar, et al.[3-44].

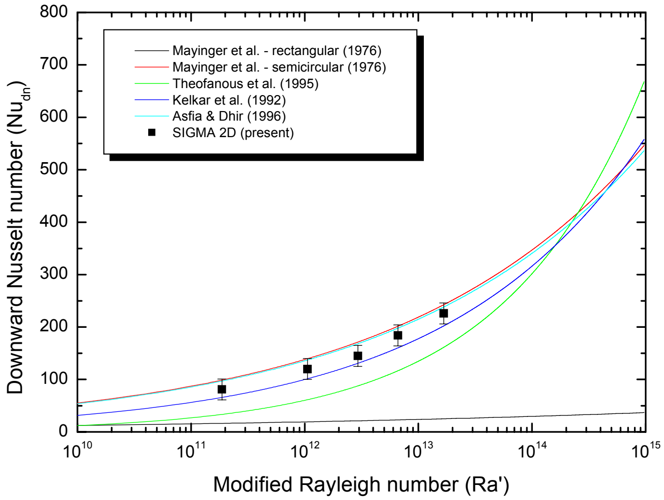

Figure 3-32. Average downward Nusselt number.

3.4.4. SIGMA 3D Test Apparatus

While a number of investigations have dealt with the rectangular and semicircular pools, relatively few experimental data exist for the hemispherical pool. SIGMA 3D considers the hemispherical pool employing the same internal heating method as was already used in SIGMA 2D. The radius of the test section is 250 mm as depicted schematically in Figure 3-33, and in more detail in Figure 3-34.

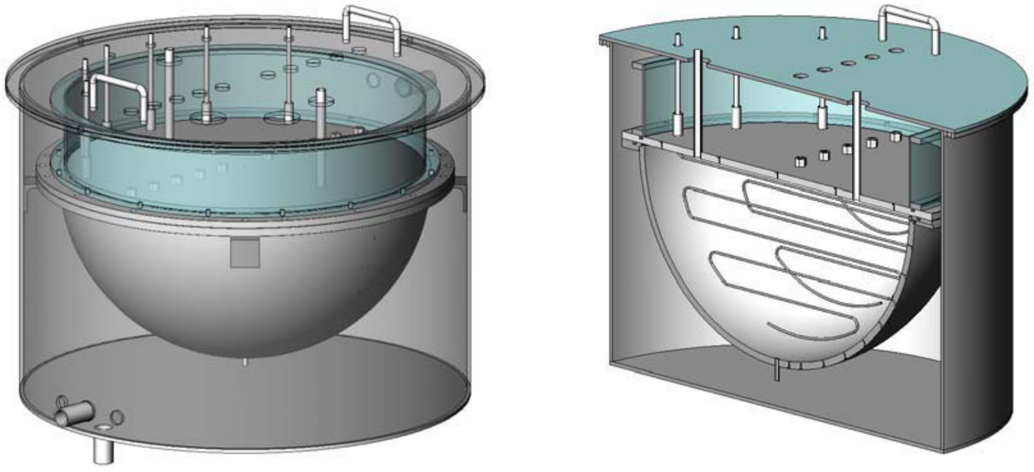

Figure 3-33. Schematic of the SIGMA 3D test section.

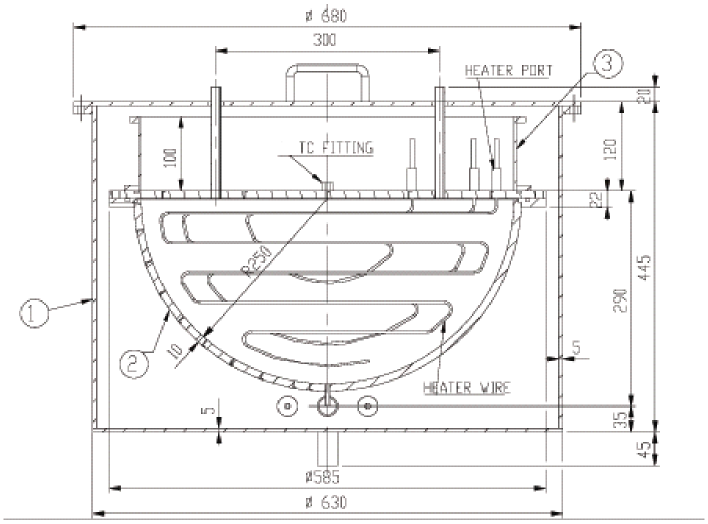

Figure 3-34. Detailed drawing of the SIGMA 3D test section.

The pool's upper flat wall and hemispherical curved wall, with a 10 mm thick stainless steel plate, are cooled by a regulated water loop. A water-cooling system is used to maintain the temperature of water surrounding the test section constant with time. Over the period of two hours, the maximum variation of water temperature in the outer pool was less than 1 K. Six thin cable-type heaters, with a diameter of 6 mm and a pair of the length of 1980 mm, 1760 mm, and 640 mm respectively, are used to simulate internal heating in the pool. They are uniformly distributed in the hemispherical section and thus they can supply a maximum of 7.8 kW power to the pool yielding Ra′ as high as 2.3×10^{13}.

Figure 3-35 depicts the SIGMA 3D test pool. There are two tubes, one of which is connected to the water source, while the other is attached to the expansion tank.

Figure 3-35. Picture of the SIGMA 3D test pool.

Figure 3-36 demonstrates the SIGMA 3D test section and heaters. The right side picture reveals six internal heaters, which serve to produce uniform heating. Heaters are located at top below about 20 mm and also at the curved lower surface above about 20 mm.

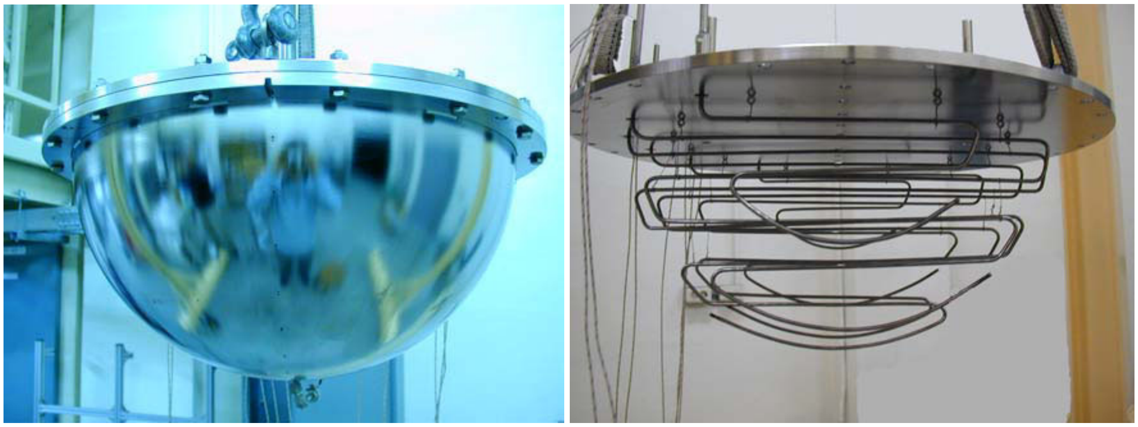

Figure 3-36. Picture of the SIGMA 3D test section and internal heaters.

Figure 3-37 shows the conceptual diagram of the SIGMA 3D test loop. This consists of a demineralized water system, the test section, and chiller. The SIGMA 3D water test is conducted to check on the performance of the water cooling circuit, cable-type heaters, thermocouples and the data acquisition system (DAS) against the available data on natural convection.

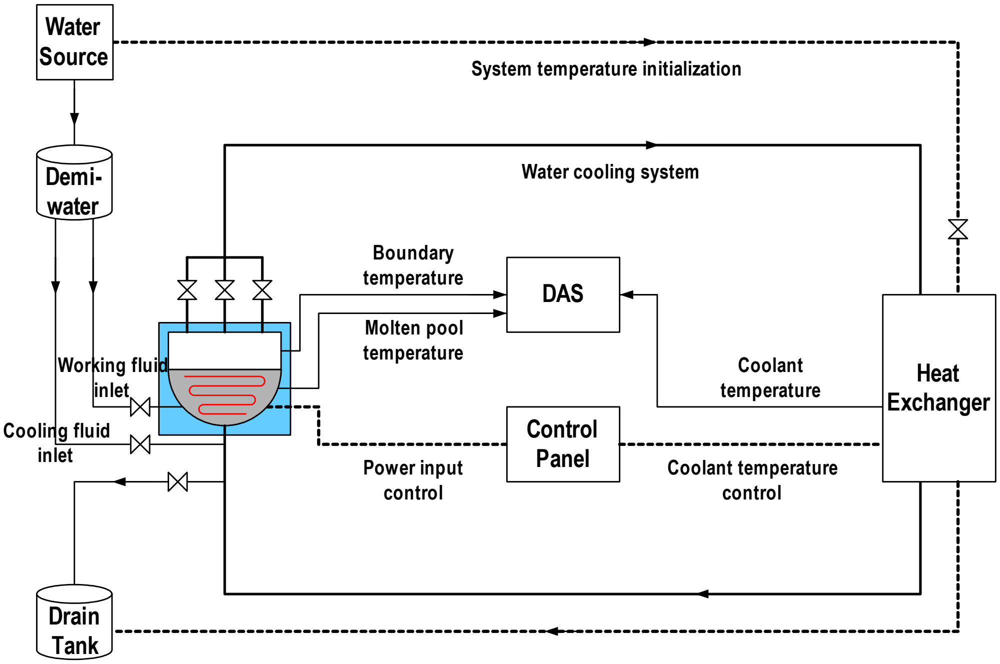

Figure 3-37. Schematic diagram of the SIGMA 3D test loop.

3.4.5. SIGMA 3D Test Procedure

After the water leakage test, the thermocouples were calibrated by ISOTECH TRU (Temperature Reference Unit) Model 740. Forty thermocouples were submerged sequentially in a constant temperature pool. The thermocouple outputs were compared with the temperature reading from a separate thermometer. The DAS bias error was thus calibrated so as to minimize the measurement error. After calibration, the thermocouples were placed in their designated locations. Initially the working fluid in the test section and water cooling system temperature reached a steady state. The water cooling system maintains the upper and lower boundaries isothermal. A performance test of this water cooling system showed temperature difference within ±0.5 K spanning 5^{o} to 80^{o}. The pool was then allowed to heat up. DAS was initially adjusted to record the temperature every 1 sec to check on the uniformity of the heat generating rate.

The thermocouples were submerged sequentially in a constant temperature pool. Using these data, calibration curves were drawn for each thermocouple. From these curves, relative error in reading from a particular thermocouple could be determined. Once all the thermocouples were calibrated, they were placed in designated spots. Figure 3-38 shows the thermocouple locations. Table 3-4 presents the location of each thermocouple. Twenty thermocouples were mounted at the surface of the stainless steel wall and through the test section from the bottom (= 0°) to just below the equator (= 88°) to obtain the azimuthal heat flux. Ten thermocouples were installed at the upper plate. Another ten thermocouples were planted in the water pool.

Table 3-4. Thermocouple installation location.

	No.	Location	Note
Pool	10	-225, -180, -135, -90, -45, 0, 30, 60, 90, 135, 180, 225	
Horizontal	5	-220, -110, 0, 110, 220	Z = 252
Horizontal	5	-219, -109, 1, 111, 221	Z = 259
Azimuthal (stainless steel)	10	5º, 10º, 20º, 30º, 40º, 50º, 60º, 70º, 80º, 88º	R = 252
Azimuthal (stainless steel)	10	5º, 10º, 20º, 30º, 40º, 50º, 60º, 70º, 80º, 88º	R = 259
Total	40		Unit: mm

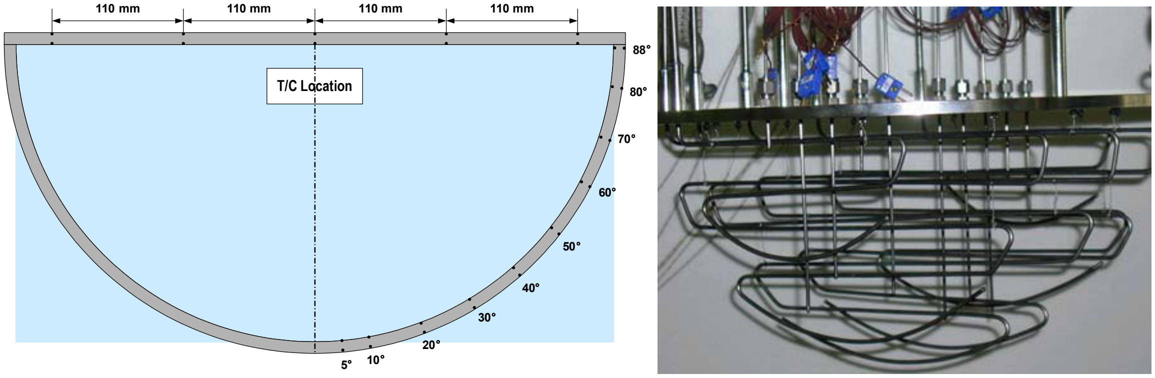

Figure 3-38. Schematic of the SIGMA 3D heater and thermocouple location.

3.4.6. SIGMA 3D Test Matrix

Tests are currently being performed with two different top boundary conditions as summarized in Table 3-5: cooled top surface and insulated top surface. An acryl cylinder is used to isolate the top surface from the coolant as shown in Figure 3-35.

Table 3-5.

Pool Surface Condition	Pool Height (mm)	Total Heat (W)
Insulated top surface	250	64
		258
		579
		1030
		1608
		2316
		3152
		4117
		5210
		6432
		7783
Cooled top surface	250	64
		258
		579
		1030
		1608
		2316
		3152
		4117
		5210
		6432
		7783

3.4.7. Summary and Conclusions

There exist several methods to simulate the uniform heat source in the molten pool such as microwave heating, direct current heating, cooldown, and internal heater heating. The present study has proved that the internal heating is a best choice for both SIGMA 2D and SIGMA 3D. Further refinement of the experimental database of the molten pool behavior is deemed desirable. The geometry effect is being examined by comparing the results from the SIGMA 2D and SIGMA 3D tests. Major findings from SIGMA 2D experiments may be summarized as follows.

The average Nu_{up} numbers concur with most of the literature data except Mayinger et al.'s numerical analysis.[3-43] The average Nu_{dn} numbers fall between Mayinger et al.[3-43] and Kelkar, et al.[3-44]

The ratio of the local to average Nu on the upper wall was unity at all locations. All cases yielded the same results. The results followed closely Kymäläinen et al.'s experimental values.[3-45] The heat flux profile along the lower wall and average upward heat transfer within this Ra′ range were in good agreement with the data obtained from other numerical and experimental studies. The heat input increase results in an increase in Nu_{up} and Nu_{dn}, but with no change in the heat split ratio (Nu_{up}/Nu_{dn}) which was about 1.7, except for the case where $Ra' = 2.94\times10^{12}$ and $Nu_{up}/Nu_{dn} = 2.1$. The lowest heat transfer occurred at the bottom of the pool, which was a stagnation point, while the highest value was observed in the upper corner of the pool.

When the top surface of the pool was insulated, the local heat flux was greater than in the other case by about 6%. In case of the adiabatic upper boundary condition, the internal heat transported by the strong buoyancy-induced flows was transferred sideward rather than upward in the upper region.

3.5. Large Scale Simulant Testing

Korea Atomic Energy Research Institute

3.5.1. Introduction

Simulant melt experiments, LAVA-GAP, were performed to investigate thermal and metallurgical performance of the IVCC at KAERI. The main objectives of the LAVA-GAP experiments are to examine the feasibility and sustainability of the IVCC under the various test conditions using rather small hemispherical test sections and simulant melt compared to the prototypic situations. The uniqueness of the LAVA-GAP experiments is the adoption of internally coated hemispherical IVCC in direct contact with the high temperature of simulant melt, which could provide the raw data on the thermal and metallurgical performance of the internally coated IVCC under the severe and various test conditions.

The experiments were performed using 60kg of Al_2O_3 thermite melt as a core material simulant with a 1/8 linear scale mock-up of the reactor vessel lower plenum. The hemispherical IVCC was installed inside the lower head vessel maintaining a uniform gap of 5 mm or 10 mm from the inner surface of the lower head vessel. Two types of the core catchers were used in these experiments. The first one was a single layered IVCC without internal coating and the second one was a two layered IVCC with an internal coating of 0.5 mm-thick ZrO_2 via the plasma spraying process. During this project period, KAERI completed the total 6 tests from LAVA-GAP-2 to LAVA-GAP-7 tests varying the experimental conditions such as material of base steel, gap size between the IVCC and the lower head vessel, and material of internal coating and bond coat, etc. Thermal analyses using LiLAC code[3-7] and metallurgical inspections were performed to precisely investigate the core catcher performance. LiLAC is a multi-dimensional thermal-hydraulic analysis code which was developed at KAERI to simulate the thermal and flow behavior of molten pool and lower head vessel. The main objectives of the metallurgical inspections were to investigate the performance of the coating material and the base carbon steel. The crack and chemical compositions variation of the coating material were checked and the chemical compositions, oxidation, and interaction with coating layer of the base carbon steel were examined. The thermal histories of the base carbon steel were postulated pursuant to the crystal structures.

3.5.2. Experimental Facility and Measurements

The LAVA-GAP facility provides KAERI a unique method for investigating core catcher response using simulant materials to represent relocated core materials. The LAVA facility,[3-8] which was originally developed to investigate the potential for debris-to-vessel gap formation and cooling, consists of a thermite melt generator, a melt separator, a test section of the vessel lower head, and a gas supply system for internally pressurizing the LAVA facility (peak test pressure in the LAVA facility is 3.0 MPa). In the LAVA-GAP tests, the Al_2O_3 component of the thermite melt is used as a corium simulant. The experiments have been conducted using 60 kg of Al_2O_3 thermite melt as a corium simulant with a 1/8 linear scale mock-up of the reactor vessel lower plenum. The lower head vessel was made of carbon steel with an inner diameter of 500 mm and a thickness of 25 mm. After being generated in the melt crucible, the thermite melt was first delivered to the melt separator and then poured into the lower head vessel through the melt delivery nozzle with an inner diameter of 8 mm. A hemispherical core catcher, made of carbon steel or stainless steel, was installed inside the lower head vessel maintaining a uniform gap of 5 mm or 10 mm from the inner surface of the lower head vessel depending on the experimental conditions. Figure 3-39 is a schematic diagram of the LAVA-GAP experiments.

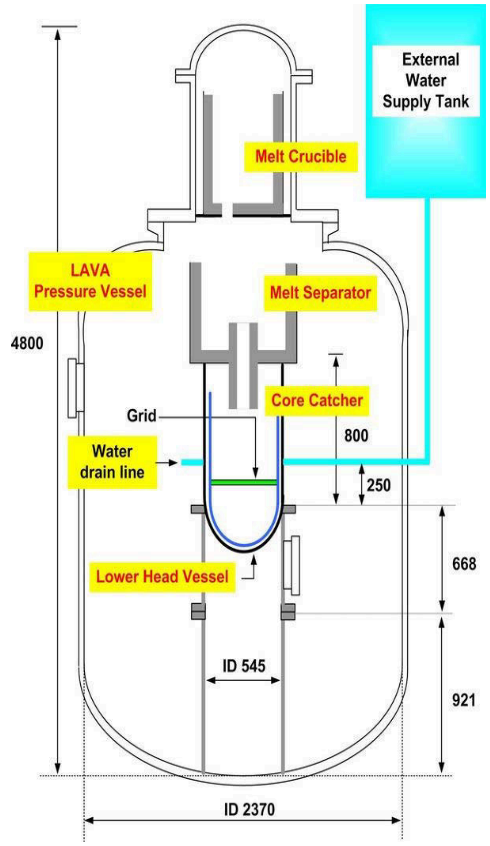

Figure 3-39. Schematic diagram of the LAVA-GAP facility (dimensions in mm).

Temperature histories of the lower head vessel wall were measured by K-type thermocouples embedded radially 3 mm deep into the vessel outer surface, and temperature histories of the core catcher were measured by K-type thermocouples embedded radially 3 mm and 5 mm (* mark in Figure 3-40) deep into the core catcher outer surface. Figure 3-40 shows the K-type thermocouple locations in both the lower head vessel and the IVCC

3.5.3. Experimental Conditions

During this project period, KAERI completed the total 6 tests from LAVA-GAP-2 and LAVA-GAP-7 tests varying the experimental conditions such as material of base steel, gap size between the IVCC and the lower head vessel, and material of internal coating and bond coat, etc. Table 3-6 summarizes the detailed experimental conditions. LAVA-GAP-2 and LAVA-GAP-3 tests,[3-7] which were conducted to investigate the performance of the IVCC, focused on the effects of an internal coating. Except for the existence of the coating on the IVCC, the other experimental conditions were the same in both the tests. The single layered IVCC was used in the LAVA-GAP-2 test, and the two layered IVCC was used in the LAVA-GAP-3 test. In the two layered IVCC, the base material of the core catcher had the same geometrical dimension as the single layered IVCC. The two layered core catcher was internally coated with a 0.5 mm thick layer of

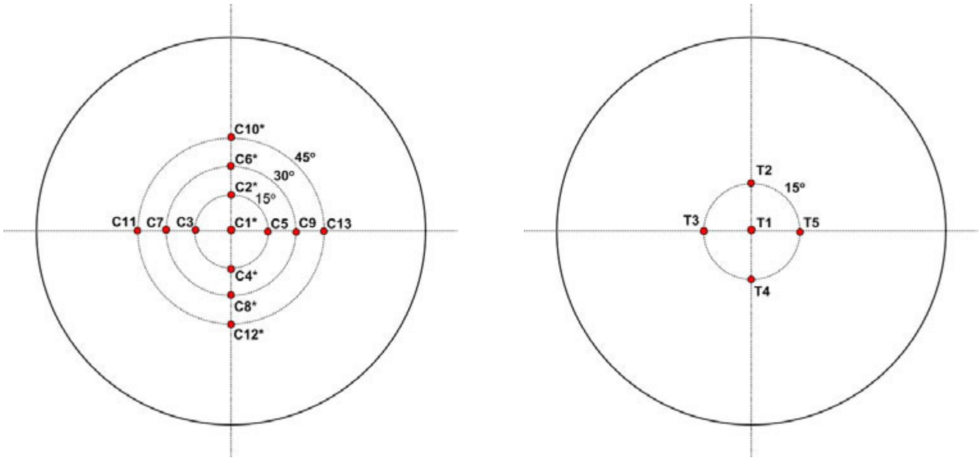

(a) IVCC (b) lower head vessel

Figure 3-40. K-type thermocouple locations.

ZrO_2. The coating material was applied via a plasma spraying process which produces coatings that have a typically 85 ~ 90% density. The actual composition of the coating material for the LAVA-GAP-3 test was 92% of ZrO_2 and 8% of Y_2O_3. A 95% Ni and 5% Al undercoat (bond coat) was applied on the base carbon steel prior to applying the ZrO_2 coating.

Table 3-6. Experimental conditions.

Test	Simulant Melt	Gap Size	Base Steel	Internal Coating	Bond Coat
LAVA-GAP-2	Al_2O_3, 60kg	10 mm	Carbon steel	Not applied	Not applied
LAVA-GAP-3	Al_2O_3, 60kg	10 mm	Carbon steel	92% ZrO_2 + 8% Y_2O_3, 0.5 mm	95% Ni + 5% Al
LAVA-GAP-4	Al_2O_3, 60kg	5 mm	Stainless steel	92% ZrO_2 + 8% Y_2O_3, 0.5mm	95% Ni + 5% Al
LAVA-GAP-5	Al_2O_3, 60kg	5 mm	Stainless steel	92% ZrO_2 + 8% Y_2O_3, 0.6mm	Not applied
LAVA-GAP-6	Al_2O_3, 60kg	10 mm	Stainless steel	92% ZrO_2 + 8% Y_2O_3, 0.5mm	Inconel 718
LAVA-GAP-7	Al_2O_3, 60kg	5 mm	Stainless steel	92% ZrO_2 + 8% Y_2O_3, 0.5mm	Inconel 718

In the LAVA-GAP-4 and LAVA-GAP-5 tests,[3-9] the gap thickness between the core catcher and the lower head vessel was 5mm. Actual composition of the coating material for the LAVA-GAP-4 test was same as the LAVA-GAP-3 test. In the LAVA-GAP-3 and LAVA-GAP-4 tests, the thickness of ZrO_2 internal coating was 0.5 mm. To examine the effects of the coating material, IVCC with a 0.6 mm-thick ZrO_2 coating without bond coat was used in the LAVA-GAP-5 test. Gap sizes were 10 mm and 5mm in the LAVA-GAP-6 and the LAVA-GAP-7 tests,[3-10] respectively. The IVCC has a plasma-sprayed ZrO_2 coating (92% ZrO_2, 8% Y_2O_3) with bond coating of Inconel 718 in both the tests. In the previous LAVA-GAP tests, the bond coating material was the 95% of Ni and 5% of Al. Uniquely, the outer surface of the IVCC has a stainless steel coating in the LAVA-GAP-7 test. In the LAVA-GAP-7 test, the effect of the coating at the outer surface of the IVCC was examined focused on the improvement of heat removal rate via porous coating material.

3.5.4. Experimental Results

The thermal and metallurgical integrity of the IVCC was examined by analyzing the temperature histories of the IVCC and by post examination in all the LAVA-GAP tests. The IVCC failed and stuck to the lower head vessel in the LAVA-GAP-2 test. Contrary to the LAVA-GAP-2 test, the IVCC was intact in the LAVA-GAP-3 test. Figure 3-41 shows a cross-sectional view of the core catcher and the vessel in the LAVA-GAP-2 test and the LAVA-GAP-3 test. The core catcher was penetrated, and resolidified core catcher material was found inside the gap between the vessel and the core catcher in the LAVA-GAP-2 test. Although we intended to have poured pure Al_2O_3 melt, a small amount of the iron was included in the melt due to incomplete melt separation and dissolution of iron into Al_2O_3 at high temperatures. Accordingly, this solidified iron cake may come not only from the melted core catcher base material but also from the initially relocated iron. The core catcher was intact and the coating layer was clearly visible at the interface between the core catcher and the solidified alumina iron thermite melt in the LAVA-GAP-3 test.

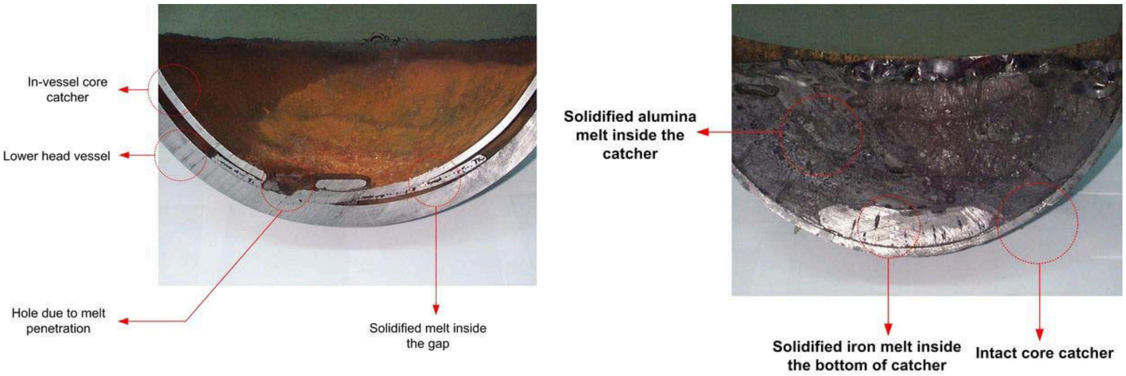

(a) LAVA-GAP-2 test (b) LAVA-GAP-3 test

Figure 3-41. Cross-sectional view of test sections from the LAVA-GAP-2 and LAVA-GAP-3 tests.

By comparing the experimental results of the two tests, the coating on the inner surface of the core catcher played a key role in maintaining the integrity of the core catcher in the LAVA-GAP-2 and the LAVA-GAP-3 tests. In the LAVA-GAP-2 test performed using the uncoated IVCC, the core catcher failed; and the lower head vessel got into direct contact with the high temperature melt. In the LAVA-GAP-3 test, however, the lower head vessel did not have any thermal attack due to the intact IVCC. Figure 3-42 illustrates the temperature histories of the IVCC recorded at 45^{o} azimuthal angle in the LAVA-GAP-2 and the LAVA-GAP-3 tests, respectively. With rupture of the core catcher, most K-type thermocouples failed on the lower part of the core catcher in the LAVA-GAP-2 test. Also most K-type thermocouples failed on the lower part of the core catcher in the LAVA-GAP-3 test although the core catcher did not mechanically yield. The temperatures of the core catcher demonstrated rather different cooling characteristics depending on the locations even at the same latitude. Because the gap between the core catcher and the vessel is hemispherical, heat removal through boiling inside the gap may most likely be asymmetric. The sequential rapid cooldown of the core catcher was observed. At the initial stage of high temperature, water boiled off the outer surface of the IVCC. Then, the effective cooling of the core catcher characterized by quenching was achieved at a specific location due to direct contact of water with the core catcher outer surface at that point.

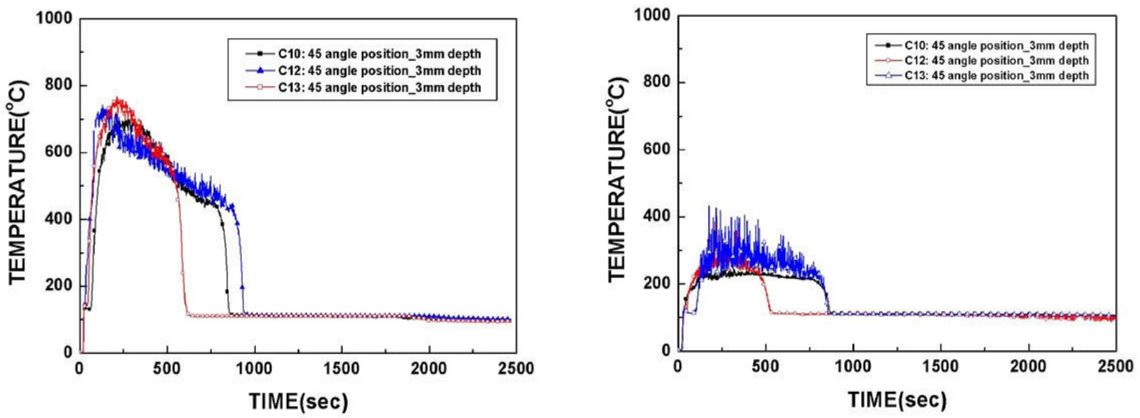

(a) LAVA-GAP-2 test

(b) LAVA-GAP-3 test

Figure 3-42. Temperature histories of the core catcher measured at 45^{o} azimuthal angle in the LAVA-GAP-2 and LAVA-GAP-3 tests.

The IVCC was failed and stuck to the inner surface of the lower head vessel in the LAVA-GAP-4 and LAVA-GAP-5 tests. The gap size of these tests is small compared with that in the LAVA-GAP-3 test. The small gap size may prevent the sufficient water ingression and steam venting through the gap in the LAVA-GAP-4 and LAVA-GAP-5 tests. Figure 3-43 shows the cross-sectional view of the core catcher and the vessel in the LAVA-GAP-4 test and the LAVA-GAP-5 test.

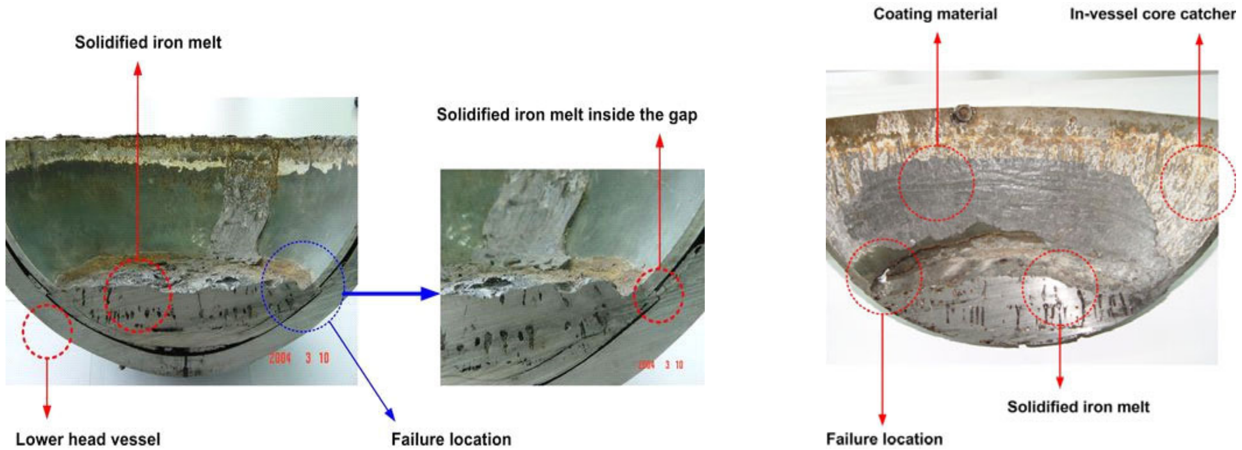

(a) LAVA-GAP-4 test

(b) LAVA-GAP-5 test

Figure 3-43. Cross-sectional view of test section from the LAVA-GAP-4 and LAVA-GAP-5 tests.

The IVCC failed and stuck to the lower head vessel in the LAVA-GAP-6 and the LAVA-GAP-7 tests. Figure 3-44 and 3-45 show the cross-sectional view of the core catcher in the LAVA-GAP-6 and the LAVA-GAP-7 tests, respectively. During the cutting of the core catcher, the bottom of the core catcher was separated from the upper part in the LAVA-GAP-6 test, which indicates that the core catcher at the interface between the iron melt and the alumina melt was extremely ablated due to the focused thermal load. Contrary to the LAVA-GAP-6 test, the bottom of the core catcher failed and the core catcher and the vessel stuck together in the LAVA-GAP-7 test. Actually, in the other LAVA-GAP tests which the IVCC was failed, the failure location was the interface between the iron melt and the alumina melt. Uniquely, the IVCC was failed at the bottom in the LAVA-GAP-7 test. The grid was installed at 200 mm upper position to prevent the jet impingement effect of the relocated melt in the LAVA-GAP experiments. In the LAVA-GAP-7, however, the grid didn't function very well and so the jet impingement effect couldn't be excluded perfectly. Jet impingement of relocated melt can severely affect the integrity of the core catcher. There are, however, some uncertainties in related with the initial jet impingement effect in the LAVA-GAP experiments. The precise evaluations on the effect of jet impingement should be required to settle down this problem.

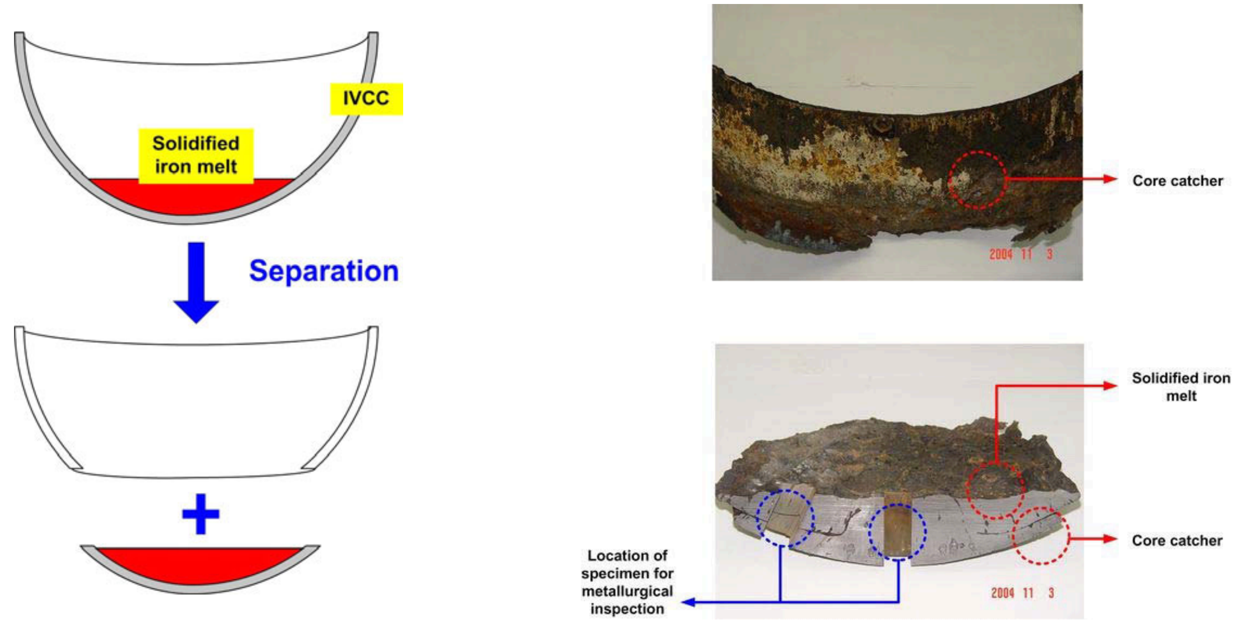

Figure 3-44. Cross-sectional view of the test section in the LAVA-GAP-6 test.

The gap size of the LAVA-GAP-6 test is same as the LAVA-GAP-3 test by 10 mm. In the LAVA-GAP-6 test, however, the core catcher was failed contrary to the LAVA-GAP-3 test. The primary differences between these two tests were material of bond coat and base steel. Even though the IVCC was intact in the LAVA-GAP-3 test, the IVCC experienced high thermal load to the extent that the microstructure of the base steel was changed considering the results of the metallurgical inspections. Therefore, minor change of the experimental conditions could bring about the failure of the IVCC in the LAVA-GAP-6 test. In the LAVA-GAP-6 test, the base stainless steel was melted and stuck to the upper iron melt. And the configuration of the interface between the base steel and the upper iron melt layer was totally changed as shown in Figure 3-44. The stainless steel having rather low melting temperature compared to the carbon steel, which could be attributed to the total melting of the internal coating layer and the base steel. Another factor inducing the failure of the IVCC in the LAVA-GAP-6 test could be the repeatability of the test process. Actually, in the LAVA-GAP-6 test, the mass of iron relocated to the bottom of the IVCC was larger than that of the LAVA-GAP-3 test. The superheated iron melt has a higher potential to ablate and melt the internal coating and base steel compared to the alumina melt.

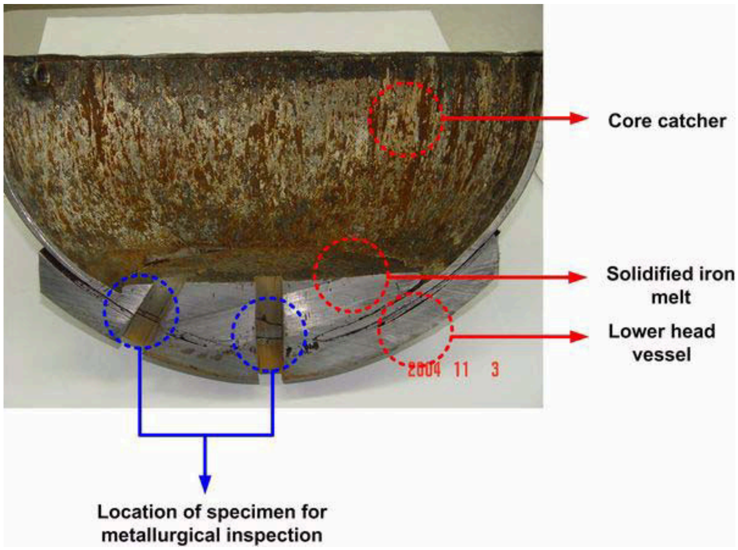

Figure 3-45. Cross-sectional view of the test section from the LAVA-GAP-7 test.

In the LAVA-GAP-7 test, the outer surface of the core catcher has a stainless steel coating to examine the enhancement of the heat removal via capillary effect of porous coating. In order to enhance the heat removal, the coating layer should be porous enough to enable water ingression at the outer surface of the core catcher. The LAVA-GAP-7 test, however, reached an unexpected result of core catcher failure. PSU performed boiling experiments to estimate the effects of surface coating on the enhancement of CHF in this K-INERI program. PSU experimental results address that Cu. or Al surface coating enhanced the CHF by 50 to 100% depending on the vessel angular positions compared with the plain vessel. In this study, the stainless coating layer at the outer surface of the core catcher was examined for the check of the coating performance and comparison of the coating configurations with the PSU test. Figure 3-46 shows a photograph of the stainless coating layer and Al coating layer in the LAVA-GAP-7 test and the PSU experiments, respectively.

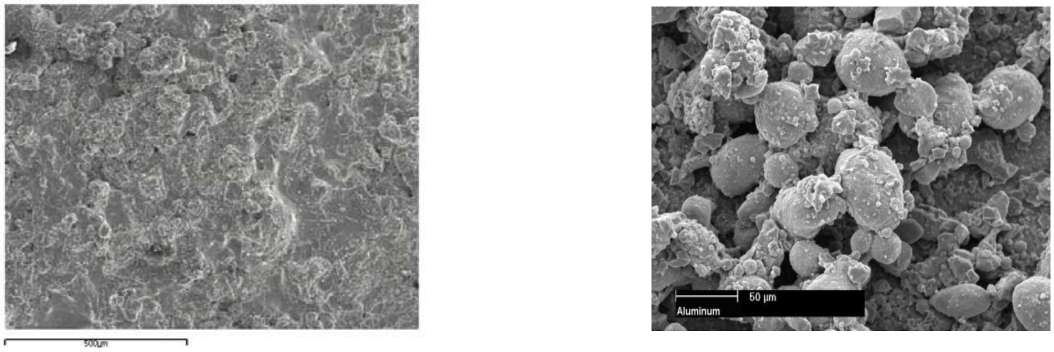

(a) LAVA-GAP-7 test

(b) PSU test

Figure 3-46. Photograph of the stainless and Al coating layer in LAVA-GAP-7 and PSU experiments.

In case of the PSU test, porous coating layer is clearly visible. On the other hand, at the most part, the porous coating layer could not be formed and the coating layer melted inherently during the coating process as shown in Figure 3-46, which could be attributed to the coating process of high temperature plasma coating in the LAVA-GAP-7 test. In the PSU test, the normal operation condition of the coating is around 100 ^{o}C at atmospheric pressure. The normal operation condition of the coating layer in the LAVA-GAP-7 test, however, is very severe and the operating temperature is above 300 ^{o}C. Therefore, different coating process was applied in both the tests. After all, these non-porous coating configurations could not enhance the heat removal and on the contrary might become a drag on heat transfer at the outer surface of the core catcher in the LAVA-GAP-7 test.

3.5.5. Thermal Analyses using LiLAC Code

Thermal analyses using LiLAC code were performed to precisely investigate the thermal response of the uncoated and the coated IVCC. LiLAC is a multi-dimensional thermo-hydraulic analysis code that uses Reynolds-averaged Navier-Stokes and energy equations as its governing equations. In the LiLAC code, turbulent flows are modeled by a two-equation turbulence model and the molten pool crust is modeled using an enthalpy-porosity method. Two-dimensional analyses on the molten pool behaviors and thermal responses of the IVCC were performed. The initial conditions such as melt mass, system pressure, and core catcher dimensions were assumed to be consistent with the current experimental conditions of the LAVA-GAP-2 and the LAVA-GAP-3 tests. Figure 3-47 is a schematic of the lower head vessel used for the LiLAC code analyses and the meshes for the molten pool and the IVCC.

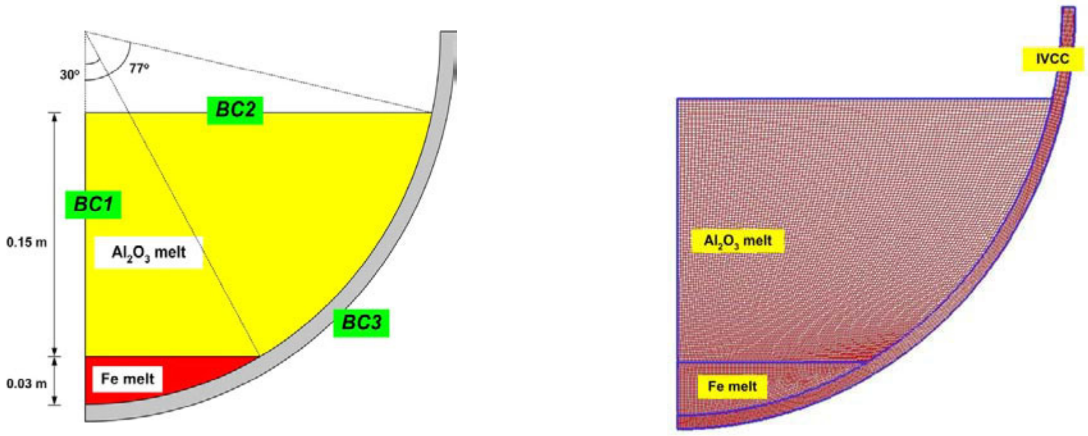

Figure 3-47. Schematic diagram of the LiLAC code analyses and the mesh.

The analytical results of the LiLAC code calculation for the uncoated IVCC suggest that active natural circulation flow inside the melt pool induced the concentration of the thermal load on the upper edge of the melt pool and finally the core catcher failed at that point. On the other hand, the melting front could not reach to the outer surface of the core catcher even on the upper part in the LAVA-GAP-3 calculation. Figure 3-48 demonstrates distribution of the temperature and the melt fraction of the molten pool and the core catcher at the computation time of 100 sec. For melt fractions shown in Figure 3-48 of the melt fraction, the index nearing 1.0 indicates the state of melting and the index nearing 0.0 indicates the state of solid. Figure 3-49 shows the temperature distributions of iron melt and core catcher at the calculation time of 100 sec in the LAVA-GAP-2 and the LAVA-GAP-3 calculations. Temperature variations of the core catcher were different according to the presence of the internal coating. The internal coating acted as a thermal barrier, and lower temperatures were predicted for the LAVA-GAP-3 calculation compared to those predicted for the LAVA-GAP-2 calculation. These LiLAC calculation results suggest that the coating layer lessened the thermal attack transferred to the core catcher, improving the integrity of the core catcher in the LAVA-GAP-3 test.[3-11]

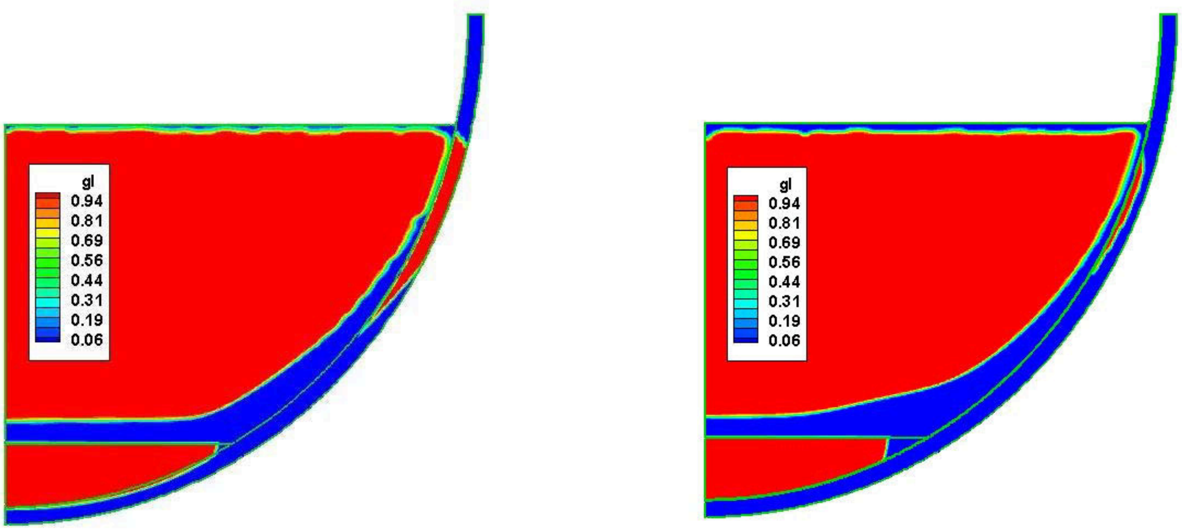

(a) LAVA-GAP-2 simulation (b) LAVA-GAP-3 simulation

Figure 3-48. Distribution of the melt fraction at the calculation time of 100 second.

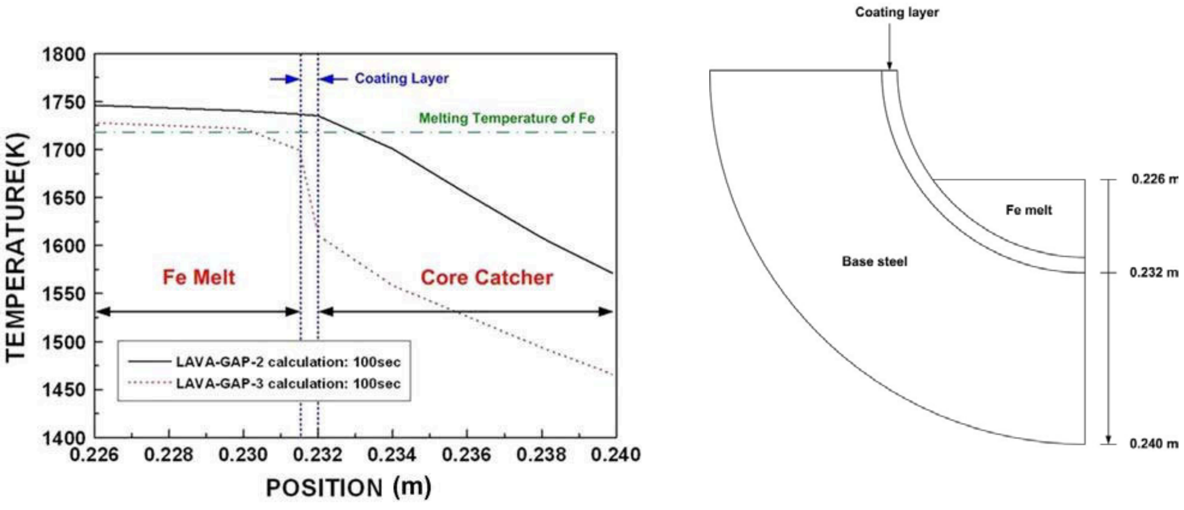

Figure 3-49. Temperature distributions of iron melt and core catcher at the bottom.

3.5.6. Metallurgical Inspections

Metallurgical inspections were carried out on the test specimens of the each test. The main objectives of the metallurgical inspections were to investigate the performance of the coating material and the base carbon steel. The crack and chemical compositions variation of the coating material were checked and the chemical compositions, oxidation, and interaction with coating layer of the base carbon steel were examined. The thermal histories of the base carbon steel were postulated pursuant to the crystal structures. Detailed photographs were taken using an optical microscope with a 10 to 200X magnification to precisely investigate the structures of the test specimen and to postulate the thermal histories of the base carbon steel. SEM (Scanning Electron Microscopy) analyses with EDX (Energy Dispersive X-ray) were performed to check on the chemical properties and oxidation of the test specimens. The test specimens were cut out of the solidified iron melt and the core catcher at the bottom.

Figure 3-50 shows a photograph taken by SEM with a 100X magnification for the specimen of the LAVA-GAP-3 test. According to the chemical analyses, in the coating material, additions of Al and Fe do not exist, which implies that chemical interactions of the coating material with the upper melt and the base carbon steel didn’t occur in the LAVA-GAP-3 test. The crack inside the coating material, however, was clearly visible in Figure 3-50, which could be attributed to the expansion and shrinkage during the heat up and cooling. Figure 3-51 and Figure 3-52 show the microstructure of the test specimen cut out of the upper region and bottom part of the IVCC, respectively. The white alpha-ferrite grains and the dark pearlite grains are visible and the working direction of the original steel (SS400) from the rolling process can be seen by the directionality of the ferrite. Compared with the test specimen from the upper part without melt contact, the microstructure is completely changed. There is no more evidence of the working direction and the white alpha-ferrite and dark pearlite grains are much larger and globular. These changes in the microstructures are caused by phase transformations during the heatup and cooldown and also by the grain growth at high temperatures. The grain growth and recrystallization of the microstructures indicate that the phase transformations of the test specimen were induced by a high temperature field of above 1000 ^{o}C. According to the metallurgical inspections for the LAVA-GAP-3 test specimen, the base carbon steel had experienced severe thermal attack to the extent that the microstructures were changed and re-crystallization occurred. The carbon steel showed stable and pure chemical compositions without any oxidation and interaction with the coating layer. In terms of material performance, these metallurgical inspection results suggest that the ZrO_2 coating has a quite good performance.[3-12]

Figure 3-53 shows the locations and specimen names of line-scanned EDX examinations for the LAVA-GAP-6 test. Figure 3-54 shows a photograph taken by SEM with 100 magnifications and the chemical compositions of the S-GAP-6-2 specimen in the LAVA-GAP-6 test. According to Figure 3-54, at the interface part of the base steel with the internal coating, Zr does not exist in the LAVA-GAP-6 test. This result implies that the coating layer might melt and disperse in the solidified iron melt and the base steel. As shown in Figure 3-53, the physical geometry of the coating layer was totally destroyed and melted and the base stainless steel was stuck to the upper iron melt layer. In the LAVA-GAP-6 test, the base steel was stainless steel having rather low melting temperature compared to the carbon steel and so it has less rigidity, which could be attributed to the total melting of the internal coating layer and the base steel.

3.5.7. Conclusions

The LAVA-GAP experiments were performed to investigate the performance of the IVCC by relocated molten material in severe accident. The major technical conclusions are as follows:

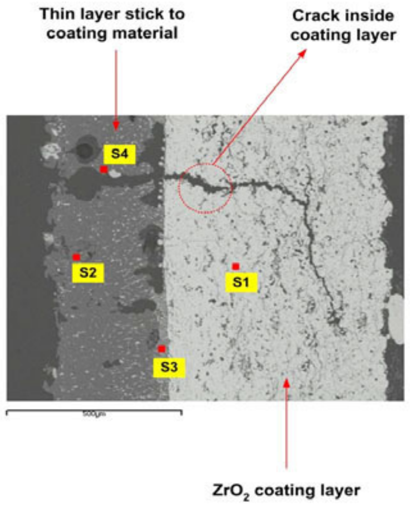

	O	Mg	Al	Si	Fe	Zr	Tot.
S1	63.95	-	-	-	-	36.05	100
S2	54.38	5.94	39.33	-	0.35	-	100
S3	57.38	7.39	32.00	-	-	3.23	100
S4	-	-	-	2.08	97.92	-	100

Figure 3-50. Photograph taken by SEM for the test specimen of the coating layer and the thin layer stuck to the coating material (100X magnification) in the LAVA-GAP-3 test.

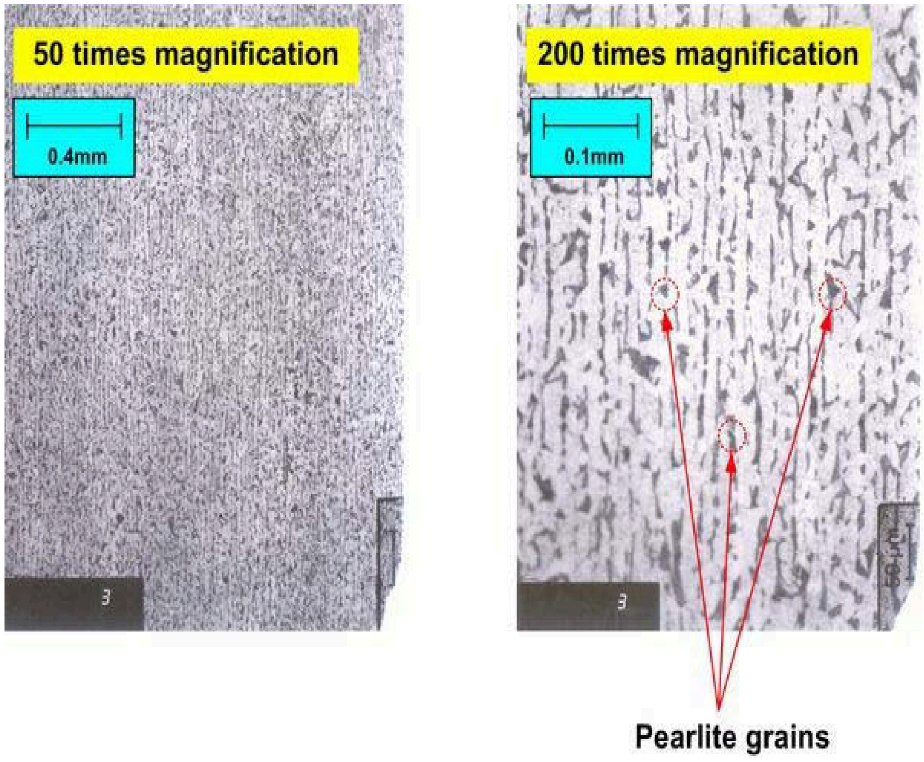

Figure 3-51. Photograph taken by optical microscope of the LAVA-GAP-3 test for the test specimen at the upper part where the melt was not directly filled.

- From the LAVA-GAP-2 and LAVA-GAP-3 test results it was found that the internally coated IVCC has better thermal performance compared with the uncoated IVCC.

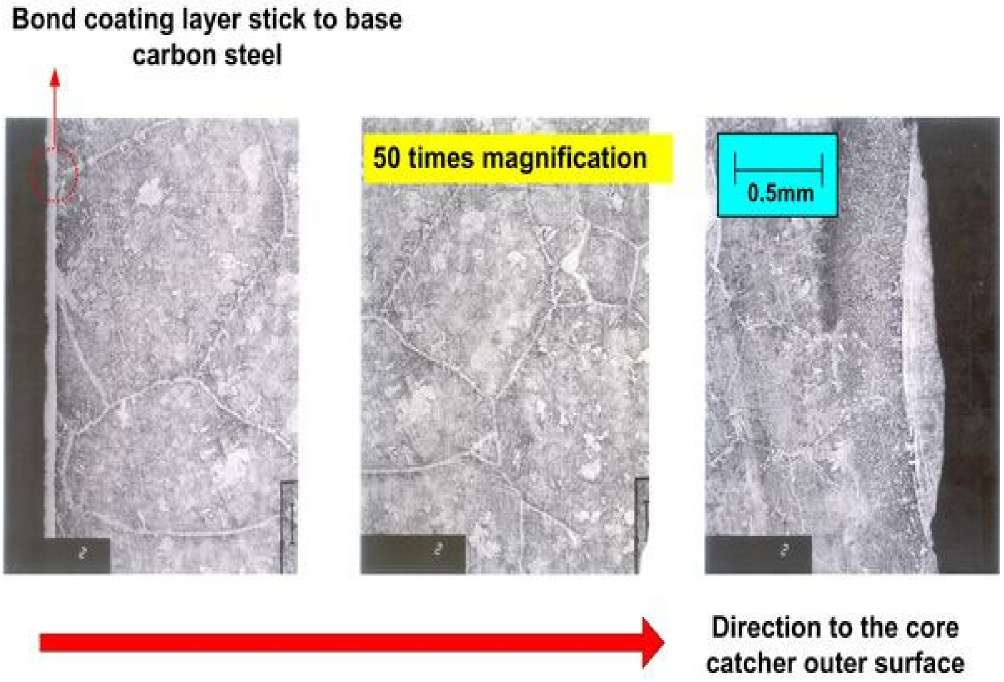

Figure 3-52. Photograph taken by optical microscope of the LAVA-GAP-3 test for the test specimen at the bottom part.

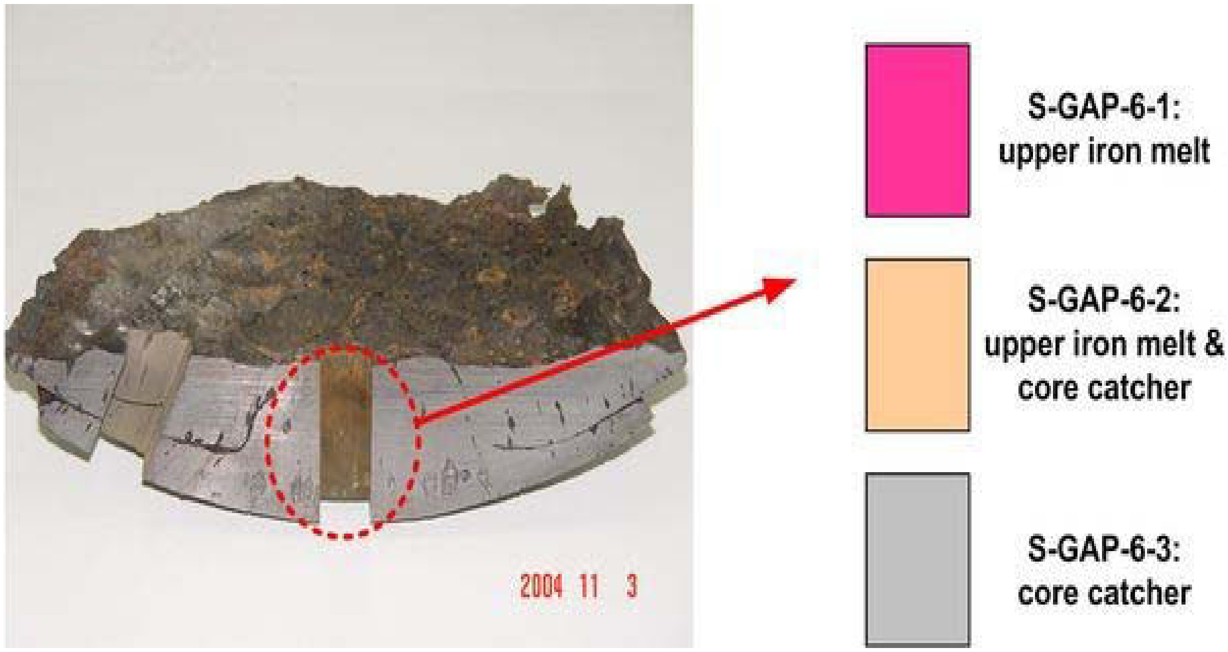

Figure 3-53. Locations and specimen names of line-scanned EDX examinations for the LAVA-GAP-6 test.

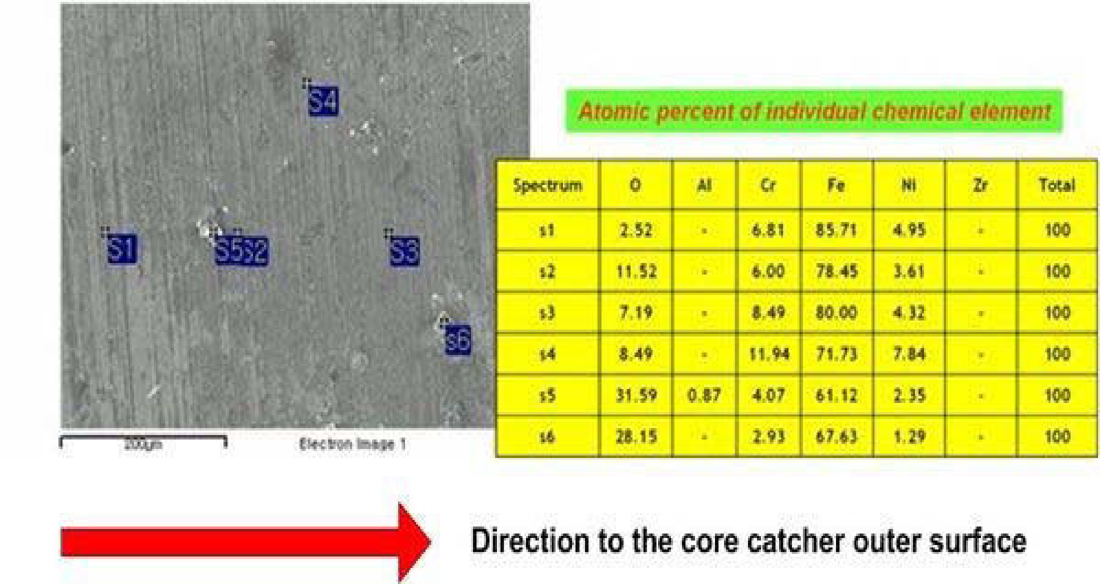

Atomic percent of individual chemical element

Spectrum	O	Al	Cr	Fe	Ni	Zr	Total
s1	2.52	-	6.81	85.71	4.95	-	100
s2	11.52	-	6.00	78.45	3.61	-	100
s3	7.19	-	8.49	80.00	4.32	-	100
s4	8.49	-	11.94	71.73	7.84	-	100
s5	31.59	0.87	4.07	61.12	2.35	-	100
s6	28.15	-	2.93	67.63	1.29	-	100

Figure 3-54. Photograph taken by SEM with 100X magnification and the chemical composition of the S-GAP-6-2 specimen from the LAVA-GAP-6 test.

- LiLAC calculation results suggest that the coating layer lessened the thermal attack transferred to the core catcher and resulted in improving the integrity of the core catcher in the LAVA-GAP-3 test.
- According to the metallurgical inspections for the LAVA-GAP-3 test specimen, the base carbon steel showed stable and pure chemical compositions without any oxidation and interaction with the internal coating layer. In terms of the material aspects, these metallurgical inspection results suggest that the ZrO_2 coating has quite a good performance.
- In the other tests, however, the core catchers were failed even though they were internally coated. The differences of the experimental conditions such as gap size and material of the base steel could be attributed to the failure of the IVCC. Also the conservative experimental conditions of non-existence of water inside the IVCC and uncertainties of repeatability in the test process could affect the thermal and mechanical performance of the IVCC.
- The thermal margin which could provide the sufficient cooling of the core catcher is quite limited in the LAVA-GAP experimental conditions. LAVA-GAP-4 and LAVA-GAP-5 test results imply that 5mm thick gap is rather small for sufficient water ingression and steam venting through the gap. In case of small gap size, water is boiled off and steam increases pressure inside the gap and so water can not ingress into the gap at the initial heat up stage.
- Additional improvement of the heat removal capacity inside the gap should be considered for the practical implementation of the current IVCC concept. The improvement of heat removal rate by applying the rather large gap size between the IVCC and the lower head vessel and the adoption of the IVCC with the outer surface for the enhancement of the heat removal via capillary effect of porous coating could be one of the most promising suggestions. However, the definite conclusions are pre-mature in our experiments and so further study should be performed related with these issues.

3.6. Prototypic Testing

The objective of the prototypic testing effort in this task was to evaluate if candidate core catcher materials do not interact with high-temperature materials expected to relocate during a severe accident. The designs for the test assembly and heater used for these prototypic tests are described below. Results from these protoypic tests are also summarized. More detailed information about these tests may be found in Reference 3-3.

3.6.1. Facility Design

Figure 3-55 illustrates the design of the test assembly, and Figure 3-56 shows the test assembly used for prototypic testing. These designs were developed so that they could easily interface with existing INEEL High Temperature Test Laboratory (HTTL) equipment. As shown in Figure 3-56, the crucible stands within a stainless steel enclosure ideally suited for high temperature testing with radioactive materials. Within the carbon steel crucible are placed high temperature, insulating materials, such as the RS-100 insulation board, the ZYFB-3 insulation board, and graphite. The simulated core catcher or "trough" is fabricated by machining out a curved region in a rectangular metal block. As discussed in Section 3.2, the simulated core catcher consisted of a stainless steel (SS 304) substrate material on which thermal plasma spraying techniques were used to apply a 100-200 μm bond coat of Inconel 718 beneath a 500 μm thick coating of zirconium dioxide.

For each test, approximately 1.3 kg of corium material was placed in the core catcher and heated using a resistance heater that is connected to an existing power supply at the HTTL. Tests were conducted using a corium material with a composition similar to that of material that relocated during the Three Mile Island Unit 2 (TMI-2) accident. Specifically, the corium was approximately 80% uranium dioxide and 20% zirconium dioxide.

3.6.2. Heater Design

Based on INEEL experience with developing and testing various types of heaters, a unique resistance heater design was developed for these tests. This resistance heater was composed of rhenium wires that were laser-welded together to obtain a varying diameter profile that increases away from the center. After the rhenium wires were laser-welded together, a 0.080 μm thick hafnia coating is applied via air plasma spraying. Molybdenum leads (0.64 cm diameter) were attached to each end of the resistance heater (via laser welding) after the hafnia coating was applied.

Resistance heater materials were selected based on their thermal and electrical properties.[3-46,3-47] Rhenium was selected for the electrode because of its high melting point (3450 K), its ductility, and its low electrical resistivity. Hafnia was selected because of its high electrical resistivity and its high melting point (3085 K). As shown in Figure 3-57, these two materials have similar coefficients of thermal expansion over a wide range of temperatures (which prevents the hafnia from cracking when the electrode reaches high temperatures). Less expensive molybdenum was selected for the leads because it has a relatively high melting temperature (2898 K) and because of its lower resistivity and cost (relative to rhenium).

Figure 3-58 compares the electrical resistivity of hafnia and rhenium. As shown in this figure, the electrical resistivity of hafnia drops exponentially with increasing temperature. At 3200 K, the electrical resistivity is only six orders of magnitude greater than the resistivity of the rhenium electrode. This small

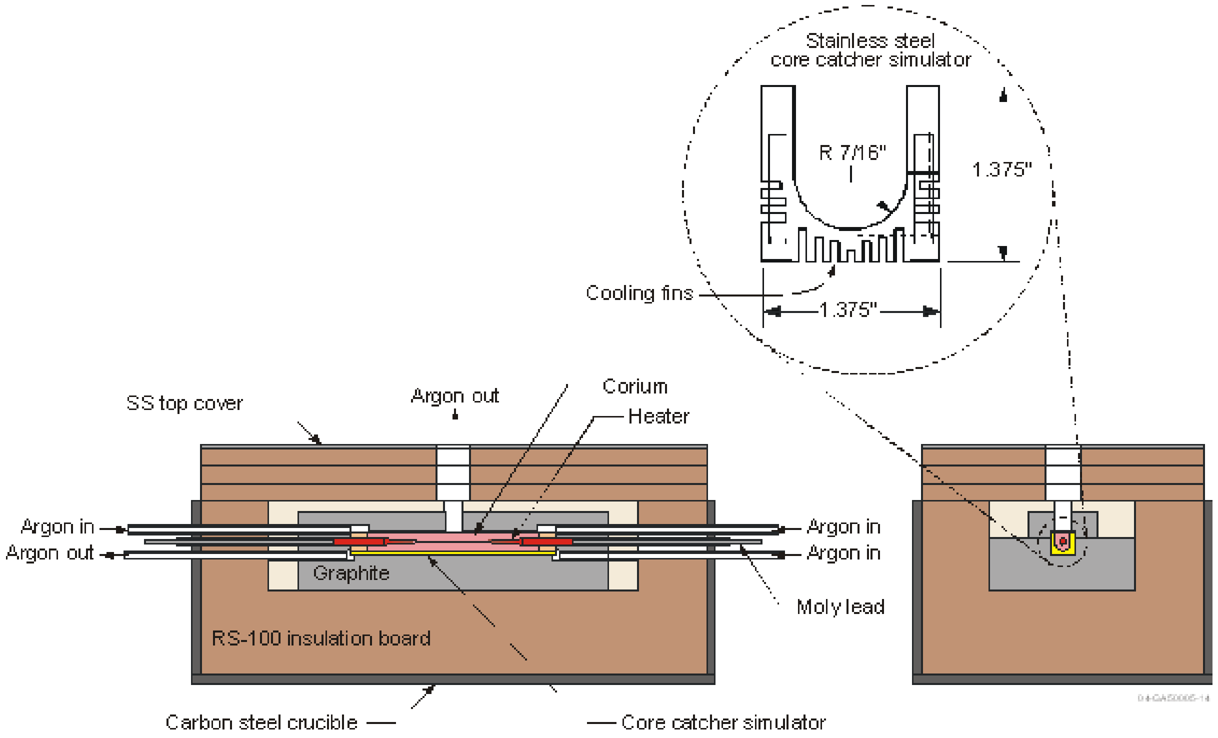

Figure 3-55. Assembly for prototypic testing.

difference in electrical resistivity between the hafnia insulator and the rhenium electrode allows current to flow through the hafnia as well as the rhenium. The net result is a reduction in the total resistance of the heater and the development of a non-uniform axial voltage gradient in the electrode. The joule-heating rate in the electrode is then no longer uniform, resulting in large axial temperature gradients in the rhenium electrode. To overcome this difficulty, a combined electrical / thermal analysis was performed to iteratively develop an electrode shape that produces a near-constant axial temperature profile at a power level and at temperatures sufficient to melt the corium. Using corium thermal properties,[3-15] calculations predict that approximately 1.5×10^6 J of heat are required to melt the entire 1.3 kg of corium contained in a perfectly insulated core catcher (this mass neglects any corium displacement by the resistance heater). Although it is recognized that additional heat must be delivered to the test facility to compensate for heat losses to the surrounding test assembly structures, this amount of heat provides a lower bound for the amount of heat that must be produced by the resistance heater for these tests.

Prior to conducting any tests with prototypic materials, the design and operation of the heater and test assembly were optimized with a series of heater verification tests and system checkout tests. These preliminary tests provided insights for improving the performance and reliability of the heater and test assembly.

3.6.3. Test Results

In this K-INERI, two tests with prototypic materials were completed. The procedure followed for each test was similar. In both tests, the power to the heater was increased by increases in current (rather than voltage). For these tests, the range in current was an order of magnitude higher than the range in voltage.

Figure 3-56. Carbon steel crucible in stainless steel enclosure.

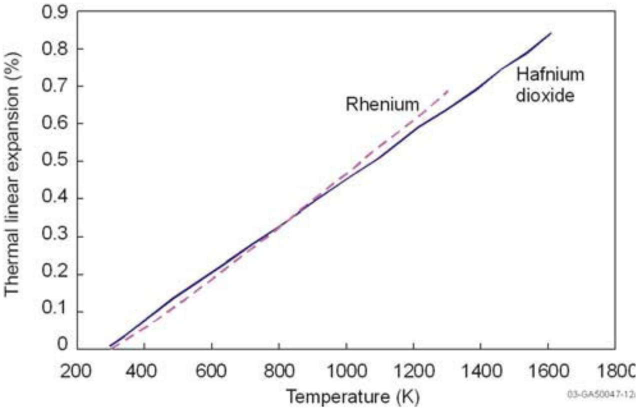

Figure 3-57. Thermal coefficients of expansion for hafnia and rhenium.

Hence, the larger span in current allowed the test to be controlled more precisely when it was incremented by increases in current. The primary difference between the two tests was the atmosphere. The P-1 test used argon to cool the exterior surface of the trough and the interior regions of the corium filled trough. The P-2 test used argon to cool exterior surfaces of the trough and interior regions of the corium-filled trough during the initial and final stages of the test, but injected steam into interior regions of the corium-filled trough during the heatup phase of the test.

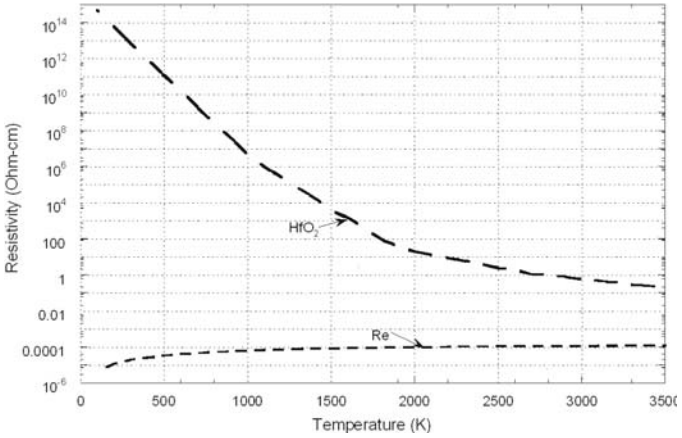

Figure 3-58. Electrical resistivity of hafnia compared to rhenium as a function of temperature.

Highlights from each test and post-test examinations are summarized below.

- *Corium was completely molten during testing.* In both cases, the energy produced by the resistance heater was sufficient to melt the corium within the trough. In both tests, over 3 MJ of energy was delivered to the corium. Data from the P-1 and P-2 tests suggest that direct electrical heating may have also occurred at later times during these tests after the heaters failed. In both tests, abrupt changes in the heater resistance caused the heater power to rapidly increase and remain at a higher level for a limited time period, and then abruptly decrease (e.g., see P-1 power and energy profile in Figure 3-59). It is speculated that the abrupt increase in power (corresponding to an abrupt increase in heater resistance) corresponds to a time when arcing or direct electrical heating occurred in the corium.

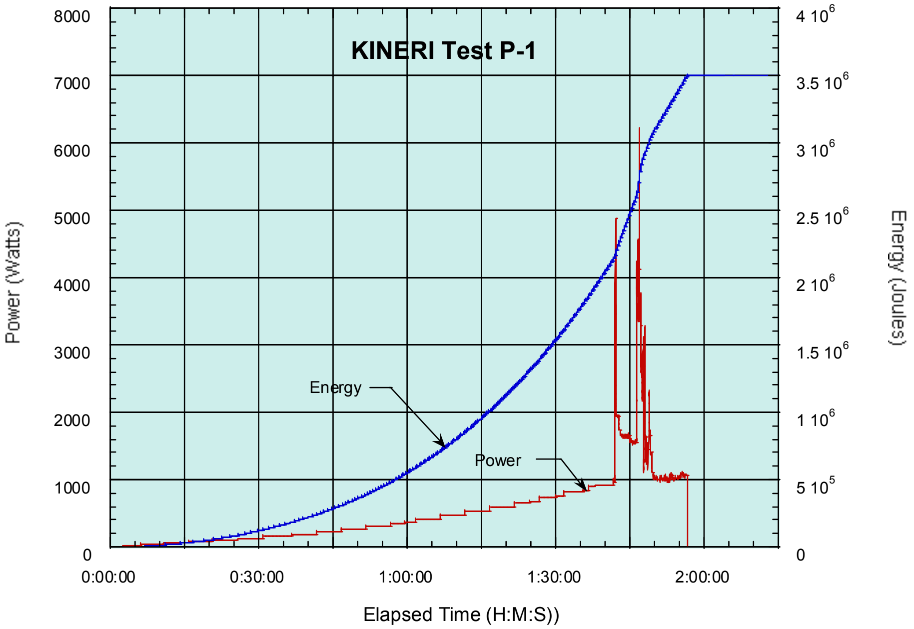

Figure 3-59. Power and energy produced by P-1 heater.

- *No materials interactions occurred between corium and core catcher coating materials.* Scanning Electron Microscope (SEM) exams (in the P-1 test) and visual exams from mechanically removing previously molten corium material (in the P-2 test) indicate that the core catcher oxide coatings continued to protect the substrate material during testing. As indicated in Figure 3-60, SEM examinations of sections from the P-1 trough suggest that no materials interactions occurred between the SS substrate (as indicated by the presence of iron and nickel), the Inconel 718 bond coating (as indicated by the presence of nickel and niobium), and the oxide thermal spray coating (as indicated by the presence of zirconium).

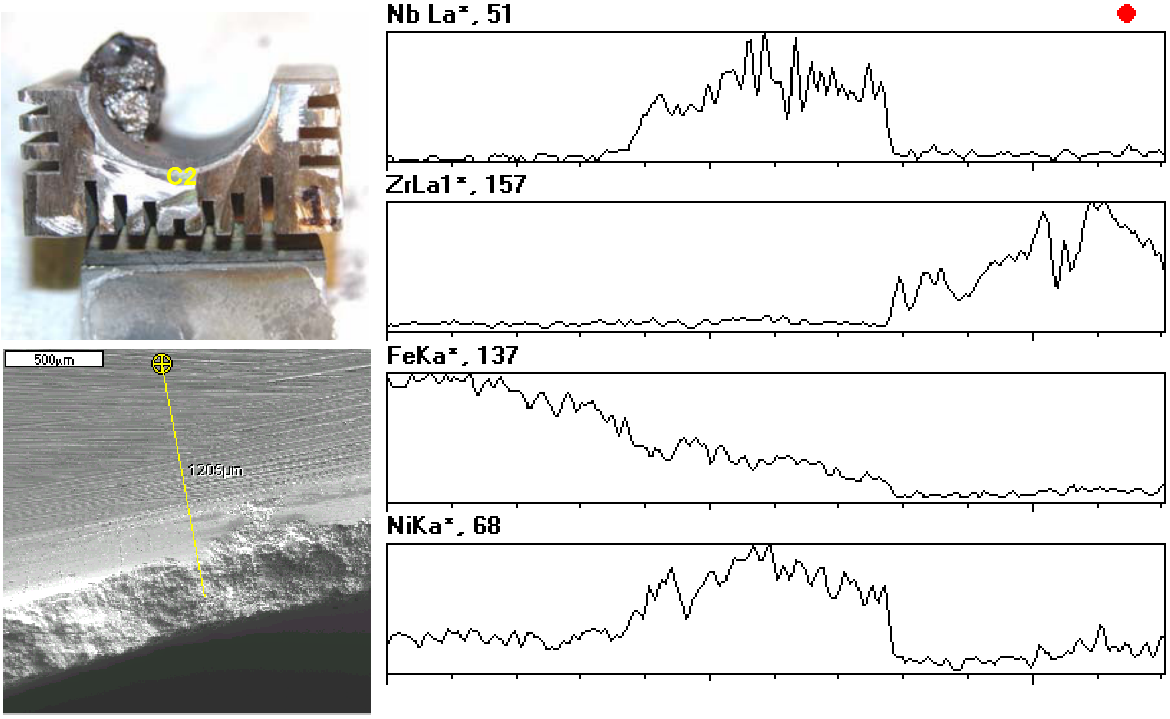

Figure 3-60. Macro photograph with qualitative SEM analysis starting at location C2 (coating surface toward the substrate) on section from P-1 trough.

- *Corium was contained within the simulated core catcher trough.* Although localized failures of the simulated core catcher trough coatings and damage to the trough substrate material was observed in both tests, no corium materials were released from the trough during testing. In particular, the trough subjected to steam injection in the P-2 test experienced localized failures due to attack by molten corium materials (see Figure 3-61). However, post-test examinations revealed that no molten corium materials relocated from the trough to the underlying graphite insert.

In summary, results from prototypic tests indicate that the proposed core catcher materials and coatings would provide additional protection to the reactor vessel from materials that relocate from the reactor core during a severe accident. Tests indicate that the proposed coating materials protect the core catcher substrate without any interactions with prototypic corium materials. However, it should be noted that these tests are only part of a preliminary core catcher design and evaluation effort. More detailed studies and testing are needed before a core catcher could be implemented into a reactor design. In particular, tests are needed to confirm the long-term endurance of the proposed materials to hydrodynamic loads during operating and accident conditions. In addition, confirmatory tests of irradiation and coolant chemistry effects on coating performance may be warranted.

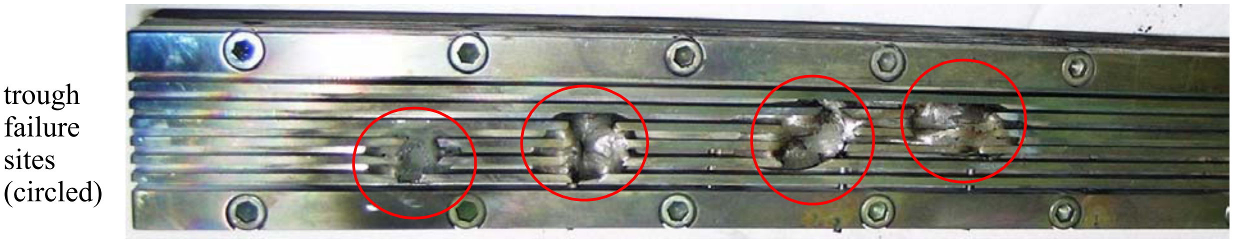

(a) bottom view of trough with easily separated corium removed

(b) side view of trough with easily separated corium removed

(c) corium-filled trough after removing all easily separated corium

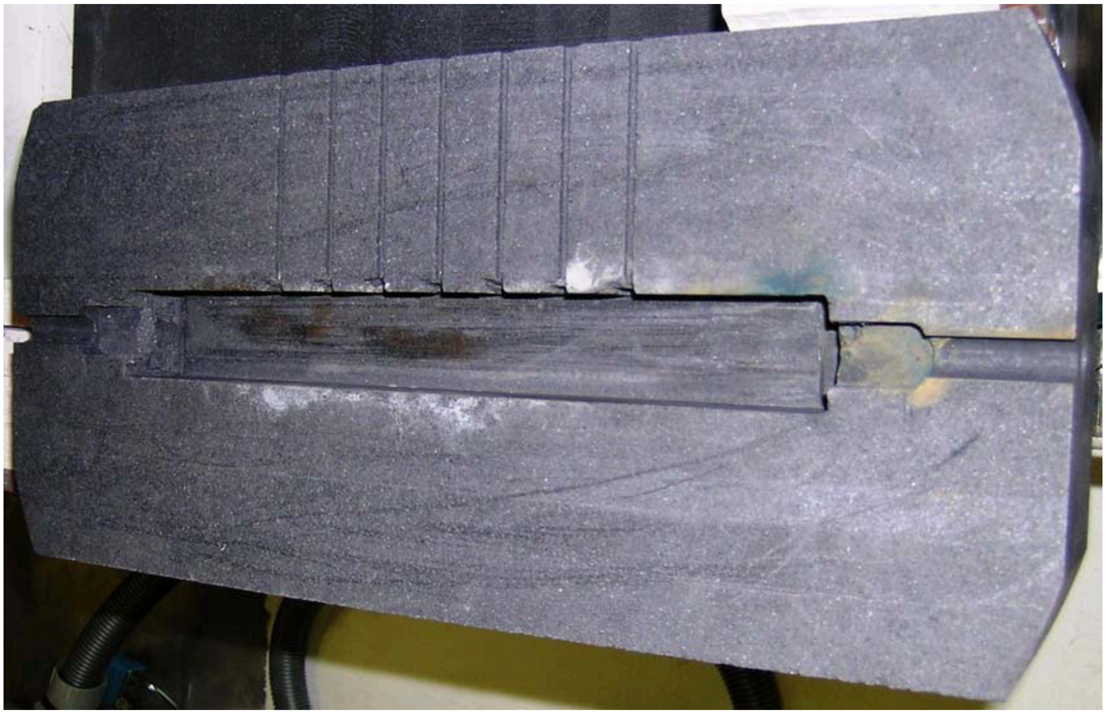

(d) graphite insert after removal of the P-2 trough

Figure 3-61. P-2 trough and graphite insert.

3.7. Summary and Conclusions

The objective of Task 2 is to develop a core catcher design for the APR1400 and provide sufficient data to evaluate if this core catcher design will enhance in-vessel debris coolability in the reactor. As discussed in Section 3.1, initial efforts focused on developing a preliminary in-vessel design. This was done at INEEL using a combination of scoping materials, flow, thermal, and structural analyses and scoping materials interaction tests. In addition, more detailed experimental data were obtained in two areas to support analysis of this IVCC. First, data were obtained from the SNU GAMMA facilities to estimate the heat that can be removed from the narrow "engineered" gap between the IVCC and the inner surface of the reactor vessel lower head. Second, data were obtained to understand the heat loads to the core catcher and demonstrate the viability of materials proposed for the IVCC. In particular, tests were conducted at the SNU SIGMA facilities to develop natural convection heat transfer correlations, the KAERI LAVA-GAP facility to assess the impact of a core catcher on thermal heat loads to a reactor vessel, and the INEEL HTTL to assess the potential for materials interactions. Key conclusions and insights resulting from this effort are summarized below.

A conceptual IVCC design for the APR1400 was completed. The core catcher design proposed in this INERI consists of several interlocking sections that are machined to fit together when inserted into the lower head. The use of interconnected sections of the core catcher reduces manufacturing costs and simplifies installation. Each section of the core catcher consists of two material layers with an option to add a third layer (if deemed necessary): a base material, which has the capability to support and contain the mass of core materials that may relocate during a severe accident; an oxide coating material on top of the base material, which resists interactions with high-temperature core materials; and an optional coating on the bottom side of the base material to prevent any potential oxidation of the base material during the lifetime of the reactor.

Results from scoping thermal and structural analyses suggest that an IVCC is feasible and could offer significant protection to the vessel during a severe accident. Analyses results provide insights about the thickness and type of material that should be selected for each layer of the IVCC. In addition, analyses suggest that the proposed IVCC will have negligible impact on coolant flow within the vessel during normal operating conditions.

Scoping analyses and materials testing suggest that the core catcher base material should be either carbon steel or a stainless steel, such as SS 304. However, the use of stainless steel is recommended because it would preclude the need for a corrosion-resistant undercoating on the IVCC. Evaluation efforts suggest that the insulator coating should be applied using thermal plasma spray techniques. Although several coatings appear viable, results suggest that the insulator coating should consist of a 500 μm thick ZrO_2 coating over a 100-200 μm thick bond coating of Inconel 718.

Prototypic tests in the INEEL HTTL indicate that the proposed core catcher materials and coatings would provide additional protection to the reactor vessel from materials that relocate from the reactor core during a severe accident. Tests conducted in inert and steam conditions indicate that the proposed coating materials protect the core catcher substrate without any interactions with prototypic corium materials.

Key insights about predicting the heat losses from a narrow gap between the IVCC and the reactor vessel lower head that were obtained from GAMMA tests include:

- The gap size and surface orientation effects play an important role in interpreting the general two-phase flow behavior as well as the CHF data. There exists a critical gap size commensurate to the average vapor layer thickness that enhances the heat transfer rate with increasing mass flux at certain surface orientations.
- The CHF generally increases as the gap size increases, but the increasing rate decreases as the gap increases. In particular, the CHF in the 10 mm gap is smaller than the value at any other gap sizes at the fully downward-facing location, 180^o. At the vertical location, 90^o, as is generally believed, the CHF increases as the gap size increases. The CHF in gap boiling is affected by the gap size as well as by the induced flow within the channel.
- There is a transition angle for each gap size. The transition angle increases as the gap size increases in this study. The transition angles for the 2, 5 and 10 mm gaps in this study were found to be 165^o, 170^o and 175^o, respectively. However, the transition angle was not discernible for the gap size of 1 mm and the pool boiling in the unconfined space.
- A semi-empirical CHF correlation was developed for the near-vertical gap boiling using dimensional analysis of the CHF during natural convective boiling in confined channels because the existing correlation could not reasonably predict the data obtained in this study. This correlation agrees with the experimental data within ± 20%.

Key insights about the heat load from relocated corium to the IVCC that were obtained from SIGMA tests include:

- The average Nu_{up} numbers obtained from SIGMA tests concur with most of the literature data. The average Nu_{dn} numbers obtained from SIGMA tests fall between data obtained from the literature.
- The ratio of the local to average Nu on the upper wall was unity at all locations. The heat flux profile along the lower wall and average upward heat transfer within this Ra′ range were in good agreement with the data obtained from previous numerical and experimental studies. The heat input increase results in an increase in Nu_{up} and Nu_{dn}, but with no change in the heat split ratio (Nu_{up}/Nu_{dn}) which was about 1.7, except for the case where $Ra' = 2.94\times10^{12}$ and $Nu_{up}/Nu_{dn} = 2.1$. The lowest heat transfer occurred at the bottom of the pool, which was a stagnation point, while the highest value was observed in the upper corner of the pool.
- When the top surface of the pool was insulated, the local heat flux was greater than in the uninsulated case by about 6%. In case of the adiabatic upper boundary condition, the internal heat transported by the strong buoyancy-induced flows was transferred sideward rather than upward in the upper region.

Simulant melt experiments in the LAVA-GAP facility were performed to investigate the thermal and metallurgical performance of the IVCC. The main objectives of the LAVA-GAP experiments were to examine the feasibility and sustainability of the IVCC under the various test conditions using hemispherical test sections and simulant melt compared to the prototypic situations. The uniqueness of the LAVA-GAP experiments is the adoption of internally coated hemispherical IVCC in direct contact with the high temperature of simulant melt, which could provide the raw data on the thermal and metallurgical performance of the internally coated IVCC under the severe and various test conditions. The major technical conclusions from the these simulant tests and associated LiLAC calculations include:

- In several tests (LAVA-GAP-2 and LAVA-GAP-3), the internally coated IVCC has better thermal performance compared with the uncoated IVCC.

- LiLAC calculation results suggest that the coating layer lessened the thermal attack transferred to the core catcher and improved the integrity of the core catcher for LAVA-GAP-3 test conditions.
- Metallurgical inspections for the LAVA-GAP-3 test specimen indicate that the base carbon steel showed stable and pure chemical compositions without any oxidation and interaction with the internal coating layer. Hence, these metallurgical inspection results suggest that the ZrO_2 coating protected the carbon steel base material.
- In other tests, internally coated core catchers experienced failures. These failures were attributed to differences in experimental conditions, such as gap size and material of the base steel. For example, the 5 mm thick gap in the LAVA-GAP-4 and LAVA-GAP-5 tests imply that this gap size is too narrow to allow sufficient water ingression and steam venting. It should also be noted that the LAVA-GAP test conditions were conservative in that there was no water present inside the IVCC (as expected to be present during a severe accident in an LWR).
- LAVA-GAP tests suggest that the IVCC heat removal capability be enhanced by increasing the gap size between the IVCC and the vessel lower head (the gap size should be larger than 5 mm) and that the outer surface of the IVCC be coated with a microporous coating to enhance heat transfer from the IVCC.

In summary, the IVCC evaluations completed in this INERI suggest that the proposed concept is viable and will reduce heat loads to the vessel for a range of severe accident conditions. Key data obtained in this INERI allow more detailed evaluations of the IVCC to be completed. However, it should be noted that only preliminary core catcher design and evaluations were completed in this INERI project. More detailed analyses and testing are needed before a core catcher could be implemented into a reactor design. In particular, tests are needed to confirm the long-term endurance of the proposed materials to hydrodynamic loads during operating and accident conditions. In addition, confirmatory tests of irradiation and coolant chemistry effects on coating performance may be warranted.

3.8. References

3-1. Rempe, J. L., et al., *In-Vessel Retention Strategy for High Power Reactors, 2002 Annual Report,* INEEL/EXT-02-01291, October 2002.

3-2. J. L. Rempe, et al., Core Catcher Materials Selection and Fabrication, INEEL/EXT-03-00377, March 2004.

3-3. J. L. Rempe, et al., Prototypic Testing of Core Catcher Materials, INEEL/EXT-03-00378, September 2003.

3-4. J. L. Rempe, et al., "Conceptual Design of An In-vessel Core Catcher," *Nuclear Engineering and Design, Invited paper for ICONE11 Special Edition,* **230** (2004) 311-235.

3-5. J. L. Rempe, et al., "Materials Interaction Tests to Identify Base and Coating Materials for an Enhanced In-Vessel Core Catcher Design," *Twelfth International Conference on Nuclear Engineering (ICONE12)*, Washington, DC, April 2004.

3-6. J. L. Rempe, et al., Development of an Enhanced Core Catcher for Improving In-vessel Retention Margins, *Nuclear Technology, Invited paper for NURETH10 Special Edition.*

3-7. K. H. Kang, R. J. Park, and S. B. Kim, "Experiments on Enhancement of In-Vessel Corium Retention through In-Vessel Core Catcher; Experimental Results of the LAVA-GAP-2 & 3 Tests", KAERI/GP-221/2004.

3-8. K. H. Kang, S. B. Kim, "Improvement of In-Vessel Corium Retention through Internal and External Cooling using In-Vessel Core Catcher", KAERI/GP-227/2004.

3-9. K. H. Kang et. al., "Thermal and Metallurgical Performance of the Multi-layered In-Vessel Core Catcher during Severe Accidents", *The 6th International Conference on Nuclear Thermal Hydraulics, Operations and Safety (NUTHOS-6)*, Nara, Japan, October 4-8, 2004.

3-10. K. H. Kang, R. J. Park, and S. B. Kim, "Experiments on Enhancement of In-Vessel Corium Retention through In-Vessel Core Catcher; Experimental Results of the LAVA-GAP-6 & 7 Tests", KAERI/GP-228/2004.

3-11. K. H. Kang et. al., "Experiments on Enhancement of In-Vessel Corium Retention through In-Vessel Core Catcher", *The 10th International Topical Meeting on Nuclear Reactor Thermal Hydraulics (NURETH-10)*, Seoul, Korea, October 5-9, 2003.

3-12. K. H. Kang et. al., "Experiments on the Performance of a Multi-layered In-Vessel Core Catcher", 12th International Conference on Nuclear Engineering (ICONE 12), Arlington, Virginia, USA, April 25-29, 2004.

3-13. Hwang, I.S., and Suh, K.Y., "Gap Structure for Nuclear Reactor Vessel," United States Patent US 6,195,405 B1, Registered February 2001.

3-14. J. L. Rempe, et al., *Light Water Reactor Lower Head Failure Analysis*, NUREG/CR-5642, Idaho National Engineering and Environmental Laboratory, October 1993.

3-15. INEEL SCDAP/RELAP5-3D© Development Team, *SCDAP/RELAP5-3D© Code Manuals,* INEEL/EXT-02/00589, Idaho National Engineering and Environmental Laboratory, May 20, 2002.

3-16. Y. S. Touloukian, Editor, Thermophysical Properties of High Temperature Solid Materials, Volume 4: Oxides and their Solutions and Mixtures, Part I: Simple Oxygen Compounds and Their Mixtures, MacMillan Company, New York, 1967.

3-17. A. A. Winkelmann AND O. Schott, "Dependence of Thermal Resistance Coefficients of Glasses on their Chemical Composition," Ann. Physik Chem. 51, 730-745, 1894.

3-18. E. M. Levin, et al., Phase Diagrams for Ceramists, Volume I, The American Ceramic Society, Inc., Columbus, Ohio, Fifth Printing, 1985.

3-19. Wright, R.N and W. D. Swank, "Microstructure Effects on Stainless Steel Substrates from Deposition of Plasma Spray Coatings," *Thermal Spray; Surface Engineering via Applied Research*, C. C. Berndt, ed., ASM International, Materials Park, OH, pp. 9-14.3.

3-20. Y. S. Touloukian, et al., Thermal Expansion, Metallic Elements and Alloys, Thermophysical Properties of Matter, Volume 12, Plenum Publishing Company, New York, 2nd Printing, 1977.

3-21. Y. S. Touloukian, et al., Thermal Conductivity, Metallic Elements and Alloys, Thermophysical Properties of Matter, Volume 1, Plenum Publishing Company, New York, 2nd Printing, 1977.

3-22. ASM, Binary Alloy Phase Diagrams, Second Edition, Plus Updates, Version 1.0, 1996.

3-23. Y. S. Touloukian, et al., Thermophysical Properties of Matter, Volume 12, Thermal Expansion Metallic Elements and Alloys, IFI Plenum Publishing, New York, 1978.

3-24. D. Knudson, J. Rempe, K. Condie, K. Y. Suh, F. B. Cheung, and S. B. Kim, "Late-phase Melt Conditions affecting the Potential for In-Vessel Retention in High Power Reactors," *Nuclear Engineering and Design, Invited paper for ICONE11 Special Edition*, **230** (2004) 133-150.

3-25. M. Monde, H.Kusada, and H. Uehara, "Critical heat flux during natural convective boiling in vertical rectangular channels submerged in saturated liquid," *ASME Journal of Heat Transfer*, **Vol. 104,** pp. 300-303., 1982.

3-26. C. Xia, W, Hu. and Z. Guo, Z., "Natural convective boiling in vertical rectangular narrow channels," *Experimental Thermal and Fluid Science*, **Vol. 12,** pp. 313-324, 1996.

3-27. A. H. Howard, and I. Mudawar, "Orientation effects on pool boiling critical heat flux (CHF) and modeling of CHF for near-vertical surfaces," *International Journal of Heat and Mass Transfer,* **Vol. 42**, pp. 1665-1688, 1999.

3-28. S. H. Yang, W. P. Baek, and S. H. Chang, "Pool-boiling critical heat flux of water on small plates: Effects of surface orientation and size," *International Communications in Heat and Mass Transfer,* **Vol. 24**, pp. 1093-1102, 1997.

3-29. M. S. El-Genk, and Z. Guo, "Transient boiling from inclined and downward-facing surfaces in a saturated pool," *International Journal of Refrigeration,* **Vol. 6,** pp. 424-432, 1993.

3-30. J. Y. Chang, and S. M. You, "Heater orientation effects on pool boiling of micro-porous-enhanced surfaces in saturated FC-72," *ASME Journal of Heat Transfer,* **Vol. 118**, pp. 937-943, 1996.

3-31. Katto, Y. “Generalized correlation for critical heat flux of natural convective boiling in confined channels,” *Trans. JSME (in Japanese),* **Vol. 44**, pp. 3908-3911, 1978.

3-32. S. S. Kutateladze, “Heat transfer in condensation and boiling,” AEC-TR-3770, 1952.

3-33. J. H. Lienhard, V. K., Dhir, and D. M. Riherd, “Peak Pool Boiling Heat Flux Measurements on Finite Horizontal Flat Plates,” *Transaction of ASME, Journal of Heat Transfer,* pp. 477-482., 1973.

3-34. Fujita, Y., H. Ohta, and S. Uchida, “Nucleate Boiling Heat Transfer and Critical Heat Flux in Narrow Space between Rectangular Surfaces,” *International Journal of Heat and Mass Transfer,* **Vol. 31**, pp. 229~239, 1988.

3-35. S. H. Kim, W. P. Baek, and S. H. Chang, “Measurements of critical heat flux for narrow annuli submerged in saturated water,” *Nuclear Engineering and Design*, **Vol. 199**, pp. 41-48, 2000.

3-36. J. Zhang, F. Tanaka, M. Juarsa, and K. Mishima, “Calculation of Boiling Curves During Rewetting of a Hot Vertical Narrow Channel,” Proceedings of the 10th International Topical Meeting on Nuclear Reactor Thermal Hydraulics, Seoul, Korea, October 5-9, 2003.

3-37. Y. Okano, T., Kohriyama, Y. Yoshida, and M. Murase, “Modeling of Debris Cooling with Annular Gap in the Lower RPV and Verification Based on ALPHA Experiments,” *Nuclear Engineering and Design,* **Vol. 223**, pp. 145-158, 2003.

3-38. M. Murase, T. Kohriyama, Y. Kawabe, T. Yoshida, and Y. Okano, “Heat Transfer Models in Narrow Gap,” *Proceedings of the 9th International Conference on Nuclear Engineering,* Nice, France, April 8-12, 2001.

3-39. R. J. Park, K. S. Ha, S. B. Kim, and H. D. Kim, “Experimental Study on Critical Power in a Hemispherical Narrow Gap,” *Nuclear Technology,* **Vol. 140,** No. 3, pp. 266-278, 2002.

3-40. T. N. Dinh, R. R. Nourgaliev, and B. R., Sehgal, B. R., “On heat transfer characteristics of real and simulant melt pool experiments,” *Nuclear Engineering and Design,* **Vol. 169**, pp. 151-164, 1997.

3-41. G. Kolb, S. A. Theerthan, and Sehgal, B. R. “Experiments on in-vessel melt pool formation and convection with $NaNO_3$-KNO_3 salt mixture as melt simulant,” *Proceedings of the 8th International Conference on Nuclear Engineering,* paper ICONE-8639, Baltimore, MD, USA, April 2-6, 2000.

3-42. S. D. Lee and K. Y. Suh, “Natural convection heat transfer in two-dimensional semicircular slice pool,” *Journal of Nuclear Science and Technology,* **Vol. 40,** No. 10, pp. 775-782, 2003.

3-43. F. Mayinger, M. Jahn, H. H. Reineke, and V. Steinberner, “Examination of thermohydraulic processes and heat transfer in a core melt,” BMFT RS 48/1, Institut für Verfahrenstechnik der TU, Hanover, Germany, 1976.

3-44. K. M. Kelkar, R. C. Schmidt, and S. V. Patankar, “Numerical analysis of laminar natural convection of an internally heated fluid in a hemispherical cavity,” *ANS Proceedings of Natural Heat Transfer Conference*, **Vol. 6**, pp. 355-364, 1992.

3-45. O. Kymäläinen, H. Tuomisto, O. Hongisto, and T. G. Theofanous, “Heat flux distribution from a volumetrically heated pool with high Rayleigh number,” *Nuclear Engineering and Design,* **Vol. 149,** pp. 401-408, 1994.

3-46. Y. S. Touloukian, editor, *Thermophysical Properties of High Temperature Solid Materials, Volume 4: Solid Materials*, The Macmillan Company, New York, 1967.

3-47. Y. S. Touloukian, editor, *Thermophysical Properties of High Temperature Solid Materials, Volume 1: Elements,* The Macmillan Company, New York, 1965.

4. TASK 3: EXTERNAL REACTOR VESSEL COOLING ENHANCEMENT

4.1. Objective and Overview of Task 3

In Task 3, the CHF phenomena on the outer surface of a simulated APR1400 reactor vessel was studied experimentally. The goal was to select an enhanced vessel/insulation design and a suitable vessel coating for CHF enhancement so as to substantially increase the thermal margin for IVR. Toward this end, ERVC tests were conducted using prototypic water (i.e., non-ionized tap water as expected for a flooded cavity) to evaluate the performance of various coating materials and to select a suitable bottleneck configuration at the minimum gap location for the enhanced vessel/insulation design. The vessel coating should promote downward facing boiling on the vessel outer surface and a suitable bottleneck configuration should facilitate steam venting through the annular channel between the vessel and the insulation structure, both of which should lead to considerable CHF enhancement.

The major objectives of Task 3 were:

- To design and fabricate a scaled test vessel and an enhanced thermal insulation structure to simulate external reactor vessel cooling of APR1400 under severe accident conditions.
- To observe the characteristic features of vapor dynamics on the outer surface of the test vessel and steam venting through the bottleneck of the annular channel for the cases with and without vessel coating.
- To perform heat transfer measurements of the downward facing boiling process on the vessel outer surface under high-heat-flux conditions.
- To determine the effect of bottleneck configuration on the CHF limit and to quantify the amount of CHF enhancement due to enhanced vessel/insulation performance.
- To determine the effect of vessel coating on CHF and to quantify the amount of CHF enhancement due to vessel coating.
- To develop CHF enhancement correlations based on the experimental data that can be used in the assessment of thermal margin for IVR.

In Task 3, ERVC experiments in the U.S. were performed in the PSU SBLB using an improved vessel/insulation design. Two separate types of tests were conducted, one with and the other without vessel coating. For the case without vessel coating, the main focus was on the performance of the improved vessel/insulation design. For the case with vessel coating, the main focus was on CHF enhancement due to the vessel coating alone. In both types of experiments, the CHF phenomena, including the vapor dynamics and the vapor generation cycle on the vessel outer surface, are studied along with the upward co-current two-phase flow induced in the annular channel by the boiling process. In the R.O.K., two separate series of boiling tests were also performed using SNU DELTA and GAMMA facilities. The nucleate and film boiling heat transfer coefficients for the various downward facing surfaces were measured in DELTA tests. The results from this test series were compared with previous test data and various nucleate and film boiling heat transfer coefficients obtained from numerical studies. In addition, KAERI initiated several experimental and analytical activities under the T-HERMES program to investigate ERVC.

This section summarizes Task 3 results. More detailed information about various tasks described in this section may be found in References 4-1 through 4-14. Section 4.2 summarizes results from SNU DELTA and GAMMA tests. Results from the PSU SBLB tests are highlighted in Section 4.3. KAERI efforts with the HERMES-HALF facility are summarized in Section 4.4. Insights and conclusions gained from Task 3 efforts to enhance ERVC are discussed in Section 4.5.

4.2. SNU Task 3 Tests and Results

Seoul National University

4.2.1. Introduction

In the process of designing the APR1400, the concept of in-vessel retention through external vessel cooling (IVR-EVC) was chosen as a severe accident management strategy. The cavity flooding was selected as the external vessel cooling method because of simpler installation relative to flooding within the thermal insulator. In fact, the IVR-EVC concept had not been considered during the initial design phase of the APR1400. Thus, several issues surfaced while applying the IVR concept at a later stage of design.

One of these issues centered about delayed flooding of the reactor vessel because of the large volume between the cavity floor and the lower head. The cavity flooding may take as much as forty minutes depending upon the accident scenario. It is thus not certain whether the flooding time will always be shorter than the time for relocation of the molten core material to the lower plenum of the reactor vessel. Another issue relating to IVR-EVC in such high power reactor as the APR1400 is the CHF that may not be large enough for the reactor vessel to maintain its integrity especially at the equator. This is because of a potential focusing effect of the metallic layer atop the oxidic pool coupled with low circulation velocity of the external coolant on account of the wide flow area at the equator. However, only few studies have dealt with the CHF at the low mass flux, low pressure, and high local quality condition.

The most important factor for the CHF at the top is the gap size between the thermal insulator and the reactor vessel. All the relevant literature reveals that the natural circulation enhancement by the gap increases the CHF but the small gap size decreases the CHF at the top. The mass flux at the top turns out to be a minor factor because of its diminished forced convection effect. Albeit the large local quality at the top may decrease the CHF, no experimental evidence exists for quantification of the CHF decrease due to the increased local quality. The CHF values are measured in the GAMMA 3D (Gap Apparatus Mitigating Melt Attack Three Dimensional) at the low pressure and low mass flux condition with differing mass flow rates.

In addition, the initial temperature of the vessel, which should be in the vicinity of the saturation point corresponding to the primary system pressure, will far exceed temperature of the cavity flooding water during an accident. Hence, the initial heat removal mechanism for external vessel cooling will most likely be film rather than nucleate boiling. The results of this work indicate, however, that film boiling heat transfer coefficients presently available in the literature tend to underpredict the actual value for the reactor vessel lower head. In this study, film boiling heat transfer coefficients are obtained from the quenching test of DELTA (Downward Ebullient Laminar Transition Apparatus) utilizing the measured temperature histories. The test results are compared with the analytical film boiling heat transfer coefficients with and without considering the interfacial wavy motion of the vapor film. The film boiling heat transfer phenomena are visualized through a digital camera. There are three experimental programs relating to this task: DELTA 1D, DELTA 3D and GAMMA 3D.

4.2.2. Interfacial Wavy Motion of Film Boiling

Figure 4-1 presents the schematic diagram of laminar film boiling from a downward-facing hemisphere. Several assumptions were made to simplify the laminar film boiling analysis: water is saturated at 1 atm, and the wall surface temperature is high enough to maintain a stable vapor film. The vapor film thickness depends on the x axis, which follows the wall surface. Radiation heat is transferred from the wall only to the liquid. The film boiling heat transfer is carried out by conduction through the vapor film. Vapor and liquid are both assumed to be incompressible.

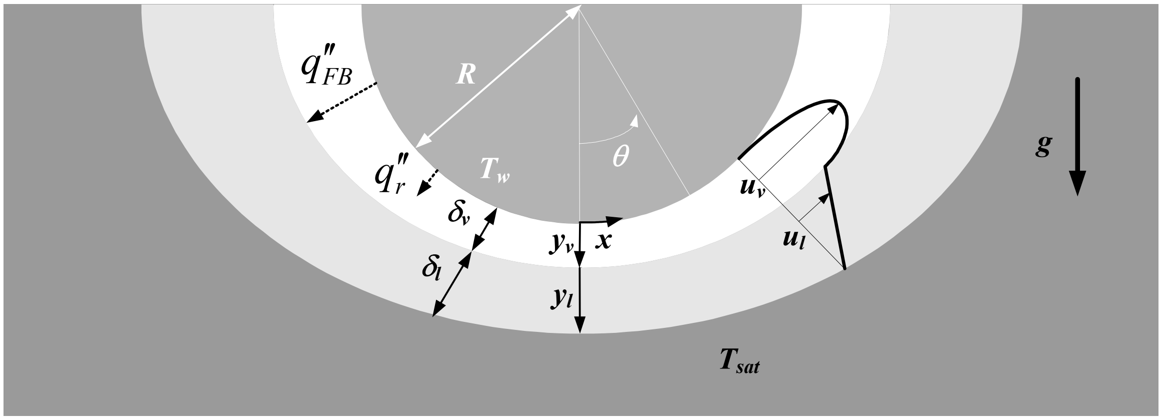

Figure 4-1. Laminar film boiling from a downward-facing hemisphere.

The momentum conservation equations for the flow in the vapor and liquid boundary layers, respectively, are

$$\mu_v \frac{\partial^2 u_v}{\partial y_v^2} = \frac{\partial p}{\partial x} + \rho_v g \sin\theta \tag{4-1}$$

$$\mu_l \frac{\partial^2 u_l}{\partial y_l^2} = \frac{\partial p}{\partial x} + \rho_l g \sin\theta \approx 0 \tag{4-2}$$

Simplification of Equation (4-2) indicates Equations (4-1) and (4-2) are rewritten as

$$\mu_v \frac{\partial^2 u_v}{\partial y_v^2} = -(\rho_l - \rho_v) g \sin\theta = -\Delta\rho g \sin\theta \tag{4-3}$$

$$\mu_l \frac{\partial^2 u_l}{\partial y_l^2} = 0 \tag{4-4}$$

Equations (4-3) and (4-4) can be integrated analytically as

$$u_v(y_v) = -\frac{\Delta\rho g \sin\theta}{2\mu_v} g y_v^2 + C_1 y_v + C_3 \tag{4-5}$$

$$u_l(y_l) = C_2 y_l + C_4 \tag{4-6}$$

The same interfacial velocity and shear stress of laminar film boiling section are used to determine the four constants in Equations (4-5) and (4-6). However, the interfacial shear stress is not zero in this section. The solutions to Equations (4-5) and (4-6), respectively, are

$$u_v(y_v) = \frac{\Delta\rho g \sin\theta \delta_v^2}{2\mu_v}\left(\frac{y_v}{\delta_v}\frac{f+2\xi}{f+\xi} - \left(\frac{y_v}{\delta_v}\right)^2\right) \tag{4-7}$$

$$u_l(y_l) = \left(1 - \frac{y_l}{\delta_l}\right)\frac{\Delta\rho g \sin\theta \delta_v^2}{2\mu_l}\frac{f\xi}{f+\xi} \tag{4-8}$$

where

$$f = {}^{\mu_l}\!/_{\mu_v} \tag{4-9}$$

$$\xi = {}^{\delta_l}\!/_{\delta_v} \tag{4-10}$$

When the boundary layer thickness ratio is zero, the interfacial velocity is zero. The infinite layer thickness ratio signifies the zero interfacial shear stress. Thus, the actual film boiling heat transfer coefficients lie within the bounding values between the cases of layer thickness ratios zero and infinite (Tou and Tso$^{4\text{-}16}$). It is assumed that the layer thickness ratio is independent of the *x* coordinate (Kolev$^{4\text{-}17}$). The cross-sectional vapor volumetric flow rate is

$$\int_0^{A_\delta} u_v dA_\delta = 2\pi R \sin\theta \int_0^\delta u_v dy_v = 2\pi R \sin\theta \frac{\Delta\rho g \sin\theta \delta_v^3}{12\mu_v}\frac{f+4\xi}{f+\xi} \tag{4-11}$$

Because the heat transfer mechanism within the vapor film is only conduction, the temperature profile in the vapor film is linear as

$$T_v - T_{sat} = \Delta T = (T_w - T_{sat})\left(1 - \frac{y_v}{\delta_v}\right) = \Delta T_{sat}\left(1 - \frac{y_v}{\delta_v}\right) \tag{4-12}$$

The cross-sectional product of wall superheat and velocity is

$$\int_0^{A_\delta} u_v \Delta T dA_\delta = 2\pi R \sin\theta \frac{\Delta T_{sat}}{2} \frac{\Delta\rho g \sin\theta \delta_v^3}{12\mu_v} \frac{f+3\xi}{f+\xi} \tag{4-13}$$

All the heat transferred from the surface to vapor film is consumed for vaporization of the liquid to develop the vapor film boundary layer. The vapor mass flow rate is equal to the liquid mass flow rate at the interface and in the increased boundary layer. The energy balance for the interface between the vapor film and liquid is written in the following form

$$q''_{FB} dA_s = \frac{d}{dx}\left[\rho_v h_{lv} \int_0^{A_\delta} u_v dA_\delta + \rho_v c_{p,v} \int_0^{A_\delta} u_v \Delta T dA_\delta\right] dx \tag{4-14}$$

The left side of Equation (4-14) signifies the conduction heat transfer through the vapor film. The right side of Equation (4-14) represents the absorbed energy for evaporation of a certain amount of steam at the surface plus the energy removed convectively for vapor heating. Equation (4-14) may be rewritten in terms of the differential terms for the azimuthal angle and the vapor film thickness as

$$n_{FB} \frac{96 Ja}{Ra} = \frac{\delta_v}{R \sin\theta} \frac{d}{d\theta}\left[\left(\frac{\delta_v}{R}\right)^3 (\sin\theta)^2\right] \tag{4-15}$$

where

$$Ja = \frac{c_{p,v} \Delta T_{sat}}{h_{lv}} \tag{4-16}$$

$$r_r = {q''_r}\Big/{q''_{FB}} = {\varepsilon\sigma\left(T_w^4 - T_{sat}^4\right)}\Big/{\left(k_v \Delta T_{sat} \delta_v^{-1}\right)} = \frac{\varepsilon\sigma\left(T_w^2 + T_{sat}^2\right)\left(T_w + T_{sat}\right)}{h} = const. \tag{4-17}$$

$$Ra = \frac{g D^3 \Delta\rho}{\mu_v \alpha_v}, \qquad D = 2R \tag{4-18}$$

$$n_{FB} = \left(\frac{f+4\xi}{f+\xi} \frac{1 + 0.5 Ja \dfrac{f+3\xi}{f+4\xi}}{1 + r_r}\right)^{-1} \tag{4-19}$$

By substitution $z = \left(\frac{\delta_v}{R}\right)^4$, Equation (4-15) can be rewritten as

$$n_{FB} \frac{128 Ja}{Ra} (\sin\theta)^{5/3} = \frac{d}{d\theta}\left[z^4 (\sin\theta)^{8/3}\right] \tag{4-20}$$

Solution of Equation (4-20) using the condition that $d\delta_v / d\theta = 0 \quad at \quad \theta = 0$ yields

$$\frac{\delta_v}{R} = n_{FB}^{0.25}\left(\frac{128Ja}{Ra}\right)^{0.25}\left[\frac{\int_0^{\theta}(\sin\phi)^{5/3}d\phi}{(\sin\theta)^{8/3}}\right]^{0.25} \tag{4-21}$$

The total heat transfer from the downward-facing hemisphere is given by

$$\begin{aligned} q &= \int_0^{\pi/2}\frac{k_v}{\delta_v}\Delta T_{sat}2\pi R^2\sin\theta d\theta \\ &= \frac{\pi D}{4}k_v\Delta T_{sat}\left(\frac{2Ra}{Ja}\right)^{0.25}n_{FB}^{-0.25}\int_0^{\pi/2}\sin^{5/3}\theta\left[\int_0^{\theta}(\sin\phi)^{5/3}d\phi\right]^{-0.25}d\theta \end{aligned} \tag{4-22}$$

Defining the average Nusselt number as $Nu = \frac{h_{avg}D}{k_v}$, it follows that

$$Nu = \frac{h_{avg}D}{k_v} = \frac{2qD}{\pi D^2\Delta T_{sat}k_v} = 0.696\left(\frac{Ra}{Ja}\right)^{0.25}\left(\frac{f+4\xi}{f+\xi}\,\frac{1+0.5Ja\dfrac{f+3\xi}{f+4\xi}}{1+r_r}\right)^{0.25} \tag{4-23}$$

For film boiling on a long vertical surface, when a sufficiently high vapor film Reynolds number is reached, transition to turbulent flow occurs and the interface generally becomes wavier. When this occurs, the interfacial waves may roll up and break releasing vapor bubbles into the adjacent liquid. Hence, the vapor film is developed from the transition position again. It is assumed that the onset of transition to turbulent flow in film boiling occurs when the vapor film Reynolds number attains a critical value. Hsu and Westwater [4-18] estimated the condition for the onset of transition to turbulent flow in film boiling as

$$Re_{\delta} = \frac{\rho_v u_{\delta}\delta_v}{\mu_v} = 100 \tag{4-24}$$

As the vapor travels up, the film continues to thicken, the vapor flow increases, and the interfacial wavy motion occurs in the vapor film. The interfacial waves then increase in wavelength, eventually becoming unstable. The angular vapor film thickness and interfacial velocity were calculated under the laminar film boiling analysis. Nishio et al.,[4-19] Nishio and Ohtake,[4-20] and Kolev[4-17] developed the film boiling model with interfacial wavy motion by the Helmholtz instability. However, the Helmholtz instability wave length could not be used as the characteristic length in the spherical geometry, because the wavelength tends to vary on the curved downward surface on account of changing inclination angles and expanding spherical surface from the bottom up. Hence, the vapor film Reynolds number was chosen as the parameter for simulation of the interfacial wavy motion on a hemispherical downward heated surface. Previous experimental results on a relatively long vertical plate indicate that Hsu and Westwater's critical vapor film Reynolds number is too large to simulate the actual interfacial wavy motion. Therefore, a sensitivity analysis was performed varying the critical values to obtain the proper critical vapor film Reynolds number. Figure 4-2 shows the calculation process for the vapor film thickness accounting for the interfacial wavy motion. Once the vapor film Reynolds number exceeds the critical value, the vapor film is collapsed and restarted to grow covering the wall surface.

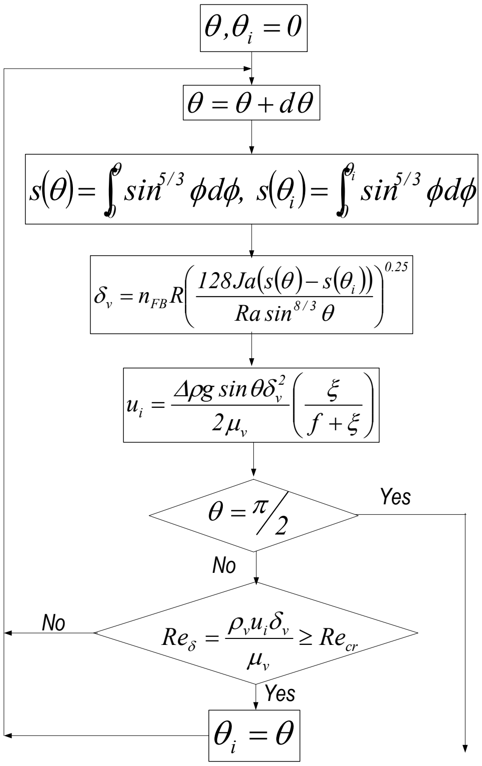

Figure 4-2. Calculation process of vapor film thickness considering interfacial wavy motion

The angular vapor film thickness is the integral value from the transition angle to interfacial wavy film flow as

$$\frac{\delta_v}{R} = n_{FB} \left(\frac{128 Ja}{Ra} \right)^{0.25} \left[\frac{\int_{\theta_i}^{\theta} (\sin\phi)^{5/3} d\phi}{(\sin\theta)^{8/3}} \right]^{0.25} \tag{4-25}$$

The average film boiling heat transfer coefficients are calculated from the angular film thickness profiles as

$$h_{avg} = \int_0^{\pi/2} \frac{k_v}{\delta_v} 2\pi R^2 \sin\theta d\theta \Big/ 2\pi R^2 = \int_0^{\pi/2} \frac{k_v}{\delta_v} \sin\theta d\theta \tag{4-26}$$

4.2.3. DELTA 1D Test Apparatus

DELTA 1D is designed to estimate the effect of the inclination angle on the interfacial wavy motion. Figure 4-3 shows the DELTA 1D experimental apparatus. It includes a test section, a viewing chamber, a boiler and a flow line to initiate and maintain the film boiling process. The test section is mounted on one side of the viewing chamber, and two glass windows are placed for the front and side views.

Figure 4-3. Picture of the DELTA 1D test apparatus.

Figure 4-4 presents the DELTA 1D test section. The test section is made of copper of size 120 × 60 × 50 mm^3. Two cartridge heaters are placed in the test section with the maximum heat flux on the outer surface reaching 160 kW/m^2. Thirty-six K-type thermocouples are installed along the boiling surface at twelve locations: 5, 15, 25, 35, 45, 55, 65, 75, 85, 95,105, and 115 mm from the edge. At each location, three thermocouples are positioned at 1.5, 15, 30 mm from the boiling surface. Four pairs of K-type thermocouples are installed at 1.5 and 30 mm from the boiling surface in four corners of the test section. There are forty-four holes on the test section in Figure 4-4. One can revolve the test section from the upward (0^o) to downward (180^o) surface at 15^o intervals as demonstrated in Figure 4-5.

When the boiling experiment is performed, the saturated water is contained in a viewing chamber, whose cross section is 160×250 mm^2. It is always filled with the saturated water during the film boiling heat transfer. An immersion heater rod located in the pool is used to maintain the water temperature at a constant value. The liquid temperature was measured with a thermocouple located in the pool.

At first, the water in the boiler and the DELTA 1D test section are heated up to 100^oC and 400^oC, respectively. The temperature of 400^oC is high enough to maintain stable film boiling heat transfer. After the test section is heated enough to maintain stable film boiling, the viewing chamber is filled with water. After the film boiling heat transfer becomes stable, the heater power in the test section was controlled with a slidacs and determined by voltmeter and ammeter readings. In the steady-state tests, the surface heat flux is calculated from the spatial temperature distribution recorded by the HP-VXI E1413C data acquisition system. The thermocouples are calibrated in ISOTECH TRU (Temperature Reference Unit) Model 740. Film boiling heat flux and heat transfer coefficient are calculated from the two dimensional steady-state temperature distributions.

Figure 4-4. Picture of the DELTA 1D test section.

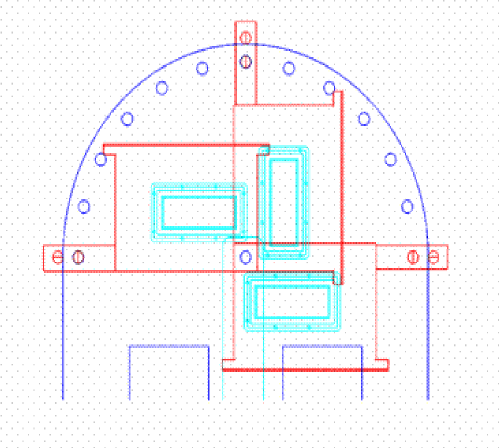

Figure 4-5. Revolution of the DELTA 1D viewing chamber.

4.2.4. DELTA 3D Test Apparatus

This experiment is performed to obtain the angular and curved effects on film boiling heat transfer. The experimental results are compared with the analytical results of the interfacial wavy motion.

Figure 4-6 presents the cross-sectional view of the test sections with diameters of 120 mm and 294 mm, respectively. The diameters of the stainless steel and Fire Stop disk on the test section, respectively, are 118 mm and 292 mm, which are smaller than the diameters of the two copper hemispheres. The 2 mm clearance ensures that the three materials of differing thermal expansion coefficients do not interfere with release of bubbles at the equator of the hemispheres. Figure 4-7 shows the thermocouples installed at 0°, 20°, 40°, 60° and 80° near the outer surface and the inner surface of both test sections. The thermocouples are also calibrated in ISOTECH TRU (Temperature Reference Unit) Model 740. The holes are drilled through the center of the stainless steel disk, stainless steel pipe, and the Fire Stop to route the wall thermocouples to the HP-VXI E1413C data acquisition system. The test section is made of copper to maintain Bi below 0.1 in the film boiling regime. In case of Bi less than 0.1 the conduction heat transfer in the solid may be neglected (see Incropera and Dewitt[4-21]). Thus, the experimental data could be compared with numerical analysis for the isothermal hemispherical surface. Peyayopanakul and Westwater[4-22] suggested that the thickness of the copper vessel was 3 cm so that data from the quenching experiment would be similar to those from the steady state experiment. If the time to traverse the top 10% of the boiling curve were greater than 1 sec, the boiling process would be in a quasi-steady state (Dhir[4-23]). The test section's inner cavity was filled with bulk fiber and covered on top with the Fire Stop disk for thermal insulation. A stainless steel disk was fastened to the test section wall using the stainless steel bolts.

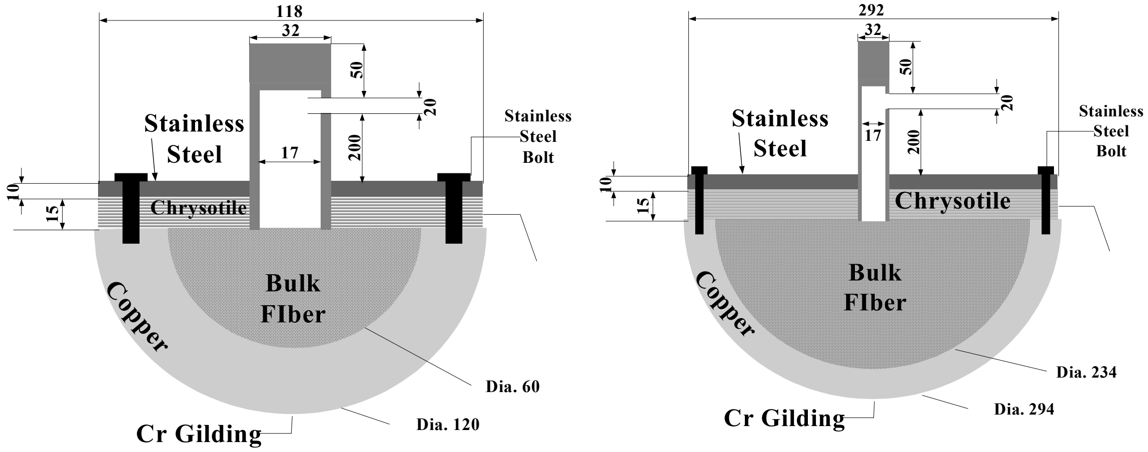

(a) 120 mm (b) 294 mm

Figure 4-6. Cross-sectional view of the DELTA 3D copper test sections.

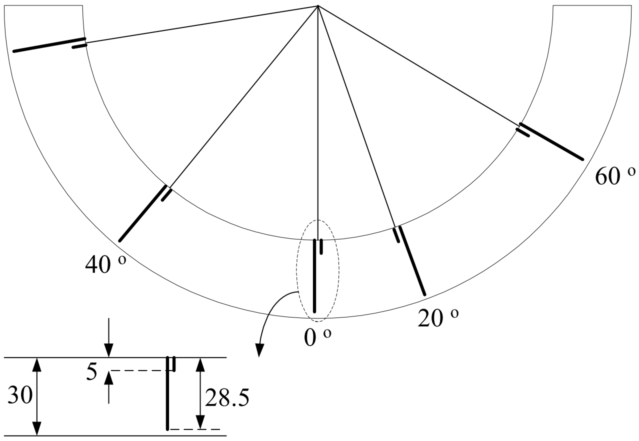

Figure 4-7. Azimuthal locations of thermocouples (length unit: mm).

Figure 4-8 presents the stainless steel hemisphere. Its diameter and thickness are 294 mm and 30 mm, respectively, which are the same as the largest copper hemisphere in the previous experiments. The stainless steel pipe was welded on top of the hemisphere to prevent water from ingress to the test section. Its outer diameter, inner diameter and height are 292 mm, 290 mm, and 100 mm, respectively. The outer diameter of the pipe is smaller than that of the hemisphere. This explains why there is no release of bubbles at the top of the hemispheres. Eighteen thermocouples were installed at 0°, 10°, 20°, 30°, 40°, 50°, 60°, 70° and 80° near the outer surface and the inner surface of both test sections. The thermocouples were also calibrated in ISOTECH TRU (Temperature Reference Unit) Model 740. The holes were drilled through the center of the stainless steel disk to route the wall thermocouples to the HP-VXI E1413C data acquisition system. The angular film boiling heat flux and heat transfer coefficient were obtained from the two dimensional transient temperature distributions.

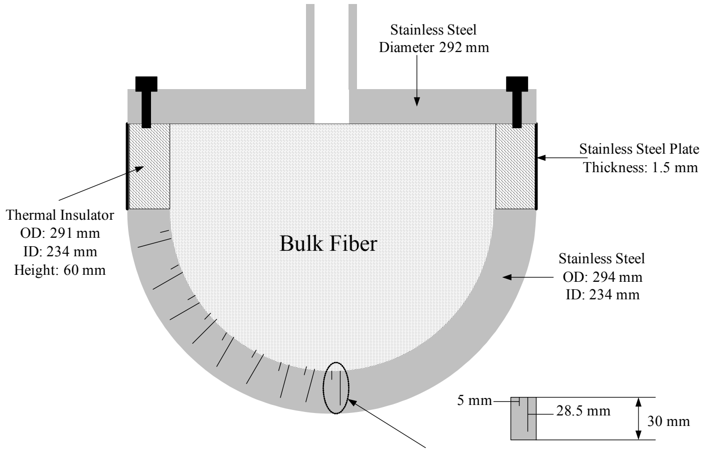

Figure 4-8. Cross-sectional view of the DELTA 3D stainless steel test sections.

The hexahedral quenching tank is of 1 × 1 × 1.1 m^3. A tank must have 3.5 times the dimension of the test section to maintain pool boiling without the effect of the quenching tank size (Westwater et al.[4-24]). It has a large glass window on one side for visual inspection and recording of pool boiling on the hemispherical surface during quenching using a video camera. During the experiment, the water in the tank was maintained at the saturated condition utilizing four 10 kW and two 7 kW heaters.

Prior to each quenching experiment, the demineralized water in the tank was degassed by boiling for thirty minutes. The test section was heated up to 280 ^{o}C. The heated test section was transferred from the furnace to the quenching tank by an automatic lift within a few seconds. The heated test section was then submerged in the quenching tank with its top surface kept at 10 cm below the water level. Figure 4-9 illustrates the DELTA 3D experimental apparatus.

4.2.5. GAMMA 3D Test Apparatus

GAMMA 3D is designed to measure the heat transfer coefficient and CHF in view of IVR-EVC. The experimental factors include the gap size, mass flow rate, pressure, the forced convection or natural circulation condition and the initial subcooling. A uniform heat flux method is adopted. The various mass flow rates are adopted as key variables for the saturated condition at the inlet.

The test section was scaled down linearly with the resulting diameter of 500 mm and height of 749 mm, respectively. The gap size between the heater assembly and vessel maintains 50 mm. A uniform gap size was assumed between the hemispherical shell and the test vessel. Under the atmospheric pressure, the

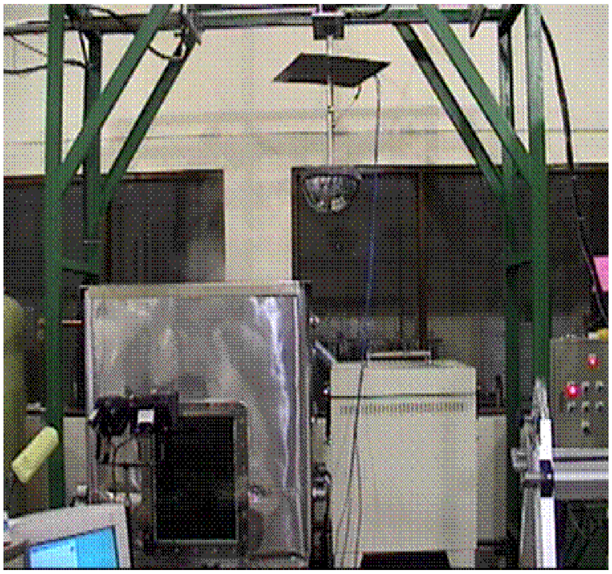

Figure 4-9. Picture of the DELTA 3D test apparatus.

minimum mass flow rate of coolant was supplied at 0.6 kg/s. There was no inlet subcooling. Fifty-six thermocouples of K-type were installed at 0^{o}, 10^{o}, 20^{o}, $30,^{o}$ 40^{o}, 50^{o}, 60^{o}, 70^{o}, 80^{o}, and 90^{o} within the shell block having the shallow and deep locations in each thermocouple hole. Three T-type thermocouples were installed in the pipes of the primary loop to control the constant inlet subcooling. As had already been described in the previous letter report, the copper block was divided into nine pieces. Whereas eight pieces of them have the same shape, the other one is of a different shape and located at the center of the shell block. The five copper blocks with a total of 102 heaters (maximum 360 kW) and four insulators were inserted in the shell block in the GAMMA 3D test section (Figure 4-10). Twenty-four heaters were inserted in each copper block and the copper block located at the center of the shell block was filled with six heaters.

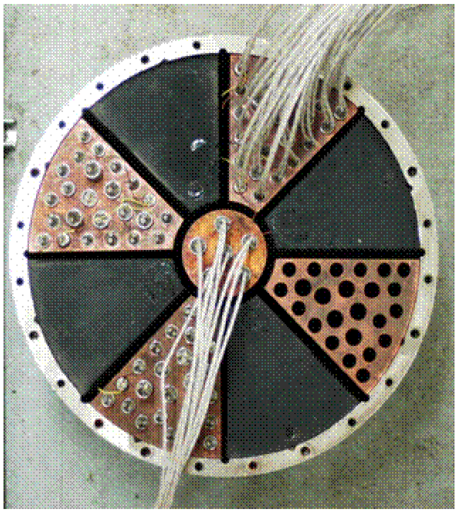

Figure 4-10. GAMMA 3D heater assembly with copper blocks and insulators.

Demineralized water is used as working fluid and filtered prior to entering the test section. A booster pump having a maximum mass flow rate of 16.5 kg/s is used for forced convection and two motorized two-way valves are installed to maintain a constant mass flow rate. Working pressure in the primary loop is 0.15 MPa. Figure 4-11 illustrates the assembly procedure for the heater assembly and vessel.

Figure 4-11. GAMMA 3D test assembly procedure.

After the primary water tank is filled with the demineralized water, the four immersion heaters in the primary water tank heat the coolant according to the initial subcooling condition. As a low mass flow rate is indicated, the primary coolant is injected into the primary loop by the booster pump and control valves. Five rectifiers in two control panels allow 102 cartridge heaters in the copper block to be heated. Then the hemispherical shell block is heated by conduction. Steady state experiments are carried out after adjusting the mass flow rate and inlet subcooling. Using the HP-VXI E1413C data acquisition system, the surface temperatures of the shell block from the fifty-six thermocouples are recorded, from which the heat transfer coefficients are obtained by the distribution of surface temperatures. Additionally, the heat flux values are measured by the WT-130 instrument.

4.2.6. DELTA 3D Test Results

Figure 4-12 compares El-Genk and Glebov's experimental results[4-25] and the laminar film boiling analysis corresponding to their experimental condition. Tou and Tso[4-16] applied two interfacial velocity boundary conditions for laminar film boiling analysis. Case 1 assumes that the interfacial velocity is zero. Case 2 presumes that the interfacial shear stress is equal in the vapor film and bulk liquid, and that the value is small enough to be neglected. The actual laminar film boiling heat transfer coefficient should lie between the two cases. In this analysis, the zero and infinite layer thickness ratios correspond to cases 1 and 2, respectively. Spanning the whole range of wall superheat, their experimental data fall within the bounding values of zero and infinite layer thickness ratios. The layer thickness ratio on the curved surface was determined therefore by El-Genk and Glebov's laminar film boiling heat transfer coefficients[4-25] on the downward-facing curved surface. The error is minimized within ± 3% when the layer thickness ratio is ten. The layer thickness ratio is henceforth assumed as ten in this film boiling analysis.

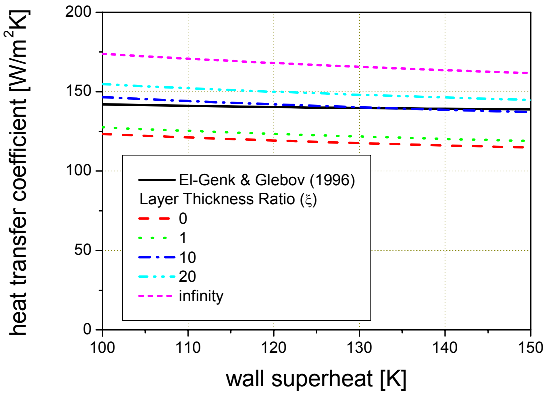

Figure 4-12. Comparison of laminar film boiling heat transfer and El-Genk and Glebov's experiments

For a wall superheat of 120 K, the heat transfer coefficients obtained from the two diameters are plotted in Figure 4-13. It is seen that the Frederking and Clark[4-26] model yields heat transfer coefficients about 50% lower than the experimental data. The film boiling heat transfer coefficients from the laminar film boiling analysis with the layer thickness ratio are higher than those from Frederking and Clark, but still lower than the experimental data. The film boiling analysis with the interfacial wavy motion fares very well with the experimental data. The critical vapor film Reynolds number decreases the transition radius of the onset of the interfacial wavy motion. The critical vapor film Reynolds number of 25.1 was used to minimize the difference between the predicted and measured heat transfer coefficients. Oscillation in the heat transfer coefficients with the interfacial wavy motion is due to the start or end of the interfacial wavy motion at the top whose surface area is greatest at the downward-facing hemisphere.

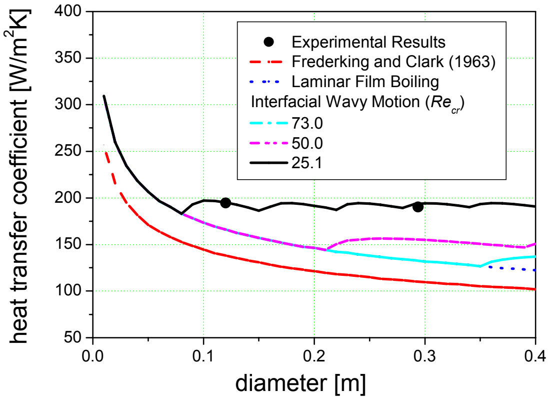

Figure 4-13. Comparison of predicted and observed dependence of heat transfer coefficient on diameter of a downward-facing hemisphere.

Figure 4-14 depicts the film boiling heat transfer coefficients varying with the wall superheat measured from diameter 294 mm and predicted by the numerical analysis. Frederking and Clark's results were calculated at the condition of zero layer thickness ratio, and the laminar film boiling analysis at the layer thickness ratio of ten. The heat transfer coefficients obtained from the tests are greater than those from the numerical analysis for laminar film boiling. Thus, the film boiling regime in the DELTA test is not simply laminar, but involves more complexities like the Helmholtz instability. The film boiling heat transfer coefficients considering the interfacial wavy motion agree better with the experimental results within ± 4.5% than those for laminar film boiling analysis without the interfacial wave consideration.

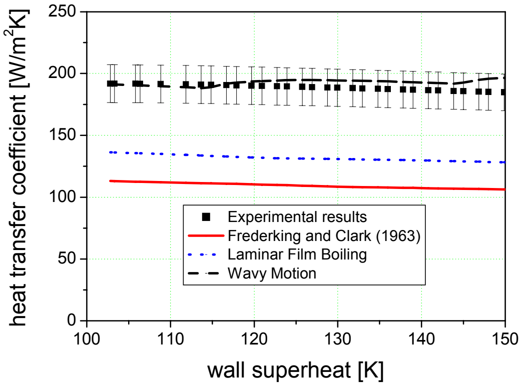

Figure 4-14. Film boiling heat transfer coefficient for test section of diameter 294 mm

Figure 4-15 shows the film boiling heat transfer coefficients with the wall superheat for diameter 120 mm resulting from the numerical analysis. The heat transfer coefficients measured from the tests are greater than those from laminar film boiling analysis. The film boiling heat transfer coefficients considering the interfacial wavy motion also agree better with the experimental results within ± 3.8% than those for laminar film boiling analysis. But the difference between laminar film boiling heat transfer coefficients and measured film boiling heat transfer coefficients is relatively smaller than those in the 294 mm diameter tests, so the simple laminar film boiling regime is considered to span a greater portion of the 120 mm test section area than of the 294 mm test section.

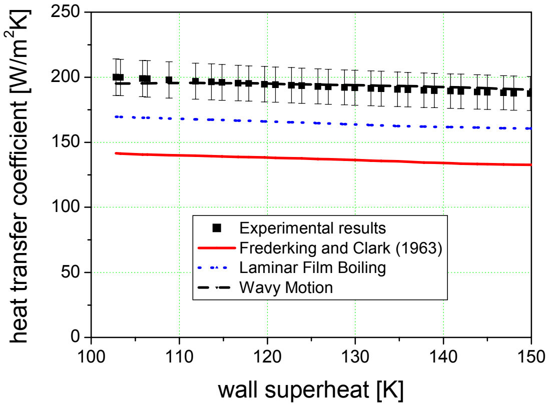

Figure 4-15. Film boiling heat transfer coefficient for test section of diameter 120 mm.

Figures 4-16 (a) and (b) depict the film boiling heat transfer mechanism for the two DELTA test sections. Snapshots were taken of film boiling with the digital camera Nikon D100 at 1000 fps. Considering the measured film boiling heat transfer coefficients, the governing mechanism was laminar film boiling. Thus, a relatively stable vapor film was formed on the 120 mm diameter downward-facing hemisphere. In case of diameter 294 mm, Figure 4-16(b) reveals a rough vapor film interface on most of the downward-facing hemisphere. This had already been anticipated from the calculated heat transfer coefficients taking account of the interfacial wavy motion. A similar vapor film instability as had already been reported by Bui and Dhir[4-27] on the vertical plate was observed on most of the downward-facing hemisphere. The wavelength by the Helmholtz instability will quantitatively be analyzed in the visualization tests.

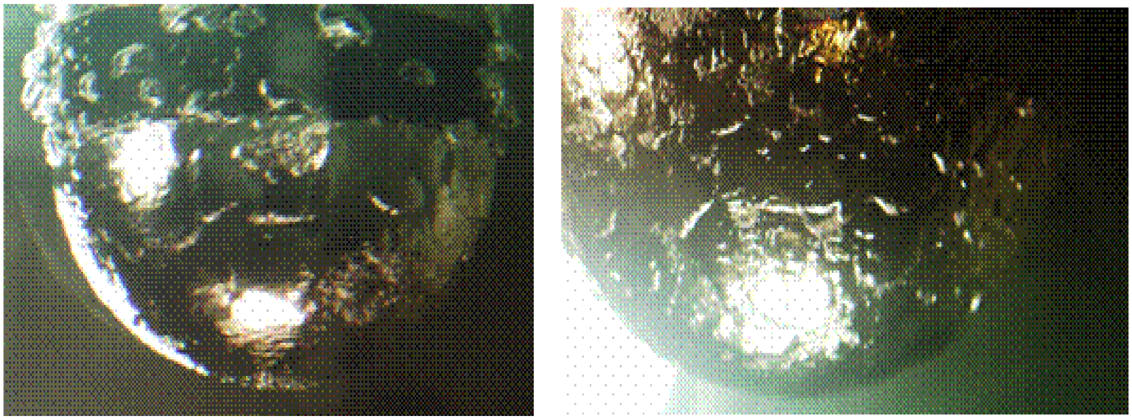

(a) 120 mm

(b) 294 mm

Figure 4-16. Film boiling visualization for the two test sections.

Figure 4-17 shows the angular vapor film thickness profiles from the film boiling analysis with the interfacial wavy motion at 120 K wall superheat of diameters 120 mm and 294 mm. For the case of 120 mm, most region of the downward-facing area is typified by the laminar vapor film. In contrast, the interfacial wavy regime spans a greater portion of the 294 mm test section. The number of the waves from the analytical results is less than those identified from the snapshot. Albeit no description is given about the interfacial wavy motion in El-Genk and Glebov's study,[4-25] the assumption that the vapor film flow is laminar in their experiment yields a greater layer thickness ratio and the critical vapor film Reynolds number than the actual values.More test results must be produced to determine the proper layer thickness ratio and the critical vapor film Reynolds number. In addition, destabilization of film boiling propagated radially inward for the 294 mm test section, but radially outward for the 120 mm test section. This is because the thinnest film region is at the bottom for the 120 mm test section, while it is at the equator for the 294 mm test section

In this analysis, the layer thickness ratio and critical vapor film Reynolds number were independent of the inclination angle. The stainless steel hemisphere DELTA 3D tests are underway to produce azimuthally varying film boiling heat transfer coefficients.

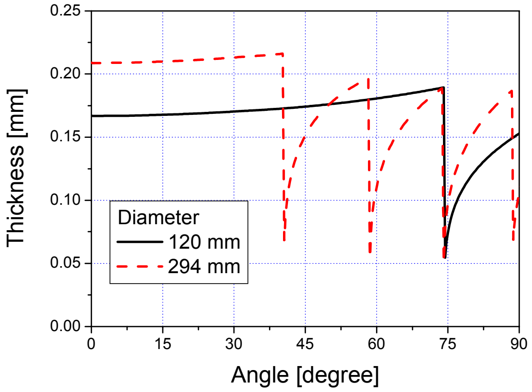

Figure 4-17. Angular vapor film thickness profiles at experimental condition.

4.2.7. DELTA 1D Test Results

In the DELTA 1D tests, a thick asbestos plate was installed around the copper test section to prevent the nucleate boiling around the test section surface. One could observe the interfacial wavy motion of vapor film. The measured wall temperatures had similar values except at 5 mm from the leading edge because of the thinnest vapor film there. A total of five heated power cases were conducted at 0^{o}, 30^{o}, 45^{o}, 60^{o}, and 90^{o}. Figure 4-18 depicts the boiling phenomena on the vertical plate. The interfacial wavelength of vapor film flow could unfortunately not be visualized due to transition or nucleate boiling around the copper surface, however.

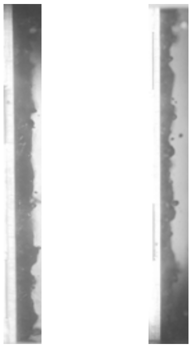

Figure 4-18. Boiling phenomena on a vertical plate.

4.2.8. GAMMA 3D Test Results

GAMMA 3D results indicated that CHF values decrease as the inclination angle increases for large inlet subcooling (Figure 4-19). In other words, the angular qualities are augmented by the increase in enthalpy as the angle increases. Cheung et al's experimental results[4-28] indicate that a perpendicular injection to the bottom heated surface increases the CHF at the bottom of the hemisphere. However, this effect was not considered in SULTAN[4-29] due to the injection direction parallel to the heated surface. Therefore, it is believed that the actual CHF values at the bottom and the inclination angles in an experiment are higher than those predicted by Rouge et al's correlation.[4-29]

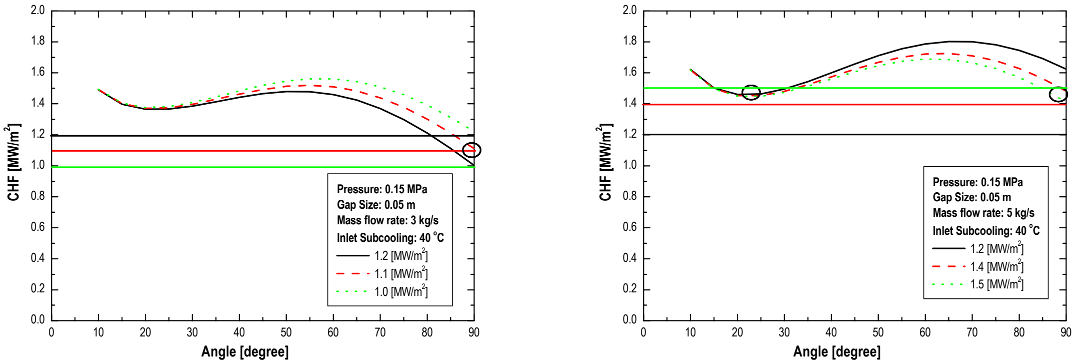

Figure 4-19. Angular CHF for uniform heat flux with coolant of ΔT= 60 K at 3 and 5 kg/s.

The film boiling heat transfer coefficients on the downward-facing hemisphere were measured and analyzed. For the case of the 120 mm diameter test section, most regions were covered with a laminar vapor film. In contrast, the interfacial wavy regime ratio of the 294 mm test section is higher than that of 120 mm. There was little difference observed between the film boiling heat transfer coefficients from the two test sections. The film boiling heat transfer coefficients for the test sections were greater than those given by the numerical solution for the laminar film boiling due mostly to limitation on the vapor film thickness imposed by the interfacial wavy motion. The interfacial wavy motion resulting from the Helmholtz instability plays an important role in limiting decrease in the film boiling heat transfer coefficient with the increasing diameter. The snapshots for film boiling phenomena did reveal that the interfacial wavy motion was the governing mechanism in determining the film boiling heat transfer coefficient in the two test sections. As expected, the film boiling analysis with the interfacial wavy motion showed excellent agreement with the experimental data from the two test sections. In addition, destabilization of film boiling propagated radially inward for the 294 mm test section, but radially outward for the 120 mm test section.

4.3. SBLB Description and Test Results

Pennsylvania State University

4.3.1. Introduction

Steady state boiling experiments using test vessels with and without coatings were conducted in the SBLB facility for the cases with and without an enhanced thermal insulation to investigate the separate effect as well as the integral effect of the enhanced insulation design and vessel coatings. The enhanced insulation design, experimental apparatus, measurement techniques, and experimental procedure are described in this section.

4.3.2. Enhanced Vessel/Insulation Structure

The enhanced vessel/insulation design employed in the SBLB experiments is shown in Figure 4-20. The enhanced design involves the use of a non-uniform gap size for the bottleneck by opening the space available for steam venting in the circumferential locations away from the four shear key positions. In so doing, the cross-section flow area of the annular channel at the bottleneck is substantially increased, thus reducing the superficial velocity of steam through the bottleneck. This allows a much higher mass flow rate of steam corresponding to a much higher wall heat flux from the corium be accommodated through the bottleneck that in turn would greatly increase the value of CLSV and enhance the CHF limit.

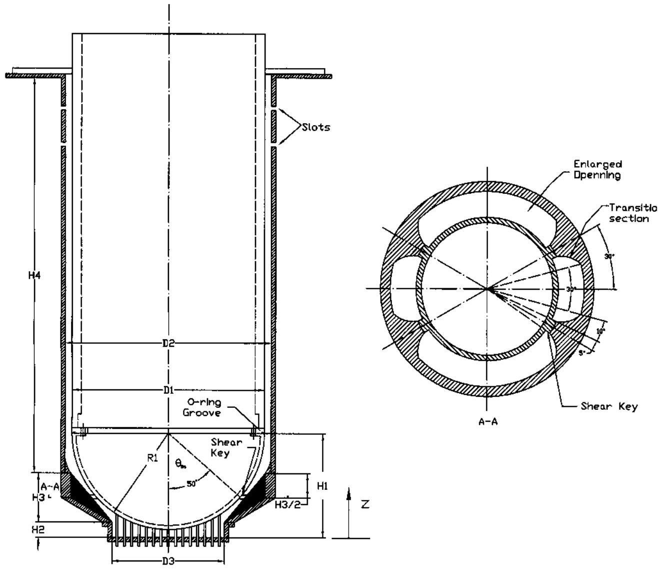

Figure 4-20. Schematic of the enhanced APR1400 vessel/insulation design.

The enhanced design consists of four interconnected sections with a smooth streamline configuration as shown schematically in Figure 4-21. These are the lower flow inlet section, the conical section, the smooth transition section, and the upper cylindrical section. The lower inlet section is a relatively short section consisting of a flow inlet cylinder with a bottom inlet plate in its lower end that has numerous holes for water ingression while allowing the In-Core Instrument (ICI) nozzles to penetrate through. The conical section comprises a lower cone and upper cone that are joined together near the shear key position (see Section A-A of Figure 4-20) with enlarged cross-sectional flow area to facilitate steam venting. The smooth transition section is also a short section that provides a smooth connection between the conical section and the upper cylindrical section. The upper cylindrical section is a relatively long section consisting of a flow outlet cylinder with slots near the top (see Figure 4-20) for the two-phase mixture to exit from the annular channel. An overall view of the SBLB water tank with an enhanced vessel/insulation design is shown in Figure 4-22.

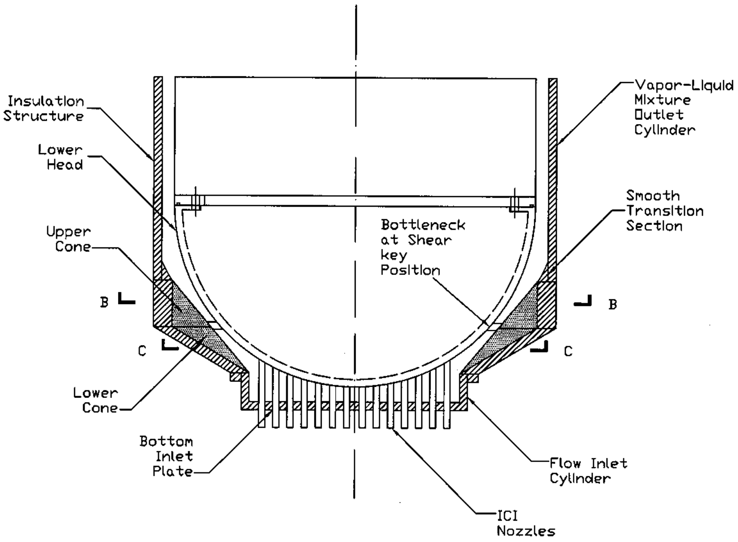

Figure 4-21. Close-up view of the lower part of enhanced vessel/insulation configuration.

Figure 4-22. Overall view of SBLB water tank with APR1400 vessel/insulation simulator.

4.3.3. Experimental Apparatus

The SBLB test facility consists of a water tank with a condenser assembly, a heated hemispherical test vessel with or without an insulation simulator, a data acquisition system, a photographic system, and a power control system, as depicted in Figure 4-23. The water tank had a diameter of 1.22 m and a height of 1.14 m. One small and two large windows were placed on two opposite sides of the tank. One large window was used for the recording system along with light sources and the other was used for additional lighting as deemed necessary. The small window was used to observe the water level while the tank was being filled with water. The windows were fastened to the tank by placing a ring on the outside of the window that was bolted to a flange. An O-ring seal was used to prevent any leaks around the windows. The tank was equipped with three immersion heaters with a total power of 36 kW for preheating the water in the tank. A condenser assembly was installed on top of the tank to maintain the water level and the pressure of the tank constant during an experiment.

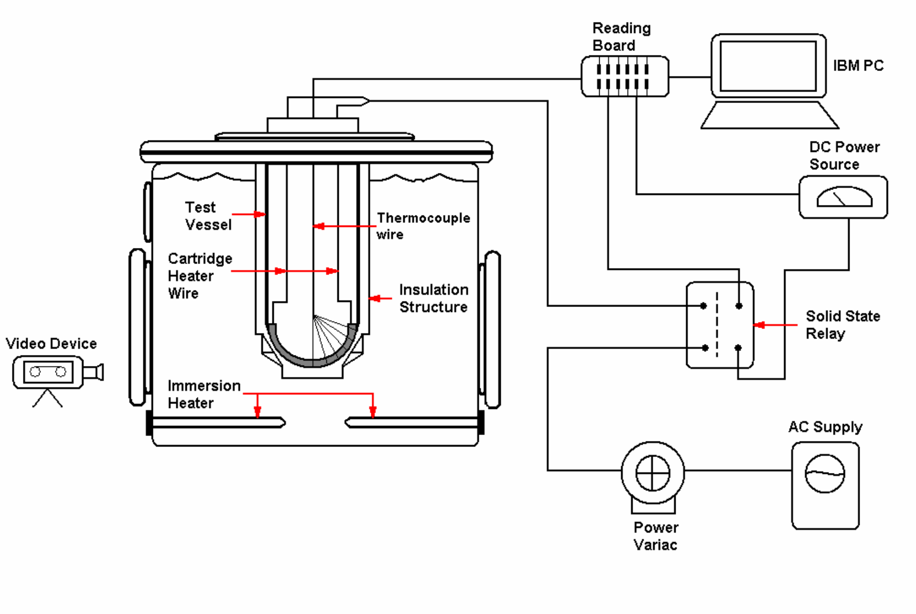

Figure 4-23. Overall schematic diagram of SBLB test apparatus.

The test vessel comprised two main parts made of aluminum: a heated lower hemispherical vessel and a non-heated upper cylindrical portion. The upper cylindrical portion had an outside diameter of 0.3 m and a wall thickness of 12.7 mm. The lower end of the upper portion had a 25.4 mm flange with a 6.35-mm groove for an o-ring and twelve 4.7 mm screw holes for attaching the upper portion to the lower hemispherical vessel. The latter had a bottom-heated section and an upper heated section. The bottom heated section consisted of inner and outer segments that were welded together and heated independently. The weld that kept the two segments together was placed on the outside at the interface between the two segments and it was the main region of contact between the two sections. Everywhere else along the circumference that separated the inner and outer segments, there was 3.18 mm air gap to minimize conduction heat transfer between the two segments. A 3.18 mm groove was also placed along the outer circumference of the outer segment to minimize heat conduction to the rest of the test vessel. The upper heated section consisted of three independently heated segments. A 0.00475-m groove was cut between segments to reduce heat conduction between them.

Cartridge heaters, 31.75 mm long and 9.52 mm thick, were employed to provide independent heating of the five segments. For the proper operations of these heaters, it was very important to minimize the air gap between the heaters and the test section. Therefore, the holes for the heaters were drilled and then reamed to provide a 0.0254 mm fit. Before inserting them in the holes, the heaters were treated with a special coating called Watlube from Watlow. This product protected against high temperature oxidation and more importantly it enhanced the heat transfer between the heaters and the test section. There were up to 32 K-type thermocouples installed in the vessel to monitor and record the temperature of the wall.

4.3.4. Measurement Techniques

The temperature at various locations of the vessel was monitored by using a 25 MHz 386 IBM compatible personal computer along with a data acquisition system. Two Strawberry Tree CPC-16 boards were installed inside the PC. Each of these boards had 16 analog inputs and 16 digital input/output channels. The CPC-16 board was capable of resolutions in the range between 12 and 16 bits, which was equivalent to 0.024% and 0.0015% of full scale, respectively. Each of the boards had six voltages ranges that could be set according to the sensor used. The boards also had a high noise rejection integration converter, which helped reject 50/60 Hz AC power line interference when used in the “low noise mode”. The CPC-16 units were also capable of accurate cold junction compensation and linearization for thermocouple devices. The two ACPC-16 boards were connected to a total of four Strawberry Tree T12 boards, which in turn were connected to the thermocouples. Each of the T12 boards had 8 analog inputs and 8 digital input/output channels. The uncertainty in the temperature measurements was estimated to be ± 0.38 ^{o}C. For heat flux levels above 0.1 MW/m^2, the temperature measurements were estimated to be ± 7%. Some selected experiments were repeated to confirm the reproducibility of the data.

For steady state experiments, the speed of the data collection was not that critical. Therefore the slower program Quicklog developed by Strawberry Tree Inc. was employed to monitor the changes in the vessel temperatures. Quicklog was also used to read and store the temperatures of the hemisphere at various locations inside the vessel wall. The data acquisition program was also used to create a control routine that used to protect the vessel from any possible meltdown in the high heat flux regime. When the critical heat flux was reached during steady state heating experiments, any further increase in the power input would result in the onset of film boiling. This was characterized by an abrupt increase in the local temperature of the heating surface. In order to protect the vessel against any possible meltdown, a power control mechanism was installed to discontinue the power supply to the heaters when a significant jump in the vessel temperature was detected in the high heat flux regime. The power control system consisted of a data acquisition system, a constant DC power source, a solid-state relay, and thermocouples to measure the vessel wall temperatures. The solid-state relay had a low voltage side connected to the constant DC power source, and a high voltage side connected to the variac supplying the heaters. The solid-state relay was needed because the high voltage of the variac could not be connected directly to the digital I/O channel of the data acquisition board.

To carry out the control strategy, a control routine was created using the computer program Quicklog from Strawberry Tree Inc. This routine started by collecting the temperatures of the vessel wall at several desired locations. These temperatures were then compared to a set point value of 250^{o}C, which was much higher than the expected wall temperature that was characteristic of nucleate boiling in water. Wall temperatures higher than 250^{o}C could have only been due to the occurrence of the critical heat flux. Under normal operating conditions, the vessel wall temperature would be less than 250^{o}C and the digital I/O channel connected to the solid-state relay would be closed. This allowed the high voltage side of the solid-state relay to stay closed for the desired power to be delivered to the vessel. When a wall temperature greater than 250^{o}C was detected, the digital I/O channel became open. As a result, the low voltage side of the solid-state relay was not powered anymore and the power supply to the heaters was discontinued, which prevented any further substantial increase in the vessel wall temperature.

4.3.5. Experimental Procedure

To prepare for a run, the tank was filled with water to the desired level. A pump was used to circulate the water through a high-performance filter. This helped remove the particles that precipitated during the heating process. Then the immersion heaters were turned on to heat the water to a prescribed temperature. If the temperature fell below the desired value during an experiment, one of the heaters was turned on again to bring the water temperature back up. Before every experiment, the water was given time to become completely quiescent. In these tests, saturation temperature was maintained for the water in the tank.

After the water was conditioned and heated to the prescribed temperature, the power supply cables and the thermocouple wires were then connected to the adjustable power suppliers and the data acquisition system, respectively. Each power supply circuit was equipped with a multimeter that allowed the voltage across and current through the adjustable power suppliers to be measured. Next, the power sources to the adjustable power suppliers were turned on and the variac and/or SCR were set to deliver the desired heat flux level. At the same time, the temperatures at various locations inside the vessel wall were monitored on the computer screen using the data acquisition program Quicklog from Strawberry Tree Inc. Once it was decided that steady state conditions were reached, the program Quicklog was used to record the steady state temperatures at various locations of the vessel wall and store them into a file for analysis.

Note that the boiling cycle on the outer surface of the bottom head simulator and the local vapor velocity in the annular channel between the test vessel and the enhanced insulation structure are two most important features of the downward-facing boiling and steam venting processes. Flow visualization was conducted in the SBLB experiments to observe these two important features, as shown in Figures 4-24 and 4-25 as examples. The local vapor velocity was measured by a dye tracking method.

Four types of steady state boiling tests were conducted. These include tests using: (i) plain test vessels without thermal insulation, (ii) coated test vessels without thermal insulation, (iii) plain test vessels with thermal insulation, and (iv) coated test vessels with thermal insulation. By comparing the results obtained in these four types of tests, the separate effect and the integral effect of vessel coating and thermal insulation could be determined. Both micro-porous aluminum coating and micro-porous copper coating were employed to explore the possible effect of coating material. The steady state boiling data obtained in these tests are presented in Section 4.3.6.

4.3.6. Results of SBLB Tests

4.3.6.1. Separate Effect Due to Vessel Coating for Case Without Insulation

For vessel lower head with micro-porous coating but no insulation, the local CHF (see Figure 4-26) along the angular location has the profile as follows:

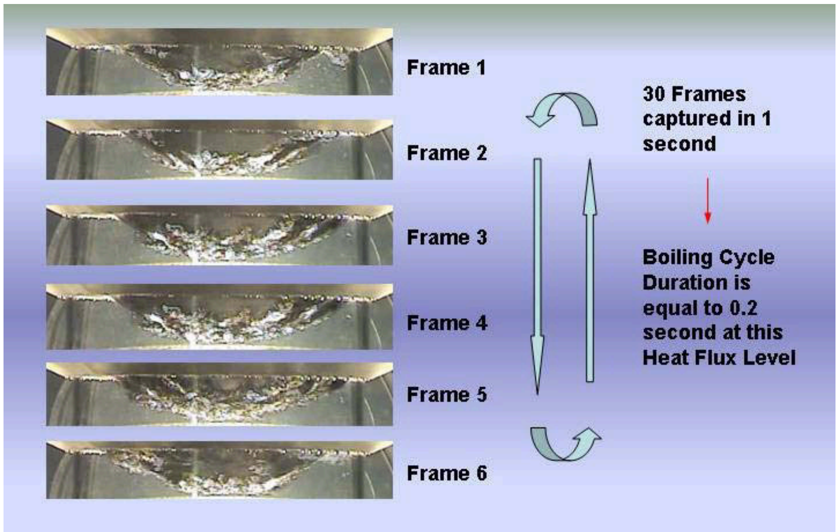

30 Frames captured in 1 second

Boiling Cycle Duration is equal to 0.2 second at this Heat Flux Level

Figure 4-24. Boiling cycle investigation for steady state test

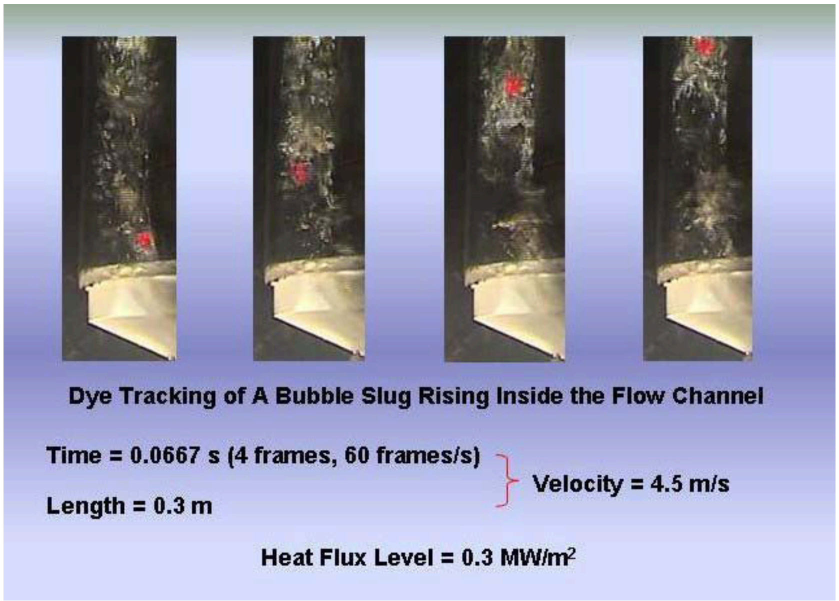

Dye Tracking of A Bubble Slug Rising Inside the Flow Channel

Time = 0.0667 s (4 frames, 60 frames/s)
Length = 0.3 m
Velocity = 4.5 m/s

Heat Flux Level = 0.3 MW/m^2

Figure 4-25. Vapor velocity dye tracking measurement.

$$\left(q''_{CHF}\right)_C = (1+0.036\Delta T_{sub})(0.8525-1.083\theta+2.63\theta^2-0.94\theta^3) \quad \text{(MW/m}^2\text{)} \tag{4-27}$$

where θ, measuring from the bottom center of the vessel, is in radian and $\Delta T_{sub}=T_{sat}-T_{water}$, accounts for the subcooling effect on the local CHF limit.

For a plain vessel without coating nor insulation structure, the local CHF (see Figure 4-26) along the angular location has the profile as follows:

$$\left(q''_{CHF}\right)_O = (1+0.036\Delta T_{sub})(0.4339+0.3467\theta+0.0604\theta^2) \quad \text{(MW/m}^2\text{)} \tag{4-28}$$

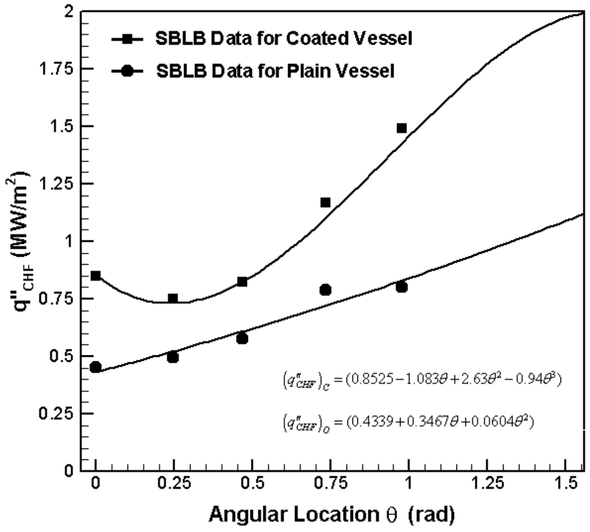

Figure 4-26. Variations of local CHF limits on the vessel outer surface for cases with and without vessel coating

The enhancement factor $(F_C)_O$ is correlated by curve fitting (see Figure 4-27) the individual CHF ratio at each test angular location as follows:

$$(F_C)_O = \frac{(q''_{CHF})_C}{(q''_{CHF})_O} = \left(1.88 - 2.35\theta + 2.37\theta^2\right) \quad \text{for } 0 < \theta < 0.38 \quad \text{(a)}$$

$$(F_C)_O = \frac{(q''_{CHF})_C}{(q''_{CHF})_O} = \left(1.73 - 2.14\theta + 3.63\theta^2 - 1.45\theta^3\right) \quad \text{for } 0.38 < \theta < 1.57 \quad \text{(b)} \qquad (4\text{-}29)$$

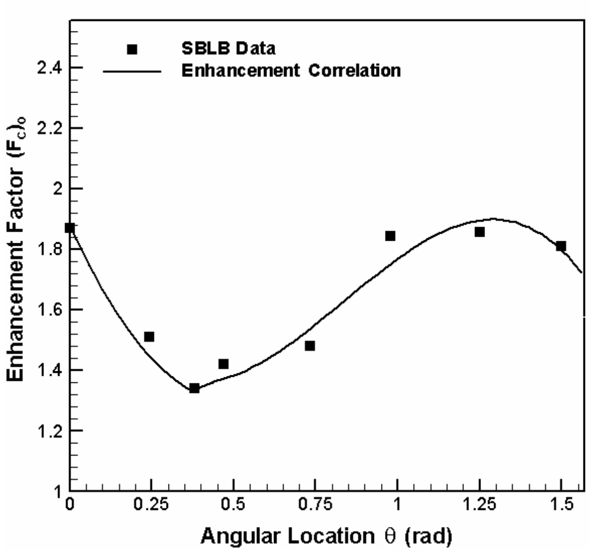

Figure 4-27. Correlation of enhancement factor, $(F_C)_O$, for coated vessel without thermal insulation

4.3.6.2. Separate Effect due to Enhanced Insulation Structure for Uncoated Vessel

For a plain vessel with enhanced insulation structure, the local CHF (see Figure 4-28) has different profiles for three separate regions of the lower head due to the variation of flow area formed between the vessel and the insulation structure.

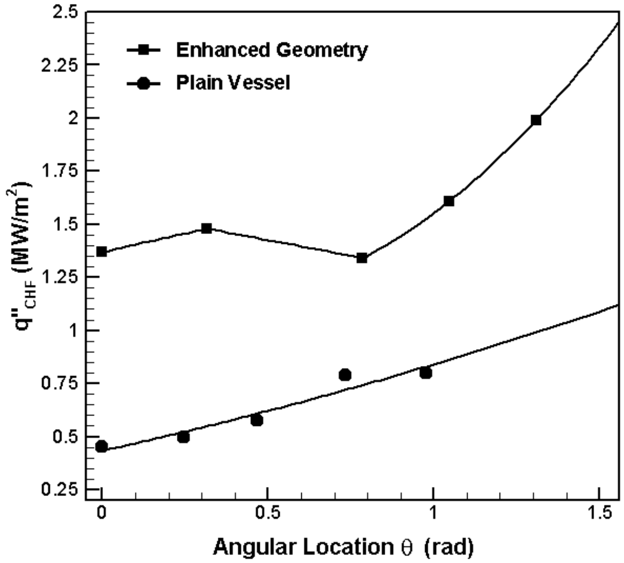

Figure 4-28. Variation of local CHF limits on outer surface of plain vessel for cases with and without enhanced insulation structure.

In the bottom center region of the channel where 0 < θ < 0.3142, the experimental results gave rise to the following CHF correlation:

$$\left(q''_{CHF}\right)_{EI} = (1.37 + 0.3501\theta) \qquad (\mathrm{MW/m^2}) \tag{4-30}$$

In the convergent region covering the upper exit of the inlet section up to the shear key location where 0.3142<<0.7854, the experimental results gave rise to the following expression:

$$\left(q''_{CHF}\right)_{EI} = \left(1.5734 - 0.2951\theta\right)\left[1 + 0.0925\left(\theta - 0.3142\right)^{1/3} \Delta T_{sub}\right] \tag{4-31}$$

where $\Delta T_{sub} = T_{sat} - T_{water.}$ The term ΔT_{sub} accounts for the subcooling effect on local CHF limit.

In the divergent region covering the upper part of the channel beyond the shear key location where 0.7854 < θ < 1.5708, the experimental results gave rise to the following expression:

$$\left(q''_{CHF}\right)_{EI} = \left(1.19 - 0.4393\theta + 0.8025\theta^2\right)\left[1 + 0.0746\left(1 - 0.573\left(\theta - 0.7854\right)\right)\Delta T_{sub}\right] \tag{4-32}$$

where ΔT_{sub} accounts for the subcooling effect.

The enhancement factor F_{EI} is correlated (see Figure 4-29) by comparing the test data to the plain vessel CHF profile, i.e.,

$$F_{EI} = \frac{\left(q''_{CHF}\right)_{EI}}{\left(q''_{CHF}\right)_O} = F_{sub}\left(3.0243 - 1.0423\theta\right) \quad \text{for } 0 < \theta < 0.3142 \quad \text{(a)}$$

$$F_{EI} = \frac{\left(q''_{CHF}\right)_{EI}}{\left(q''_{CHF}\right)_O} = F_{sub}\left(3.2933 - 1.8983\theta\right) \quad \text{for } 0.3142 < \theta < 0.7854 \quad \text{(b)}$$

$$F_{EI} = \frac{\left(q''_{CHF}\right)_{EI}}{\left(q''_{CHF}\right)_O} = F_{sub}\left(1.5467 + 0.3254\theta\right) \quad \text{for } 0.7854 < \theta < 1.5708 \quad \text{(c)} \qquad (4\text{-}33)$$

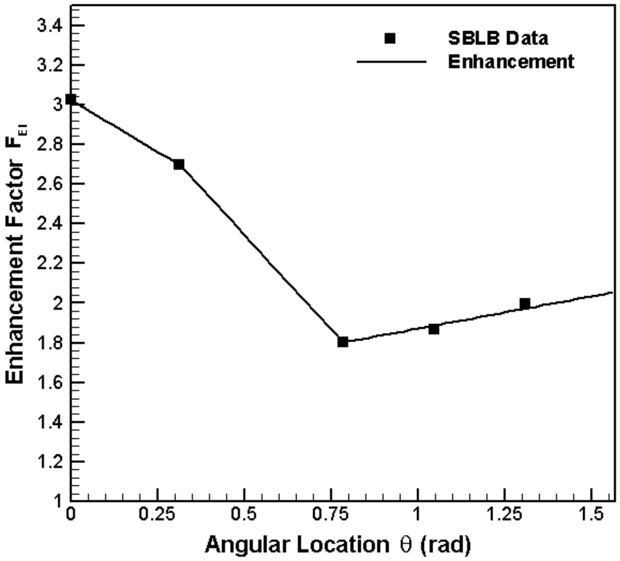

Figure 4-29. Correlation of enhancement factor, F_{EI}, for plain vessel with enhanced insulation structure

The subcooling effect for different angular locations are given by

$$F_{sub} = \begin{cases} (1+0.036\Delta T_{sub})^{-1} \quad \text{for } 0 < \theta < 0.3142 \\ \left[1+0.0925\left(\theta-0.3142\right)^{1/3}\Delta T_{sub}\right](1+0.036\Delta T_{sub})^{-1} \quad \text{for } 0.3142 < \theta < 0.7854 \\ \left[1+0.0746\left(1-0.573\left(\theta-0.7854\right)\right)\Delta T_{sub}\right](1+0.036\Delta T_{sub})^{-1} \quad \text{for } 0.7854 < \theta < 1.5708 \end{cases} \qquad (4\text{-}34)$$

4.3.6.3. Separate Effect Due to Enhanced Design Alone for the Uncoated Vessel

For a plain vessel with insulation structure that has not been enhanced (i.e., such as the design proposed for the Korean Next Generation Reactor), the local CHF (see Figure 4-30) has different profiles for three separate regions of the lower head due to the variation of flow area formed between the vessel and the insulation structure.

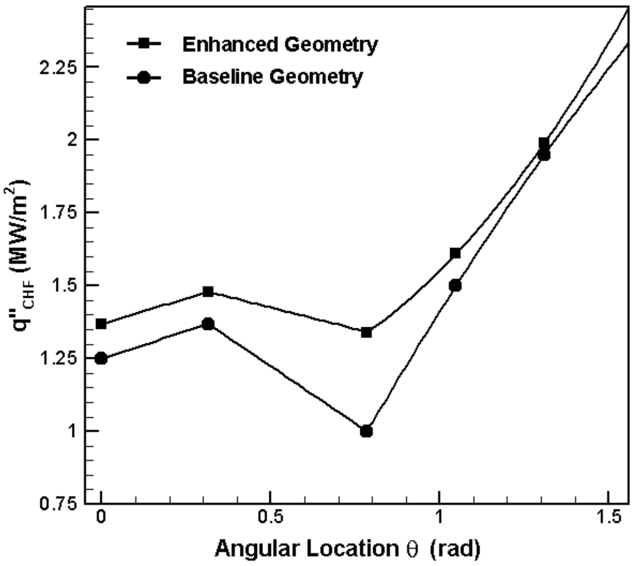

Figure 4-30. Variation of the local CHF limits on the outer surface of a plain vessel surrounded by an insulation structure with and without enhanced design

In the bottom center region of the channel where 0 < θ < 0.3142, the previous experimental results for KNGR gave rise to the following CHF correlation:

$$\left(q''_{CHF}\right)_I = (1.25 + 0.3819\theta) \qquad (\text{MW/m}^2) \qquad (4\text{-}35)$$

In the convergent region covering the upper exit of the inlet section up to the minimum gap location where 0.3142 < θ < 0.7854, the experimental results gave rise to the following expression:

$$\left(q''_{CHF}\right)_I = \left(1.6167 - 0.7852\theta\right)\left[1 + 0.0925\left(\theta - 0.3142\right)^{1/3} \Delta T_{sub}\right] \qquad (4\text{-}36)$$

where $\Delta T_{sub} = T_{sat}\text{-}T_{water.}$ The term ΔT_{sub} accounts for the subcooling effect on local CHF limit.

In the divergent region covering the upper part of the channel beyond the minimum gap location where 0.7854 < θ < 1.5708, the experimental results gave rise to the following expression:

$$\left(q''_{CHF}\right)_I = \left[1.225 + 2.5783\left(\theta - 0.7854\right) - 0.3648\theta^2\right]\left[1 + 0.0746\left(1 - 0.573\left(\theta - 0.7854\right)\right)\Delta T_{sub}\right] \qquad (4\text{-}37)$$

where ΔT_{sub} accounts for the subcooling effect.

The enhancement factor F_E is correlated (see Figure 4-31) by comparing the result given by Equations. (4-30)-(4-32) to the result given by Equations (4-35)-(4-37):

$$F_E = \frac{\left(q''_{CHF}\right)_{EI}}{\left(q''_{CHF}\right)_I} = F_{sub}\left(1.096 - 0.509\theta\right) \qquad \text{for } 0 < \theta < 0.3142 \qquad (a)$$

$$F_E = \frac{\left(q''_{CHF}\right)_{EI}}{\left(q''_{CHF}\right)_I} = F_{sub}\left(0.9071 + 0.5511\theta\right)$$

for 0.3142< θ <0.7854 (b)

$$F_E = \frac{\left(q''_{CHF}\right)_{EI}}{\left(q''_{CHF}\right)_I} = F_{sub}\left(3.4235 - 3.8783\theta + 1.5604\theta^2\right)$$

for 0.7854< θ <1.5708 (c) (4-38)

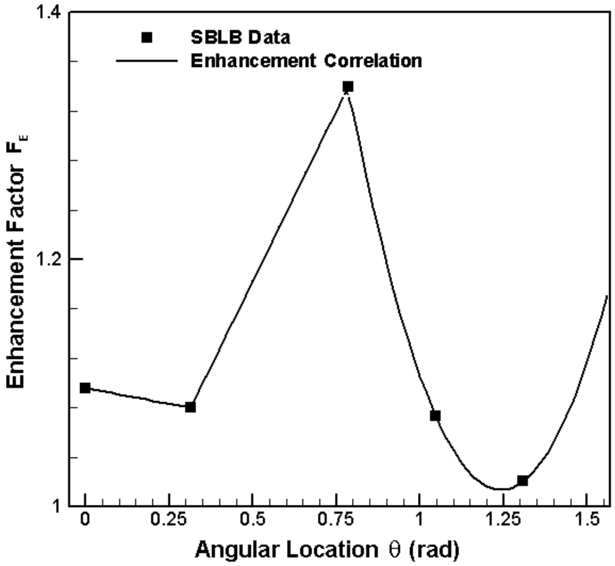

Figure 4-31. Correlation of enhanced factor, F_E, for plain vessel surrounded by an enhanced insulation structure.

4.3.6.4. Separate Effect Due to Enhanced Insulation Structure for Coated Vessel

For a coated vessel with enhanced insulation structure, the local CHF (see Figure 4-32) has different profiles for three separate regions of the lower head due to the variation of flow channel formed between the vessel and the insulation structure.

In the bottom center region of the channel where 0 < θ < 0.3142, the experimental results gave rise to the following CHF correlation:

$$\left(q''_{CHF}\right)_{C+EI} = (1.49 + 0.3183\theta) \text{ (MW/m}^2\text{)} \tag{4-39}$$

In the convergent region covering the upper exit of the inlet section up to the shear key location where 0.3142< θ <0.7854, the experimental results gave rise to the following expression:

$$\left(q''_{CHF}\right)_{C+EI} = \left(1.65 - 0.191\theta\right)\left[1 + 0.0925\left(\theta - 0.3142\right)^{1/3} \Delta T_{sub}\right] \tag{4-40}$$

In the divergent region covering the upper part of the channel beyond the shear key location where 0.7854<<1.5708, the experimental results gave rise to the following expression:

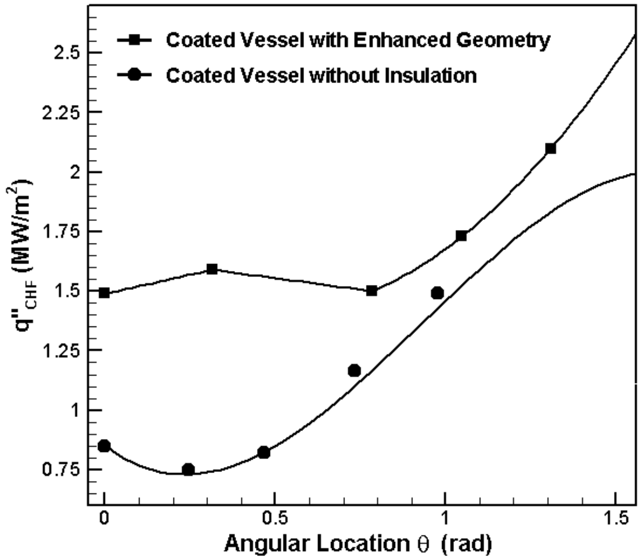

Figure 4-32. Variations of the local CHF limits on the outer surface of a coated vessel with and without thermal insulation

$$\left(q''_{CHF}\right)_{C+EI} = \left(1.65 - 0.9931\theta + 1.0213\theta^2\right)\left[1 + 0.0746\left(1 - 0.573\left(\theta - 0.7854\right)\right)\Delta T_{sub}\right] \qquad (4\text{-}41)$$

The enhancement factor $(F_C)_{EI}$ is correlated (see Figure 4-33) by comparing the result given by Equations (4-39)-(4-41) to the result given by Equation (4-27):

$$\left(F_C\right)_{EI} = \frac{\left(q''_{CHF}\right)_{C+EI}}{\left(q''_{CHF}\right)_C} = F_{sub}\left(1.7478 + 1.2858\theta\right) \quad \text{for } 0 < \theta < 0.3142 \qquad \text{(a)}$$

$$\left(F_C\right)_{EI} = \frac{\left(q''_{CHF}\right)_{C+EI}}{\left(q''_{CHF}\right)_C} = F_{sub}\left(2.7257 - 1.8266\theta\right) \quad \text{for } 0.3142 < \theta < 0.7854 \qquad \text{(b)}$$

$$\left(F_C\right)_{EI} = \frac{\left(q''_{CHF}\right)_{C+EI}}{\left(q''_{CHF}\right)_C} = F_{sub}\left(2.6717 - 2.6522\theta + 1.1388\theta^2\right) \quad \text{for } 0.7854 < \theta < 1.5708 \quad \text{(c)} \qquad (4\text{-}42)$$

4.3.6.5. Integral Effect Due to Enhanced Design and Vessel Coating

The integral enhancement effect due to the combined use of an enhanced insulation structure and vessel coating can be obtained by comparing the experimental results (see Figures 4-34 and 4-35) given in Equations (4-38)-(4-40) to the results given in Equation (4-28).

$$F_{C+EI} = \frac{\left(q''_{CHF}\right)_{C+EI}}{\left(q''_{CHF}\right)_O} = F_{sub}\left(3.2892 - 1.1544\theta\right) \quad \text{for } 0 < \theta < 0.3142 \qquad \text{(a)}$$

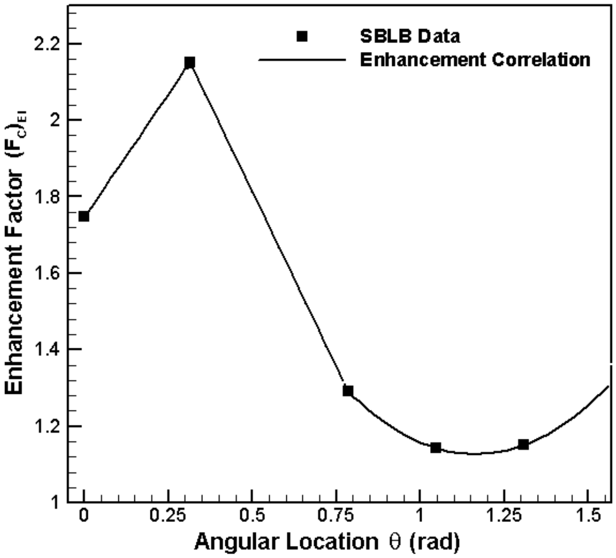

Figure 4-33. Correlation of enhancement factor, $(F_c)_{EI}$, for coated vessel with enhanced insulation structure.

$$F_{C+EI} = \frac{\left(q''_{CHF}\right)_{C+EI}}{\left(q''_{CHF}\right)_O} = F_{sub}\left(3.5283 - 1.9153\theta\right)$$

for 0.3142 < θ < 0.7854 (b)

$$F_{C+EI} = \frac{\left(q''_{CHF}\right)_{C+EI}}{\left(q''_{CHF}\right)_O} = F_{sub}\left(2.8295 - 1.7607\theta + 0.936\theta^2\right)$$

for 0.7854 < θ < 1.5708 (c) (4-43)

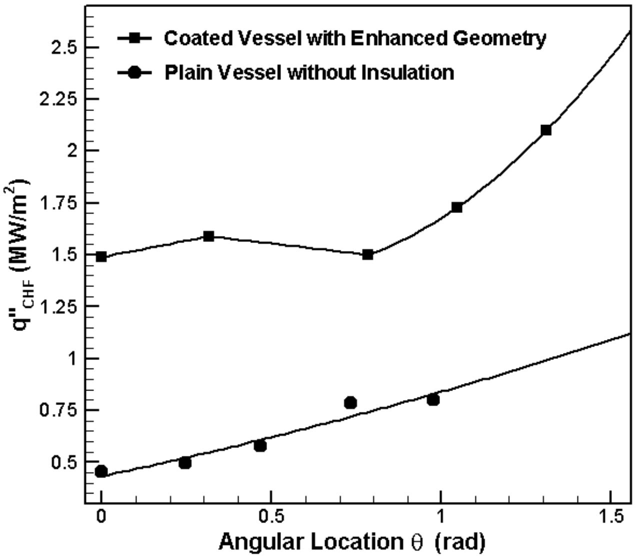

Figure 4-34. Variations of the local CHF limit on the vessel outer surface for cases with and without vessel coating and enhanced insulation

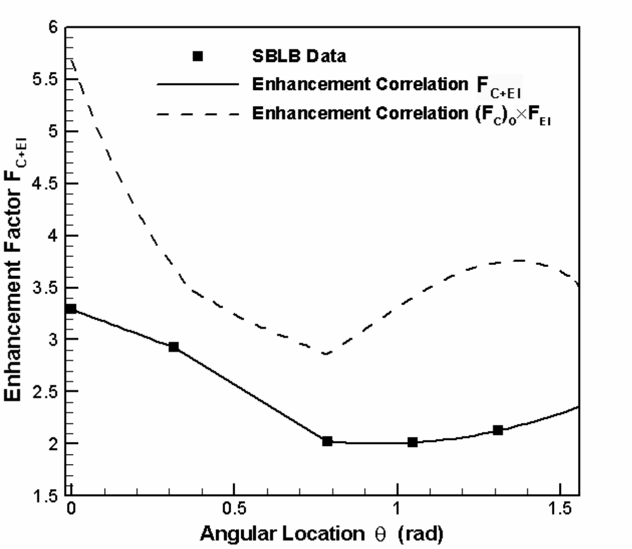

Figure 4-35. Correlation of the enhanced factor, F_{C+EI}, for a coated vessel with an enhanced insulation structure.

It can be seen that the enhancement factor, F_{C+EI}, for the integral effect is smaller than the combination of the two separate enhancement factors which is equal to $(F_c)_o{}^*F_{EI}$.

4.3.7. Summary and Conclusions

Based on the SBLB test results obtained in the project, the following conclusions for Task 3 can be made:

- For plain vessels without coatings or thermal insulation, the local boiling curve tended to shift upward and to the right as the angular position was increased from the bottom center toward the equator of the test vessel. For a given wall superheat, higher nucleate boiling rates were obtained in the locations downstream of the bottom center. The local CHF exhibited a minimum at the bottom center location and increased monotonically with the angular position toward the equator of the vessel.
- Unlike the trend observed for plain vessels, the local boiling curve for coated vessels without thermal insulation did not shift monotonically upward and to the right as the angular position was increased from the bottom center toward the equator of the test vessel. The local CHF limit at the bottom center was actually higher than the values for adjacent downstream locations up to θ = 28°. The local CHF exhibited a minimum at the θ = 14° location rather than at the bottom center. This non-monotonic behavior of the local CHF variation was largely due to the capillary effect of the micro-porous coatings, where there was a continuous liquid supply from all radial directions toward the bottom center.
- For the case with thermal insulation, the nucleate boiling rates do not exhibit monotonic trend either, i.e., the local boiling curve does not shift upward and to the right monotonically with increasing angular position. Rather, the local CHF limit tended to increase from the bottom center at first, then decrease toward the minimum gap location, and finally increase toward the equator.

This non-monotonic behavior is evidently due to the local variation of the two-phase motions in the annular channel between the test vessel and the insulation structure.

- The optical and SEM records showed that the micro-porous layer coatings had the form of a porous matrix composed of interconnected channels and different pores on the surface. Improvement in nucleate boiling heat transfer and CHF could be attributed to the structure of the porous layer itself and the capillary action it induced. The matrix of cavities and voids within the coating effectively trapped vapor, which served as active nucleation sites. These sites in turn were fed with liquid flowing through the interconnected channels. The pores on the surface of the porous coating served as flow inlets for liquid supply to the heating surface, leading to appreciable enhancements in the local CHF limits.
- Micro-porous aluminum coating appeared to be very durable. Even after many cycles of steady state boiling, the vessel coating remained rather intact, with no apparent changes in color or structure. Moreover, the heat transfer performance of the coating was found to be highly desirable with an appreciable CHF enhancement but very little effect of aging. Although similar heat transfer performance was observed for micro-porous copper coating, the latter was found to be much less durable and tended to degrade after several cycles of boiling. It appeared that the most suitable coating material for ERVC is micro-porous aluminum coating.
- For a coated hemispherical vessel with thermal insulation, the bubbles were generated at a higher frequency compared to that for a plain vessel without thermal insulation. This clearly indicates that a vessel with micro-porous surface coating would give rise to a shorter boiling cycle. This enhanced boiling cycle explains the increased nucleate boiling rate for a coated vessel because more latent heat of vaporization could be transferred per unit time from the reactor surface.
- For a coated vessel with thermal insulation, the vapor bubbles generated in the bottom center region did not tend to agglomerate. This behavior could be due to the availability of vapor escape paths provided by the porous cavities of the coating. Although vapor bubbles tended to disperse on the coated vessel, a higher boiling site density resulted in a higher rate of heat removal, i.e., higher boiling rate.
- Depending on the angular position, a local CHF enhancement of 200% to 330% over a plain vessel could be achieved using an enhanced insulation structure with vessel coatings. It appears that ERVC with the use of vessel coatings and an enhanced insulation structure could provide sufficient cooling for high-power reactors such as APR1400.

4.4. KAERI HERMES-HALF Facility Description and Test Results

Korea Atomic Energy Research Institute

4.4.1. Introduction

KAERI has studied on the insulation design modification of current KSNP (Koran Standard Nuclear Power plant)-like configuration for CHF enhancement to increase the thermal margin for IVR. Under the ERVC condition, the heated lower reactor vessel wall induces the two-phase natural circulation flow between the reactor vessel wall and the insulation material. In general, an increase in the mass flow rate of the coolant between the reactor vessel wall and the insulation material leads to an increase in the CHF at the lower outer reactor vessel wall. This results in an increase of the wall heat removal rate by the convective coolant circulation flow. This circulation flow is dependent on the configuration of the reactor vessel insulation, such as, the water inlet area and position, coolant (water and steam) outlet area and position, and the gap geometry between the reactor vessel and the insulation. For this reason, detailed study of the coolant flow in the reactor cavity during the severe accidents is necessary to enhance the IVR through external reactor vessel cooling in the APR1400.

To observe and evaluate the two-phase natural circulation phenomena through the gap between the reactor vessel and the insulation in the APR1400 under external reactor vessel cooling, a HERMES-HALF experiment has been performed in KAERI. The HERMES-HALF is a non-heating (air/water) experimental study on the two-phase natural circulation through the annular gap between the reactor vessel and the insulation. The objectives of this HERMES-HALF study are to observe and evaluate the two-phase natural circulation phenomena through the gap between the reactor vessel and the insulation in the APR1400. That is, the circulation flow rate, three dimensional effect, and flow instability in the gap between the APR1400 reactor vessel and insulation were simulated by the HERMES-HALF experiments. For these purposes, a half-scaled experimental facility was prepared utilizing the results of a scaling analysis to simulate the APR1400 reactor and insulation system.

4.4.2. Scaling and Features of Test Section

As documented in Reference 4-15, the reactor vessel/insulation system configuration of the APR1400 is shown in Figure 4-36. A total 61 In-Core Instrument (ICI) penetrations and 4-shear keys are installed in the reactor vessel. For a natural circulation flow path, it is designed that water inlets and venting slots are installed on the insulation wall. The cavity flooding water for the ERVC is filled up to about 0.91m below from the centerline of the hot legs.

Cheung's scaling law[4-28] was adapted for designing the HERMES-HALF experimental facility. The HERMES-HALF is a non-heating (air / water) experimental study on the two-phase natural circulation through the annular gap between the reactor vessel and the insulation. However, in the real APR1400 situation, steam / water system should be considered, instead of air / water system. Therefore, the scaling law is not exactly satisfied to simulate the HERMES-HALF facility to the APR1400 system due to differences between air and steam density. By the Cheung's scaling law, the gas density effect of each characteristic time ratio is as follows.

Characteristic time ratio for the boiling process: $\pi_b \sim \rho_g^{-0.5}$

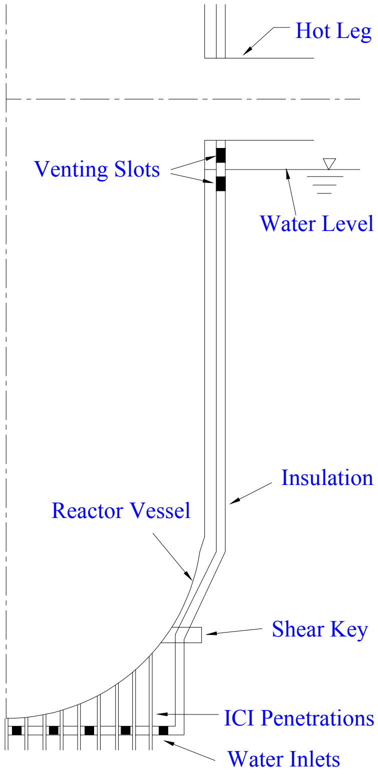

Figure 4-36. Reactor vessel/insulation system of APR1400.

Characteristic time ratio for heat conduction in the vessel wall: $\pi_w \sim \rho_g^{\ 0.4}$

Characteristic time ratio for the momentum transfer in the flow: $\pi_m \sim \rho_g^{\ -0.2}$

Characteristic time ratio for steam venting through the minimum gap: $\pi_v \sim \rho_g^{\ -0.6}$

Characteristic time ratio for water ingression through the bottom plate: $\pi_i \sim \rho_g^{\ -0.9}$

The ratio of the air density to the steam density is about 2. So, the characteristic time ratios of the HERMES-HALF facility are 1.5 – 1.9 times larger (or smaller) than the APR1400 due to the gas density difference.

The schematics diagram of the HERMES-HALF experimental facility is shown in Figure 4-37. The facility consists of 3 parts, that is, a main experimental facility, an air supply system and a water recirculation system. The main facility is a half scaled-down reactor vessel and an insulation part which is prepared utilizing the results of a scaling analysis proposed by Cheung[4-28] to simulate the APR1400 reactor and insulation system. By the scaling analysis, vessel diameter, height, water level, shear key size, and ICI nozzle diameter are linearly scaled-down, that is, a half scale. So, the radius of the vessel is 1.269 m, and the annular gap size is 0.153 m, which is equivalent to the 0.216m gap in the APR1400 reactor. Due to the conical configurations of the insulation, the minimum gap region between the reactor vessel and the insulation is located at 56.6^{o} based on the vertical axis of the reactor vessel. The minimum gap size is set at

0.063m. That is, the annular gap size and the minimum gap size are the $\sqrt{1/2}$ scaled-down. The key dimensions and sizes of the main experimental parts are summarized and compared with the Korean Standard Nuclear Plant (KSNP) and APR1400 reactor in Reference 4-15. By considering the symmetrical feature of the reactor vessel and the insulation system, only the half section of the APR1400 reactor is simulated. For visualization, windows made of polycarbonate are installed on the annular insulation part. The ICI penetration tubes and shear keys are also simulated in this experimental facility. A water reservoir is prepared to realize an equivalent pressure condition of the lower water inlet. That is, the inlet condition is controlled by changing the water level in the reservoir. For maximizing the natural circulation flow, water inlets and outlet ports exist in the insulation. The water inlet plate, that is, the bottom of the insulation, is shown in Figure 4-38. To simulate the water inlets, there are 23 holes in the central part, and 35 holes in the circumferential part of the water inlet plate. Each hole (diameter - 75 mm) can be plugged, therefore, the areas and positions of the inlets are adjustable. The maximum inlet area is up to 0.25 m^2.

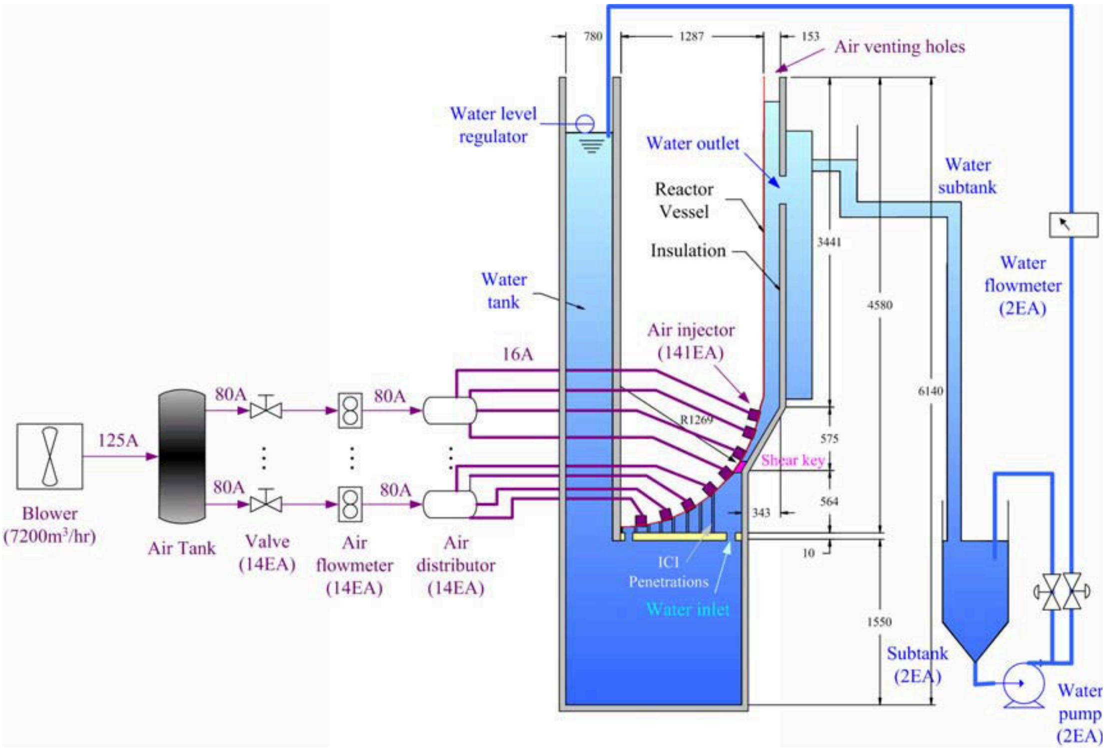

Figure 4-37. HERMES-HALF experimental facility.

The natural circulation flow is discharged to three outlets in the insulation. Three outlets have rectangular shapes, which are located at 45, 90, and 135 degrees of longitude on the annular section of the reactor vessel wall. The area and vertical position of each outlet are adjustable. The flooded water through the outlet is accumulated in the sub-tank and then the water in the sub-tank is transferred to the water reservoir by a water pump. Because the flooded water through each outlet port is independently re-circulated by the water recirculation system, the natural circulation flow in the experimental section has no effect on the water recirculation system. The recirculation flow rate is measured by a water flow meter which is installed in the recirculation water pipe between the pump and the water reservoir.

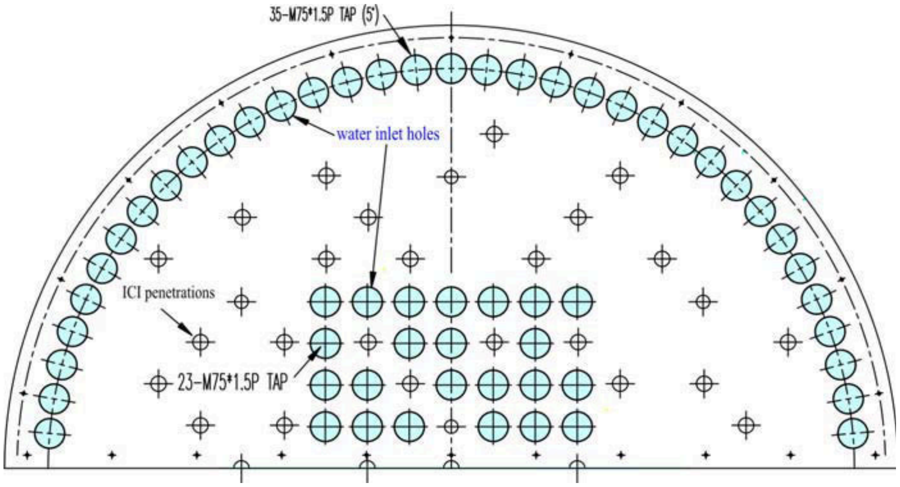

Figure 4-38. Water inlet plate of the HERMES-HALF experimental facility.

In the HERMES-HALF experiment, the two phase flow is generated by not a direct heating method but an air injection method. As a non-heating experiment, an equivalent air is injected through 141 air injectors by the air supply system. The air is generated by a blower system and the air path branches off from 14 air distributors by air ducts with 80 mm inner diameter. The air flow rate toward each air distributor is controlled and measured by an air control valve and an air flow meter. The air passing by the air distributors is supplied to the gap region through 141 air injectors installed on the lower head reactor vessel wall. Each air injector is made of a G2 glass filter which generates the fine air bubbles. The equivalent air injection diameter from each air injector is 70 mm. The experimental heat distribution along the lower head vessel wall for determining the air injection rate is obtained by IVR evaluation as shown in Figure 4-39.[4-30] Because of the higher heat flux in the top region of the vessel, the injectors are arranged in the top region of the lower head vessel. The injected air flow-rate is calculated by Equation (4-44) to simulate the equivalent heat flux condition assuming saturated water conditions.

$$\dot{V}_{a,z} = \frac{\int_{inlet}^{z} q''\xi \, dz}{h_{fg}\,\rho_g} \qquad (4\text{-}44)$$

where $\dot{V}_{a,z}$ is the total volume flow rate of air at z position,

q'' : is the wall heat flux,

ξ : is the perimeter,

h_{fg} : is the water enthalpy change of liquid to vapor,

ρ_g : is the density of vapor.

The $\dot{V}_{a,z}$ in the Equation (4-44) is the same as the volumetric vapor generation rate of the heating experiment at a given heat flux condition. Under the heating experimental condition, the vapor bubbles are naturally generated in the heated vessel. However, air bubbles with the same volumetric generation rates of the vapor are directly injected. Therefore the non-heating experiment is meaningful as a hydraulic test.

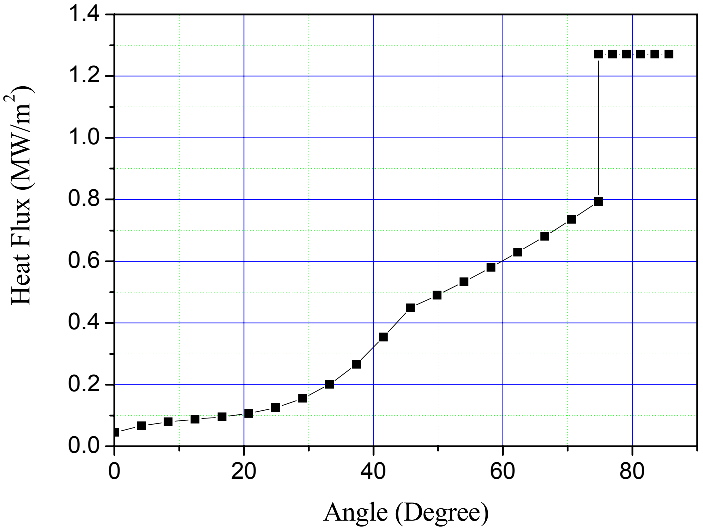

Figure 4-39. Heat flux distribution along the latitudinal position of the lower head vessel wall by the IVR evaluation.

4.4.3. Experimental Results and Discussion

The parameters of the HERMES-HALF experiments are the air flow rates, the water inlet and outlet area. The HERMES-HALF experimental conditions are the following. Two outlets located at 45 and 135 degrees longitude on the annular section of the reactor vessel wall are opened. The shape of each outlet is rectangular, that is, the horizontal size is 0.2 m and the vertical is 0.375 m. So, the total outlet area is 0.15 m^2. The height from the bottom of the reactor vessel to the center of the outlet port is 3.384 m. To adjust the water inlet area, some holes of 35 holes at the circumferential part of the water inlet plate were plugged. The angular position of inlet is the same as that of outlet, that is, 45 and 135 degrees longitude on the annular section. The external water reservoir is filled with stagnant water up to 3.571 m from the bottom of the reactor vessel.

The visualization results of the HERMES-HALF experiments for the condition of a 10% (838 m^3/hr) air injection rate of the maximum air flow rate suggested by the IVR evaluation (Figure 4-39) are shown in Figure 4-40. As shown in Figure 4-40, more bubbles in the downstream region were observed than in the upstream region. The bubbles were accumulated in the region of the shear key and the minimum gap region. Weak recirculation flows in the near region of the shear key were also observed.

Figure 4-41 shows the visualization results of the HERMES-HALF experiments for the condition of 10% (838 m^3/hr) and 15% (1257 m^3/hr) air injection rates. At the higher air injection rate condition, higher recirculation flows in the near region of the shear key were observed. All the injected air could not pass through the minimum gap region, that is, choking phenomena near the minimum gap region occurred. Because of the choking phenomena, the periodic two phase back flow was generated near the minimum gap region under the higher air injection rate condition, as shown in Figure 4-41(b). The choking phenomena were observed more severely as the air flow rate increased and outlet area decreased.

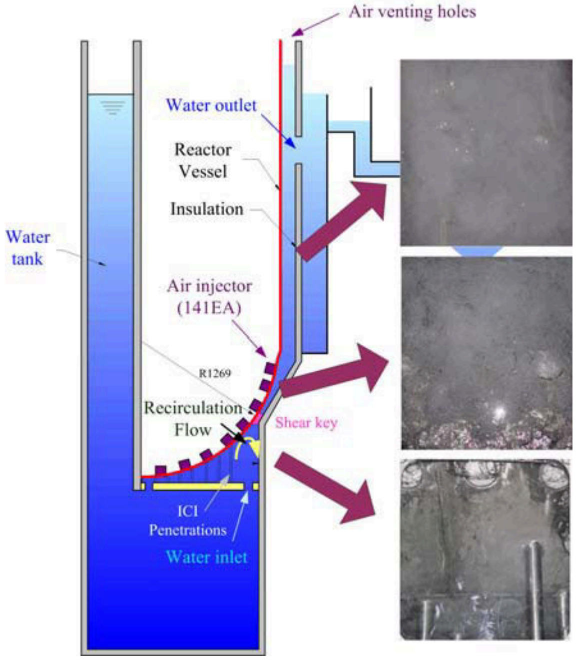

Figure 4-40. Visualization results of the HERMES-HALF experiments.

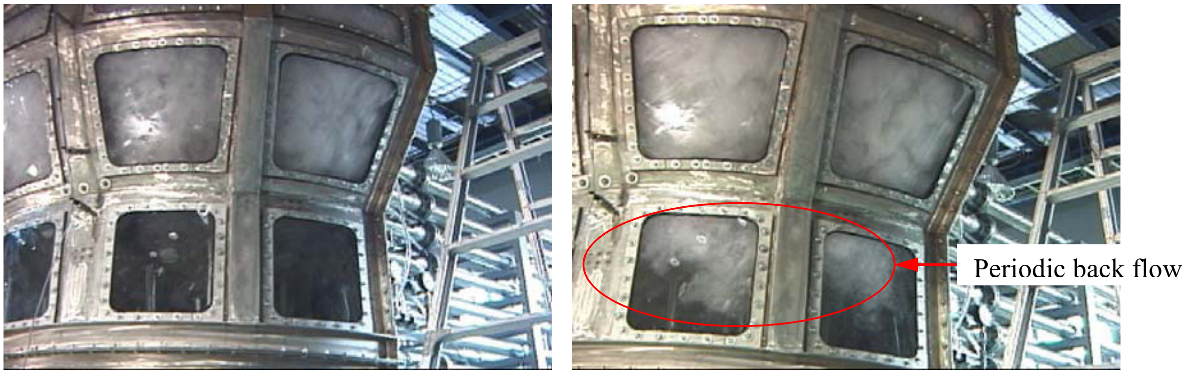

(a) Air flow rate 10%

(b) Air flow rate 15%

Figure 4-41. Choking phenomena near the minimum gap region.

Figure 4-42 shows the natural circulation flow rates by varying the air injection rate and water inlet area. In Figure 4-42, the air flow rate indicates the relative injection rate of the maximum air flow rate (8379 m^3/hr) suggested by the IVR evaluation (Figure 4-39). As shown in Figure 4-42(a), the natural circulation flow rates linearly increased as the air flow rates increased. In Figure 4-42(b), some of the circulation flow rate values were obtained by using the linear fitting curves in Figure 4-42(a). As shown in Figure 4-42(b), the natural circulation mass flow rates asymptotically increased, that is, converged on the specific value as the inlet area increased. So, a minimal water inlet area should be selected to optimize the natural circulation flow. From the experimental results, simple experimental correlations were obtained within ±10% error bound as shown in Equations (4-45) and (4-46).

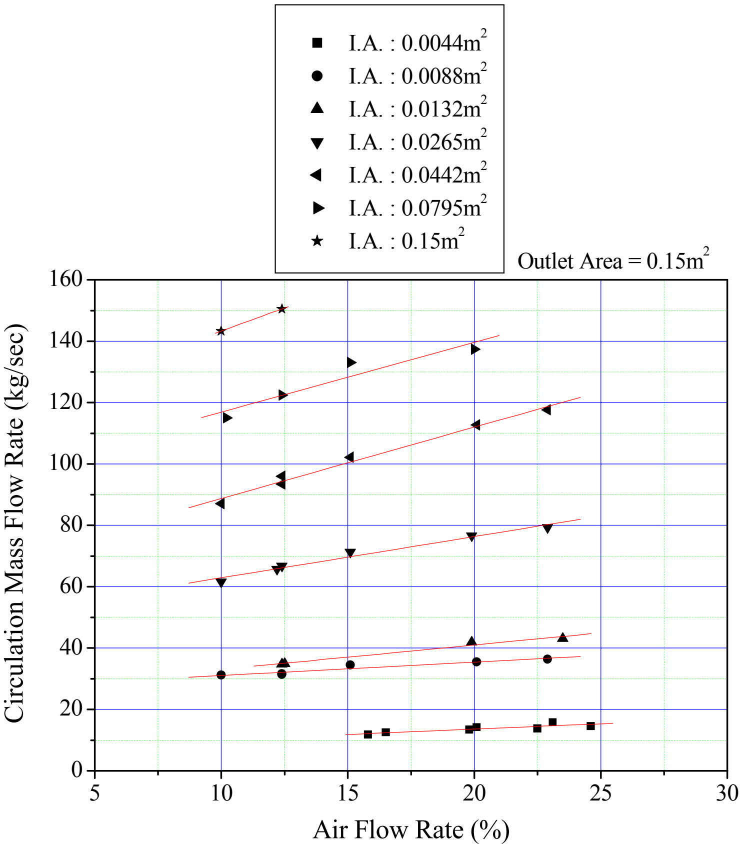

(a)

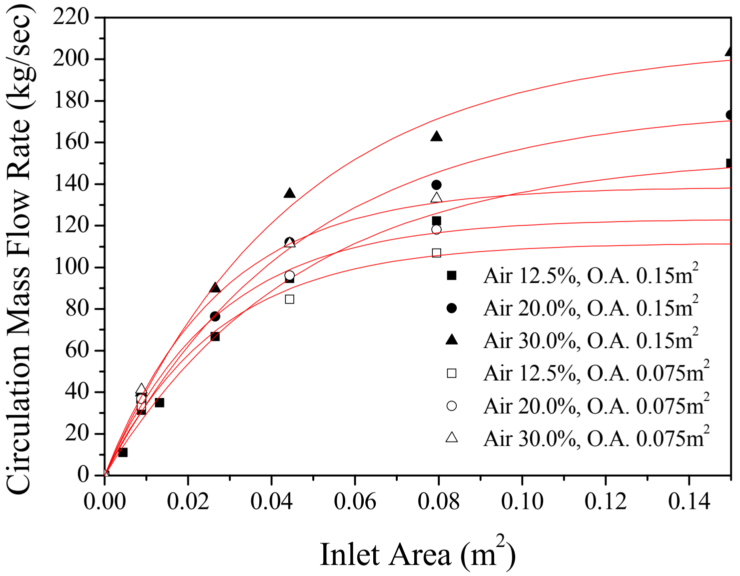

(b)

Figure 4-42. Natural circulation flow rates according to injected air flow rates and inlet areas.

$$CF = (117 + AF / 27.9)[1 - \exp(-IA / 0.0463)] \text{ at outlet area } 0.15 \text{ m}^2 \qquad (4\text{-}45)$$

$$CF = (92.5 + AF / 54.4)[1 - \exp(-IA / 0.0273)] \text{ at outlet area } 0.075 \text{ m}^2 \qquad (4\text{-}46)$$

where CF: circulation mass flow rate (kg/s),

AF: air flow rate (m^3/hr),

IA: inlet area (m^2).

In general, an increase in the mass flow rate of the coolant between the reactor vessel wall and the insulation material leads to an increase in the CHF at the lower outer reactor vessel wall. From the natural circulation mass flow rates measured by HERMES-HALF experiments, the CHF at the lower vessel wall was evaluated. Some literatures were surveyed to correlate the circulation mass flow rate with the wall CHF value. Jeong et al.[4-31]have measured the CHF on the reactor vessel outer wall using a two-dimensional slice test section at KAIST. Radius and channel areas of the test sections were 2.5 m and 10 cm × 15 cm, respectively. They have obtained CHF data under inlet subcooling of 2-25 K and mass flux 6-300 kg/m^2s. Rouge[4-32] has also conducted large-scale structure coolability by water in boiling natural convection using the SULTAN facility. By a series of SULTAN experiments with rectangular, flat, electrically heated test section, they have measured the two-dimensional two phase flow characteristics, and evaluated the circulation mass flow in large system and the limits of the CHF for wide range of thermo-dynamic (pressure: 0.1-0.6MPa, flow rate: 10-5000 kg/sec/m^2, heat flux: 0-1 or 2 MW/m^2, inlet subcooling: 0-50 ^oC) and geometric (gap size: 3-15 cm, inclination angle: 0-90 degree, heated length: 2 or 4 m) parameters. KAIST and SULTAN results are shown in Figure 4-43, that is, CHF variations according to the mass flux and water subcooling. From the HERMES-HALF experimental results, the natural circulation flow rate can be generated up to 200 kg/s by adjusting the inlet and outlet area of the insulation. This flow rate value is the same as 323 kg/m^2s mass flux value normalizing with the annular section area. As shown in Figure 4-43, the CHF values reaches about 1.3 – 1.45 MW/m^2 at the top of the lower head vessel (90 degrees) based on the 323 kg/m^2s mass flux which is measured in HERMES-HALF experiments.

4.4.4. Summary and Conclusions

Based on the HERMES-HALF experimental results, the flowing conclusions can be made:

- Flow observations indicate that choking flows occurred in the region near the shear keys. In cases with larger air injection rates and smaller outlet areas, higher recirculation flows were observed in the region near the shear keys. Because of choking phenomena, periodic air back flow occurred near the minimum gap region under conditions with higher air injection rates. Therefore, design modifications in the minimum gap region are required to ensure sufficient flow through the gap.
- Relationships between the re-circulation flow rate and the parameters in the insulation design were examined. As the water inlet areas increased, the natural circulation mass flow rates asymptotically increased and converged to a certain value. The outlet area also influenced the re-circulation flow rate. Experimental correlations on the natural circulation mass flow rates along the variation of the inlet / outlet area and wall heat flux were suggested.
- For inlet and outlet areas of 0.15 m^2, the natural circulation flow rate could be increased up to 200 kg/s at high heat flux conditions. Based on KAIST and SULTAN results, this natural circulation flow rate values leads to about 1.3 – 1.45 MW/m^2 CHF values at the top of the lower head vessel (90 degrees) which indicate more efficient cooling than occurs in pool boiling.

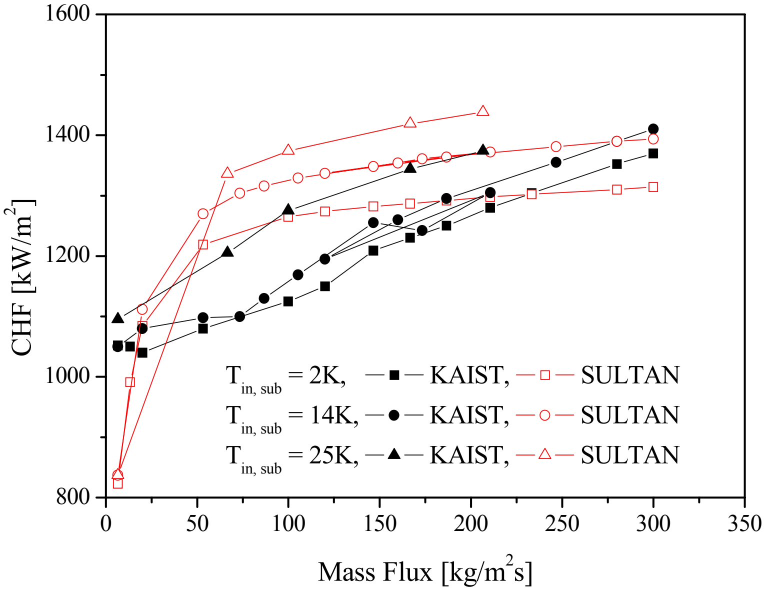

Figure 4-43. CHF variations according to the mass flux and water subcooling.

- To maximize the heat removal capability by enhancing the re-circulation flow rate through the reactor vessel/insulation gap, extensive experimental results are required to evaluate a wider range of design parameters, such as the inlet position and outlet location. Also, a detailed 3-dimensional flow analysis is necessary to evaluate the local effect, such as choking phenomena near the shear key. To apply the experimental data to the real situation, the similarity of the non-heating experiment to the heating experiment should be verified.

4.5. Summary and Conclusions

In Task 3, various types of experiments were performed at SNU, PSU, and KAERI to obtain essential information for addressing important issues on external reactor vessel cooling (ERVC) of high-power reactors such as APR1400 under severe accidents conditions. Key ERVC issues that were considered in Task 3 included delayed flooding of the reactor vessel owing to the large volume between the cavity floor and the lower head, local CHF limits for downward facing boiling on the vessel outer surface, thermal margin for maintaining the integrity of the reactor vessel, methods for ERVC enhancement, two-phase natural circulation through the gap between the reactor vessel and the insulation structure, and choking limit for steam venting during ERVC. To provide insights for addressing these key issues, boiling and two-phase flow tests were conducted in the DELTA and GAMMA facilities at SNU, the SBLB facility at PSU, and the HERMES-HALF facility at KAERI. Key insights gained from these tests are summarized in this section.

At SNU, the following insights were gained from tests conducted in the DELTA-1D, DELTA-3D, and GAMMA-3D facilities.

- In the DELTA 1D tests, one could observe the interfacial wavy motion of vapor film from the inclined flat plates. The measured wall temperatures took on similar values except at 5 mm from the leading edge because of the thinnest vapor film observed there. The interfacial wavelength of vapor film flow could unfortunately not be visualized due to thin vapor film thicknesses.
- Comparisons between DELTA-3D data and previous studies indicate that the heat transfer coefficients obtained from the DELTA tests are greater than those from numerical analysis for laminar film boiling. Thus, the film boiling regime in the DELTA-3D tests is not simply laminar, but involves more complexities like the Helmholtz instability. For the DELTA-3D tests, the film boiling heat transfer coefficients considering the interfacial wavy motion agree better with the experimental results within ± 4.5% than those for laminar film boiling analysis without interfacial wave consideration. But the difference between laminar film boiling heat transfer coefficients and measured film boiling heat transfer coefficients is relatively smaller than those in the 294 mm diameter tests, so the simple laminar film boiling regime is considered to span a greater portion of the 120 mm test section area than of the 294 mm test section.
- GAMMA 3D results indicated that CHF values decrease as the inclination angle increases for large inlet subcooling. In other words, the angular qualities are augmented by the increase in enthalpy as the angle increases. The film boiling heat transfer coefficients on the downward-facing hemisphere were measured and analyzed.

At PSU, the following insights were gained from tests conducted in the SBLB facility:

- For plain vessels without coatings or thermal insulation, the local boiling curve tended to shift upward and to the right as the angular position was increased from the bottom center toward the equator of the test vessel. For a given wall superheat, higher nucleate boiling rates were obtained in the locations downstream of the bottom center. The local CHF exhibited a minimum at the bottom center location and increased monotonically with the angular position toward the equator of the vessel.
- Unlike the trend observed for plain vessels, the local boiling curve for coated vessels without thermal insulation did not shift monotonically upward and to the right as the angular position was increased from the bottom center toward the equator of the test vessel. The local CHF limit at the bottom center was actually higher than the values for adjacent downstream locations up to $\theta = 28^{\circ}$. The local CHF exhibited a minimum at the $\theta = 14^{\circ}$ location rather than at the bottom center. This

non-monotonic behavior of the local CHF variation was largely due to the capillary effect of the micro-porous coatings, where there was a continuous liquid supply from all radial directions toward the bottom center.

- For the case with thermal insulation, the nucleate boiling rates do not exhibit monotonic trend either, i.e., the local boiling curve does not shift upward and to the right monotonically with increasing angular position. Rather, the local CHF limit tended to increase from the bottom center at first, then decrease toward the minimum gap location, and finally increase toward the equator. This non-monotonic behavior is evidently due to the local variation of the two-phase motions in the annular channel between the test vessel and the insulation structure.
- The optical and SEM records showed that the micro-porous layer coatings had the form of a porous matrix composed of interconnected channels and different pores on the surface. Improvement in nucleate boiling heat transfer and CHF could be attributed to the structure of the porous layer itself and the capillary action it induced. The matrix of cavities and voids within the coating effectively trapped vapor, which served as active nucleation sites. These sites in turn were fed with liquid flowing through the interconnected channels. The pores on the surface of the porous coating served as flow inlets for liquid supply to the heating surface, leading to appreciable enhancements in the local CHF limits.
- Micro-porous aluminum coating appeared to be very durable. Even after many cycles of steady state boiling, the vessel coating remained rather intact, with no apparent changes in color or structure. Moreover, the heat transfer performance of the coating was found to be highly desirable with an appreciable CHF enhancement but very little effect of aging. Although similar heat transfer performance was observed for micro-porous copper coating, the latter was found to be much less durable and tended to degrade after several cycles of boiling. It appeared that the most suitable coating material for ERVC is micro-porous aluminum coating.
- For a coated hemispherical vessel with thermal insulation, the bubbles were generated at a higher frequency compared to that for a plain vessel without thermal insulation. This clearly indicates that a vessel with micro-porous surface coating would give rise to a shorter boiling cycle. This enhanced boiling cycle explains the increased nucleate boiling rate for a coated vessel because more latent heat of vaporization could be transferred per unit time from the reactor surface.
- For a coated vessel with thermal insulation, the vapor bubbles generated in the bottom center region did not tend to agglomerate. This behavior could be due to the availability of vapor escape paths provided by the porous cavities of the coating. Although vapor bubbles tended to disperse on the coated vessel, a higher boiling site density resulted in a higher rate of heat removal, i.e., a higher boiling rate.
- Depending on the angular position, a local CHF enhancement of 200% to 330% over a plain vessel could be achieved using an enhanced insulation structure with vessel coatings. It appears that ERVC with the use of vessel coatings and an enhanced insulation structure could provide sufficient cooling for high-power reactors such as APR1400.

Based on results from tests conducted in the KAERI HERMES-HALF facility, the flowing conclusions can be made:

- Flow observations indicate that choking flows occurred in the region near the shear keys. In cases with larger air injection rates and smaller outlet areas, higher recirculation flows were observed in the region near the shear keys. Because of choking phenomena, periodic air back flow occurred near the minimum gap region under conditions with higher air injection rates. Therefore, design modifications in the minimum gap region are required to ensure sufficient flow through the gap.

- Relationships between the re-circulation flow rate and the parameters in the insulation design were examined. As the water inlet areas increased, the natural circulation mass flow rates asymptotically increased and converged to a certain value. The outlet area also influenced the re-circulation flow rate. Experimental correlations on the natural circulation mass flow rates along the variation of the inlet / outlet area and wall heat flux were suggested.
- For inlet and outlet areas of 0.15 m^2, the natural circulation flow rate could be increased up to 200 kg/s at high heat flux conditions. Based on KAIST and SULTAN results, this natural circulation flow rate values leads to about 1.3 – 1.45 MW/m^2 CHF values at the top of the lower head vessel (90 degrees) which indicate more efficient cooling than occurs in pool boiling.
- To maximize the heat removal capability by enhancing the re-circulation flow rate through the reactor vessel/insulation gap, extensive experimental results are required to evaluate a wider range of design parameters, such as the inlet position and outlet location. Also, a detailed 3-dimensional flow analysis is necessary to evaluate the local effect, such as choking phenomena near the shear key. To apply the experimental data to the real situation, the similarity of the non-heating experiment to the heating experiment should be verified.

4.6. References

4-1. Y. H. Kim, S. J. Kim, S. W. Noh, K. Y. Suh, J. L. Rempe, F. B. Cheung, S. B. Kim, "Visualization of Boiling Phenomena in Inclined Rectangular Gap, *International Journal of Multiphase Flow,* April 2004.

4-2. M. B. Dizon, J. Yang, F. B. Cheung, J. L. Rempe, K. Y. Suh, and S. B. Kim, "Effects of Surface Coating on the Critical Heat Flux for Pool Boiling from a Downward Facing Surface, *Journal of Enhanced Heat Transfer,* Vol. 11, pp. 133-150, 2004.

4-3. F. B. Cheung, J. Yang, M. B. Dizon, J. L. Rempe, K. Y. Suh, and S. B. Kim, "Scaling of Downward Facing Boiling and Steam Venting in a Heated Hemispherical Annular Channel," I*nternational Journal of Transport Phenomena,* Vol. 6, pp. 81-96, 2004

4-4. F. B. Cheung, J. Yang, and M. B. Dizon, *A Hydrodynamic CHF Model for Downward Facing Boiling on a Coated Vessel,* Report #PSU/MNE-2004-INEEL-1, July 1, 2004.

4-5. F. B. Cheung, J. Yang, and M. B. Dizon, *SBLB Results for Task 3 on External Reactor Vessel Cooling (ERVC) Design Enhancements,* Report #PSU/MNE-2003-INEEL-3, September 25, 2003.

4-6. J. Yang, M. B. Dizon, and F. B. Cheung, *Numerical Analysis of Steam Venting in the Annular Channel of an Enhanced Vessel/Insulation Design,* Report #PSU/MNE-2003-INEEL-2, June 24, 2003.

4-7. M. B. Dizon, J. Yang, and F. B. Cheung, *Effects of Surface Coating on the Enhancement of the Critical Heat Flux on the Outer Surface of a Hemispherical Test Vessel,* Report #PSU/MNE-2003-INEEL-1, June 24, 2003.

4-8. F. B. Cheung and M. B. Dizon, *Literature Survey on the Enhancement of Nucleate Boiling Heat Transfer and Critical Heat Flux Using Surface Coatings and/or Other Relevant Techniques,* Report #PSU/MNE-2002-INEEL-1, June 30, 2002.

4-9. K. Y. Suh, Y. H. Kim, C. S. Kim, S. J. Kim, and S. W. Noh, *SNU Letter Report Describing Additional GAMMA 3D, DELTA 1D and 3D Results,* Report #SNU/NE-2003-INEEL-2, November 28, 2003.

4-10. K. Y. Suh, Y. H. Kim, J. J. Kim, S. J. Kim, S. W. Noh, *SNU Letter Report Summarizing GAMMA 1D and 2D Interim Results,* Report #SNU/NE-2003-INEEL-1, November 28, 2003.

4-11. K. Y. Suh, Y. H. Kim C. S. Kim, S. J. Kim, and S. W. Noh, *Literature Survey on Experiments on Heat Transfer Coefficients for the External Reactor Vessel Cooling,* SNU/NE-2002-INEEL-4, August 7, 2002.

4-12. K. Y. Suh and S. D. Lee, *Report on SIGMA 2D & 3D Modifications, Feasibility Study, and Test Plan*, SNU/NE-2002-INEEL-3, August 7, 2002

4-13. K. Y. Suh, Y. H. Kim and S. J. Kim, *Literature Survey on the Effect of Surface Orientation and Gap Size on the Critical Heat Flux in the Narrow Gap Cooling Experiments,* Report #SNU/NE-2002-INEEL-2, August 7, 2002.

4-14. K. Y. Suh, Y. H. Kim and S. J. Kim, *Critical Heat Flux in the Narrow Gap Cooling Experiments - GAMMA 1D and 2D Experiments*, Report #SNU/NE-2002-INEEL-1, September 30, 2002.

4-15. K. S. Ha and S. B. Kim, *Scaling Effect and 3-D Effect Based on T-HERMES Results,* Report #KAERI/GP-223/2004, July 30, 2004.

4-16. S. K. Tou and C. P. Tso, "Improvement on the Modeling of Film Boiling on Spheres," *International Communications in Heat and Mass Transfer,* **Vol. 24**, No. 6, pp. 879-888, 1997.

4-17. N. I. Kolev, "Film Boiling on Vertical Plates and Spheres," *Experimental Thermal and Fluid Science,* **Vol. 18,** pp. 97-115, 1998.

4-18. Y. Y. Hsu and J. W. Westwater, "Approximate Theory for Film Boiling on Vertical Surfaces," *Chem. Engr. Prog. Symp. Ser.,* **Vol. 56**, No. 30, pp. 15-24, 1960.

4-19. S. Nishio, G. R. Chandratilleke, and T. Ozu, "Natural-Convection Film-Boiling Heat Transfer (Saturated Film Boiling with Long Vapor Film)," *JSME International Journal Series II,* **Vol. 34,** No. 2, pp. 202-211, 1992.

4-20. S. Nishio, and H. Ohtake, "Vapor-film-unit Model and Heat Transfer Correlation for Natural-Convection Film Boiling with Wave Motion under Subcooled Conditions," *International Journal of Heat and Mass Transfer*, **Vol. 36,** No. 10, pp. 2541-2552, 1993.

4-21. F. P. Incropera and D. P. Dewitt, *Introduction to Heat Transfer,* 3rd ed., Ch. 5, John Wiley and Sons, Inc., New York, NY, USA, 1966.

4-22. W. J. Peyayopanakul and W. Westwater, "Evaluation of the Unsteady-state Quenching Method for Determining Boiling Curves," *International Journal of Heat and Mass Transfer,* **21**, pp. 1437-1445. 1978.

4-23. V. K. Dhir, "Boiling Heat Transfer," *Annual Review of Fluid Mechanics,* **30**, pp. 365-401, 1998.

4-24. J. W. Westwater, J. J. Hwalek, and M. E. Irving, "Suggested Standard Boiling Curves by Quenching," *Ind. Eng. Chem. Fundam.,* 25, pp. 685-692., 1986.

4-25. El-Genk, M. S., Glebov, A. G., "Film Boiling from a Downward-Facing Curved Surface in Saturated and Subcooled Water," *International Journal of Heat and Mass Transfer*, **Vol. 39**, No. 2, pp. 275-288, 1996.

4-26. T. H. Frederking and J. A. Clark, "Natural Convection Film Boiling on a Sphere," *Advanced Cryogenic Engineering*, **Vol. 8**, pp. 501-506, 1963.

4-27. T. D. Bui and V. K. Dhir, "Film Boiling Heat Transfer on Vertical Plates and Spheres," J*ournal of Heat Transfer*, Vol. 107, pp. 764-771, 1985.

4-28. F. B. Cheung and Y. C. Liu, *CHF experiments to support in-vessel retention feasibility study for an evolutionary ALWR design*, PSU/MNE-99-263J, 1999.

4-29. S. Rouge, I. Dor, and G. Geffray, “Reactor vessel external cooling for corium retention SULTAN experimental program and modeling with CATHARE code,” *Workshop on In-Vessel Core Debris Retention and Coolability,* Garching, Germany, March 3-6., 1998.

4-30. J. W. Park and D. W. Jeong, “An Investigation of Thermal Margin for External Reactor Vessel Cooling (ERVC) in Large Advanced Light Water Reactors (ALWR)”, *Proceedings of the Korean Nuclear Society Spring Meeting*, Kwangju, Korea, May, 1997.

4-31. Y. H. Jeong, S. H. Chang, and W. P. Baek, “CHF Experiments on the Reactor Vessel Wall using 2-D Slice Test Section”, *Proceedings of the 10th International Topical Meeting on Nuclear Reactor Thermal Hydraulics (NURETH-10)*, Seoul, Korea, October 5-9, 2003.

4-32. S. Rouge, “SULTAN Test Facility for Large-Scale Vessel Coolability in Natural Convection at Low Pressure”, *Nuclear Engineering and Design*, **Vol.69**, pp. 185-195, 1997.

5. TASK 4: ASSESSMENT OF IMPROVED MARGIN FOR SELECTED ENDSTATES

5.1. Objective and Overview of Task 4

The objective of Task 4 is to assess the impact of Task 2 and 3 IVR design recommendations. Scenarios evaluated in Task 1 (see Section 2) are re-evaluated using Task 2 and 3 design recommendations to enhance core catcher and ERVC performance. As discussed in Section 1, assessments were conducted using several analytical tools. In these evaluations, INEEL applied the SCDAP/RELAP5-3D© and VESTA codes. KAERI applied the LILAC and RELAP codes and a lumped parameter model.

Results from Task 4 are summarized in this section. More detailed information about various tasks described in this section may be found in References 5-1 and 5-2. Section 5.2 highlights results from INEEL VESTA and SCDAP/RELAP5-3D© calculations. KAERI efforts to apply the LILAC code are other analytical approaches are summarized in Section 5.3. Insights and conclusions gained from Task 4 efforts are discussed in Section 5.4.

5.2. INEEL Efforts to Quantify IVR Enhancements

Idaho National Engineering and Environmental Laboratory

5.2.1. VESTA Calculations

The methodology, debris configurations, model description, input assumptions, and results associated with the VESTA calculations are outlined in the sections that follow.

5.2.1.1 Methodology

INEEL developed the VEssel Statistical Thermal Analysis (VESTA) code to independently verify University of California at Santa Barbara (UCSB) AP600 study results and assess the impact of additional uncertainties and other debris configurations. As documented in References 5-12 through 5-15, the VESTA model was developed with funding from the U.S. Nuclear Regulatory Commission (NRC) as a tool to assess the analyses presented for design certification of the Westinghouse AP600.[5-16]

A key assumption in assessing the heat load to the vessel from relocated debris is the configuration for the relocated material. At the time of the AP600 analyses, a FInal Bounding State (FIBS) was postulated that was supposed to "bound" thermal loads from any other configuration that can reasonably be expected. This FIBS assumed a molten ceramic pool lies beneath a metallic layer. The ceramic pool was assumed to contain all of the oxide core components (mainly UO_2 and ZrO_2). Heat transfer from such a pool is governed by turbulent natural convection associated with volumetric heat sources. The molten pool can experience sufficient cooling that it becomes surrounded by thin crusts that impose uniform temperature boundary conditions on the melt (i.e., its liquidus temperature). The metallic layer is also assumed to contain all unoxidized metallic components. It is heated from below and cooled from above and its sides.

However, only the side boundary temperature is fixed -- at the metallic layer liquidus temperature as long as some portion of the vessel wall remains intact.

However, as noted in Reference 5-12, several of peer reviewers of the AP600 design certification submittal noted that the assumed FIBS may not bound even the most plausible configuration for the stratification of the relocated material. Two Reference 5-12 debris endstate configurations are considered in these VESTA calculations: Configuration A, a stratified configuration with an upper metallic layer; and Configuration C, a stratified configuration with a lower metallic layer. (see Figure 5-1).

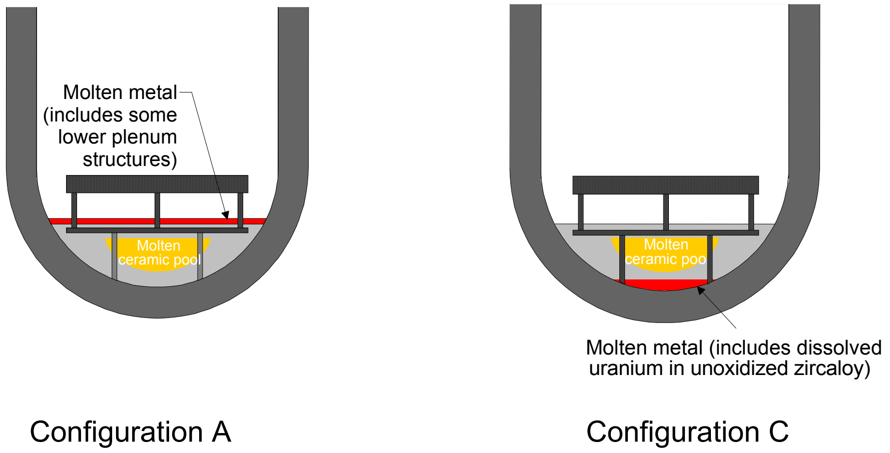

Figure 5-1. Debris configurations evaluated for the APR1400.

Configuration A is similar to the FIBS, but it also considers earlier time periods, before all of the metallic and ceramic material relocates to the lower head. In the AP600 analyses performed in the NRC review, melt relocation masses were based on SCDAP/RELAP5-3D© calculation results. For the analyses conducted in this report, a similar reliance on SCDAP/RELAP5-3D© results was employed. However, a key assumption in assessing Configuration A is the mass of metallic structural material that relocates. Because this mass is not known (SCDAP/RELAP5-3D© analyses were stopped at the time that lower head failure was predicted in a very conservative case), a range of metallic masses was evaluated to consider melting of structural materials that may occur if vessel failure is delayed. Configuration C represents a case where sufficient uranium dissolves into unoxidized zirconium to form a heavier metallic layer. As noted in Reference 5-12, there were several source of data supporting U-Zr formation at the time that the AP600 underwent design certification. Since that time, data from the RASPLAV and MASCA tests also support the potential for such a configuration.[5-17] As in the FIBS postulated for the AP600, this configuration assumes that more dense components have segregated from less dense components. However, the metallic layer sinks in this configuration. Heat loads are "focussed" on the bottom of the lower head where heat rejection is a minimum.[5-6] As in the Configuration A, a range of relocated metallic masses were evaluated for Configuration C. Only 4760 kg of the relocating 108,000 kg of uranium was assumed to dissolve in the metallic layer. Although this mass is below the 40 wt% maximum cited in Reference 5-12, this amount was sufficient for the density of this material to exceed that of the oxide layer (and cause it to sink beneath this layer).

In VESTA, statistical distributions for the heat flux to the vessel wall from the molten pool are compared with statistical distributions calculated for the critical heat flux (CHF) from the submerged vessel surface. VESTA uncertainty distributions are Bayesian distributions, which are ultimately combined by a Monte Carlo sampling to yield a distribution on the probability of vessel heat fluxes exceeding the CHF (or if the vessel isn't submerged, the heat transfer rate from the vessel to the reactor cavity). VESTA can consider several types of debris configurations (stratified, uniform, etc.), decay heat power production associated with actinide and fission product heating, heat sources in the metallic material, and uncertainty distributions for a wide range of parameters. VESTA can be applied to obtain point estimates and probability density functions (pdfs). Heat transfer processes and phenomena modeled by VESTA are described in Reference 5-12.

Many of VESTA's capabilities were implemented so that this code could be used to address issues raised by peer reviewers of the AP600 design certification submittal. Hence, VESTA is an ideal tool for assessing the impact of various features explored in this INERI. Prior to applying VESTA for these calculations, several modifications were implemented into the Reference 5-12 code. First, VESTA was upgraded so that it could run under a Windows XP operating system. Second, an error in the Reference 5-12 version was corrected that affected Configuration C predictions. Results from the revised code for Configuration C were verified using hand calculations.

5.2.1.2 Cases for Evaluation

In this task, VESTA analyses were first completed for the "bounding" APR1400 base case for each configuration. As discussed in Section 2, SCDAP/RELAP5-3D$^{©}$ calculations completed in Task 1 identified an APR1400 "bounding case" that corresponded to relocation conditions associated with a large a loss-of-coolant accident (LOCA). These bounding late-phase melt conditions were then used to quantify improvements in IVR margins that are achievable through the use of ERVC enhancements and the IVCC designed in this program.

The VESTA code was applied to evaluate the two debris endstates shown in Figure 5-1. Several types of cases were evaluated for each debris endstate.

- A base case without an IVCC or enhanced ERVC.
- Bases case sensitivities to assumed steel relocation mass.
- Sensitivities that simulate the use of an IVCC (which was simulated by sensitivities to assumed decay heat).
- Sensitivities to various types of enhanced ERVC.

As noted above, the impact of an IVCC was simulated in these calculations by only considering the reductions in relocated material decay heat. Clearly, a detailed evaluation of the impact of this structure would require a thermal analysis that considered cooling of the relocated material contained within the IVCC (prior to any failure), the dilution in decay power density if the IVCC were to fail and become subsumed in the melt, and the decrease in heat flux to the vessel from relocated material due to delays associated with holdup in the IVCC. Because of project schedule constraints, it was only possible to consider decreases in decay heat associated with the increased time before relocating material comes in contact with the vessel. As discussed in Section 5.4, it is recommended that additional SCDAP/RELAP5-3D$^{©}$ analyses be completed with newly obtained narrow gap cooling correlations to gain additional insights about the impact of the IVCC.

Reference 5-1 lists the VESTA input assumptions for these calculations. As discussed in Reference 5-1, many values were consistent with values assumed in the NRC review of the Westinghouse submittal.

For example, coefficients required to simulate natural convection heat transfer from the molten pool were selected that were consistent with values obtained from tests conducted in support of the AP600 reactor evaluation. Because of project schedule constraints, it was not possible to consider newly obtained heat transfer correlations to simulate natural convection heat transfer in a volumetrically heated pool. As discussed in Section 5.4, it is recommended that additional SCDAP/RELAP5-3D© analyses be completed with these newly obtained correlations (although initial evaluations suggest that these new correlations are similar to those used in the AP600 evaluations).

A key benefit of the VESTA code is that it allows users to consider the impact of input parameter uncertainties. Hence, the user must specify values to characterize median values and uncertainty parameters for calculation inputs. Reference 5-1 summarizes the basis for the uncertainties assumed in VESTA calculations.

The use of microporous coatings and an enhanced vessel/insulation configuration were both investigated as methods to enhance ERVC in this INERI. As discussed in Reference 5-11, correlations were developed to predict heat transfer from the vessel for various heat transfer conditions. These correlations were applied to obtain fifth order polynomial equations for estimating CHF correlations that could be implemented into VESTA. Figure 5-2 compares the CHF correlations obtained for various ERVC conditions. As shown in this figure, the CHF may be increased by factors significantly with proposed ERVC enhancements.

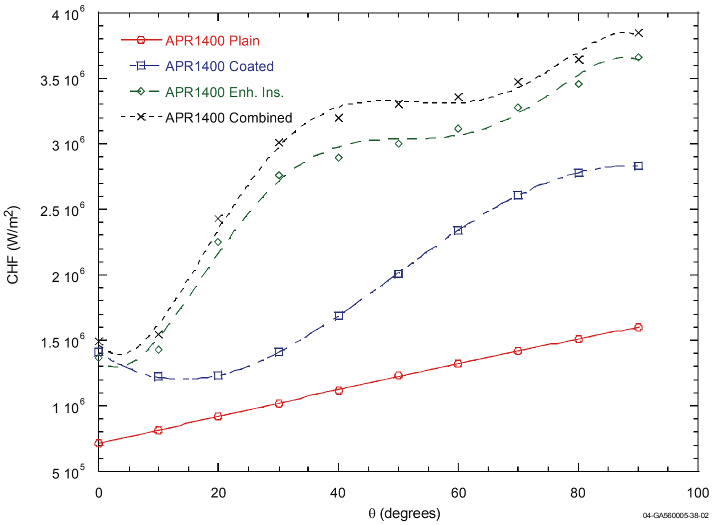

Figure 5-2. CHF associated with various ERVC conditions (assumes subcooling due to gravity).

5.2.1.3 Results

As noted in Section 5.2.1.2, two debris endstate configurations were considered in these calculations. Results for Configuration A, a stratified configuration with an upper metallic layer, and results for Configuration C, a stratified configuration with a lower metallic layer, are discussed in this section.

VESTA output includes a wide range of variables, such as angularly-dependent crust thickness, angularly-dependent vessel thickness, peak, bulk, and average temperatures in the ceramic and metallic pools, crust temperature, and core barrel temperature. However, results here focus on VESTA predictions for heat flux and ratios of this vessel heat flux to the CHF because these variables best reflect IVR margins.

Configuration A - Stratified with Upper Metallic Layer

Base Case - without in-vessel core catcher or enhanced ERVC

For this configuration, VESTA calculations were first performed for a "base case" that was based on the relocation conditions predicted by Task 1 SCDAP/RELAP5-3D$^{©}$ results. However, as noted above, VESTA base case calculations considered additional melting of structural material, so that the mass of SS was 100,000 kg. Figures 5-3 and 5-4 contain selected VESTA results for this "base case". Figure 5-3(a) contains VESTA predictions for the heat flux to the vessel wall as a function of angle. As illustrated in this figure, heat fluxes to the vessel at locations adjacent to the ceramic pool (e.g., less than 70°) are significantly lower than heat fluxes to the vessel at locations adjacent to the metallic pool. This result is due to the presence of heat sources in the metallic pool in conjunction with the lack of an insulating ceramic crust that is present at locations near the ceramic pool.

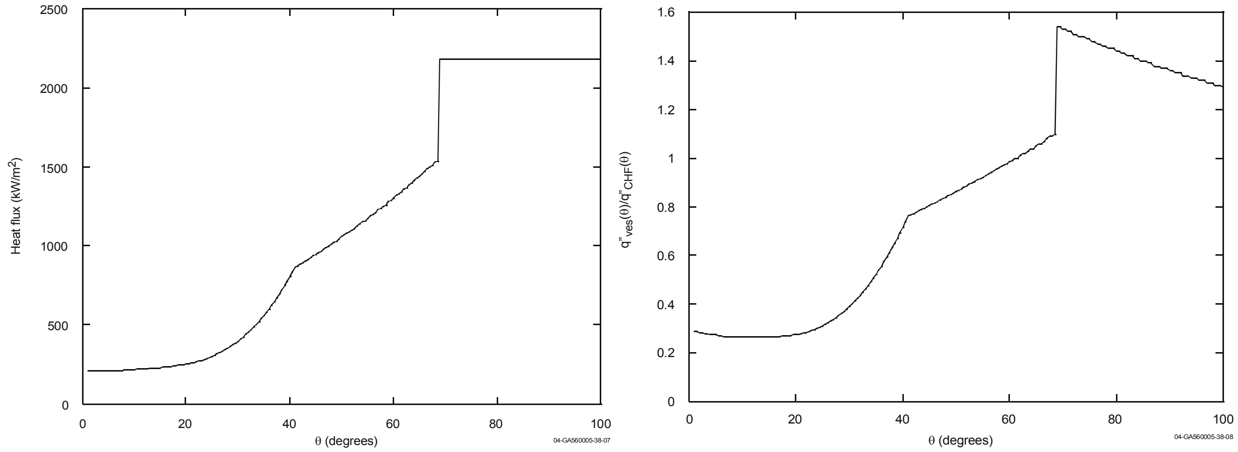

(a) Heat flux

(b) CHF ratio

Figure 5-3. Configuration A base case point estimate results.

Figure 5-3(b) shows the corresponding CHF ratios (e.g., the ratio of the heat flux to the vessel to the CHF) for this base case. For point estimates, base case values are calculated in VESTA by dividing the angularly dependent heat fluxes in Figure 5-3(a) by CHF values for the plain vessel shown in Figure 5-2. As shown in Figure 5-3(b), vessel wall heat fluxes are predicted to exceed CHF values near the top of the ceramic pool (at an angle of approximately 70°) and at all locations adjacent to the metallic layer.

As noted above, the VESTA code allows users to assess the impact of uncertainties associated with various input values in its calculations. The code can present results in terms of cumulative distribution functions (cdfs) and probability distribution functions (pdfs). Figure 5-4 illustrates the pdfs for the ratios of vessel heat flux to the CHF at five locations that occur within the ceramic pool (0, 10, 20, 30, and 40°). As indicated in this figure, uncertainties in input values suggest that vessel wall heat fluxes may exceed unity

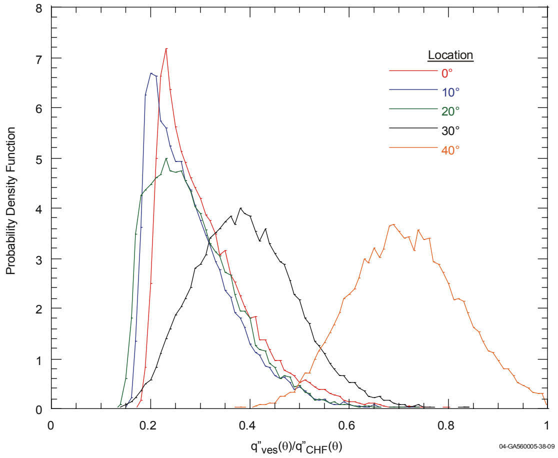

Figure 5-4. CHF ratio pdfs for Configuration A base case.

at locations above 40º (although point estimates suggest that median values remain below unity until a location of nearly 70º).

Sensitivities to steel relocation mass

As documented in Reference 5-12, one of the key assumptions in the Westinghouse AP600 submittal was the amount of steel mass assumed to relocate and form the metallic layer. Because steel melt mass assumptions significantly impact analysis results, a single pdf that encompasses the entire range of possible postulated melt masses would not yield meaningful results. Hence, VESTA point estimate calculations were completed to assess the impact of assumed steel relocation masses.

Results from these calculations are shown in Figure 5-5. As shown in Figure 5-5(a), variations in assumed steel relocation masses (from the 100,000 kg assumed in base case calculations) only affect metallic layer predictions because ceramic pool heat fluxes are independent of metallic layer mass assumptions. Although steel melt relocation mass assumptions affect metallic layer heat fluxes and associated CHF ratios, melt mass increases cannot reduce this ratio below 1.0 because it exceeds unity at locations adjacent to the ceramic pool (see Figure 5-5(b)).

Enhancements to simulate an in-vessel core catcher

As discussed in Reference 5-3, an IVCC may delay or prevent molten corium material from directly contacting the vessel wall due to the narrow gap cooling that occurs between the vessel and in-vessel core catcher, Furthermore, the decay heat in the relocated material is decreased, if the IVCC delays relocation of core materials to the lower head, or diluted, if the IVCC is subsumed into the relocated melt masses. Schedule constraints prevented detailed SCDAP/RELAP5-3D© calculations from being conducted with the newly-obtained narrow gap cooling correlations to assess the impact of such a structure on the bounding case. However, VESTA sensitivity calculations were conducted to gain insights about the benefit associated with an in-vessel core catcher by considering the reduction in the magnitude of decay power if there is a delay in the time when the relocated material contacts the vessel wall. For these calculations, the decay power was reduced in increments consistent with 0.5 hr, 1 hr, 2 hr, and 4 hr delays in melt relocation. Figure 5-6 illustrates the reduction in heat flux and associated CHF ratios for each assumed relocation delay. As shown in Figure 5-6(a), a four hour delay in relocation is required to obtain point

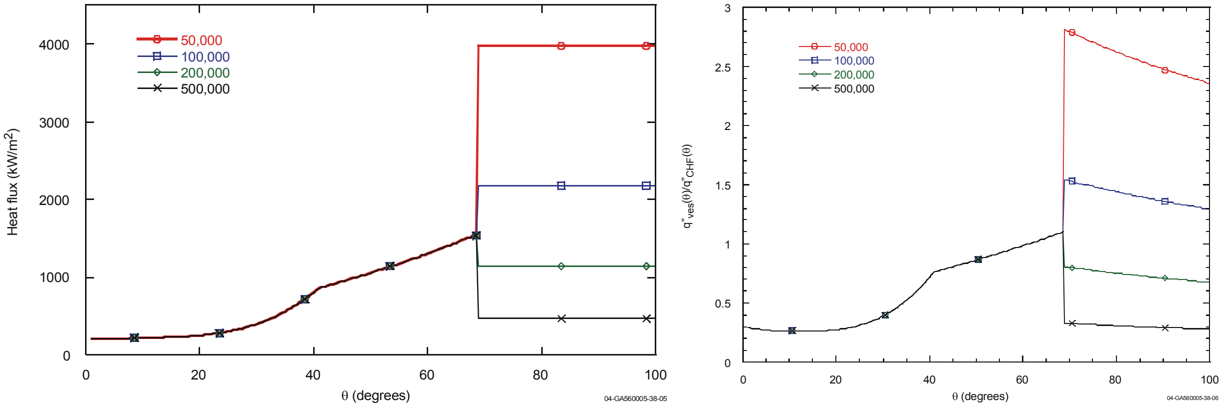

(a) Heat flux

(b) CHF ratio

Figure 5-5. Configuration A point estimate results assuming various metallic layer steel masses.

estimates for CHF ratios that approach unity. Although some additional reduction in decay heat may occur if the material associated with the IVCC is subsumed into the relocated corium, it is clear that the IVCC must survive for at least 4 hours in order to reduce vessel heat loads to values below the CHF for this case.

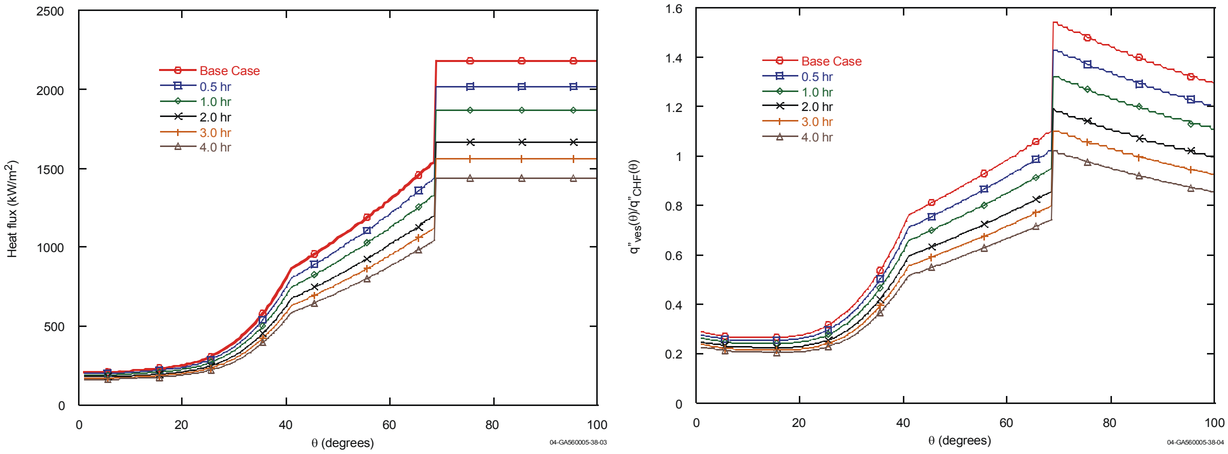

(a) Heat flux

(b) CHF ratio

Figure 5-6. Configuration A point estimate results assuming various relocation time delays.

Enhancements to ERVC

Figure 5-7 compares ratios of vessel heat flux to the CHF from point estimate calculations for proposed ERVC enhancements with values for a plain (uncoated and uninsulated) vessel. As shown in this figure, ratios are significantly decreased with proposed enhancements. Point estimate calculations suggest that vessel microporous coatings alone are sufficient to prevent vessel heat fluxes from exceeding the CHF. Even greater reductions in the CHF ratio are obtained with the enhanced insulation arrangement proposed in References 5-11. It is interesting to note that the proposed enhancements are not additive (e.g., the additional benefit of using microporous coatings on a vessel surrounded by the proposed enhanced insulation structure was smaller than the sum of the benefits associated with each option alone). Results in Figure 5-8 suggest that the CHF ratios are below unity even when input uncertainties are considered. Note that in all three cases, uncertainty distributions are centered around the highest CHF ratios at locations near 70º. This result is consistent with results from the point estimate calculations presented in Figure 5-7.

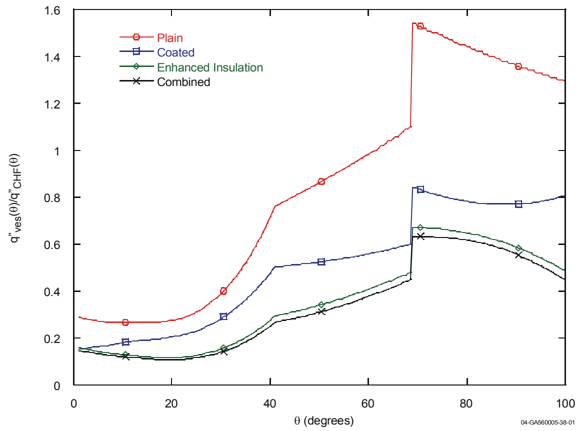

Figure 5-7. CHF ratios assuming various ERVC enhancements for Configuration A base case.

Configuration C - Stratified with Lower Metallic Layer

Base Case - without in-vessel core catcher or enhanced ERVC

VESTA calculations were also performed for a Configuration C "base case" that corresponded to the relocation conditions predicted by Task 1 SCDAP/RELAP5-3D© results. Figures 5-9 and 5-10 contain selected VESTA results for this "base case".

Figure 5-9(a) contains VESTA predictions for the heat flux to the vessel wall as a function of angle. As illustrated in this figure, heat fluxes to the vessel at locations adjacent to the ceramic pool (e.g., greater than 70º) are significantly higher than heat fluxes to the vessel at locations adjacent to the metallic pool. As shown in Figure 5-9(b), point estimate calculations indicate that Configuration C CHF ratios remain below unity at all locations. However, the peak values for CHF ratios are predicted to occur at two locations: near the bottom center of the vessel, where ratios are lower; and near the top of the ceramic pool, where heat fluxes to the vessel are higher.

Figure 5-10 shows the pdfs for the CHF ratios at five locations that occur within the ceramic pool (0, 15, 45, 65, and 85º). As indicated in this figure, the inclusion of uncertainties suggests that there is a very small, non-zero probability for Configuration C heat fluxes to exceed the CHF at two locations: at 0º (near the bottom center of the vessel) and at 85º (near the top of the ceramic layer).

Sensitivities to steel relocation mass

VESTA point estimate calculations were completed to assess the impact of the assumed steel relocation masses for Configuration C. Results from these calculations are summarized in Figure 5-11. As shown in Figure 5-11(a), a reduction in steel relocation mass for this configuration (from the 100,000 kg assumed in base case calculations to 50,000 kg) increases heat flux predictions at all angles. In the metallic

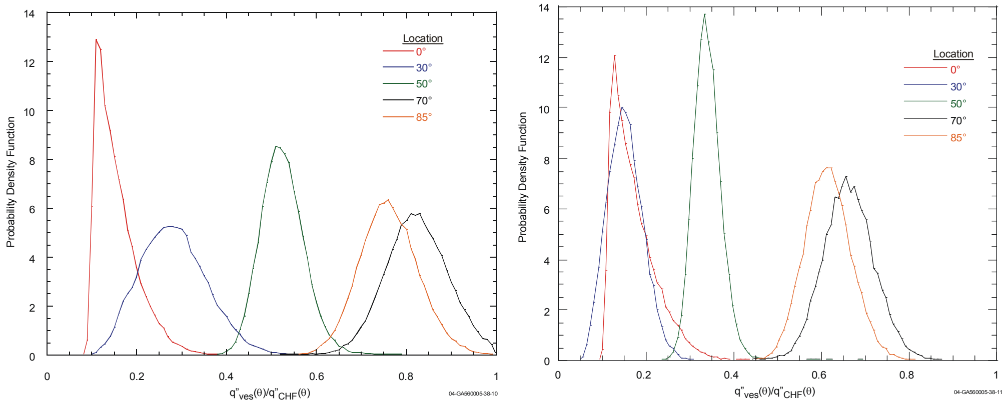

(a) coated vessel (b) enhanced vessel/insulation design

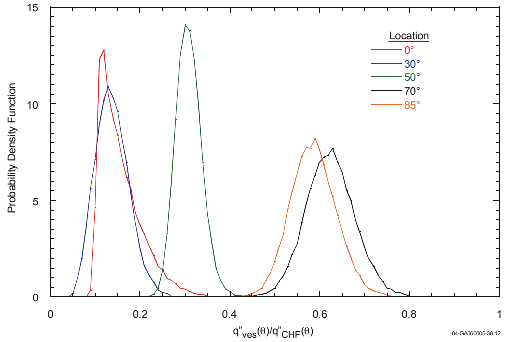

(c) coated vessel with enhance vessel/insulation design

Figure 5-8. CHF ratio pdfs for Configuration A base case with vessel coating.

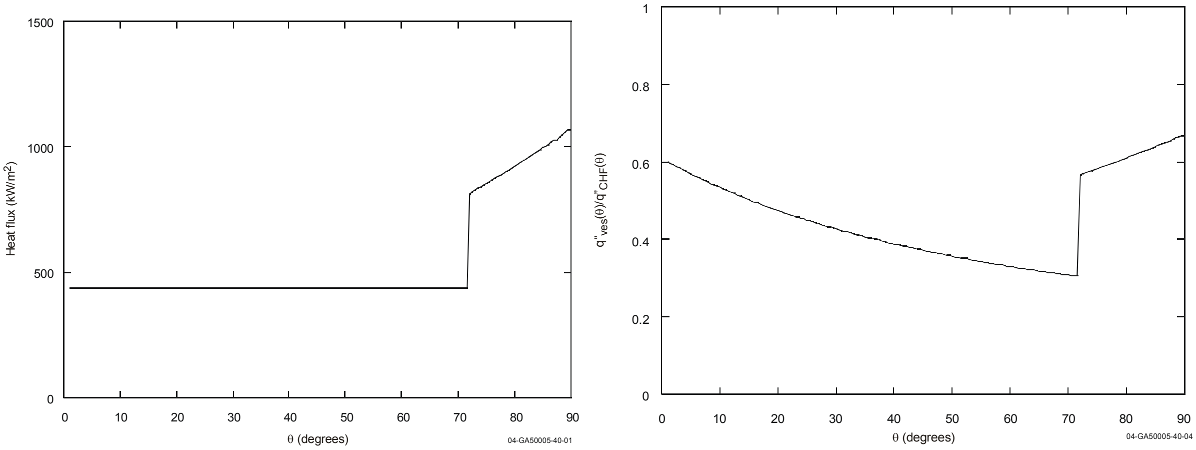

(a) Heat flux (b) CHF ratio

Figure 5-9. Configuration C base case point estimate results.

layer, this is due to an increased power density when steel relocation mass is reduced. At locations above the metallic layer, the heat flux increases because these locations are now adjacent to the ceramic layer. As

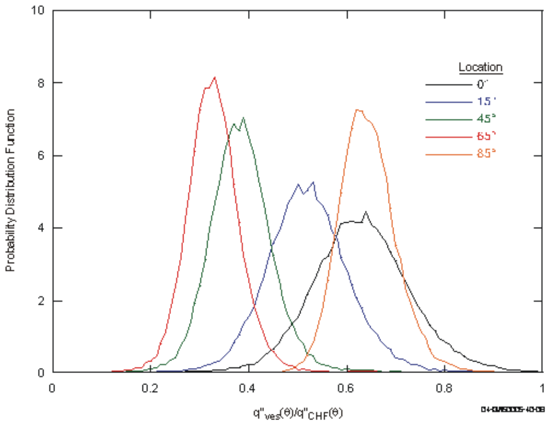

Figure 5-10. CHF ratio pdfs for Configuration C base case.

shown in Figure 5-11(b), the CHF ratios are also increased at all locations. Note that CHF ratios predicted with lower steel relocations masses yield peak CHF ratios near the bottom center of the vessel. Hence, a bottom center location of the vessel may be more susceptible to failure in such configurations.

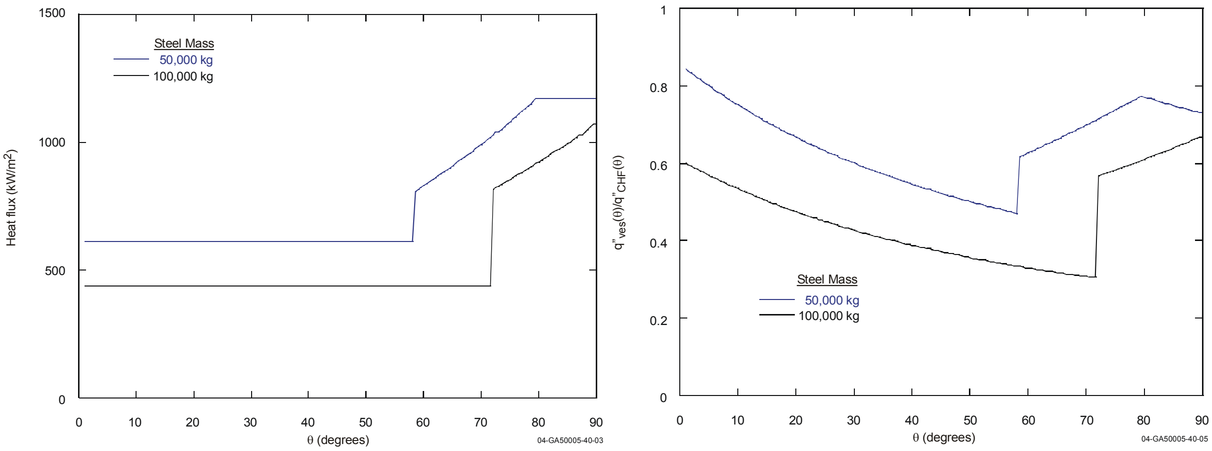

(a) Heat flux

(b) CHF ratio

Figure 5-11. Heat fluxes for various metallic layer steel masses in Configuration C base case.

Enhancements to In-Vessel Retention

VESTA sensitivity calculations were also conducted for Configuration C to gain insights about the benefits associated with IVCC and ERVC enhancements. For these calculations, the maximum benefits explored for each IVR method was assumed. For example, an IVCC that delayed melt contact with the vessel for 4 hours and an “ERVC-Combined” case using a coated vessel with an enhanced insulation structure were assumed. As shown in Figure 5-12, both options significantly reduce CHF ratios. Uncertainty calculation results suggest that CHF ratio pdfs remain below unity for both options. Although the reduction is generally greater for the “Combined” case with a coated vessel and an enhanced insulation structure, it is interesting to note that the IVCC offers the largest reduction at locations near the bottom center of the vessel, one of the locations of most concern in Configuration C endstates. Hence, the enhanced margin offered by various options is dependent upon the melt relocation configuration.

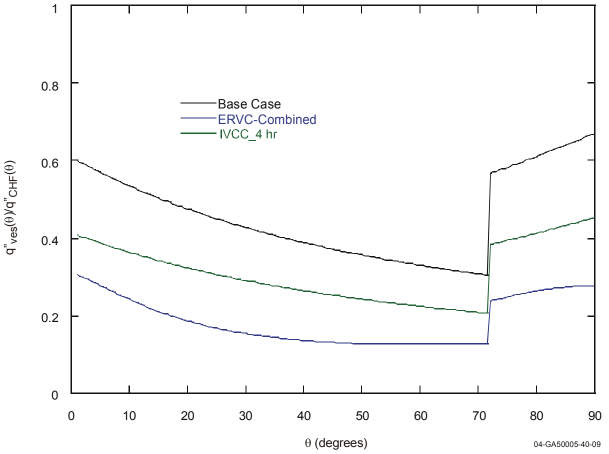

Figure 5-12. CHF ratios assuming various IVR enhancements for Configuration C base case.

5.2.1.4 Summary

VESTA calculations were completed for two debris endstate configurations to assess the impact of IVR enhancements considered in this INERI. This section summarizes insights from these calculations.

For base case conditions in a Configuration A endstate:

- Peak heat fluxes and associated CHF ratios are predicted to occur near the top of the ceramic pool beneath the metallic layer.
- If uncertainties in input values are considered, a small, but non-zero, probability exists for the CHF ratio to exceed 1.0.
- Point estimate calculations suggest that an IVCC must prevent melt relocation for at least 4 hours in order to maintain vessel heat fluxes below the CHF.
- Point estimate calculations suggest that either of the explored ERVC enhancements are sufficient to reduce vessel heat fluxes below the CHF. If one considers uncertainties, the additional reduction offered by an enhanced insulation design is required to maintain heat fluxes below the CHF.
- An IVCC must decrease heat fluxes by at least a factor of 2 for this configuration.
- ERVC enhancements may decrease heat fluxes by factors of 2 to 5.

For base case conditions in a Configuration C endstate:

- Higher heat fluxes are predicted to occur at vessel locations adjacent to the ceramic layer for this configuration. However, CHF ratios peak at two locations for this configuration: near the bottom center of the vessel and near the top of the ceramic pool.
- Point estimate and uncertainty calculations suggest that either an IVCC, which can prevent relocation onto the vessel for at least 4 hours) or a vessel with the combined ERVC enhancements considered in this study are sufficient to maintain vessel heat fluxes below the CHF.

In summary, either of the proposed IVR enhancements can preclude vessel heat fluxes from exceeding the CHF. Depending upon the enhancement selected and debris endstate configuration selected, IVR margins may increase by factors ranging from two to four. The benefit associated with each enhancement is dependent upon the debris endstate (a condition that is not possible to predict at this time).

5.2.2. SCDAP/RELAP5-3D© Calculations

As previously noted, the objective of Task 4 in this INERI project is to use VESTA and SCDAP/RELAP5-3D©[5-18] to evaluate potential improvements in the margins for successful IVR in high power reactors that may be achieved through use of an IVCC and ERVC enhancements. For purposes of this project, APR1400 was used as a representative of high power reactors. Applications of VESTA to satisfy this objective were described in Section 5.2.1. This section contains a discussion of the corresponding SCDAP/RELAP5-3D© efforts.

It is important to understand that SCDAP/RELAP5-3D© provides a detailed analytical approach for predicting certain critical aspects of APR1400 behavior. While VESTA is well suited for completing a variety of sensitivity calculations, VESTA lacks the ability to simulate transient behavior and is limited by its treatment of boundary conditions. These kind of code-versus-code distinctions dictate the need for SCDAP/RELAP5-3D©. The possibility of APR1400 vessel wall thinning is a notable example. VESTA can be used to estimate a steady-state endpoint for wall thickness. However, SCDAP/RELAP5-3D© provides the only means for simulating time-dependent vessel wall conditions. Depending on the balance between propagation of the thermal front from the molten corium and the rate of heat removal from the surface of the vessel, the actual wall thinning (which SCDAP/RELAP5-3D© can approximate) may or may not correspond with the VESTA steady-state endpoint. For these, and other related reasons, SCDAP/RELAP5-3D© calculations are needed for a complete IVR analysis.

5.2.2.1 Methodology

The approach used here essentially consists of making SCDAP/RELAP5-3D© calculations of the APR1400 lower head thermal response following a 'limiting' molten corium relocation with and without an IVCC and ERVC enhancements. Comparing results from these calculations then allows determination of the potential IVR benefits that may be derived if some specific reactor design changes were actually implemented.

Conditions defining the 'limiting' molten corium relocation were taken from SCDAP/RELAP5-3D© results generated in Task 1 of this project (see Section 2). Calculations with and without an IVCC and ERVC enhancements were made possible by modifying SCDAP/RELAP5-3D© to allow simulation of results from experiments conducted in Tasks 2 and 3. Those code modifications are described in some detail in Section 5.2.2.2, the associated modeling assumptions are outlined in Section 5.2.2.3, results are provided in Section 5.2.2.4, and a summary of the effort is given in Section 5.2.2.5. Before proceeding, it should be noted that only lower head ERVC enhancement effects were considered relative to high power reactor IVR margins. IVCC was not addressed in any SCDAP/RELAP5-3D© calculation due to schedule and budget constraints.

5.2.2.2 Code Modifications

ERVC enhancements that were considered included the effects of microporous coatings (to promote nucleation during the boiling process), the effects of an optimized vessel insulation configuration (to promote water downflow and steam venting), and the effects of microporous coatings combined with optimized vessel insulation. SCDAP/RELAP5-3D© was modified to allow simulation of those (three) ERVC enhancement options based primarily on PSU experimental results collected under Task 3.[5-11] In addition, PSU experimental results for a plain reactor vessel lower head (without coatings or insulation)[5-

[11] were incorporated into the code to serve as a reference for gauging any potential IVR margin improvements. In all cases (for plain, coated, insulated, and coated/insulated vessels), the PSU experimental results consisted of correlations for the CHF (as a function of angular position and water subcooling) and correlations for nucleate boiling and transition boiling (as functions of angular position and the vessel wall superheat).

Correlations for the CHF were provided in the form

$$q_{CHF} = f(\theta)f(\Delta T_{sub}) \tag{5-1}$$

where

q_{CHF} = the critical heat flux (MW/m^2),

θ = the angle shown in Figure 5-13 (radians),

ΔT_{sub} = $T_{sat} - T_{water}$ (^{o}C)

T_{sat} = the water saturation temperature (K), and

T_{water} = the water temperature (K).

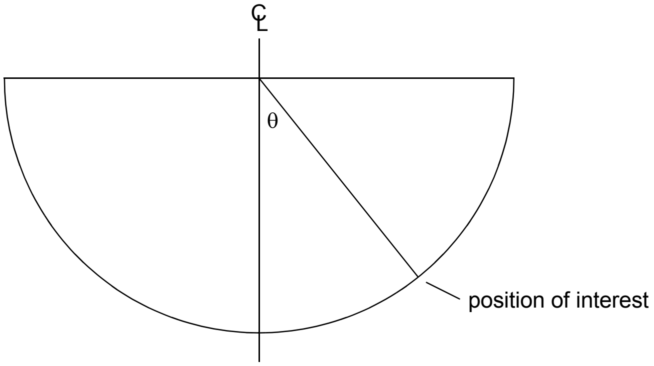

Figure 5-13. Illustration of an angular position relative to heat transfer from a hemispherical surface.

Unlike the CHF, correlations for nucleate and transition boiling were provided only at discrete angular positions. However, at each discrete angular position studied, correlations were provided in the form

$$q = a(\ln\Delta T)^3 + b(\ln\Delta T)^2 + c(\ln\Delta T) + d \tag{5-2}$$

where

q = the (nucleate or transition) boiling heat flux (MW/m^2),

ΔT = $T_w - T_{sat}$ (^{o}C),

T_w = the vessel wall surface temperature (K), and

$a, b, c, and\ d$ = correlation constants.

PSU results for a coated vessel at an angle of 0.98 rad (56^{o}) is shown in Figure 5-14 as an example. In this figure, nucleate and transition curves are depicted for saturated boiling at atmospheric pressure. The

CHF is also shown. SCDAP/RELAP5-3D© was modified to allow the appropriate simulation of heat transfer corresponding with figure. Similarly, code modifications were also completed for all other angular positions studied in plain, coated, insulated, and coated/insulated configurations.

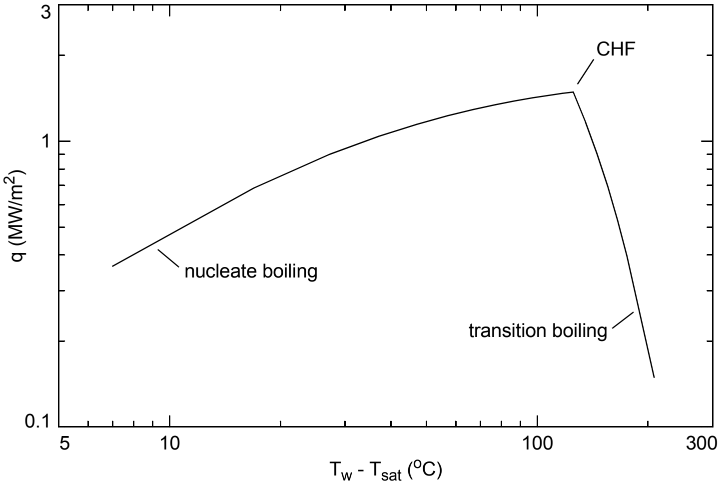

Figure 5-14. Curves for saturated boiling at atmospheric pressure from a vessel with a microporous coating at 0.98 rad (56°).

In all cases, the code modifications included transient treatment of subcooling effects. This was accomplished by calculating a saturation temperature at each time and angular position of interest consistent with the total pressure, which is the sum of the position-dependent hydrostatic head and the system pressure of the water surrounding the reactor vessel. The resulting time- and position-dependent saturation temperature allowed calculation of a corresponding time- and position-dependent CHF.

The time- and position-dependent CHF was then used to linearly scale nucleate and transition boiling curves in the modified code. This approach was used because the CHF was provided as functions of subcooling and position while nucleate and transition boiling curves were available only at a limited number of discrete positions under saturated conditions. Scaling was always applied to the nucleate and transition boiling curves from the nearest reported angular position (for the configuration being analyzed). This scaling approach retains the shape of the experimentally-determined boiling curves while ensuring consistency of the curves with the experimentally-determined CHF.

The code modifications also included heat transfer prior to the onset of nucleate boiling. This was accomplished by calculating heat transfer at the reported onset of boiling (i.e., 0.37 MW/m^2 @ ΔT = 7 °C in Figure 5-14) and then linearly ramping this result to zero as the ΔT goes to zero. Calculating lower head response beyond the transition boiling region was not included and was not necessary because vessel failure is unavoidable after the CHF is reached. This occurs because bubble sizes increase as heat transfer increases until the CHF is reached. At that point, bubbles are large enough to begin blanketing the vessel, ultimately blocking water contact with the wall and limiting heat flow to that transferred across the steam film. The effect can be seen in Figure 5-14 where heat transfer actually drops as vessel wall temperatures increase beyond the CHF. The result is an unavoidable spiral of ever decreasing heat transfer and ever increasing wall temperatures. Burnout in the wall will eventually develop somewhere in a film boiling regime in such a case.

For each angular position of interest on the reactor vessel lower head, implementation of the code modifications just described included time-dependent logic to

- calculate the corresponding angle (θ),
- calculate the water saturation temperature consistent with the total pressure,
- determine the appropriate vessel configuration (plain, coated, insulated, or coated/insulated),
- calculate the corresponding CHF accounting for subcooling effects,
- use the current wall superheat (ΔT) to determine the appropriate heat transfer regime (pre-nucleate boiling, nucleate boiling, or transition boiling) based on data reported for the nearest angle,
- calculate heat transfer based on the current wall superheat and the curve associated with the appropriate heat transfer regime (which may require linear extrapolation from heat transfer at the onset of nucleate boiling to zero if the pre-nucleate boiling regime is applicable),
- scale heat transfer based on the calculated CHF,
- repeat the foregoing logic until the lower head temperature solution converges, and
- then repeat the foregoing logic to advance the simulation time.

5.2.2.3 Models and Input Assumptions

All calculations were based on a simplified SCDAP/RELAP5-3D© model of the lower head thermal-hydraulics and a more detailed COUPLE model of the lower head structure. The SCDAP/RELAP5-3D© model, as shown in Figure 5-15, is consistent with the full plant model of the APR1400. However, the simplified version included time-dependent volumes to represent the core, downcomer, and the reactor cavity. Initial and boundary conditions were taken from results generated in Task 1 of this project.

The lower head structure was modeled using the two-dimensional finite-element mesh shown in Figure 5-16. The mesh, which overlies three lower head hydrodynamic volumes (numbered V190, V200, and V210), includes a total of 588 nodes and 540 elements. Any transition from the lower head hemispherical geometry to the cylindrical vessel geometry was ignored due to the lack of specific information. Provisions were included, however, to allow simulation of a contact resistance between a solidified corium crust and the vessel wall, if a crust is predicted to form. Code modifications to simulate ERVC enhancements were applied to the exterior surfaces of this model.

All calculations were completed using relocation conditions associated with a large loss-of-coolant accident (LOCA) in the APR1400. Those conditions, which are summarized as LOCA-1 in Table 5-1, were selected because they include the highest power density and the highest relocation temperature of all transients considered (under Task 1 of this project). In addition, the relocation conditions include a relatively large relocation mass and a relatively high decay power level. This is expected to result in a near limiting set of conditions relative to the severity of lower head thermal attack. (It should be noted that the probability of such conditions may be quite low.[5-8]). Additional information about this analysis may be found in Section 2.

The calculations were also completed assuming steady-state natural convection within molten regions of the (volumetrically-heated) corium pool. This is a somewhat conservative assumption because transient natural convection is lower than steady-state natural convection and because a finite period of time (which was ignored) is required before the transition from transient to steady-state convection will occur. The corium pool was assumed to be homogeneously mixed. This assumption was adopted out of consideration

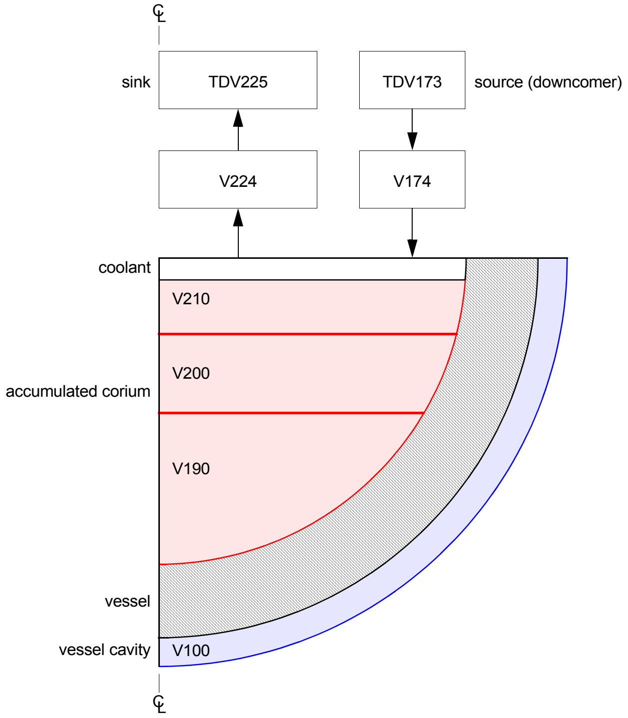

Figure 5-15. Simplified SCDAP/RELAP5-3D$^{©}$ model of the APR1400 lower head thermal-hydraulics.

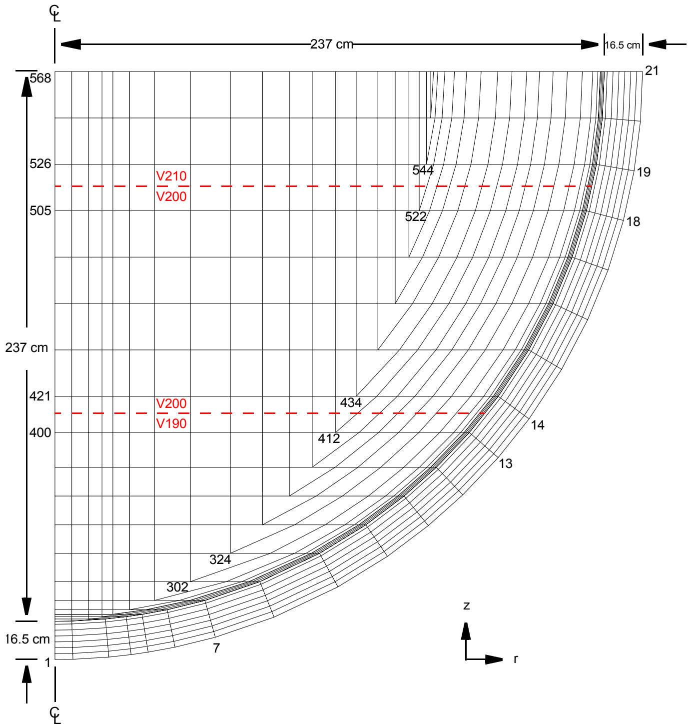

Figure 5-16. COUPLE two-dimensional finite-element mesh representing the lower head of the APR1400 reactor vessel (with selected node numbers).

Table 5-1. Late-phase melt conditions for APR1400 transients.

Transient	Time of Relocation (s)	Relocated Constituents (kg)				Corium Characteristics at Time of Relocation				
		UO_2	ZrO_2	Zr	Total	Depth (m)	Temperature (K)	Decay Power (MW)	Power Density (MW/m^3)	Est Average Vessel Heat Flux (MW/m^2)[a]
SBO-1	11,100	111,000	24,200	6,440	145,000[b]	1.86	3,300	47.4	2.49	0.147 to 1.32
SBO-2	8,630	99,600	18,500	6,940	125,000[c]	1.57	3,010	47.2	3.28	0.170 to 1.53
SBO-3	10,600	111,000	21,200	8,300	144,000[d]	1.86	3,390	52.0	2.72	0.161 to 1.45
LOCA-1	4,990	108,000	5,180	3,520	119,000[e]	1.60	3,460	51.2	3.48	0.182 to 1.64

a. Assuming a hemispherical configuration, without sensible heat effects, for quasi-steady conditions, with estimated limits of heat loss from the upper corium surface (at 10 and 90% of the total decay heat level).

b. Includes 110 kg Zr, 2,270 kg of control rod absorber material, and 76 kg of stainless steel from earlier relocations.

c. Includes 261 kg of control rod absorber material and 12 kg of stainless steel from earlier relocations.

d. Includes 250 kg Zr, 2,350 kg of control rod absorber material, and 180 kg of stainless steel from earlier relocations.

e. Includes 276 kg Zr, 2,350 kg of control rod absorber material, and 95 kg of stainless steel from earlier relocations.

Note: VESTA calculations considered additional melting of structural material, so that the mass of SS was 100,000 kg.

for time and budget constraints and the fact that sensitivities relative to segregation of the melt were treated in VESTA calculations. (SCDAP/RELAP5-3D©, however, does have provisions for modeling melt segregation.)

Conditions in the reactor vessel cavity were modeled as constants (although the code is capable of simulating any time-dependency of interest). A constant reactor cavity water depth of 7.1 m was included based on guidance from Korean collaborators. This should result in a flooding level near the elevation of the reactor hot legs. The cavity water was assumed to remain saturated at atmospheric pressure throughout the calculations.

5.2.2.4 Results

Models and input assumptions just described (in Section 5.2.2.3) were used in conjunction with code modifications outlined in Section 5.2.2.2 to evaluate the effects of ERVC enhancements on the potential for IVR in APR1400. During this process, however, a deficiency in a code model was discovered. This deficiency arises from the fact that his model in the code was never designed to explicitly simulate any significant melting of the reactor vessel. Given this discovery, it seems appropriate to distinguish between modeling deficiencies and errors. After this distinction is made, specific information regarding the nature of the deficiency and steps to remedy the problem will be discussed.

Errors occur if/when the code model fails to perform as designed. On the other hand, deficiencies can surface if/when the code model is used beyond its design limits. In this particular application, significant melting of the reactor vessel occurs. As such, the results lie in a realm beyond the design of the model. Hence, the problem with the model is best described as a deficiency, not an error.

The deficiency basically arises from details associated with modeling heat transfer from the molten corium to the reactor vessel. As the code currently exists, there are two possibilities associated with this heat transfer path: one where some amount of corium has solidified to form a crust adjacent to the inner surface of the vessel wall and one without a solidified crust.

The most common situation, at least in previous applications, is the case where heat transfer from the molten corium is high enough, relative to the corium decay power, to lead to the formation of a solidified corium crust. In this case, heat flows by convection to the inner most crust surface, by conduction through the crust, through a crust-to-vessel contact resistance, by conduction through the vessel, and finally, through convection to the cavity water. Under these conditions, the reactor vessel is protected from melting by the presence of the solidified crust. The other possibility for heat transfer from the molten corium to the reactor vessel arises when the heat transfer from the corium is low, relative to the decay power, so that temperatures near the vessel remain high and a solidified corium crust adjacent to the reactor vessel does not form. Under these conditions, the vessel is more directly exposed to molten pool temperatures, which is the situation encountered in this analysis. This result appears to be a direct consequence of modeling high power reactors with decay heat levels above those previously considered.

The code automatically simulates corium crust growth and shrinkage throughout all calculations. This is accomplished by comparing heat added to the crust from the molten pool side to the heat removed from the crust on the vessel side. If more heat is added than removed, the crust must shrink consistent with the conservation of energy. If/when the crust completely disappears, the code currently uses an arbitrary fixed heat transfer coefficient of 10,000 W/m^2-K to approximate direct molten corium-to-vessel heat transfer. This fixed coefficient was selected partly as a means to promote rapid crust solidification, as expected during the relocation process while the vessel is relatively cold. Thereafter, it was implicitly assumed that heat transfer through the vessel will be sufficient, relative to the decay power, to maintain some crust thickness. Selection of this fixed coefficient was also influenced by the fact that experimental data for this heat transfer situation does not exist.

When the fixed coefficient (of 10,000 W/m^2-K) is applied in these calculations, very rapid vessel melting occurs. The process is so rapid that melt-through is near complete before vessel surface temperatures have time to increase. With vessel surface temperatures relatively low, heat rejection to water in the cavity remains relatively low, which tends to further promote the melting process. Given those results, comparisons of the heat flux from the molten corium pool with the heat flux to the vessel wall were needed.

Heat flux from the side of the molten corium pool was calculated using correlations contained in the code for steady state natural convection in a volumetrically heated pool given by[5-19,5-20]

$$h = 0.54\left(\frac{k}{R}\right)Ra^{0.18}f(\theta) \tag{5-3}$$

where

h = local heat transfer coefficient,

k = thermal conductivity of the melt in the boundary layer adjacent to the interface,

R = effective radius of the molten region (in a hemispherical geometry),

$Ra = \frac{g\beta\dot{Q}R^5}{\alpha\nu k}$ = Rayleigh number associated with the molten pool,

g = gravitational constant,

β = coefficient of volumetric expansion,

$\dot{Q}$ = volumetric heat generation rate,

α = thermal diffusivity,

ν = kinematic viscosity of the molten materials, and

$f(\theta)$ = the relationship between local and mean heat transfer reflected in Figure 5-17.

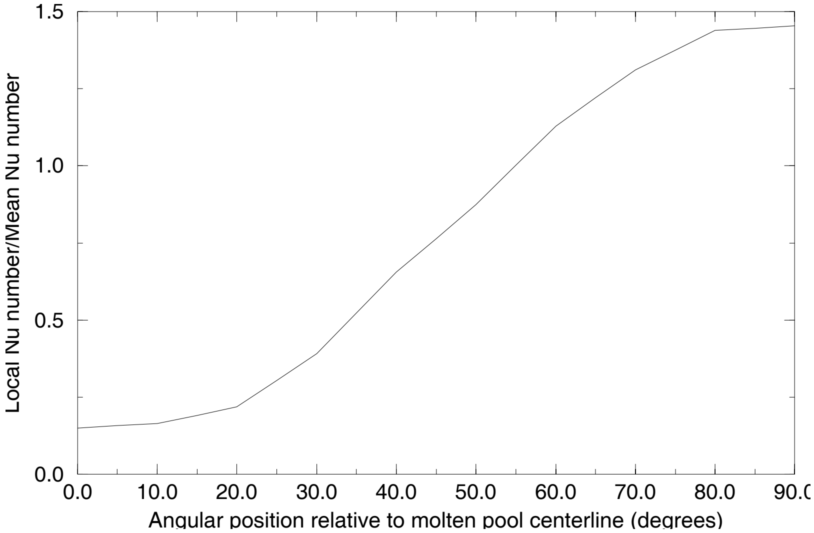

Figure 5-17. Nusselt number ratio as a function of the angle from molten pool centerline.

After a limited number of comparisons, it became clear that code use of the fixed coefficient of 10,000 W/m^2-K results in heat flow to the inner surface of the vessel wall well above that predicted by Eq. (4-3). In fact, discrepancies ranged from ~100 to ~300% for positions and points in time that were sampled. In other words, the use of 10,000 W/m^2-K can yield vessel heat loads that far exceed the decay power generated in the molten pool.

Time and budget constraints in this project did not allow resolution of this model deficiency. However, the following represents some of the modifications needed to add code capabilities to appropriately account for the absence of a solidified corium crust and melting of the reactor vessel wall.

- The arbitrary fixed heat transfer coefficient of 10,000 W/m^2-K from the molten pool to the inner surface of the vessel wall should be replaced with time-dependent values calculated to yield heat flow equal to that associated with natural convection from the volumetrically heated molten pool. This approach is expected to result in an upper bound on heat flow to the wall because any convective film drop is ignored. This could be refined if/when experimental data for the specific convective process become available.
- Vessel melting, including the latent heat of fusion associated with melting the reactor vessel wall, should be added to SCDAP/RELAP5-3D©.
- The composition of the molten pool should be modified as a function of time to account for the progression of vessel steel melting.
- Thermal properties of the molten pool should replace the thermal properties of steel in those regions where the reactor vessel has melted.

Although these modifications could not be implemented during this project, some insights may be gained by reviewing results from a limited number of calculations that were completed. In these calculations, the molten pool-to-vessel heat transfer coefficient was reduced from 10,000 to 600 W/m^2-K. This reduction was specifically selected so complete melt through would not occur in vessels with microporous coatings. The basis for this selection was not entirely arbitrary; instead, it was noted that

- heat transfer coefficients that would be needed to yield heat flow equal to that associated with natural convection from the volumetrically heated molten pool were much closer to 600 than 10,000 W/m^2-K,
- the convective heat flux from the molten pool predicted using Eq. (4-3) is less than the CHF (as long as molten pool temperatures remain reasonable),
- scoping calculations indicate that the CHF from vessels with microporous coatings should be sufficient to reject the total decay power (of 51.2 MW), and
- VESTA results (Section 5.2.1.3) indicate that vessels with microporous coatings will not completely melt through.

The ratio of vessel surface heat flux to the CHF for vessels with microporous coatings at 9000 s (~1.1 hr after molten fuel relocation) is shown in Figure 5-18. These results indicate that the selected molten corium-to-vessel heat transfer coefficient of 600 W/m^2-K can lead to large vessel surface heat fluxes, with some closely approaching the CHF at specific angular positions. As desired, however, the selected coefficient was just adequate to prevent complete melt through of coated vessels. The asymptotic behavior of vessel wall temperatures shown in Figure 5-19 would indicate that wall melting has stabilized by ~8000 s and that further increases in heat flux ratios (with additional time) will be small. Figure 5-19 also indicates the approach to a quasi-stable vessel thickness of ~5 cm. Similar vessel wall thinning due to melting extended over the region from Nodes 8 to 16 (see node locations in Figure 5-16). Results shown in Figure 5-20 support this observation.

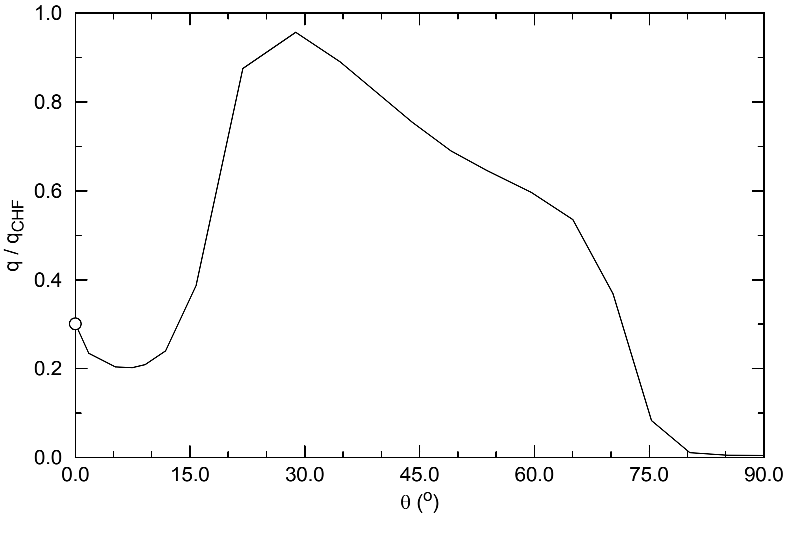

Figure 5-18. The ratio of vessel surface heat flux to the CHF for a coated vessel at 9000 s.

A limitation of using any fixed molten corium-to-vessel heat transfer coefficient is that a constant can never correctly account for heat transfer variations that can develop with time. In calculations for coated vessels, this limitation becomes most apparent with respect to ever-increasing molten pool temperatures.

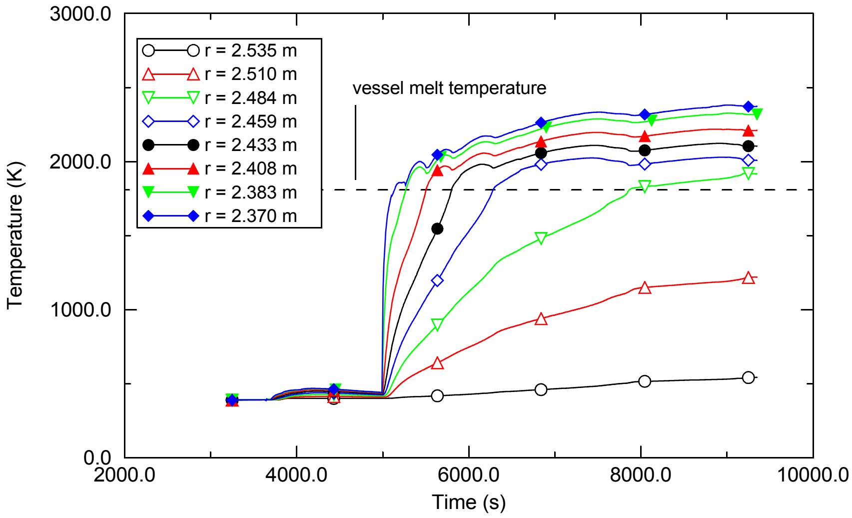

Figure 5-19. Through-wall temperature profile (Node 9 in Figure 5-16) for a coated vessel.

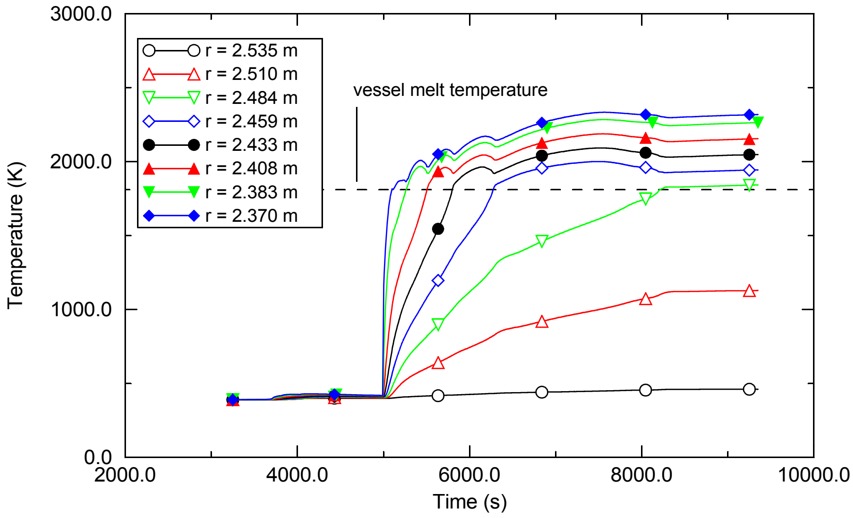

Figure 5-20. Through-wall temperature profile (from Node 12 in Figure 5-16) for a coated vessel.

As pool temperatures increase, heat flux from the corium to the vessel increases (consistent with Eq. (4-3). Results shown in Figure 5-21 reflect this trend. Considerable improvement in the simulation would be expected if time-dependent coefficients were calculated to balance heat flow to the vessel with heat flow from the corium. Assuming the total decay power does not exceed CHF limits, one would expect corium temperatures to stabilize and then gradually decrease under these conditions. Results shown in Figure 5-22 were generated at a time before most of the corium pool temperature increase. As such, these results may be more representative of heat flux ratios that may be achieved with appropriate code modifications.

Calculations with a fixed corium-to-vessel heat transfer coefficient of 600 W/m^2-K were also completed for plain vessels. Although use of a fixed coefficient has limitations, this at least provides a common basis for comparison with coated vessels results.

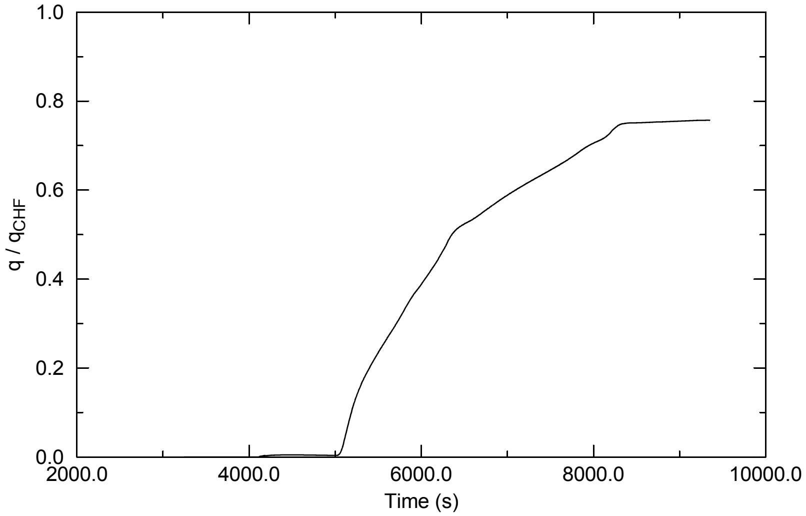

Figure 5-21. The ratio of vessel surface heat flux to the CHF for Node 12 on a coated vessel (see Figure 5-16 for node position).

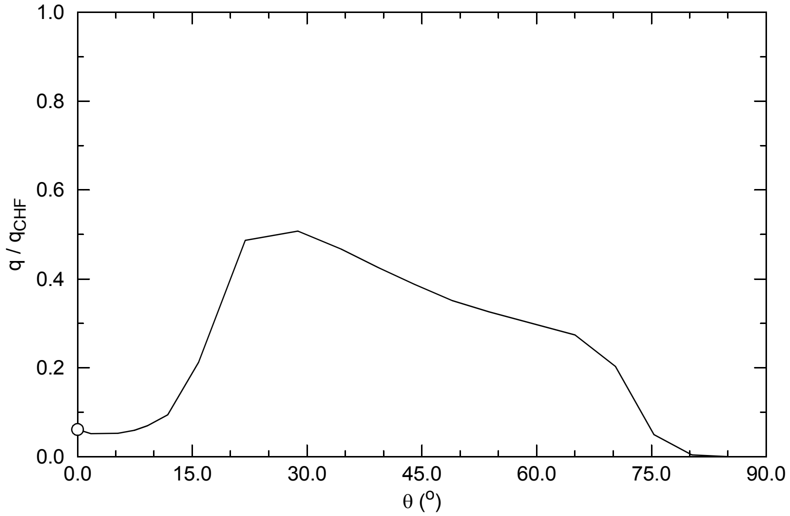

Figure 5-22. The ratio of vessel surface heat flux to the CHF for a coated vessel at 6000 s.

Results for plain vessels indicate complete melt through over a region bounded by Nodes 7 and 12 by 9000 s (~1.1 hr after molten fuel relocation). Figures 5-23 and 5-24 are representative of the vessel thermal response in the failed regions. Based on the results shown, further melting is probable given that temperatures are continuing to rise. Failure of plain vessels for the modeled conditions is not unexpected because

- the convective heat flux from the molten pool predicted using Eq. (4-3) is greater than the CHF (even at moderate molten pool temperatures),
- scoping calculations indicate that the CHF from plain vessels is not sufficient to reject the total decay power (of 51.2 MW), and
- VESTA results (Section 5.2.1.3) indicate that plain vessels will melt through.

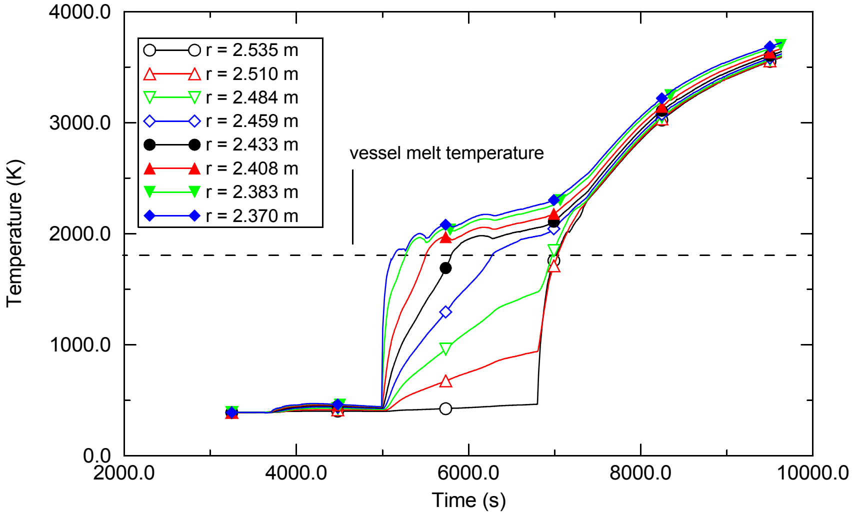

Figure 5-23. Through-wall temperature profile (from Node 9 in Figure 5-16) for a plain vessel.

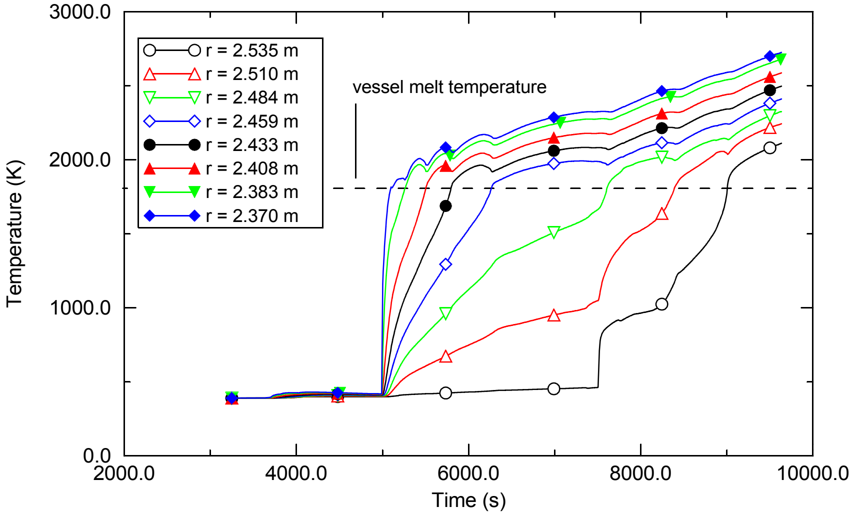

Figure 5-24. Through-wall temperature profile (from Node 12 in Figure 5-16) for a plain vessel.

Complete melt through in the plain vessel calculation stands in contrast to the results for the coated vessel where wall thinning was ultimately controlled by ERVC. Although the absolute value of the results can be questioned (because a fixed corium-to-vessel coefficient was used), the results clearly indicate significant IVR benefits are achievable through the use of microporous coatings. Given time and budget constraints and the limitations associated with the identified model deficiency, a decision was made to defer calculations for the remaining ERVC enhancement options (i.e., insulated and coated/insulated vessels). Results that were calculated and the information provided in Figure 5-2, however, is sufficient to indicate that IVR benefits can be extended by exercising insulated and coated/insulated ERVC enhancement options. SCDAP/RELAP5-3D© modifications are needed before these improvements can be quantified. The effort to complete the code modifications certainly appears justified given the potential benefits for validating IVR in high power reactors.

5.2.2.5 Summary

SCDAP/RELAP5-3D© was modified to allow simulation of ERVC from reactor vessels with microporous coatings, optimized insulation, and the combination of coatings and insulation based on PSU experimental results. Modifications were also added to simulate ERVC from plain vessels as a reference for gauging any potential IVR improvements that may be derived from implementing any of the ERVC enhancements. Models of the Korean APR1400 lower head were developed to allow evaluation the potential for IVR in high power reactors.

Calculations using the ERVC modifications and the APR1400 model led to discovery of a deficiency in a code model. The deficiency is related to the fact that the model was not designed to simulate significant reactor vessel melting. The following recommendations were derived after evaluating this deficiency.

- The arbitrary fixed heat transfer coefficient of 10,000 W/m^2-K from the molten pool to the inner surface of the vessel wall should be replaced with time-dependent values calculated to yield heat flow equal to that associated with natural convection from the volumetrically heated molten pool.
- Vessel melting, including the latent heat of fusion associated with melting the reactor vessel wall, should be added to SCDAP/RELAP5-3D©.
- The composition of the molten pool should be modified as a function of time to account for the progression of vessel steel melting.
- Thermal properties of the molten pool should replace the thermal properties of steel in those regions where the reactor vessel has melted.

Because project time and budget constraints precluded resolution of the model deficiency, a limited number of calculations were completed using a more reasonable molten pool-to-vessel coefficient of 600 W/m^2-K. Results from these calculations indicate plain vessels will fail by melt through while coated vessel wall thinning will be limited (before vessel failure) by ERVC, given the same modeling assumptions and limitations. Although the absolute value of the results can be questioned (because a fixed corium-to-vessel coefficient was used), comparing plain and coated vessel results clearly indicates the use of microporous coatings has significant IVR benefits. Available information is sufficient to indicate that IVR benefits can be extended by exercising insulated and coated/insulated ERVC enhancement options. SCDAP/RELAP5-3D© modifications are needed before these improvements can be quantified. The effort to complete the code modifications certainly appears justified given the potential benefits for validating IVR in high power reactors.

5.3. Assessment of IVR Enhancement

Korea Atomic Energy Research Institute

5.3.1. Introduction

Based on the results of Task 2 and 3 for quantification of the increased margin offered with an in-vessel core catcher (IVCC) and an enhanced external reactor vessel cooling (ERVC), respectively, Task 4 evaluates the improved margin associated with proposed IVR modifications. INEEL initiated SCDAP/RELAP5-3D and VESTA analyses efforts to evaluate the impact of various features proposed in this project to increase IVR margin. KAERI performed a separate assessment to implement the enhancement of IVR to high power reactor (APR1400) using SDCAP/RELAP5 and LILAC codes.

Initially, the accident sequence analyses using SCDAP/RELAP5 were performed for dominant core damage sequences, to set up the debris configuration and initial conditions of melt pool in the reactor vessel lower plenum. LILAC is a multi-dimensional thermal-hydraulic analysis code to simulate the detailed phenomena in melt pool. In this study, the LILAC code was planned to evaluate the melt pool behavior for various accident conditions with an in-vessel core catcher installed in the reactor vessel lower head. Because of the difficulty of the high Rayleigh number melt pool analysis in a real scale reactor vessel, however, the detailed analysis using LILAC is confined to a typical situation of stratified melt pool to verify a simple lumped parameter analysis. Mostly, thermal loads from the molten pool to the reactor vessel were calculated by a simple lumped parameter model. To just evaluate the feasibility of the design improvement for IVR, only the point estimate calculation for a given sequence was done for the stratified molten pool with metallic layer on top (Configuration I). As noted in Section 5.2.1, other debris configurations (Configuration II and III) are possible. In this study, however, LILAC evaluations concentrated on the focusing effect in the situation of Configuration I as a bounding case.

The effect of the ERVC enhancement was evaluated, compared to the current design without any design improvement. More extensive study is needed to reach general conclusions on IVR with considering uncertainties in accident sequence and late melt progression. Currently, the effectiveness of an IVCC is not evaluated, due to the limitation of the modeling of IVCC. To evaluate the enhancement of IVR through IVCC, a more sophisticated model is necessary with implementation of the gap cooling model to estimate the heat removal through an IVCC. The experimental results and the boiling heat transfer correlations for the gap cooling in IVCC performed in Task 2 will be implemented in near future to estimate the cooling capacity of IVCC. In case of APR1400, the internal thermal load from the molten pool is relatively very high, possibly it need special attention to remove enough heat through the gap or to reduce the thermal load to the IVCC. A detailed description of this activity may be found in Reference 5-2.

5.3.2. Initial Conditions of Corium in the Lower Plenum

To identify the state of the in-vessel materials in the reactor vessel lower plenum at vessel failure in the high and low pressure sequences in APR 1400, high-pressure transients for a total loss of feed water (TLFW) to the steam generators with and without the safety depressurization system (SDS) and a station blackout (SBO) and low-pressure transients due to 1.35 inch, 2 inch, 3 inch, 4.28 inch, and 9.6 inch break Loss of Coolant Accidents (LOCAs) without safety injection have been evaluated using the SCDAP/RELAP5/MOD3.3 computer code.

Table 5-2 shows the final melt compositions in the lower plenum of the APR 1400 reactor vessel in the high pressure sequences. In all sequences, approximately 80 – 90% of the core material of 154.2 tons was melted and relocated to the lower plenum of the reactor vessel at the time of reactor vessel failure in the APR 1400, which resulted in reactor vessel failure by creep. In this table, ZrO_2 and Zr masses are dependent on the oxidation fraction in Table 5-2. The volumetric heat source in the corium pool was estimated as 2.23-2.37 MW/m^3. Corium temperature was approximately 2,800 – 3,300 K at reactor vessel failure.

Table 5-2. Melt compositions in the lower plenum at vessel failure in high pressure APR1400 sequences.

Events	TLFW		SBO
	Without SDS	With SDS	
Reactor Vessel Failure Time (sec)	9,109	10,305	13,242
Total Decay Heat (MW)	47.8	46.0	44.8
Corium Depth (m)	1.86	1.64	1.83
Corium Mass (ton); Total = 154.2	145.7	120.2	142.9
Fuel Mass (ton); Total =120.0	113.2	94.7	110.8
ZrO_2 Mass (ton)	18.2	9.8	19.0
Zr Mass (ton); Total =33.6	11.7	13.6	10.8
Corium Temperature (K)	>2,900	2,852	3,311
Heat Generation Rate (MW/m^3)	2.37	2.36	2.23

Table 5-3 shows the final melt composition in the lower plenum of the APR 1400 reactor vessel in the low pressure sequences. In all sequences, approximately 80 – 90% of the core material of 154.2 tons was melted and relocated to the lower plenum of the reactor vessel at the time of reactor vessel failure in the APR1400, which resulted in reactor vessel failure by creep. Volumetric heat source in the corium pool was estimated as 1.9-3.7 MW/m^3. The corium temperature was predicted to be approximately 2,900 – 3,400 K at the time of reactor vessel failure. The highest volumetric heat source sequence is the 9.6 inch break LOCA without safety injection in APR 1400, because this sequence leads to early reactor vessel failure.

Table 5-3. Melt compositions in the lower plenum at vessel failure in low pressure APR1400 sequences.

Events	1.35 inch	2 inch	3 inch	4.28 inch	9.6 inch
Reactor Vessel Failure Time (sec)	24,400	17,890	21,835	9,550	4,910
Total Decay Heat (MW)	37.8	41.3	39.6	48.5	57.9
Corium Depth (m)	1.82	1.65	1.67	1.54	1.54
Corium Mass (ton); Total = 154.2	143.1	121.9	124.3	121.5	114.1
Fuel Mass (ton); Total = 120.0	112.9	99.6	100.8	99.2	107.3

Table 5-3. Melt compositions in the lower plenum at vessel failure in low pressure APR1400 sequences.

Events	1.35 inch	2 inch	3 inch	4.28 inch	9.6 inch
Reactor Vessel Failure Time (sec)	24,400	17,890	21,835	9,550	4,910
ZrO_2 Mass (ton)	15.2	13.4	10.7	8.6	2.8
Zr Mass (ton); Total = 33.6	12.7	6.7	10.5	11.0	4.7
Corium Temperature (K)	3,378	3,083	3,380	2,910	3,150
Heat Generation Rate (MW/m^3)	1.9	2.2	2.1	2.6	3.7

5.3.3. LILAC Analysis of a Molten Pool Natural Convection in the APR1400 RPV

LILAC is a multi-dimensional thermal-hydraulic analysis code that solves the Reynolds-averaged Navier-Stokes and energy equations as governing equations. Turbulent flows are modeled by two-equation turbulence models (κ-ε - and κ-ω models) or large eddy simulation, and a molten pool crust is modeled using an enthalpy-porosity method. The main purpose of the LILAC code is the analysis of thermal-hydraulic phenomena of core melt that relocates to a reactor vessel lower head. Currently, LILAC can simulate multi-layered conjugate heat transfer with melt solidification. A gap-cooling module based on counter-current flow limitation was implemented and validated with data from LAVA experiments.[5-21] A solution domain can be 2-dimensional, axisymmetric, and 3-dimensional. LILAC is based on unstructured mesh technology to discretize a solution domain. The advantage of a control volume formulation is its ability to treat complex geometry and physics in a simple and clear fashion. To discretize the spatial domain in context with the unstructured grid finite volume method, a cell-centered collocated scheme was employed.

To simulate natural convection heat transfer and to estimate the heat flux distribution on the reactor vessel wall using the LILAC code, a 3 inch LOCA sequence was chosen. Masses of the molten materials relocated in the lower head during the 3 inch LOCA was obtained from the SCDAP/RELAP/MOD3.3 analysis in Table 5-3 (see Section 2). In this study, it is assumed that a much larger steel mass (50 ton) becomes molten during relocation process and the materials are mixed and form two separate layers, i.e. oxidic and metallic layers. The oxide mixture is composed of Uranium oxide and Zirconium oxide; and the metallic mixture is made of Zirconium and steel melts. These two layers are stratified in the lower head of the reactor vessel by the density difference. Thermal properties of the oxidic and metallic mixtures are calculated using correlations described in MATPRO.

High Rayleigh number natural convection in a stratified two-layer molten pool can be solved using a sophisticated CFD code; and corium crust development is possibly simulated by a solidification model. At first, it was tried to solve the thermally conjugated stratified molten pool with a crust formation at the interfaces between the pool boundary and vessel inner wall using the LILAC code. But it was not possible to get the converged numerical solution for the multi-physical problem because of the limited capability of the LILAC code. Even though the converged solution was not obtained, it was found in the intermediate numerical data that a crust formed on the vessel inner wall and the interface of lower and upper layers. It is thought that these results are physically reasonable because the melting temperature of the metallic mixture of the upper layer is about 1,000 K lower than oxidic material of the lower layer. Results from the BALI experiment[5-22] suggest that the lower oxidic pool is fully surrounded by the oxidic crust.

For the analysis of the stratified molten pool in the lower head, lower and upper layers are decoupled; and each layer is solved separately with appropriate boundary conditions. Because the oxidic layer is fully surrounded by its crust, an isothermal boundary condition with oxide melting temperature is imposed on the pool boundary. Natural convection heat transfer in the oxidic pool occurs by the volumetric heat generation from the decay heat. Some part of the heat is released through the downward surface and the remaining is transferred to the upper surface by turbulent natural convection. The upward heat from the oxidic layer is imposed on the lower surface of the metallic layer. The side wall of the metallic layer gets the isothermal boundary condition with vessel melting temperature. On the upper wall, the heat transfer mechanism is dependent on the accident progression. If a metallic crust is formed on the upper wall by cooling water injected in a late phase, the isothermal boundary condition similar to that on the side wall can be imposed on the upper wall. If not, there exists a radiative heat transfer mechanism between the upper wall and the remaining structures in the reactor vessel. For the current study, the radiative heat transfer boundary condition is imposed on the upper wall of the metallic pool.

The thermal characteristics of the 3 inch LOCAs were analyzed using a lumped-parameter (LP) model which will be described in next section. Table 5-4 summarizes the results from the lumped-parameter analysis. The expected Rayleigh number of the oxidic layer is about 5×10^{15}, but it is about 7×10^{9} for the metallic layer, which means the turbulent natural convection regimes are different in the two layers. The main interesting point of the stratified two-layer molten pool is the heat flux distribution (or thermal loads on the reactor vessel) and thermal focusing effect by the molten pool stratification. The heat flux concentration factor is expected to be 1.8 by the LP model.

Table 5-4. Thermal characteristics of 3 inch LOCA calculated by LP model

Oxide pool angle = 68.3 degrees
Ra number of oxide layer = 5.01e+15
Pool temperature = 3106.4 K
Upward heat flux of oxide layer = 1.15e+06 W/m^2
Downward heat flux of oxide layer = 7.03e+05 W/m^2
Thermal Splitting $P_{up}/P_{tot} = 0.54$

Angle of upper surface of the metallic layer = 81.8 degrees
Ra number of metallic pool = 6.9e+09
Metallic pool temperature = 1775.0 K
Side wall heat flux from metallic layer = 2.05e+06 W/m^2
Heat flux concentration factor = 1.80

In this study, the stratified molten pool is solved separately using the LILAC code. The oxidic pool was modeled using a quasi 3-dimensional approach with a single computational cell in the circumferential direction; and it was solved using a time-marching method instead of an iterative method because of a convergence problem, which originated from the very high volumetric heat source. After 2500 s, a quasi-steady solution was obtained. Figure 5-25 depicts the calculated temperature distribution in the oxidic pool. A thermal boundary layer developed near the curved downward surface and thermal jet formed in the upper part of the pool are shown is the figure. The calculated upward heat from the oxidic pool is 1.23 MW/m^2 which is similar to the value from the LP model. The metallic layer was simulated with RANS-LES (Reynolds averaged NS with large eddy simulation) hybrid method. The mesh used for the calculation is shown in Figure 5-26, where the number of computational cells is about 1 million. Figure 5-27 is the instantaneous vector field at the center surface. The calculated heat flux concentration factor using the LILAC code is 1.68 which is a little lower than the value expected using the LP model. The vector field looks like the Rayleigh-Benard convection. The side wall heat fluxes from the metallic layer calculated using the Lilac code were very scattered because of the unsteadiness of the flow structure. The side wall heat fluxes are fitted into a linear curve. The final heat flux distribution obtained by the LILAC code simulation is plotted and compared with results from the LP model in Figure 5-28. Some discrepancy is found in the figure, but the pattern of the heat flux distribution is similar each other. In the LP model, the heat flux is assumed uniform at the upper layer, but it is linearly distributed in LILAC results.

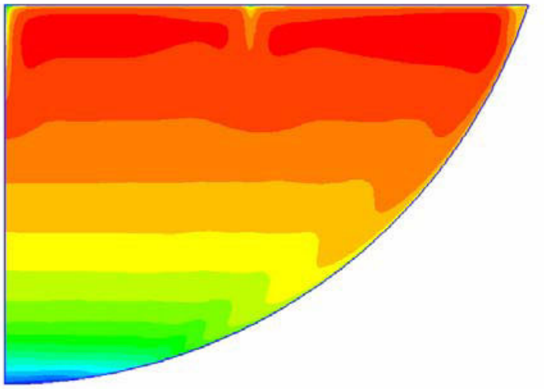

Figure 5-25. Temperature distribution in the oxidic pool.

Figure 5-26. Computational mesh for the upper metallic layer, number of cells is 1028040.

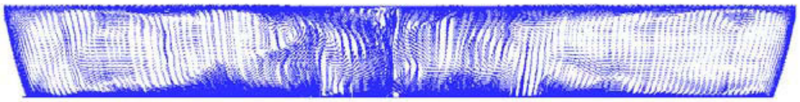

Figure 5-27. Calculated vector field in the center plane for the metallic layer.

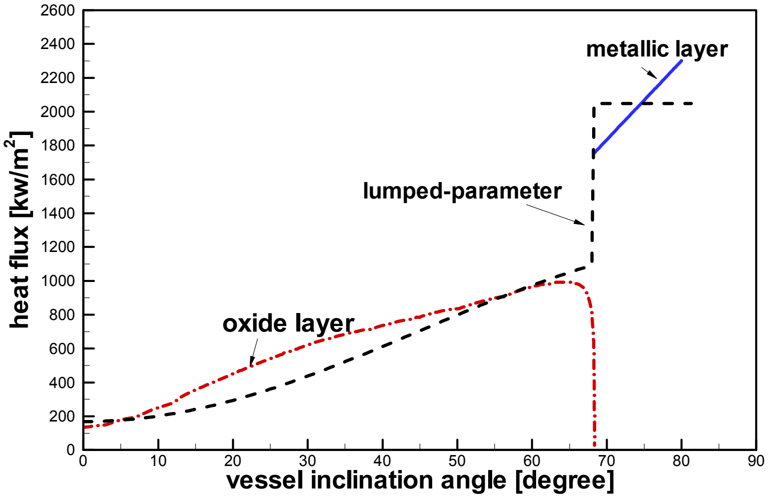

Figure 5-28. Heat flux distributions from the LILAC code and LP model.

5.3.4. ERVC Evaluation using Lumped Parameter Method

5.3.4.1 Lumped-parameter Model

During a hypothetical severe accident, reactor fuel rods and structures supporting materials are melted and relocated in the lower head of the reactor vessel. These relocated molten materials are separated by their density difference and constructs metal/oxide stratified pools in the lower head. The decay heat generated from the fuel material is transferred to the vessel wall and upper structures remained in the reactor vessel by natural convection. A two-layered stratified molten pool is assumed to be developed in the reactor vessel lower head, as shown in Figure 5-29. Because oxidic layer constructed by the mixture of uranium oxide and zirconium oxide is heavier than metallic layer composed of steel and zircaloy, it occupies the lower part of the molten pool. The oxidic pool is bounded thermally and fluid-dynamically by the developed crust. By this boundedness, the heat transfer structure in the stratified oxidic/metallic pool can be solved separately. The thermal boundary condition of the oxidic pool is isothermal with constant melting temperature of the oxidic material. The decay heat is transferred to the side wall (crust formed around vessel inner surface) and upper interface between oxidic and metallic layer (crust formed between them). The heat transferred from the bottom oxidic layer is imposed to the upper metallic layer. This transferred heat in the metallic pool is removed through side and upper surface, which is augmented also by natural convection developed in the pool. To evaluate the heat balance of the molten pool, a simplified lumped-parameter (LP) model using heat transfer correlations was developed in this study, instead of a detailed analysis associated with a sophisticated numerical tool, such as the LILAC code. Detailed descriptions of the LP model is given in Reference 5-2.

5.3.4.2 Numerical results

For eight cases of hypothetical severe accident sequences introduced in Table 5-2 and Table 5-3, the initial conditions of relocated molten material masses are imported into the lumped-parameter (LP) code. The LP code assumes that the molten materials relocated in the APR1400 RPV lower head are stratified

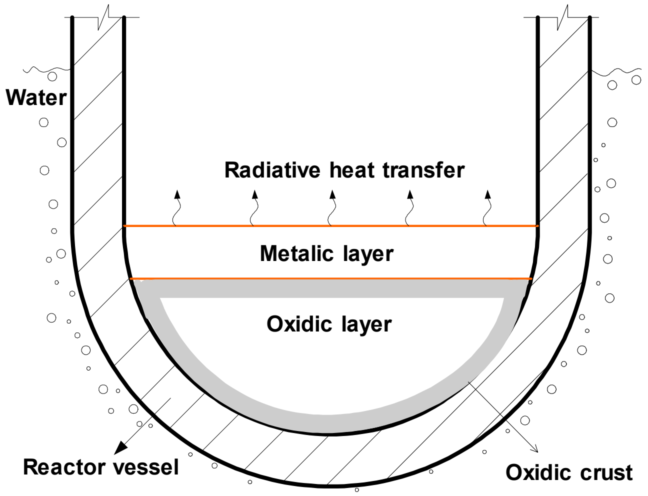

Figure 5-29. Metal-oxide stratified pool, reference[5-22]

into two layers such as oxidic and metallic layers. Here, additional mass of steel (50 ton) is assumed to be included in the metallic layer as a base case. Thermal properties of oxidic/metallic mixtures were calculated using correlations described in the MATPRO code. With mixture density of each layer, molten pool configurations are defined. Table 5-5 depicts geometric information such as pool depth, aspect ratio and pool angle for two-layer stratified pools. The oxidic material is filled in APR1400 lower head from 67 to 72 degrees from the bottom center. The aspect ratio H/R of the oxidic layer is about 06 ~ 0.7. From the BALI experiment,[5-22] thermal splitting defined as upward heat flow to total power of heat generation is in the range of 0.52 ~ 0.54 for these pool configurations.

Table 5-5. Molten pool geometries for the accident scenarios.

Case	TLFW w/o SDS	TLFR w SDS	SBO	1.35” LOCA
Oxide Layer				
Depth (m)	1.67	1.44	1.67	1.64
Aspect ratio, H/R	0.70	0.60	0.70	0.69
Pool Angle, degrees	72.90	66.90	72.70	71.90
Metallic Layer				
Depth (m)	0.59	0.63	0.58	0.60
Aspect ratio, H/R	0.26	0.28	0.24	0.26
Pool Angle, degrees	87.50	82.60	87.00	86.70
Case	**2.00” LOCA**	**3.00” LOCA**	**4.28” LOCA**	**9.60” LOCA**
Oxide Layer				
Depth (m)	1.52	1.49	1.46	1.45
Aspect ratio, H/R	0.64	0.63	0.61	0.61
Pool Angle, degrees	69.00	68.30	67.30	67.20
Metallic Layer				
Depth (m)	0.55	0.59	0.61	0.54
Aspect ratio, H/R	0.24	0.26	0.28	0.24
Pool Angle, degrees	82.80	83.20	82.70	80.80

The calculated results using LP code are summarized in Table 5-6. The Rayleigh number of the oxidic layer ranges from 5×10^{15} to 1×10^{16} because of the high values of the volumetric heat generation in the pool which is in all the cases above 2 MW/m^3. It means that the natural convection in the oxidic layer by decay heat in uranium oxide is in the highly turbulent regime. The maximum heat flux to the vessel wall is largely dependent on the accident scenarios. For the 9.6 inch LOCA, it reaches 1.75 MW/m^2. Its minimum value is obtained for the case of the 1.35 inch LOCA, which is 1.08 MW/m^2. The thermal splitting number calculated from the LP code is very similar to the BAIL experimental results. The upward heat from the oxidic layer directly affects natural heat transfer in the metal layer. The calculated upward heat flux is above 1 MW/m^3 in all of the cases considered, and its maximum is 1.84 MW/m^3 for the 9.60 inch LOCA.

Table 5-6. Calculated thermal loads for the accident scenarios.

Case	TLFW w/o SDS	TLFR w SDS	SBO	1.35” LOCA
Oxide Layer				
Volumetric heat generation, W/m^3	2.91E+06	2.95E+06	2.62E+06	2.32E+06
Ra number	1.06E+16	4.81E+15	9.45E+15	7.40E+15
Bulk temperature, K	3143.7	3133.4	3122.9	3097.3
Maximum side heat flux, W/m^2	1.38E+06	1.22E+06	1.24E+06	1.08E+06
Upward heat flux, W/m^2	1.47E+06	1.30E+06	1.32E+06	1.15E+06
Thermal Splitting, P_{up}/P_{tot}	0.51	0.53	0.51	0.52
Metallic Layer				
Ra number of metallic pool	9.02E+09	8.88E+09	8.27E+09	7.94E+09
Bulk temperature, K	1772.0	1748.0	1766.0	1749.0
Average side heat flux, W/m^2	2.53E+06	1.97E+06	2.31E+06	1.93E+06
Heat flux concentration factor	1.72	1.52	1.76	1.68
Case	**2.00” LOCA**	**3.00” LOCA**	**4.28” LOCA**	**9.60” LOCA**
Oxide Layer				
Volumetric heat generation, W/m^3	2.54E+06	2.53E+06	3.19E+06	4.15E+06
Ra number	5.60E+15	5.01E+15	5.43E+15	6.28E+15
Bulk temperature, K	3108.1	3106.4	3154.4	3307.3
Maximum side heat flux, W/m^2	1.10E+06	1.09E+06	1.34E+06	1.75E+06
Upward heat flux, W/m^2	1.18E+06	1.16E+06	1.42E+06	1.84E+06
Thermal Splitting, P_{up}/P_{tot}	0.53	0.53	0.53	0.53
Metallic Layer				
Ra number of metallic pool	7.42E+09	7.92E+09	9.29E+09	9.60E+09
Bulk temperature, K	1756.0	1746.0	1759.0	1804.0
Average side heat flux, W/m^2	2.05E+06	1.87E+06	2.20E+06	3.21E+06
Heat flux concentration factor	1.75	1.62	1.55	1.74

Compared to the oxidic layers, the metallic layers are in the low Rayleigh number natural convection regime. The metallic layers heated from the bottom surface; and the heat is transferred to the top and side surfaces. For the bottom wall heated pool like the metallic layer above the oxide pool in the reactor lower head, heat transfer is governed by Rayleigh-Benard natural convection mechanism. Existing experimental and numerical research shows that the top heat transfer rate is lower than the rate from the side wall. Because of the low heat transfer coefficient at the top surface of the metallic layer (in the current study, the top surface is cooled by radiation heat transfer), much of the heat from the bottom wall is released through the side wall. The most important parameter of the stratified molten pool is the heat flux concentration factor, which is the ratio between average side heat flux and imposed bottom heat flux. For the molten pool configurations considered in this study, the heat flux concentration factor is about 1.52 ~ 1.76, and the average side heat flux of the metallic layer is in the range of 1.87 ~ 3.21 MW/m^3. In the case of the 9.6 inch LOCA, the side heat flux reaches 3.2 MW/m^3.

In Figure 5-30, all the heat flux profiles (thermal loads on the reactor vessel) for non-LOCA and LOCA accidents in the APR1400 are shown and compared to the CHF on the vessel outer wall enhanced by surface coating and vessel insulation structure, proposed by Cheung.[5-11] For the TLFW with SDS and small break LOCA (1.35 inch, 2.0 inch, and 3.0 inch LOCAs), the thermal loads from the molten pool in the reactor vessel are below the enhanced CHF on the vessel outer wall. It means that for those severe accidents the corium pool in the reactor vessels could be cooled by the external reactor vessel cooling when the CHF is enhanced by the surface coating and vessel insulation structure. But for the TLFW without SDS and 9.6 inch large LOCA, the heat flux from the two-layered molten pool exceeds the available CHF. Also, the SBO accident and 4.28 inch mid LOCA are thought to be bounding cases for the external vessel cooling. Figure 5-31 shows the thermal load distributions for the accidents scenarios with CHF correlations with 5 degree subcooling. Though the subcooling of the external vessel cooling water increases the magnitudes of the plain CHF, it is still lower than the thermals loads from all the cases considered. But in the case of the enhanced CHF, it is greater than the thermal loads from all the cases except the 9.6 inch LOCA. It means that the enhanced CHF with subcooling can effectively remove the thermal loads from the stratified molten pools in most cases.

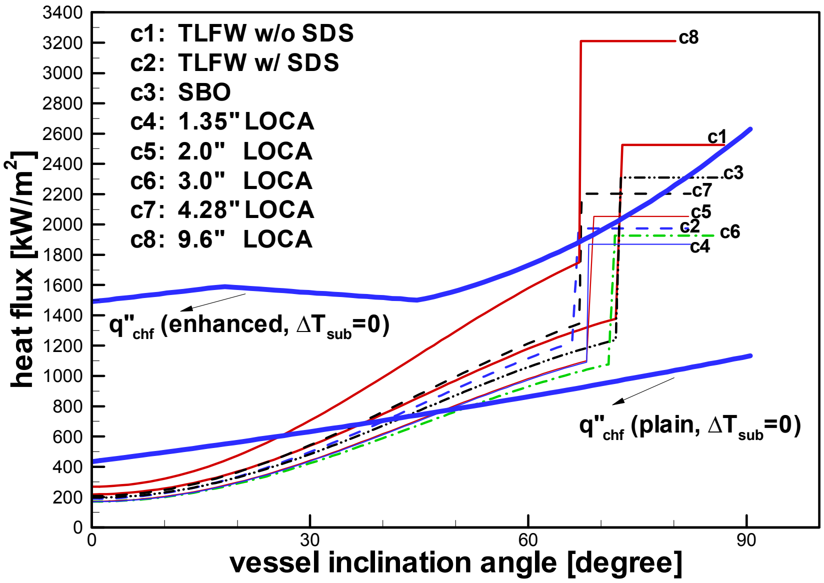

Figure 5-30. Comparisons of the thermal load distributions for the accidents scenarios with CHF correlations without subcooling.

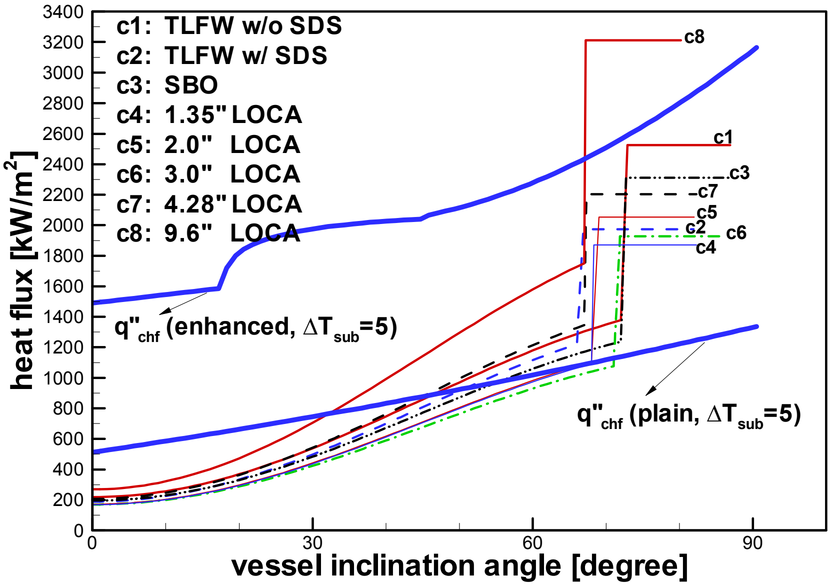

Figure 5-31. Comparisons of the thermal load distributions for the accidents scenarios with CHF correlations with 5 degree subcooling.

5.4. Conclusions

The objective of Task 4 is to assess the impact of Task 2 and 3 IVR design recommendations. Scenarios evaluated in Task 1 (see Section 2) are re-evaluated using Task 2 and 3 design recommendations to enhance core catcher and ERVC performance. As discussed in Section 1, assessments were conducted using several analytical tools. In these evaluations, INEEL applied the SCDAP/RELAP5-3D$^{©}$ and VESTA codes. KAERI applied the LILAC and a lumped parameter model.

Results from these analyses clearly show that the proposed enhancements are needed to provide additional margin for IVR when the vessel is subjected to the heat loads for Section 2 bounding conditions. In many of the cases evaluated, the enhanced cooling associated with a coated reactor vessel and an enhanced vessel/insulation configuration were sufficient to ensure IVR. Analyses also suggest that significant additional cooling may be possible with an IVCC. However, schedule and budget constraints precluded detailed analyses of the IVCC with newly-obtained narrow gap cooling heat transfer correlations being evaluated in this INERI.

In some of these calculations, analyses considered extreme conditions that had not been previously analyzed with these methods. As discussed in this section, certain model parameters were identified as inappropriate for simulating these conditions. Additional tasks for future analyses of such applications were identified to improve these models and provide additional insights about IVR.

5.4.1. INEEL Results

VESTA

Two debris endstate configurations were considered in the VESTA calculations: Configuration A, a stratified configuration with an upper metallic layer; and Configuration C, a stratified configuration with a lower metallic layer.

VESTA results for base case conditions in a Configuration A endstate indicate:

- Peak heat fluxes and associated CHF ratios occur near the top of the ceramic pool beneath the metallic layer.
- A small, but non-zero, probability exists for the CHF ratio to exceed 1.0.
- An IVCC must prevent melt relocation for at least 4 hours in order to maintain vessel heat fluxes below the CHF.
- Either of the explored ERVC enhancements are sufficient to reduce vessel heat fluxes below the CHF. If one considers uncertainties, the additional reduction offered by an enhanced insulation design is required to maintain heat fluxes below the CHF.
- An IVCC must decrease heat fluxes by at least a factor of 2 for this configuration.
- ERVC enhancements may decrease heat fluxes by factors of 2 to 5.

VESTA results for base case conditions in a Configuration C endstate suggest:

- Higher heat fluxes occur at vessel locations adjacent to the ceramic layer.
- CHF ratios peak at two locations for this configuration: near the bottom center of the vessel and near the top of the ceramic pool.

- Ether an IVCC, which can prevent relocation onto the vessel for at least 4 hours) or a vessel with the combined ERVC enhancements considered in this study are sufficient to maintain vessel heat fluxes below the CHF.

VESTA results suggest that either of the proposed IVR enhancements can preclude vessel heat fluxes from exceeding the CHF. Depending upon the selected IVR enhancement and debris endstate configuration, IVR margins may increase by factors ranging from two to four. The benefit associated with each enhancement is dependent upon the debris endstate (a condition that is not possible to predict at this time).

SCDAP/RELAP5-3D©

SCDAP/RELAP5-3D© was modified to allow simulation of ERVC from reactor vessels with microporous coatings, optimized insulation, and the combination of coatings and insulation based on PSU experimental results. Modifications were also added to simulate ERVC from plain vessels as a reference for gauging any potential IVR improvements that may be derived from implementing any of the ERVC enhancements.

SCDAP/RELAP5-3D© calculations using the ERVC modifications and the APR1400 model led to discovery of a deficiency in a code modeling parameter. The deficiency is related to the fact that the code model was not designed to simulate significant reactor vessel melting. Because project time and budget constraints precluded resolution of the deficiency, a limited number of calculations were completed using a fixed molten pool-to-vessel coefficient of 600 W/m^2-K. Results from these calculations indicate plain vessels will fail by melt through while coated vessel wall thinning will be limited (before vessel failure) by ERVC, given the same modeling assumptions and limitations. Although the absolute value of the results can be questioned (because a fixed coefficient was used), comparing plain and coated vessel results clearly indicates the use of microporous coatings has significant IVR benefits. Available information is sufficient to indicate that IVR benefits can be extended by exercising insulated and coated/insulated ERVC enhancement options. SCDAP/RELAP5-3D© modifications are needed before these improvements can be quantified.

Suggestions for Future Analyses

In completing this work, the following tasks were identified for future evaluations:

- Additional VESTA sensitivity studies to assess the impact of several input parameters and associated uncertainty distributions that were based on the Reference 5-12 analyses.
- Additional debris endstate configurations. VESTA currently models 3 distinct endstate configurations and SCDAP/RELAP5-3D© currently models 2 endstate configurations. It is suggested that these codes be applied to the remaining configurations that weren't considered in this INERI.
- A detailed SCDAP/RELAP5-3D© calculation to determine IVCC failure time and associated decay heat at the time that melt relocates to the vessel lower head. This SCDAP/RELAP5-3D© would incorporate SNU narrow gap cooling correlations that were recently developed in this INERI. VESTA calculations would then be performed using the IVCC failure time and a decay heat that is revised to considered the IVCC failure time and any dilution due to the IVCC being subsumed in the relocated corium.

- Additional VESTA calculations using a version that is updated with newly obtained SNU heat transfer correlations to simulate natural convection heat transfer in a volumetrically heated pool.
- The arbitrary fixed heat transfer coefficient of 10,000 W/m^2-K from the molten pool to the inner surface of the vessel wall currently in SCDAP/RELAP5-3D© should be replaced with time-dependent values calculated to yield heat flow equal to that associated with natural convection from the volumetrically heated molten pool.
- Vessel melting, including the latent heat of fusion associated with melting the reactor vessel wall, should be added to SCDAP/RELAP5-3D©.
- The composition of the SCDAP/RELAP5-3D© molten pool should be modified as a function of time to account for the progression of vessel steel melting.
- Thermal properties of the SCDAP/RELAP5-3D© molten pool should replace the thermal properties of steel in those regions where the reactor vessel has melted.

Although the above tasks are not included in the workscope for this INERI, results from these tasks would provide additional insights about the benefits of proposed ERVC enhancements.

5.4.2. KAERI Analyses

Severe accident analyses of APR 1400 was performed to identify melt state of the in-vessel materials in the reactor vessel lower plenum at vessel failure in the high and low pressure sequences using SCDAP/RELAP5 computer code. High-pressure transients of a TLFW to the steam generators and a SBO, as well as low-pressure transients of 1.35 inch, 2.00 inch, 3.00 inch, 4.28 inch, and 9.60 inch break Loss of Coolant Accident (LOCA) without safety injection were evaluated from transient initiation to reactor vessel failure. As discussed in Section 2, SCDAP/RELAP5 results indicate that in all sequences, approximately 80 – 90% of the core material of 154.2 tons was melted and relocated to the lower plenum of the reactor vessel at the time of reactor vessel failure in the APR 1400, which resulted in reactor vessel failure by creep. Volumetric heat source in the corium pool was estimated as 1.9-3.7 MW/m^3. Corium temperature was predicted to be approximately 2,800 – 3,400 K at the time of reactor vessel failure. The highest volumetric heat source sequence is the 9.6 inch break LOCA without safety injection in APR 1400, because this sequence leads to early reactor vessel failure.

LILAC

The thermal characteristics of a molten pool in the lower head vessel for the 3 inch LOCA cases were analyzed using the LILAC code, and the calculated thermal load on the reactor vessel wall was compared to that obtained using a lumped parameter model. In this study, the stratified two-layer molten pool is solved separately based on the postulation that the oxidic layer is entirely surrounded by its crust. The calculated heat flux distribution along with pool angle is very similar to that of the lumped parameter analysis. The thermal load from the metallic layer is linearly distributed in the result of the LILAC code simulation. But the averaged heat flux is approximately same as the result of the lumped parameter calculation. From this comparative study between the CFD and lumped parameter analyses, it could be concluded that the lumped parameter analysis is simple but useful for evaluating the thermal loads on the reactor vessel during a severe accident.

Lumped Parameter Method

Using a lumped-parameter (LP) model, the thermal load to the reactor vessel from the molten pool was analyzed for the APR1400. For eight cases of hypothetical severe accidents simulated using the SCDAP/RELAP code, the relocated molten material masses was imported into the lumped parameter code. The heat flux distribution in the vessel wall for the chosen severe accidents were calculated using the lumped parameter code and compared to the CHF values that are applied on the vessel outer wall during ERVC. The plain CHF, which is normally found in literature, is too low to remove the thermal loads applied during the severe accidents. When the CHF is enhanced by surface coating and vessel insulation structure, it is seen that the thermal loads from the half of the selected severe accidents especially small break LOCA and TLFW with SDS can be effectively removed by the ex-vessel cooling. The subcooling of the cooling water increases the magnitude of the critical heat flux a little. The enhanced CHF with the effect from the 5 degree subcooling is greater than the thermal loads from all the cases except the 9.6 inch LOCA. It means that the enhanced CHF with subcooling can effectively remove the thermal loads from the stratified molten pools in most cases.

This study is confined to point value evaluation of IVR for a specific accident condition with some assumptions, to find a possibility of design improvement for IVR enhancement. Because many uncertainties still remained in late melt progression and melt pool behavior, a more extensive study is needed to conclude feasibility of new design features, especially IVCC, as a future work.

5.5. References

5-1. J. L. Rempe and D. L. Knudson, *Margin for In-Vessel Retention in the APR1400 - VESTA and SCDAP/RELAP5-3D© Analyses,* INEEL/EXT-04-02549, December 2004.

5-2. J.T. Kim, R.J. Park and S.B. Kim, “Assessment of IVR Enhancement using SCDAP/RELAP5 and LILAC Codes,” KAERI/GP-230/2005, KAERI, Dec. 2004.

5-3. J. Rempe, et al., “An Enhanced In-Vessel Core Catcher for Improving In-Vessel Retention Margins,” *Invited paper, Nuclear Technology NURETH10 Special Edition,* to be published 2005.

5-4. Y. H. Kim, S. J. Kim, S. W. Noh, K. Y. Suh, J. L. Rempe, F. B. Cheung, S. B. Kim, “Visualization of Boiling Phenomena in Inclined Rectangular Gap, *submitted to the International Journal of Multiphase Flow*, April 2004.

5-5. M. B. Dizon, J. Yang, F. B. Cheung, J. L. Rempe, K. Y. Suh, and S. B. Kim, “Effects of Surface Coating on the Critical Heat Flux for Pool Boiling from a Downward Facing Surface, *Journal of Enhanced Heat Transfer,* Vol. 11, pp. 133-150, 2004.

5-6. F. B. Cheung, J. Yang, M. B. Dizon, J. L. Rempe, K. Y. Suh, and S. B. Kim, “Scaling of Downward Facing Boiling and Steam Venting in a Heated Hemispherical Annular Channel,” *International Journal of Transport Phenomena,* Vol. 6, pp. 81-96, 2004.

5-7. J. L. Rempe, D. L. Knudson, K. G. Condie, K. Y. Suh, F. B. Cheung, and S. B. Kim, “Conceptual Design of an In-Vessel Core Catcher,” *Nuclear Engineering and Design,* invited paper for ICONE11 Special Edition, 230 (2004) 311-235.

5-8. D. L. Knudson, J. L. Rempe, K. G. Condie, K. Y. Suh, F. B. Cheung, and S. B. Kim, "Late-Phase Melt Conditions affecting the Potential for In-Vessel Retention in High Power Reactors," *Nuclear Engineering and Design,* invited paper for ICONE11 Special Edition, 230 (2004), 133-150.

5-9. J. L. Rempe, D. L. Knudson, K. G. Condie, K. Y. Suh, F. B. Cheung, and S. B. Kim, "Corium Retention for High Power Reactors by an In-Vessel Core Catcher in Combination with External Reactor Vessel Cooling," *Nuclear Engineering and Design,* invited paper for ICONE11 Special Edition, 230 (2004), 293-309.

5-10. C. S. Kim, K. Y. Suh, J. L. Rempe, F. B. Cheung, S. B. Kim, "Effect of Interfacial Wavy Motion on Film Boiling Heat Transfer from Isothermal Downward-facing Hemispheres," *submitted to Nuclear Engineering and Design*, August 2004.

5-11. F. B. Cheung, J. Yang, and M. B. Dizon, "SBLB Results for Task 3 on External Reactor Vessel Cooling (ERVC) Boiling Data and CHF Enhancement Correlations," PSU Letter Report #PSU/MNE-2004-INEEL-2, September 30, 2004.

5-12. J. L. Rempe, et al., *Potential for In-Vessel Retention through Ex-vessel Flooding*, INEEL External Report INEEL/EXT-97-00779, December 1997. *Document submitted to ACRS as part of AP600 design certification review.*

5-13. J. L. Rempe, et. al, "Impact of Uncertainties on the Response of an Externally Flooded Vessel," *published in the transactions from the Fourth International Conference on Probabilistic Safety Assessment and Management (PSAM-4)*, September 13-18, 1998, New York, NY.

5-14. J. L. Rempe, et al, "Evaluation of In-Vessel Retention through Ex-vessel Flooding," *Transactions from the Sixth International Conference on Nuclear Engineering (ICONE-6),* May 1998, San Diego, CA.

5-15. J. L. Rempe, et al., "Potential for In-Vessel Retention through Ex-vessel Flooding," *paper published in transactions of OECD/ CSNI Workshop on In-Vessel Debris Retention and Coolability*, March 3-6, 1998, Garching, Germany.

5-16. T. G. Theofanous et al., *In-Vessel Coolability and Retention of a Core Melt,* DOE/ID-10460, Revised October 1996.

5-17. OECD MASCA Project website: www.nsi.kiae.ru.

5-18. The SCDAP/RELAP5-3D© Development Team, *SCDAP/RELAP5-3D© Code Manuals*, INEEL/EXT-02/00589, Idaho National Engineering and Environmental Laboratory, May 2002.

5-19. F. Mayinger et al., *Examination of Thermal-Hydraulic Processes and Heat Transfer in a Core Melt*, BMFT RS 48/1, Institute for Verfahrenstechnik der T. U. Hanover, 1976.

5-20. M. Jahn and H. H. Reineke, "Free Convection Heat Transfer with Internal Heat Source, Calculations and Measurements", *Proceedings of the International Meeting on Thermal Nuclear Reactor Safety*, NUREG/CR-0027, February 1983.

5-21. K.H. Kang, et al., "An Experimental Study on In-vessel Debris Retention through Gap Cooling," KAERI/TR-1334/99, KAERI, 1999.

5-22. J. M. Bonnet and C. Villermaux, “BALI-metal Test Reports: Focusing Effect Investigation”, SETEX/LTEM/01-263, CEA, France, 2001.

6. CONCLUSIONS

Key accomplishments from this three year program are highlighted in this section. Note that these accomplishments include items required to meet task objectives outlined in the original proposal for this project and items that meet overall NERI objectives. As indicated below, this project not only advanced the state-of-the art in research pertaining to in-vessel retention, but also helped prepare graduate students to join the nuclear engineering workforce.

➔ ***Task 1 SCDAP/RELAP5-3D© and SCDAP/RELAP5MOD3.3 calculations completed to provide late-phase melt conditions.***

The objective of the Task 1 effort was to obtain quantify representative late-phase melt conditions that could affect the potential for in-vessel retention (IVR) of core melt following a severe accident in the Korean Advanced Power Reactor 1400 MWe (APR1400). The late-phase melt conditions of specific interest include the melt mass and its composition, temperature, and power (due to decay heat generation). Several severe accident transients were selected for analysis that would lead to bounding estimates of the potential melt conditions. Results generated through completion of this task were used as inputs in the design of a core catcher (in Task 2) and the enhancement of external reactor vessel cooling (ERVC) (in Task 3). The results were also used in Task 4 as base values to estimate improvements in IVR margins that could be achieved through incorporation of concepts developed through the Task 2 and 3 design efforts. To accomplish the task objective, INEEL applied the SCDAP/RELAP5-3D© code and KAERI applied the SCDAP/RELAP5/MOD3.3 and SCDAP/RELAP5-3D© codes to the APR1400 plant. Some of the key conclusions and insights from this task are highlighted below.

SBO and LOCA transients were selected for analysis.

Although an extensive series of severe accident calculations is required to identify bounding transients, Loss of Coolant Accidents (LOCAs), Station BlackOuts (SBOs), and Loss of Feedwater (LOFW) scenarios were assumed to be major IVR scenarios. Accordingly, a cold leg break (representing the LOCA response) and an SBO with LOFW (to combine remaining dominant IVR scenarios) were selected for analysis.

SCDAP/RELAP5/MOD3.3 results are similar to SCDAP/RELAP5-3D© results.

Predicted values for vessel failure time, hydrogen generation, melt relocation masses, melt relocation volumes, decay heat in the relocated corium, and power densities in the relocated corium were compared, and differences were not considered significant.

Calculation results indicate a LOCA yields the most severe lower head thermal loads.

A 0.0465 m^2 break in one of the cold legs in the primary coolant loop containing the pressurizer resulted in core melt and relocation into the lower head by 4,990 s. The timing of this relocation was earlier than all other transients analyzed (by as much as 6,110 s). Consequently, power retained in the melt was relatively high (because the decay period after reactor trip was relatively short). The high decay power associated with this relocation yielded the highest thermal load for the APR1400 lower head.

Late-phase melt conditions include large masses that relocate at high temperatures.

Regardless of the transient considered, results for all calculations include relocation of large melt masses (~100,000 kg total, or more) at high temperatures (~3,000 K, or higher). These results appear to be consistent with the nature of the transients considered. Specifically, all cases involved complete core dryout and subsequent core heatup in a steam environment. Protracted periods (~1 h, or more) of complete core uncovery were sustained in each calculation, leading to development of large core melt masses at temperatures well above the fuel liquidus.

In the absence of any ERVC enhancements, estimated heat fluxes that must be removed from the lower head to ensure IVR of core melt in APR1400 exceed predicted heat fluxes and corresponding CHF values predicted for the Westinghouse AP600 reactor.

Estimated lower head average heat fluxes for the APR1400 transients considered ranged from 0.147 to 1.64 MW/m^3, which exceed peak lower head heat fluxes predicted for the Westinghouse AP600 reactor by factors as high as ~2.3. Furthermore, the estimated APR1400 average heat fluxes exceed the current estimates of the maximum CHF by as much as a factor of ~1.2. These results indicate IVR may not be feasible without additional measures such as the use of a core catcher and/or modifications to enhance ERVC.

➔ ***Task 2 activities to develop and evaluate an enhanced In-Vessel Core Catcher completed.***

The objective of Task 2 was to develop an enhanced in-vessel core catcher (IVCC) design for the APR1400 and provide sufficient data to evaluate if this design will enhance in-vessel debris coolability in the reactor. This effort included developing a preliminary in-vessel design with a combination of scoping materials, flow, thermal, and structural analyses and scoping materials interaction tests. In addition, more detailed experimental data were obtained in two areas to support analysis of this IVCC. First, data were needed to estimate the heat that can be removed from the narrow “engineered” gap between the IVCC and the inner surface of the reactor vessel. Such data were obtained from the GAMMA facilities at SNU and the CHFG facility at KAERI to formulate a complete “narrow gap” boiling curve. Second, data were needed to understand the heat loads to the core catcher and demonstrate the viability of materials proposed for the IVCC. These needs were addressed by conducting tests in several facilities: the SIGMA facilities at SNU were used to develop natural convection heat transfer correlations, the LAVA-GAP facility at KAERI was used to assess the impact of the IVCC on thermal heat loads to the vessel, and INEEL's High Temperature Test Laboratory (HTTL) was used to assess the potential for materials interactions.

Evaluations completed in this INERI suggest that the proposed IVCC concept is viable and will reduce heat loads to the vessel for a range of severe accident conditions. However, it should be noted that only preliminary IVCC design and evaluations were completed in this INERI. More detailed analyses and testing are needed before an IVCC could be implemented into a reactor. In particular, tests are needed to confirm the long-term endurance of proposed materials to hydrodynamic loads during operating and accident conditions. In addition, confirmatory tests of irradiation and coolant chemistry effects on coating performance may be warranted. Key conclusions and insights from this effort are summarized below.

Conceptual IVCC design for the APR1400 completed.

Several in-vessel and ex-vessel core catcher concepts proposed in the literature were reviewed by INEEL as an initial step for developing an IVCC design. After reviewing these various approaches, a list of design goals and criteria was formulated for developing an APR1400 IVCC design. These goals and criteria provided guidance in selecting the configuration, dimensions, and materials for the APR1400 IVCC. The core catcher design proposed by INEEL in this INERI consists of several interlocking sections that are machined to fit together when inserted into the lower head. The use of interconnected sections of the core catcher reduces manufacturing costs and simplifies installation. Each section of the IVCC consists of two material layers with an option to add a third layer (if deemed necessary): a base material, which has the capability to support and contain the mass of core materials that may relocate during a severe accident; an oxide coating material on top of the base material, which resists interactions with high-temperature core materials; and an optional coating on the bottom side of the base material to prevent any potential oxidation of the base material during the lifetime of the reactor.

Scoping analyses and materials testing used to select IVCC materials.

INEEL used a combination of scoping materials, flow, thermal, and structural analyses and scoping materials interaction tests to identify IVCC materials. Results suggest that the core catcher base material should be either carbon steel or a stainless steel, such as SS 304. However, the use of stainless steel is recommended because it would preclude the need for a corrosion-resistant undercoating on the IVCC. Evaluation efforts suggest that the insulator coating should be applied using thermal plasma spray techniques. Although several candidate coatings appear viable, results suggest that the insulator coating should consist of a 500 μm thick ZrO_2 coating over a 100-200 μm thick bond coating of Inconel 718.

Key insights and a new correlation to quantify heat transfer in the narrow gap between the IVCC and the reactor vessel lower head developed using GAMMA facilities.

SNU completed a series of fundamental studies to develop engineering correlations and to visualize the complex flow patterns in narrow gaps using the GAMMA 1D (Gap Apparatus Mitigating Melt Attack One Dimensional) apparatus. In addition, the GAMMA 2D (Gap Apparatus Mitigating Melt Attack Two Dimensional) experiments were performed to investigate the effects of gap size and pressure on CHF. Key insights from these studies are summarized below.

- The gap size and surface orientation effects play an important role in interpreting the general two-phase flow behavior as well as the CHF data. There exists a critical gap size commensurate to the average vapor layer thickness that enhances the heat transfer rate with increasing mass flux at certain surface orientations.
- The CHF generally increases as the gap size increases, but the increasing rate decreases as the gap increases. In particular, the CHF in the 10 mm gap is smaller than the value at any other gap sizes at the fully downward-facing location, 180^o. At the vertical location, 90^o, as is generally believed, the CHF increases as the gap size increases. The CHF in gap boiling is affected by the gap size as well as by the induced flow within the channel.
- There is a transition angle for each gap size. The transition angle increases as the gap size increases in this study. The transition angles for the 2, 5 and 10 mm gaps in this study were found to be 165^o, 170^o and 175^o, respectively. However, the transition angle was not discernible for the gap size of 1 mm and the pool boiling in the unconfined space.
- A semi-empirical CHF correlation was developed for the near-vertical gap boiling using dimensional analysis of the CHF during natural convective boiling in confined channels because the existing correlation could not reasonably predict the data obtained in this study. This correlation agrees with the experimental data within ± 20%.

New data and insights about the heat load from relocated corium to the IVCC obtained using SIGMA tests.

The SIGMA (Simulant Internal Gravitated Material Apparatus) tests considered high modified Rayleigh number, Ra′, turbulent natural convection in a molten pool. The main results include the heat split fraction, angular heat flux distribution, and temperature distribution inside the molten pool. Tests were conducted in SIGMA 2D, which is a two-dimensional semicircular pool with diameter, height, and width of 500 mm, 250 mm, and 100 mm and in SIGMA 3D, which is a hemispherical pool employing the same internal heating method used in SIGMA 2D. Some key insights gained from these tests are highlighted below.

- The average Nu_{up} numbers obtained from SIGMA tests concur with most of the literature data. The average Nu_{dn} numbers obtained from SIGMA tests fall between data obtained from the literature.
- The ratio of the local to average Nu on the upper wall was unity at all locations. The heat flux profile along the lower wall and average upward heat transfer within this Ra′ range were in good agreement with the data obtained from previous numerical and experimental studies. The heat input increase results in an increase in Nu_{up} and Nu_{dn}, but with no change in the heat split ratio (Nu_{up}/Nu_{dn}) which was about 1.7, except for the case where $Ra' = 2.94\times10^{12}$ and $Nu_{up}/Nu_{dn} = 2.1$. The lowest heat transfer occurred at the bottom of the pool, which was a stagnation point, while the highest value was observed in the upper corner of the pool.
- When the top surface of the pool was insulated, the local heat flux was greater than in the uninsulated case by about 6%. In case of the adiabatic upper boundary condition, the internal heat transported by the strong buoyancy-induced flows was transferred sideward rather than upward in the upper region.

Simulant melt experiments completed in LAVA-GAP facility to investigate IVCC thermal and metallurgical performance.

The main objectives of the KAERI LAVA-GAP experiments were to examine the feasibility and sustainability of the IVCC under the various test conditions using hemispherical test sections and simulant melt. The uniqueness of the LAVA-GAP experiments is its ability to provide thermal and metallurgical data on the performance of an internally coated hemispherical IVCC in direct contact with high temperature simulant melt in a unique one-tenth scale facility. As part of this INERI, a total of six tests were completed that evaluated the impact of vary several condition parameters, such as the material of IVCC base material, the gap size between the IVCC and the lower head vessel, and the insulator coating and bond coat material. The major technical conclusions from the these simulant tests and associated LILAC calculations are summarized below.

- In several tests (LAVA-GAP-2 and LAVA-GAP-3), the internally coated IVCC has better thermal performance compared with the uncoated IVCC.
- LILAC calculation results suggest that the coating layer lessened the thermal attack transferred to the core catcher and improved the integrity of the core catcher for LAVA-GAP-3 test conditions.
- Metallurgical inspections for the LAVA-GAP-3 test specimen indicate that the base carbon steel showed stable and pure chemical compositions without any oxidation and interaction with the internal coating layer. Hence, these metallurgical inspection results suggest that the ZrO_2 coating protected the carbon steel base material.

- In other tests, internally coated core catchers experienced failures. These failures were attributed to differences in experimental conditions, such as gap size and material of the base steel. For example, the 5 mm thick gap in the LAVA-GAP-4 and LAVA-GAP-5 tests imply that this gap size is too narrow to allow sufficient water ingression and steam venting. It should also be noted that the LAVA-GAP test conditions were conservative in that there was no water present inside the IVCC (as expected to be present during a severe accident in an LWR).
- LAVA-GAP tests suggest that IVCC heat removal capability be enhanced by increasing the gap size between the IVCC and the vessel lower head (the gap size should be larger than 5 mm) and that the outer surface of the IVCC be coated with a microporous coating to enhance heat transfer.

HTTL prototypic materials tests investigate IVCC thermal and metallurgical performance.

Prototypic tests were completed at the INEEL High Temperature Test Laboratory (HTTL) to evaluate if candidate core catcher materials interact with high-temperature materials expected to relocate during a severe accident. Results from prototypic tests indicate that proposed core catcher materials and coatings would provide additional protection to the reactor vessel from materials that relocate from the reactor core during a severe accident. Tests conducted in inert and steam conditions indicate that proposed coating materials protect the core catcher substrate without any interactions with prototypic corium materials.

➔ ***Task 3 activities for developing and evaluating options to enhance ERVC completed.***

In Task 3, CHF on the outer surface of a simulated APR1400 reactor vessel was studied experimentally. The goal was to select an enhanced vessel/insulation design and a suitable vessel coating for CHF enhancement so as to substantially increase the thermal margin for IVR. Toward this end, ERVC tests were conducted using prototypic water (i.e., non-ionized tap water as expected for a flooded cavity) to evaluate the performance of various coating materials and to select a suitable bottleneck configuration at the minimum gap location for the enhanced vessel/insulation design. The vessel coating should promote downward facing boiling on the vessel outer surface and a suitable bottleneck configuration should facilitate steam venting through the annular channel between the vessel and the insulation structure, both of which should lead to considerable CHF enhancement.

In Task 3, various types of experiments were performed at SNU, PSU, and KAERI to obtain essential information. Key ERVC issues that were considered in Task 3 included delayed flooding of the reactor vessel owing to the large volume between the cavity floor and the lower head, local CHF limits for downward facing boiling on the vessel outer surface, thermal margin for maintaining the integrity of the reactor vessel, methods for ERVC enhancement, two-phase natural circulation through the gap between the reactor vessel and the insulation structure, and choking limit for steam venting during ERVC. To provide insights for addressing these key issues, boiling and two-phase flow tests were conducted in the DELTA and GAMMA facilities at SNU, the SBLB facility at PSU, and the HERMES-HALF facility at KAERI. Key insights gained from these tests are summarized below.

ERVC investigated with SNU DELTA-1D, DELTA-3D, and GAMMA-3D facilities.

At SNU, Task 3 tests were completed using three facilities: DELTA 1D, DELTA 3D, and GAMMA 3D.

- DELTA 1D is designed to estimate the effect of the inclination angle on interfacial wavy motion. In the DELTA 1D tests, one could observe the interfacial wavy motion of vapor film from the inclined flat plates. The measured wall temperatures took on similar values except at 5 mm from the leading edge because of the thinnest vapor film observed there. The interfacial wavelength of vapor film flow could unfortunately not be visualized due to thin vapor film thickness.

- DELTA 3D quenching tests were performed to observe the angular and curved effects on film boiling heat transfer. Comparisons between DELTA-3D data and previous studies indicate that the heat transfer coefficients obtained from the DELTA tests are greater than those from numerical analysis for laminar film boiling. Thus, the film boiling regime in the DELTA-3D tests is not simply laminar, but involves more complexities like the Helmholtz instability. For the DELTA-3D tests, the film boiling heat transfer coefficients considering interfacial wavy motion agree better with the experimental results within ± 4.5% than those for laminar film boiling analysis without the interfacial wave consideration. But the difference between laminar film boiling heat transfer coefficients and measured film boiling heat transfer coefficients is relatively smaller than those in the 294 mm diameter tests, so the simple laminar film boiling regime is considered to span a greater portion of the 120 mm test section area than of the 294 mm test section.
- GAMMA 3D is designed to measure the heat transfer coefficient and CHF for ERVC conditions. The experimental factors include the gap size, mass flow rate, pressure, the forced convection or natural circulation condition and the initial subcooling. GAMMA 3D results indicated that CHF values decrease as the inclination angle increases for large inlet subcooling. In other words, the angular qualities are augmented by the increase in enthalpy as the angle increases. The film boiling heat transfer coefficients on the downward-facing hemisphere were measured and analyzed.

Insights and correlations for ERVC enhancements gained from PSU SBLB tests.

Steady state boiling experiments using test vessels with and without coatings were conducted in the PSU Subscale Boundary Layer Boiling (SBLB) facility for the cases with and without an enhanced thermal insulation to investigate the separate effect as well as the integral effect of the enhanced insulation design and vessel coatings. The SBLB test facility consists of a water tank with a condenser assembly, a heated hemispherical test vessel with or without an insulation simulator, a data acquisition system, a photographic system, and a power control system. Key insights from these investigations are summarized below.

- For plain vessels without coatings or thermal insulation, the local boiling curve tended to shift upward and to the right as the angular position was increased from the bottom center toward the equator of the test vessel. For a given wall superheat, higher nucleate boiling rates were obtained in the locations downstream of the bottom center. The local CHF exhibited a minimum at the bottom center location and increased monotonically with the angular position toward the equator of the vessel.
- Unlike the trend observed for plain vessels, the local boiling curve for coated vessels without thermal insulation did not shift monotonically upward and to the right as the angular position was increased from the bottom center toward the equator of the test vessel. The local CHF limit at the bottom center was actually higher than the values for adjacent downstream locations up to $\theta = 28^o$. The local CHF exhibited a minimum at the $\theta = 14^o$ location rather than at the bottom center. This non-monotonic behavior of the local CHF variation was largely due to the capillary effect of the micro-porous coatings, where there was a continuous liquid supply from all radial directions toward the bottom center.
- For the case with thermal insulation, the nucleate boiling rates do not exhibit monotonic trend either, i.e., the local boiling curve does not shift upward and to the right monotonically with increasing angular position. Rather, the local CHF limit tended to increase from the bottom center

at first, then decrease toward the minimum gap location, and finally increase toward the equator. This non-monotonic behavior is evidently due to the local variation of the two-phase motions in the annular channel between the test vessel and the insulation structure.

- The optical and SEM records showed that the micro-porous layer coatings had the form of a porous matrix composed of interconnected channels and different pores on the surface. Improvement in nucleate boiling heat transfer and CHF could be attributed to the structure of the porous layer itself and the capillary action it induced. The matrix of cavities and voids within the coating effectively trapped vapor, which served as active nucleation sites. These sites in turn were fed with liquid flowing through the interconnected channels. The pores on the surface of the porous coating served as flow inlets for liquid supply to the heating surface, leading to appreciable enhancements in the local CHF limits.
- Micro-porous aluminum coating appeared to be very durable. Even after many cycles of steady state boiling, the vessel coating remained rather intact, with no apparent changes in color or structure. Moreover, the heat transfer performance of the coating was found to be highly desirable with an appreciable CHF enhancement but very little effect of aging. Although similar heat transfer performance was observed for micro-porous copper coating, the latter was found to be much less durable and tended to degrade after several cycles of boiling. It appeared that the most suitable coating material for ERVC is micro-porous aluminum coating.
- For a coated hemispherical vessel with thermal insulation, the bubbles were generated at a higher frequency compared to that for a plain vessel without thermal insulation. This clearly indicates that a vessel with micro-porous surface coating would give rise to a shorter boiling cycle. Such enhanced boiling cycle explains the increased nucleate boiling rate for a coated vessel because more latent heat of vaporization could be transferred per unit time from the reactor surface.
- For a coated vessel with thermal insulation, the vapor bubbles generated in the bottom center region did not tend to agglomerate. This behavior could be due to the availability of vapor escape paths provided by the porous cavities of the coating. Although vapor bubbles tended to disperse on the coated vessel, a higher boiling site density resulted in a higher rate of heat removal, i.e., higher boiling rate.
- Depending on the angular position, a local CHF enhancement of 200% to 330% over a plain vessel could be achieved using an enhanced insulation structure with vessel coatings. It appears that ERVC with the use of vessel coatings and an enhanced insulation structure could provide sufficient cooling for high-power reactors such as APR1400.

Key insights about enhanced vessel /insulation configuration heat transfer gained from tests conducted in HERMES-HALF facility.

To observe and evaluate the two-phase natural circulation phenomena through the gap between the reactor vessel and the insulation in the APR1400 under external reactor vessel cooling, a HERMES-HALF experiment was performed in KAERI. The HERMES-HALF is a non-heating (air/water) experimental study on the two-phase natural circulation through the annular gap between the reactor vessel and the insulation. The objectives of this HERMES-HALF study are to observe and evaluate the two-phase natural circulation phenomena through the gap between the reactor vessel and the insulation in the APR1400. That is, the circulation flow rate, three dimensional effect, and flow instability in the gap between the APR1400 reactor vessel and insulation were simulated by the HERMES-HALF experiments. For these purposes, a half-scaled experimental facility was prepared utilizing the results of a scaling analysis to simulate the APR1400 reactor and insulation system.

- From flow observations, the choking flows in the near region of the shear key were observed. On the larger air injection rate and smaller outlet area condition, higher recirculation flows in the near region of the shear key were observed. Because of the choking phenomena, the periodical air back flow was generated near the minimum gap region under the higher air injection rate condition. Therefore, the design modification of the minimum gap region is required to ensure sufficient flow through the gap.
- Relationships between the re-circulation flow rate and the parameters in the insulation design were examined. As the water inlet areas increased, the natural circulation mass flow rates asymptotically increased and converged to a certain value. The outlet area also influenced the re-circulation flow rate. Experimental correlations on the natural circulation mass flow rates along the variation of the inlet / outlet area and wall heat flux were suggested.
- A certain condition of the inlet and outlet area of 0.15 m^2, the natural circulation flow rate could be increased up to 200 kg/s at high heat flux condition. These natural circulation flow rate values lead to about 1.3 – 1.45 MW/m^2 CHF values at the top of the lower head vessel (90 degrees).
- To maximize the heat removal capability by enhancing the re-circulation flow rate through the gap between the reactor vessel and the insulation, extensive experimental results are required for a wider range of design parameters such as the inlet position and outlet location. And also, a detailed 3-dimensional flow analysis is necessary to evaluate the local effect such as choking phenomena near the shear key. To implement the experimental data to real situation, the similarity of the non-heating experiment to the heating experiment should be verified.

➔ ***Task 4 activities completed to evaluate enhanced IVR margin associated with options proposed in this INERI.***

The objective of Task 4 is to assess the impact of Task 2 and 3 IVR design recommendations. Scenarios evaluated in Task 1 were re-evaluated using Task 2 and 3 design recommendations to enhance core catcher and ERVC performance. Assessments were conducted using several analytical tools. In these evaluations, INEEL applied the SCDAP/RELAP5-3D© and VESTA codes. KAERI applied the LILAC and RELAP codes and a lumped parameter model.

Calculation results show that proposed enhancements are needed to provide additional margin for IVR when the vessel is subjected to Task 1 bounding heat loads. In many of the cases evaluated, the enhanced cooling associated with a coated reactor vessel or an enhanced vessel/insulation configuration was sufficient to reduce heat fluxes below CHF. Even greater margins for IVR were predicted for cases with both a coated vessel and an enhanced vessel/insulation configuration. Analyses also suggest that significant additional cooling is possible with an IVCC. Highlights from these calculations are summarized below.

SCDAP/RELAP5-3D© predictions suggest proposed IVR enhancements reduce vessel heat fluxes below CHF.

For Task 4, SCDAP/RELAP5-3D© was modified to allow simulation of ERVC from reactor vessels with microporous coatings, optimized insulation, and the combination of coatings and insulation based on PSU experimental results. Modifications were also added to simulate ERVC from plain vessels as a reference for gauging any potential IVR improvements that may be derived from implementing any of the ERVC enhancements. All calculations were completed using relocation conditions associated with a large loss-of-coolant accident (LOCA) in the APR1400.

Initial evaluations indicated that the coefficient assumed by SCDAP/RELAP5-3D© for modeling heat transfer when molten materials are in direct contact with the reactor vessel (in the absence of a solidified corium crust) was invalid for molten pools with high decay heat like the LOCA-1 case. Although data are not available for quantifying this heat transfer coefficient, a series of iterative calculations were completed to determine a value (600 W/m^2-K) that appeared to yield physically reasonable results.

Results suggest that plain vessels without any of the proposed enhancements will fail by melt through. However, calculations indicate wall thinning is limited if proposed ERVC enhancements are included. SCDAP/RELAP5-3D© predictions indicate that the selected molten corium-to-vessel heat transfer coefficient of 600 W/m^2-K can lead to large vessel surface heat fluxes, with some closely approaching, but not exceeding, the CHF at specific angular positions. Hence, comparisons of plain and coated vessel SCDAP/RELAP5-3D© predictions indicate the use of microporous coatings has significant IVR benefits.

> ***VESTA results suggest that either of the proposed IVR enhancements can preclude vessel heat fluxes from exceeding the CHF.***

Two debris endstate configurations were considered in the VESTA calculations: Configuration A, a stratified configuration with an upper metallic layer; and Configuration C, a stratified configuration with a lower metallic layer. Several types of cases were evaluated for each debris endstate.

- A base case without an IVCC or enhanced ERVC.
- Bases case sensitivities to assumed steel relocation mass.
- Sensitivities that simulate the use of an IVCC.
- Sensitivities to various types of enhanced ERVC.

VESTA results for base case conditions in a Configuration A endstate indicate:

- Peak heat fluxes and associated CHF ratios occur near the top of the ceramic pool beneath the metallic layer.
- A small, but non-zero, probability exists for the CHF ratio to exceed 1.0.
- An IVCC must prevent melt relocation for at least 4 hours in order to maintain vessel heat fluxes below the CHF.
- Either of the explored ERVC enhancements are sufficient to reduce vessel heat fluxes below the CHF. If one considers uncertainties, the additional reduction offered by an enhanced insulation design is required to maintain heat fluxes below the CHF.
- An IVCC must decrease heat fluxes by at least a factor of 2 for this configuration.
- ERVC enhancements may decrease heat fluxes by factors of 2 to 5.

VESTA results for base case conditions in a Configuration C endstate suggest:

- Higher heat fluxes occur at vessel locations adjacent to the ceramic layer.
- CHF ratios peak at two locations for this configuration: near the bottom center of the vessel and near the top of the ceramic pool.

- Either an IVCC, which can prevent relocation onto the vessel for at least 4 hours) or a vessel with the combined ERVC enhancements considered in this study are sufficient to maintain vessel heat fluxes below the CHF.

In summary, VESTA results suggest that any of the proposed IVR enhancements maintain vessel heat fluxes below the CHF. Depending upon the selected IVR enhancement and debris endstate configuration, IVR margins may increase by factors ranging from two to four.

LILAC results similar to values predicted by lumped parameter model.

The thermal characteristics of a molten pool in the lower head vessel for the 3 inch LOCA cases were analyzed using the LILAC code, and the calculated thermal load on the reactor vessel wall was compared to that obtained using a lumped parameter model. In this study, the stratified two-layer molten pool is solved separately based on the assumption that the oxidic layer is entirely surrounded by its crust. The calculated heat flux distribution along with pool angle is very similar to that of the lumped parameter analysis. The thermal load from the metallic layer is linearly distributed in results from the LILAC code simulation. However, the average heat flux is approximately the same as the result of the lumped parameter calculation (see below). From this comparative study between the CFD and lumped parameter analyses, it was concluded that the lumped parameter analysis is a simple, but useful, method for predicting the thermal loads on the reactor vessel during a severe accident.

Lumped Parameter method applied.

Using a lumped-parameter (LP) model, the thermal load to the reactor vessel from the molten pool was analyzed for the APR1400. For the eight cases of hypothetical severe accidents simulated using the SCDAP/RELAP code, the relocated molten material masses were imported into the LP code. The heat flux distribution in the vessel wall for the chosen severe accidents were calculated using the LP code and compared to the CHF values that are applied on the vessel outer wall during ERVC. The plain CHF, which is normally found in literature, is too low to remove the thermal loads applied during severe accidents. When the CHF is enhanced with a micro-porous coating and modified vessel/insulation structure, it is seen that the thermal loads from the half of the selected severe accidents, especially a small break LOCA and TLFW with safety depressurization system (SDS), can be effectively removed by ex-vessel cooling. The subcooling of the cooling water slightly increases the magnitude of the CHF. The enhanced CHF with the effect from the 5 degree subcooling is greater than the thermal loads from all the cases except the 9.6 inch LOCA. This suggests that enhanced CHF with subcooling can effectively remove the thermal loads from the stratified molten pools in most cases.

➔ ***Supported six students that successfully completed graduate degrees.***

University participation in this INERI allowed the following seven students to obtain graduate degrees.

- S. J. Kim, M.S. in Nuclear Engineering, Seoul National University, February 2003.
- Y. H. Kim, PhD in Nuclear Engineering, Seoul National University, February 2004.
- H. M. Son, M.S. in Nuclear Engineering, Seoul National University, February 2006 (Expected).
- C. S. Kim, PhD in Nuclear Engineering, Seoul National University, February 2006 (Expected).
- S. W. Noh, PhD in Nuclear Engineering, Seoul National University, February 2007(Expected).
- S. D. Lee, PhD in Nuclear Engineering, Seoul National University, February 2007(Expected).
- M. B. Dizon, M.S. in Mechanical Engineering, Pennsylvania State University, December 2002.

- J. Yang, M.S. in Mechanical Engineering, Pennsylvania State University, December 2002.
- J. Yang, PhD in Mechanical and Nuclear Engineering, Pennsylvania State University, August 2005 (Expected).

➔ ***Completed programmatic requirements on or ahead of schedule.***

As discussed in Section 7, all programmatic requirements were completed on schedule.

➔ ***Completed fifty-one peer-reviewed papers for publication (ten in archival journals and forty-one in conference proceedings). and twenty-six letter reports.***

As discussed in Section 7, this INERI has yielded (and continues to produce) several peer-reviewed conference and journal publications. Most of these papers were collaborative efforts.

7. PROGRAMMATIC INFORMATION

7.1. Project Milestone and Schedule

Figure 7-1 contains a project milestone schedule Gant chart, and Table 7-1 lists project milestones. As indicated in this figure and table, all programmatic requirements were completed on (or ahead of) schedule.

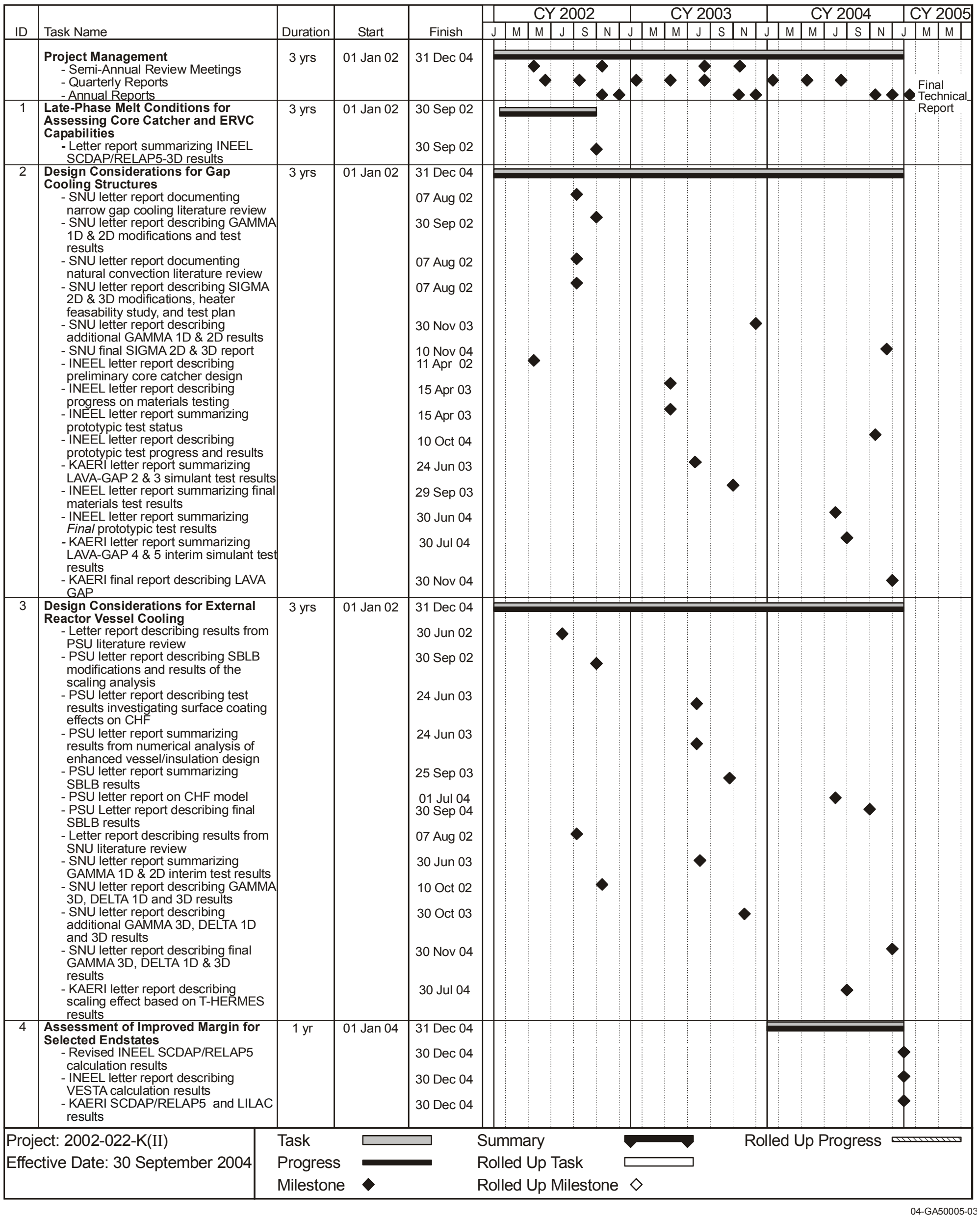

ID	Task Name	Duration	Start	Finish
	Project Management	3 yrs	01 Jan 02	31 Dec 04
	- Semi-Annual Review Meetings			
	- Quarterly Reports			
	- Annual Reports			
1	**Late-Phase Melt Conditions for Assessing Core Catcher and ERVC Capabilities**	3 yrs	01 Jan 02	30 Sep 02
	- Letter report summarizing INEEL SCDAP/RELAP5-3D results			30 Sep 02
2	**Design Considerations for Gap Cooling Structures**	3 yrs	01 Jan 02	31 Dec 04
	- SNU letter report documenting narrow gap cooling literature review			07 Aug 02
	- SNU letter report describing GAMMA 1D & 2D modifications and test results			30 Sep 02
	- SNU letter report documenting natural convection literature review			07 Aug 02
	- SNU letter report describing SIGMA 2D & 3D modifications, heater feasability study, and test plan			07 Aug 02
	- SNU letter report describing additional GAMMA 1D & 2D results			30 Nov 03
	- SNU final SIGMA 2D & 3D report			10 Nov 04
	- INEEL letter report describing preliminary core catcher design			11 Apr 02
	- INEEL letter report describing progress on materials testing			15 Apr 03
	- INEEL letter report summarizing prototypic test status			15 Apr 03
	- INEEL letter report describing prototypic test progress and results			10 Oct 04
	- KAERI letter report summarizing LAVA-GAP 2 & 3 simulant test results			24 Jun 03
	- INEEL letter report summarizing final materials test results			29 Sep 03
	- INEEL letter report summarizing *Final* prototypic test results			30 Jun 04
	- KAERI letter report summarizing LAVA-GAP 4 & 5 interim simulant test results			30 Jul 04
	- KAERI final report describing LAVA GAP			30 Nov 04
3	**Design Considerations for External Reactor Vessel Cooling**	3 yrs	01 Jan 02	31 Dec 04
	- Letter report describing results from PSU literature review			30 Jun 02
	- PSU letter report describing SBLB modifications and results of the scaling analysis			30 Sep 02
	- PSU letter report describing test results investigating surface coating effects on CHF			24 Jun 03
	- PSU letter report summarizing results from numerical analysis of enhanced vessel/insulation design			24 Jun 03
	- PSU letter report summarizing SBLB results			25 Sep 03
	- PSU letter report on CHF model			01 Jul 04
	- PSU Letter report describing final SBLB results			30 Sep 04
	- Letter report describing results from SNU literature review			07 Aug 02
	- SNU letter report summarizing GAMMA 1D & 2D interim test results			30 Jun 03
	- SNU letter report describing GAMMA 3D, DELTA 1D and 3D results			10 Oct 02
	- SNU letter report describing additional GAMMA 3D, DELTA 1D and 3D results			30 Oct 03
	- SNU letter report describing final GAMMA 3D, DELTA 1D & 3D results			30 Nov 04
	- KAERI letter report describing scaling effect based on T-HERMES results			30 Jul 04
4	**Assessment of Improved Margin for Selected Endstates**	1 yr	01 Jan 04	31 Dec 04
	- Revised INEEL SCDAP/RELAP5 calculation results			30 Dec 04
	- INEEL letter report describing VESTA calculation results			30 Dec 04
	- KAERI SCDAP/RELAP5 and LILAC results			30 Dec 04

Project: 2002-022-K(II)
Effective Date: 30 September 2004

Figure 7-1. INERI project schedule Gant chart.

.

Table 7-1. INERI Milestones and Completion Dates

Milestone / Task Description	Planned Completion Date	Actual Completion Date
Project Management and Integration		
Semi-Annual Review Meetings	April 15, 2002	April 15, 2002
	October 7, 2002	October 7-8, 2002
	July 8, 2003	July 8, 2003
	October 5, 2003	October 5, 2003
	June 2004	June 17-19, 2004
Quarterly Reports	May 14, 2002	May 14, 2002
	August 14, 2002	August 2, 2002
	January 15, 2003	January 15, 2003
	April 15, 2003	April 15, 2003
	July 15, 2003	July 14, 2003
	January 15, 2004	January 14, 2004
	April 15, 2004	April 12, 2004
	July 15, 2004	July 12, 2004
	October 15, 2004	October 15, 2004
Annual Reports	October 31, 2002	October 14, 2002
	October 15, 2003	October 14, 2003
Task 1: Late Phase Melt Conditions for Assessing Core Catcher and ERVC Capabilities		
Letter report summarizing INEEL SCDAP/RELAP5-3D results	November 15, 2002	September 30, 2002
Letter report summarizing KAERI SCDAP/RELAP5 results	December 15, 2004	December 15, 2004
Task 2: Core Catcher Design Enhancement		
INEEL Letter report describing preliminary core catcher design	October 10, 2002	April 11, 2002
INEEL letter report describing progress on materials testing	April 30, 2003	April 15, 2003
INEEL letter report summarizing prototypic test status	April 30, 2003	April 15, 2003
INEEL letter report summarizing interim prototypic test results	September 30, 2003	September 29, 2003
INEEL letter report summarizing final materials test results	March 18, 2004	March 18, 2004
INEEL letter report summarizing prototypic test results	June 30, 2004	June 30, 2004
SNU letter report documenting narrow gap cooling literature review	August 7, 2002	August 7, 2002
SNU letter report describing GAMMA 1D & 2D facility and test results	October 10, 2002	September 30, 2002
SNU letter report documenting natural convection literature review	August 7, 2002	August 7, 2002
SNU letter report describing SIGMA 2D & 3D, heater feasibility study, & test plan	August 7, 2002	August 7, 2002
SNU letter report summarizing GAMMA 1D and 2D interim results.	June 30, 2003	June 30, 2003
SNU letter report describing additional GAMMA 1D & 2D results	November 30, 2003	November 28, 2003
SNU letter report with SIGMA 2D & 3D results	November 30, 2004	November 30, 2004
KAERI letter report describing LAVA facility & test plans, and results	October 19, 2002	October 19, 2002
KAERI letter report summarizing LAVA-GAP 2 &3 simulant test results	June 30, 2003	June 24, 2003
KAERI letter report summarizing LAVA-GAP 4 & 5 interim simulant test results	July 30, 2004	July 30, 2004
KAERI letter report summarizing LAVA-GAP simulant test results	November 30, 2004	November 28, 2004
Task 3: External Reactor Vessel Cooling Design Enhancement		
Letter report describing results from SNU literature review	August 7, 2002	August 7, 2002
Letter report describing results from PSU literature review	June 30, 2002	June 25, 2002
PSU letter report describing SBLB modifications and results of scaling analysis	September 30, 2002	September 30, 2002
PSU letter report describing test results investigating surface coating effects on CHF	June 30, 2003	June 24, 2003
PSU letter report summarizing numerical analysis of improved vessel/insulation	June 30, 2003	June 24, 2003
PSU letter report summarizing tests investigating surface coating and improved vessel/insulation arrangement.	September 30, 2003	September 25, 2003
PSU letter report describing the development of a hydrodynamic CHF model	July 1, 2004	July 1, 2004
PSU letter report describing final SBLB results	September 30, 2004	September 30, 2004
SNU letter report describing GAMMA 3D, DELTA 1D & 3D modifications and results	October 10, 2002	October 10, 2002
SNU letter report describing additional GAMMA 3D, DELTA 1D & 3D test results	November 30, 2003	November 27, 2003
SNU final letter report describing GAMMA 3D, DELTA 1D & 3D results	November 30, 2004	November 27, 2004
KAERI letter report describing scaling and 3-D effects based on T-HERMES results	July 30, 2004	July 30, 2004
Task 4: Assessment of Improved Margin		
INEEL VESTA and SCDAP/RELAP5 results	December 30, 2004	December 29, 2004
KAERI SCDAP/RELAP5, LILAC, and Lumped Parameter results	December 30, 2004	December 29, 2004

7.2. Publications

As listed in Table 7-2, this INERI has yielded (and continues to produce) several peer-reviewed conference and journal publications. Most of these papers were collaborative efforts. All of these documents received appropriate export control reviews prior to their release. Electronic copies of final papers are available on the CD transmitted with this report.

Table 7-2. INERI Publications

Publications	Status
Archival Journals	
Y. H. Kim, S. J. Kim, K. Y. Suh, J. L. Rempe, F. B. Cheung, S. B. Kim, "Internal Vessel Cooling Feasibility Attributed by Critical Heat Flux in Inclined Rectangular Gap, *submitted to Nuclear Technology,* January 2005.	Draft paper submitted
Y. H. Kim, S. J. Kim, S. W. Noh, K. Y. Suh, J. L. Rempe, F. B. Cheung, S. B. Kim, "Visualization of Boiling Phenomena in Inclined Rectangular Gap," *submitted to the International Journal of Multiphase Flow,* January 2005.	Final paper submitted
C. S. Kim, K. Y. Suh, J. L. Rempe, F. B. Cheung, S. B. Kim, "Effect of Interfacial Wavy Motion on Film Boiling Heat Transfer from Isothermal Downward-facing Hemispheres," *submitted to Nuclear Engineering and Design*, January 2005.	Draft paper accepted
K.H. Kang, R.J. Park, S.B. Kim, F. B. Cheung, K. Y. Suh, and J. L. Rempe, "Simulant Melt Experiments on Thermal and Metallurgical Performance of the In-vessel Core Catcher," *submitted to Nuclear Technology,* June 2004.	Draft paper submitted
J. Rempe, D. Knudson, K. Condie, K. Y. Suh, F. B. Cheung, and S. B. Kim, "An Enhanced In-Vessel Core Catcher for Improving In-Vessel Retention Margins," *Invited paper, submitted to Nuclear Technology for NURETH10 Special Edition*, May 24, 2004.	Final paper submitted
M. B. Dizon, J. Yang, F. B. Cheung, J. L. Rempe, K. Y. Suh, and S. B. Kim, "Effects of Surface Coating on the Critical Heat Flux for Pool Boiling from a Downward Facing Surface, *Journal of Enhanced Heat Transfer*, Vol. 11, pp. 133-150, 2004.	Final paper published
F. B. Cheung, J. Yang, M. B. Dizon, J. L. Rempe, K. Y. Suh, and S. B. Kim, "Scaling of Downward Facing Boiling and Steam Venting in a Heated Hemispherical Annular Channel," *International Journal of Transport Phenomena,* Vol. 6, pp. 81-96, 2004	Final paper published
J. Rempe, D. Knudson, K. Condie, K. Y. Suh, F. B. Cheung, and S. B. Kim, "Conceptual Design of an In-vessel Core Catcher," *Nuclear Engineering and Design*, *Invited paper for ICONE11 Special Edition*, **230** (2004) 311-325.	Final paper published
J. Rempe, D. Knudson, K. Condie, K. Y. Suh, F. B. Cheung, and S. B. Kim, "Corium Retention for High Power Reactors by an In-vessel Core Catcher in Combination with External Reactor Vessel Cooling," *Nuclear Engineering and Design*, *Invited paper for ICONE11 Special Edition*, **230** (2004) 293-309.	Final paper published
D. Knudson, J. Rempe, K. Condie, K. Y. Suh, F. B. Cheung, and S. B. Kim, "Late-phase Melt Conditions affecting the Potential for In-Vessel Retention in High Power Reactors," *Nuclear Engineering and Design, Invited paper for ICONE11 Special Edition*, **230** (2004) 133-150.	Final paper published
Conference Proceedings and Presentations	
C. S. Kim, M. J. Yu, K. Y. Suh, J. Rempe, F. B. Cheung, and S.-B. Kim, "Film Boiling on Downward Facing Flat Plates with Varying Inclination Angles," 2005 ASME Heat Transfer Conference, San Francisco, CA, July 17-22, 2005.	Abstract submitted
S. D. Lee, H. M. Son, K. Y. Suh, J. Rempe, F. B. Cheung, and S.-B. Kim, "Prandtl Number Dependent Natural Convection in a Rectangular Pool with Internal Heat Sources," 2005 ASME Heat Transfer Conference, San Francisco, CA, July 17-22, 2005.	Abstract accepted
J. Yang, F. B. Cheung, J. L. Rempe, K. Y. Suh, and S. B. Kim, Correlations of Nucleate Boiling Heat Transfer and Critical Heat Flux for External Reactor Vessel Cooling, 2005 ASME Heat Transfer Conference, San Francisco, CA, July 17-22, 2005.	Draft paper submitted
J. Rempe, K. Y. Suh, F.-B. Cheung, and S.-B. Kim, "Insights from Investigations of In-Vessel Retention for High Power Reactors," *submitted to the 11th International Topical Meeting on Nuclear Reactor Thermal-Hydraulics (NURETH-11),* Popes Palace Conference Center, Avignon, France, October 2-6, 2005.	Abstract accepted
S. W. Noh, Y. H. Yu, J. K. Lee, K. Y. Suh, J. L. Rempe, F. B. Cheung, S. B. Kim, "Critical Heat Flux in Inclined Rectangular Narrow Long Channel," 2005 International Congress on Advances in Nuclear Power Plants (ICAPP'05), Seoul, Korea, May 15-19, 2005.	Abstract accepted
J. Yang, F. B. Cheung, J. Rempe, K. Suh, and S.-B. Kim, "Critical Heat Flux for Downward-facing Boiling on a Coated Hemispherical Vessel Surrounded by an Insulation Structure," *2005 International Congress on Advances in Nuclear Power Plants (ICAPP'05),* Seoul, Korea, May 15-19, 2005.	Draft paper submitted
J. L. Rempe, D. L. Knudson, K. G. Condie, F. B. Cheung, K. Y. Suh, and S. B. Kim, "Increased Margin Associated with Options to Enhance In-Vessel Retention," *2005 International Congress on Advances in Nuclear Power Plants (ICAPP'05),* Seoul, Korea, May 15-19, 2005.	Draft paper submitted

Table 7-2. INERI Publications

Publications	Status
C. S. Kim, K. Y. Suh, J. L. Rempe, F. B. Cheung, S. B. Kim, "Film Boiling Heat Transfer Modeling for Relatively Large-Diameter Downward-Facing Hemisphere," *4th Japan-Korea Symposium on Nuclear Thermal Hydraulics and Safety*, Sapporo, Japan, November 28 – December 1, 2004.	Presented and published
J. J. Kim, Y. H. Kim, S. J. Kim, S. W. Noh, K. Y. Suh, "Boiling Visualization and Critical Heat Flux Phenomena in Narrow Rectangular Gap," *4th Japan-Korea Symposium on Nuclear Thermal Hydraulics and Safety*, Sapporo, Japan, November 28 – December 1, 2004.	Presented and published
K. H. Lee, S. D. Lee, K. Y. Suh, "Natural Convection Heat Transfer with Low Prandtl Number Fluid," *ANS Winter Meeting*, Washington D. C., USA, November 14-18, 2004.	Presented and published
J. J. Kim, Y. H. Kim, K. Y. Suh, "Critical Heat Flux Propagation in Asymmetric Narrow Circular Channel," *ANS Winter Meeting*, Washington D. C., USA, November 14-18, 2004.	Presented and published
Y. H. Kim, S. J. Kim, J. J. Kim, S. W. Noh, K. Y. Suh, J. L. Rempe, and F. B. Cheung, S. B. Kim, "Critical Heat Flux Phenomena in One-Dimensional Narrow Gap," *3rd International Symposium on Two-Phase Flow Modeling and Experimentation*, Pisa, Italy, 22-24 September 2004	Presented and published
J. Yang, F. B. Cheung, J. L. Rempe, K. Y. Suh, and S. B. Kim, "Downward Facing Boiling and Steam Venting under Simulated ERVC Conditions," *Sixth International Topical Meeting on Nuclear Reactor Thermal Hydraulics, Operations and Safety (NUTHOS6),* Nara, JAPAN, October 4-8, 2004.	Presented and published
J. Yang and F. B. Cheung, "A Hydrodynamic CHF Model for Downward Facing Boiling on a Coated Vessel, *Sixth International Topical Meeting on Nuclear Reactor Thermal Hydraulics, Operations and Safety (NUTHOS6),* Nara, JAPAN, October 4-8, 2004.	Presented and published
K. H. Kang, R. J. Park, S. B. Kim, K. Y. Suh, F. B. Cheung, and J. L. Rempe, "Thermal and Metallurgical Performance of the Multi-layered In-vessel Core Catcher During Severe Accident," *Sixth International Topical Meeting on Nuclear Reactor Thermal Hydraulics, Operations and Safety (NUTHOS6),* Nara, JAPAN, October 4-8, 2004.	Presented and published
J. Rempe, K. Y. Suh, F.-B. Cheung, and S.-B. Kim., "In-Vessel Retention - Recent Efforts and Future Needs," *Sixth International Topical Meeting on Nuclear Reactor Thermal Hydraulics, Operations and Safety (NUTHOS6),* Nara, JAPAN, October 4-8, 2004.	Presented and published
J. Yang, M. B. Dizon, F-B. Cheung, J. L. Rempe, K. Y. Suh, and S-B. Kim, "Critical Heat Flux for Downward Facing Boiling on a Coated Hemispherical Surface," 2004 *Heat Transfer/Fluids Engineering Summer Conference*, Charlotte, NC, July 2004.	Final paper submitted
J. Yang, M. B. Dizon, F-B. Cheung, J. L. Rempe, K.Y. Suh, and S-B. Kim, "CHF Enhancement by Vessel Coating for External Reactor Vessel Cooling," *2004 International Congress on Advances in Nuclear Power Plants (ICAPP '04),* Pittsburgh, PA, USA, June 13-17, 2004.	Presented and published
K. H. Kang, R. J. Park, W. S. Ryu, S-B. Kim, K.Y. Suh, F-B. Cheung, and J. L. Rempe, "Thermal and Metallurgical Response of the In-vessel Core Catcher According to the Gap Size with the Lower Head Vessel," *International Congress on Advances in Nuclear Power Plants (ICAPP '04),* Pittsburgh, PA, USA, June 13-17, 2004.	Presented and published
K. Condie, J. Rempe, D. Knudson, K. Y. Suh, F-B. Cheung, and S-B. Kim, "Design and Evaluation of an Enhanced In-Vessel Core Catcher," *2004 International Congress on Advances in Nuclear Power Plants (ICAPP '04),* Pittsburgh, PA, USA, June 13-17, 2004.	Presented and published
J. J. Kim, Y. H. Kim, S J Kim, S. W. Noh, K.Y. Suh, J.L. Rempe, F-B. Cheung, and S-B. Kim, "Critical Heat Flux in Inclined Rectangular Narrow Gaps," *2004 International Congress on Advances in Nuclear Power Plants (ICAPP'04)*, Pittsburgh, PA, USA, June 13-17, 2004.	Final paper presented
K. H. Lee, S.D.Lee, K.Y. Suh, J.L. Rempe, F-B. Cheung, and S-B. Kim, "Prandtl Number Dependent Natural Convection with Internal Heat Sources," *2004 International Congress on Advances in Nuclear Power Plants (ICAPP'04)*, Pittsburgh, PA, USA, June 13-17, 2004.	Final paper presented
C. S. Kim, K. Y. Suh, J. L. Rempe, F.-B. Cheung, and S.-B. Kim, "Film Boiling on Downward Quenching Hemisphere of Varying Sizes," *Twelfth International Conference on Nuclear Engineering (ICONE12),* Washington, DC, April 2004	Presented and published
K. H. Kang, R. J. Park, S. B. Kim, K. Y. Suh, F. B. Cheung, and J. L. Rempe, Experiments on Performance of the Multi-Layered In-Vessel Core Catcher, *Twelfth International Conference on Nuclear Engineering (ICONE12),* Washington, DC, April 2004.	Presented and published
J. Rempe, D. Knudson, K. Condie, W. D. Swank, K. Y. Suh, F.-B. Cheung, and S.-B. Kim, "Materials Interaction Tests to Identify Base and Coating Materials for an Enhanced In-Vessel Core Catcher Design," *Twelfth International Conference on Nuclear Engineering (ICONE12)*, Washington, DC, April 2004.	Presented and published
S. W. Noh, Y. H. Kim, S. J. Kim, K. Y. Suh, J. L. Rempe, F. B. Cheung, and S. B. Kim, "An Experimental Study of Critical Heat Flux in Large Inclined One-Dimensional Channels," *Tenth International Topical Meeting on Nuclear Reactor Thermal Hydraulics (NURETH-10),* Seoul, Korea, October 2003	Presented and published
F. B. Cheung, J. Yang, M. B. Dizon, J. L. Rempe, K. Y. Suh, F.-B. Cheung, and S.-B. Kim, "On the Enhancement of External Reactor Vessel Cooling of High-Power Reactors." *Tenth International Topical Meeting on Nuclear Reactor Thermal Hydraulics (NURETH-10),* Seoul, Korea, October 2003.	Presented and published

Table 7-2. INERI Publications

Publications	Status
F. B. Cheung, et al., "Limiting Factors for External Reactor Vessel Cooling, *Tenth International Topical Meeting on Nuclear Reactor Thermal Hydraulics (NURETH-10),* Seoul, Korea, October 2003.	Presented and published
J. L. Rempe, D. L. Knudson, K. G. Condie, K. Y. Suh, F.-B. Cheung, and S.-B. Kim, "Development of an Enhanced In-Vessel Core Catcher for Improving IVR Margins," *Tenth International Topical Meeting on Nuclear Reactor Thermal Hydraulics (NURETH-10),* Seoul, Korea, October 2003.	Presented and published
K. H. Kang, R. J. Park, S. B. Kim, K. Y. Suh, F. B. Cheung, and J. L. Rempe, "Experiments on Enhancement of In-vessel Corium Retention through In-Vessel Core Catcher," *Tenth International Topical Meeting on Nuclear Reactor Thermal Hydraulics (NURETH-10),* Seoul, Korea, October 2003.	Presented and published
S. J. Kim, Y.H. Kim, S. W. Noh, K. Y. Suh, J. L. Rempe, F. B. Cheung, and S. B. Kim "Experimental Study of Critical Heat Flux in Inclined Rectangular Gap," *GENES4/ANP2003*, Kyoto, Japan; September 2003.	Presented and published
Y. H. Kim, S.J. Kim, S. W. Noh, and K. Y. Suh, "Critical Heat Flux in Narrow Gap in Two-Dimensional Slices under Uniform Heating Condition," *the 17th International Conference on Structural Mechanics in Reactor Technology (SMiRT-17)*, Prague, Czech, August 2003	Presented and published
M. B. Dizon, J. Yang, F. B. Cheung, J. L. Rempe, K. Y. Suh, and S. B. Kim, "Effects of Surface Coating on Nucleate Boiling Heat Transfer from a Downward Facing Surface, *2003 ASME Summer Heat Transfer Conference*, Las Vegas, Nevada, July 2003.	Presented and published
F. B. Cheung, J. Yang, M. B. Dizon, J. L. Rempe, K. Y. Suh, and S. B. Kim, "Scaling of Downward Facing Boiling and Steam Venting in a Reactor Vessel/Insulation System," *2003 ASME Summer Heat Transfer Conference*, Las Vegas, Nevada, July 2003.	Presented and published
S. D. Lee and K. Y. Suh, "Natural Convection Heat Transfer in a Small Hemispherical Vessel, *Second International Conference on Heat Transfer, Fluid Mechanics and Thermodynamics*, Victoria Falls, Zambia, June 2003	Presented and published
Y.H. Kim, S. J. Kim, S. W. Noh, and K. Y. Suh, "Critical Heat Flux in One-Dimensional Downward-Heated Channel," *American Nuclear Society (ANS) Annual Meeting*, San Diego, California, June 2003	Presented and published
Y. H. Kim and K. Y. Suh, "Maximum Boiling Heat Transfer in Two-Dimensional Slice Narrow Gap with Downward-Facing heating," *Second International Conference on Heat Transfer, Fluid Mechanics and Thermodynamics*, Zambia, June 2003	Presented and published
K. Y. Suh, Y. H. Kim, S. D. Lee, C. S. Kim, J. L. Rempe, F. B. Cheung, and S. B. Kim, "Engineered Safety Features for In-Vessel Retention of Large Power Reactors,*" Second International Congress on Advanced Power Plants*, Cordoba, Spain, May 2003.	Presented and published
S.J. Kim, Y.H. Kim, K. Y. Suh, J. L. Rempe, F. B. Cheung, and S. B. Kim, "One-Dimensional Downward-facing Critical Heat Flux Concerning Surface Orientation and Gap Size Effects," *Second International Congress on Advanced Power Plants,* Cordoba, Spain, May 2003.	Presented and published
J. L. Rempe, D. L. Knudson, K. G. Condie, K. Y. Suh, F.-B. Cheung, and S.-B. Kim, "A Strategy to Develop Enhanced In-Vessel Retention for Higher Power Reactors," *Eleventh International Conference on Nuclear Engineering (ICONE11),* Tokyo, Japan, April 2003.	Presented and published
J. L. Rempe, D. L. Knudson, K. G. Condie, K. Y. Suh, F.-B. Cheung, and S.-B. Kim, "Preliminary Investigations to Develop an Enhanced In-vessel Core Catcher Design," *Eleventh International Conference on Nuclear Engineering (ICONE11),* Tokyo, Japan, April 2003.	Presented and published
D. L. Knudson, J. L. Rempe, K. G. Condie, K. Y. Suh, F.-B. Cheung, and S.-B. Kim, "Late-Phase Melt Conditions Affecting the Potential for In-Vessel Retention in High Power Reactors," *Eleventh International Conference on Nuclear Engineering (ICONE11),* Tokyo, Japan, April 2003.	Presented and published
Project Reports (In additional to input received for Quarterly and Annual Reports, the following reports were exchanged).	
J. Rempe and D. Knudson, *Margin for In-Vessel Retention in the APR1400 - VESTA and SCDAP/RELAP5-3D Analyses,* INEEL/EXT-04-02549, December 2004.	Final Report Issued
J. T. Kim, R. J. Park, and S. B. Kim, A*ssessment of IVR (In-Vessel Retention) Enhancement using SCDAP/RELAP5 and LILAC Codes,* KAERI/GP-230/2005, December 2004.	Final Report Issued
F. B. Cheung, J. Yang, and M. B. Dizon, *SBLB Results for Task 3 on External Reactor Vessel Cooling (ERVC) Boiling Data and CHF Enhancement Correlations*, PSU/MNE-2004-INEEL-3, December 2004.	Final Report Issued
K. Y. Suh, C. S. Kim, and S. W. Noh, *Report on DELTA 1D & 3D Experiments and GAMMA 3D Results,* SNU/NE-2004-INEEL-2, November 30, 2004.	Final Report Issued
K. Y. Suh, S. D. Lee, and K. H. Lee, *Report on SIGMA 3D Experiments and Results,* SNU/NE-2004-INEEL-1, November 30, 2004.	Final Report Issued
K. H. Kang, R. J. Park, S. B. Kim, Experiments on Enhancement of In-vessel Corium Retention through In-vessel Core Catcher; Experimental Results of the LAVA-GAP-6 & 7 Tests, KAERI/GP-228/2004, November 2004.	Final Report Issued
F. B. Cheung, J. Yang, and M. B. Dizon, *SBLB Results for Task 3 on External Reactor Vessel Cooling (ERVC) Boiling Data and CHF Enhancement Correlations,* PSU/MNE-2004-INEEL-2, September 30, 2004.	Final Report Issued